

**From space to the ground:  
spectroscopic and weak lensing  
analysis of galaxy observations and  
simulations**

**DISSERTATION**

zur

Erlangung des Doktorgrades (Dr. rer. nat.)

der

Mathematisch-Naturwissenschaftlichen Fakultät

der

Rheinischen Friedrich-Wilhelms-Universität Bonn

vorgelegt von

**Diana Scognamiglio**

aus

Torre del Greco – Italien

Bonn, August 2022

Angefertigt mit Genehmigung der Mathematisch-Naturwissenschaftlichen Fakultät  
der Rheinischen Friedrich-Wilhelms-Universität Bonn

- 1. Gutachter: Prof. Dr. Peter Schneider
- 2. Gutachter: Prof. Dr. Cristiano Porciani

Tag der Promotion: 25.11.2022  
Erscheinungsjahr: 2022

*To myself, when I was 10*



---

## Abstract

---

Cosmology and astrophysics have entered an era of increasing rich data sets, not only from ground- and space-based observations, but also from simulations. This has allowed to advance in the most compelling science issues to better understand the Universe as a whole, using techniques, such as weak gravitational lensing (WL) and spectroscopic analyses.

On one side, wide-field space-based surveys such as *Euclid* will collect an unprecedented amount of data, enabling shear measurements based on the analysis of more than a billion galaxies in order to extract cosmological information. The increase of the accuracy with which we aim to understand the components of the Universe turns in an increase in our understanding and controlling of systematic errors. A common approach to correct the residual systematic biases in cosmic shear analyses is to calibrate shape measurement methods by using image simulations with known shear.

In this work we describe in detail a testing environment, which consists of creating *Euclidized* galaxy images, thought the ‘euclidization’ setup making use of emulated HST-like galaxy images as input and, compare them to ‘direct’ emulated *Euclid*-like images. For this we use the Kaiser-Squires-Broadhurst (KSB) shape measurement algorithm and galaxy model fits. This procedure allows us to test if the HST-observed galaxy images can be used to emulate *Euclid* observations of sheared galaxy images and to investigate if uncertainties in the HST Point-Spread Function (PSF) model introduce significant biases in the WL shear calibration.

On the other side, we use data from ground-based telescopes to investigate the nature of the descendants of massive early-type galaxies observed in the early Universe, Ultra-compact massive galaxies (UCMGs). UCMGs, i.e. galaxies with stellar masses  $M_\star > 8 \times 10^{10} M_\odot$  and effective radii  $R_e < 1.5$  kpc, are very rare

---

systems, in particular at low and intermediate redshifts. Their origin as well as their number density across cosmic time is still under scrutiny, especially because of the paucity of spectroscopically confirmed samples.

In this thesis, we present the results from a current investigation using targets from the Kilo Degree Survey (KiDS) conducted by the VLT Survey Telescope (VST) to carry out a spectroscopic analysis of UCMGs, building the largest sample of confirmed UCMGs. We present photometrical and structural parameters of 33 new candidates at redshifts  $0.15 \lesssim z \lesssim 0.5$  and confirm 19 of them as UCMGs, based on their nominal spectroscopically inferred  $M_*$  and  $R_e$ . From the spectra, acquired at the INT and TNG telescopes, we estimate their spectroscopic redshifts and velocity dispersions, and the latter are used to derive a preliminary mass–velocity dispersion correlation. We also quantify the impact of systematics on the UCMG photometric selection. We conclude with a summary and a discussion of our perspectives on future studies in the two fields investigated in the presented thesis.

---

# Contents

---

<b>Abstract</b>	<b>v</b>
<b>1. Introduction</b>	<b>1</b>
<b>2. Theoretical framework</b>	<b>5</b>
2.1. Modern Cosmology . . . . .	6
2.1.1. General Relativity . . . . .	7
2.1.2. The isotropic and homogeneous Universe . . . . .	8
2.1.3. Cosmological distances . . . . .	10
2.1.4. The $\Lambda$ CDM Model . . . . .	12
2.2. The physics of galaxy formation and evolution . . . . .	14
2.2.1. Galaxy classification . . . . .	16
2.2.2. Physical processes . . . . .	18
2.2.3. Tools for modeling galaxy formation and evolution . . . . .	19
2.2.4. Two-phase formation model . . . . .	20
2.2.5. Stellar population synthesis models . . . . .	21
2.2.6. Ultra-Compact Massive Galaxies . . . . .	23
2.3. Gravitational lensing . . . . .	26
2.3.1. Lens equation . . . . .	27
2.3.2. Deflection angle and deflection potential . . . . .	27
2.3.3. Image distortions . . . . .	30
2.3.4. Weak gravitational lensing . . . . .	32
2.4. Measuring weak lensing . . . . .	33
2.4.1. Sources of bias and calibration . . . . .	34
2.4.2. Shape measurements - KSB method . . . . .	38
2.4.3. Parameter measurements - Galaxy model fits . . . . .	40

<b>3. The surveys</b>	<b>41</b>
3.1. Space-based telescopes	41
3.1.1. The <i>Euclid</i> mission	42
3.1.2. The <i>Hubble</i> Space Telescope	45
3.2. Ground-based telescopes	48
3.2.1. Telescopio Nazionale Galileo	48
3.2.2. Isaac Newton Telescope	48
3.2.3. Data reduction	50
<b>4. Weak lensing image simulations for <i>Euclid</i> using HST-emulated data</b>	<b>53</b>
4.1. Motivation	54
4.2. Shear measurement formalism	56
4.3. Simulation and analysis setup	57
4.4. Simulation size and shape noise cancellation	60
4.5. Galaxy property measurements	61
4.5.1. KSB measurements	61
4.5.2. Galaxy model fit	63
4.6. Tests and results	64
4.6.1. Test I: Native pixel scales	64
4.6.2. Test II: Finer pixel scale	66
4.6.3. Test III: Hybrid approach with a pixel scale of $0''.05$ and binning of the Euclidized images	68
4.6.4. Test IV: Different HST PSF models	70
4.6.5. Test V: Truncation radius for the input galaxies	72
4.7. Analysis of the accuracy of the TinyTim PSF model for HST	74
4.7.1. Generation and analysis of TinyTim PSF models	75
4.7.2. Low stellar density regime	77
4.8. Summary and conclusions	79
4.9. Appendix A: Signal-to-Noise ratio estimation	82
4.10. Appendix B: On the TinyTim PSF models	84
4.10.1. Quality of fit parameters for TinyTim PSF models	84
4.10.2. Relation between principal component coefficients and focus values	85
<b>5. Ultra-Compact Massive Galaxies within the Kilo Degree Survey</b>	<b>89</b>
5.1. Motivation	90
5.2. Sample definition	91
5.2.1. Galaxy data sample	91
5.2.2. UCMGs selection and our sample	91
5.3. Spectroscopic analysis	92
5.3.1. Spectroscopic signal-to-noise ratio determination	92
5.3.2. Redshift and velocity dispersion measurements	93



5.4. Results . . . . .	93
5.4.1. UCMGs validation . . . . .	93
5.4.2. Contamination and incompleteness . . . . .	95
5.4.3. UCMG number counts . . . . .	95
5.4.4. Relationship between stellar mass and velocity dispersion . . .	97
5.5. Conclusions . . . . .	99
<b>6. Summary and Conclusions</b>	<b>101</b>
6.1. Weak lensing analysis for <i>Euclid</i> using HST images as input for sim- ulations . . . . .	101
6.2. Spectroscopic analysis of Ultra-Compact Massive Galaxies within the Kilo Degree Survey . . . . .	103
<b>A. UCMGs in KiDS Paper</b>	<b>109</b>
<b>Bibliography</b>	<b>133</b>
<b>List of Figures</b>	<b>147</b>
<b>List of Tables</b>	<b>151</b>
<b>Acknowledgements</b>	<b>153</b>



# CHAPTER 1

---

## Introduction

---

*“The universe is like a safe to which there is a combination, but the combination is locked up in the safe.”*

- Peter de Vries, *Let Me Count the Ways*

Since the dawn of time, man has always wondered about the Universe. Looking up at the night sky, searching for a description of our place within the Cosmos, and understanding the continued evolution of the expanding Universe in which we reside, raise some of the most profound human questions. How did the Universe form? How will it end? Will it end? What are the seeds of our Universe? What are the dark matter and dark energy? How did the objects that populate the Universe, such as stars and galaxies, come into being? How do they evolve? These and many more are the questions, the “unknown”, that cosmology and astronomy aim to solve.

From the XVII century, which brought the invention of the telescope, we have improved and developed new technologies and methods to observe astronomical objects in all wavelength regimes. With the advent of refined numerical simulations, our understanding of the Universe and the processes through which galaxies form and evolve has greatly progressed further. While the resolution with which we measure the light emitted by the galaxies and the precision with which we map the distribution of matter and the properties of galaxies continues to increase, we are continuing to improve the telescopes and the realism of our simulations, to resolve ever smaller scales. We have learnt that observations go hand in hand with simulations, that cosmology and galaxy formation are intertwined, and the need to model them simultaneously in order to advance both fields is growing rapidly.

The information we can gather about the Universe depends on how deep we can see and the range of physical scales we can resolve. This limit is posed by the power of telescopes to detect light from faint and distant galaxies. However, when the telescope aperture is not enough, we can always do better by exploiting a phenomenon known as *gravitational lensing*. Very massive astronomical bodies, such as galaxies, galaxy clusters or the large-scale structure sometimes act like lenses. Their gravity distorts the structure of space-time, magnifying light from more distant objects. This effect lets us observe objects that would ordinarily be too faint to see and map the distribution of mass in the galaxies acting as lenses.

Over the next decade, data from large Stage IV<sup>1</sup> survey telescopes, such as *Euclid*, on which we turn our attention in this thesis, will allow us to understand why the expansion of the Universe is accelerating and what is the nature of the source responsible for this acceleration. Furthermore, gravity is insensitive to the type of matter, so the gravitational effect of dark matter can be observed in the same way as for ordinary matter.

The validity of any results from the analysis of gravitational lensing caused by large-scale structure, known as *shear*, depends sensitively upon the treatment of systematic errors and the control of observational biases. Almost all systematic effects affect the observed correlations between galaxy shapes, and thus mimic shear. To help ascertain the level of systematics and calibrate them out, simulations of galaxies having properties similar to those in the real data, but with a known input shear are essential.

One of the major topics addressed within this thesis deals with the preparation for weak lensing analyses for *Euclid*. *Euclid* observations will be obtained using a broad filter that can bias the measurements of the galaxy shapes due to the color gradient of the galaxies. To fully exploit the power of this space mission, we need to measure the shapes of galaxies with a systematic accuracy better than one part in a thousand. To this purpose, archival *Hubble* Space Telescope (HST) observations can be used as a calibration sample, provided that HST instrumental effects are corrected. This can be achieved if we create a large sample of simulated ‘*Euclidized*’ HST-emulated data and simulations of galaxies similar to those *Euclid* will directly observe. The accuracy of the HST-emulation procedure, and thus the accuracy of the calibration, can be assessed by comparing these outputs.

The second major topic of this work concerns the analysis of Ultra-Compact Massive Galaxies (UCMGs). The Universe is populated with billions of galaxies with a diversity of shapes and sizes. A fraction of the galaxies seen in the present-day

---

<sup>1</sup>With the word “Stage” we refer to the definition of dark energy experiments as described in Albrecht et al. (2006).

---

Universe are known as the giant elliptical galaxies, which are dense, spheroidal groups of old stars, and they represent the most massive galaxies in the Universe. However, for this there is a price to pay: current galaxy formation models claim that they have lived dramatic lives. During their evolution, elliptical galaxies have experienced violent processes with merging, harassment and acts of ‘cannibalism’ from other galaxies. However, a small fraction of them managed to slip untouched through the cosmic time, without having any interaction with other galaxies and becoming ultra-compact and massive galaxies.

The formation and cosmic evolution of UCMGs are currently heavily debated. Thus, finding, characterizing and building a large sample of these galaxies at different redshifts is a crucial and a very valuable way to disentangle between possible physical scenarios driving the formation and size evolution of galaxies. Thus, my work is in pursuit in this context, in particular spectroscopically confirming a new sample of UCMG candidates.

This thesis is structured as follows. In *Chapter 2*, we review the theoretical background important for this work. After a brief discussion of the General Relativity, we introduce the cosmological standard model. We explain some notions of physics of galaxy formation and evolution, focusing on the two-phase formation model and the ultra-compact massive galaxies. Then, we introduce the concepts of gravitational lensing. We also describe how to measure the lensing effect and discuss how to handle the biases in its measurement. In *Chapter 3*, we give an overview of the instruments on which this work is based. In *Chapter 4*, we describe the procedure to emulate *Euclid* observations of sheared galaxy images to test the use of HST-observed galaxy images as input to image simulations. We test our proposed ‘*euclidization*’ procedure (and variants) under different conditions in order to investigate its accuracy. We also examine if uncertainties in the HST point-spread function (PSF) model introduce significant biases in the weak lensing shear calibration. In *Chapter 5*, we present the spectroscopic analysis for 33 new KiDS UCMG candidates at redshift  $0.15 \lesssim z \lesssim 0.5$ . We estimate the number density corrected for the systematics and we also obtain the velocity dispersion measurements for the 33 new UCMGs and for 28 UCMGs from a previous work (Tortora et al., 2018). Finally, we show a preliminary investigation of the correlation between stellar mass and velocity dispersion for these rare objects. *Chapter 6* concludes this thesis with a summary of our findings and an outlook to future research.



## CHAPTER 2

---

### Theoretical framework

---

*“There is a theory which states that if ever anyone discovers exactly what the Universe is for and why it is here, it will instantly disappear and be replaced by something even more bizarre and inexplicable. There is another theory which states that this has already happened.”*

- Douglas Adam, *The Hitchhiker’s Guide to the Galaxy*

Cosmology deals with the Universe as a whole and its evolution over the course of time. Astronomy, on the other hand, looks specifically at the objects in space. In this chapter we present the theoretical context through a mathematical description of some of the physical processes taking place in the Universe, which constitutes the framework in which this thesis is developed.

In Section 2.1 we outline some aspects of modern cosmology and the cosmological standard model. A brief account on the physics of galaxies formation, their evolution and the tools used to study them is given in Section 2.2. We then quickly narrow our attention to the particular class of galaxies of interest for part of this work - the Ultra-Compact Massive Galaxies. We will then proceed with the theory of gravitational lensing in Section 2.3. The chapter will be completed with a summary of some methods for the measurements of galaxy properties and the calibration of the biases on which part of the experiments and results of this thesis are based, see Section 2.4.

## 2.1. Modern Cosmology

According to our current understanding of our Universe and its history, as summarized in Figure 2.1, cosmologists place its formation at  $\sim 13.8$  billion years ago, with a singularity in space-time, famously known as the *Big Bang*. Shortly thereafter, the Universe underwent an incredible growth spurt. During this period, which is known as *inflation* and currently estimated to have lasted only  $10^{-33}$  s, the Universe expanded exponentially. Following the inflation, all of the Universe's components lived in a hot and opaque plasma. In particular, the photons were coupled to baryonic matter, and were not free to escape.

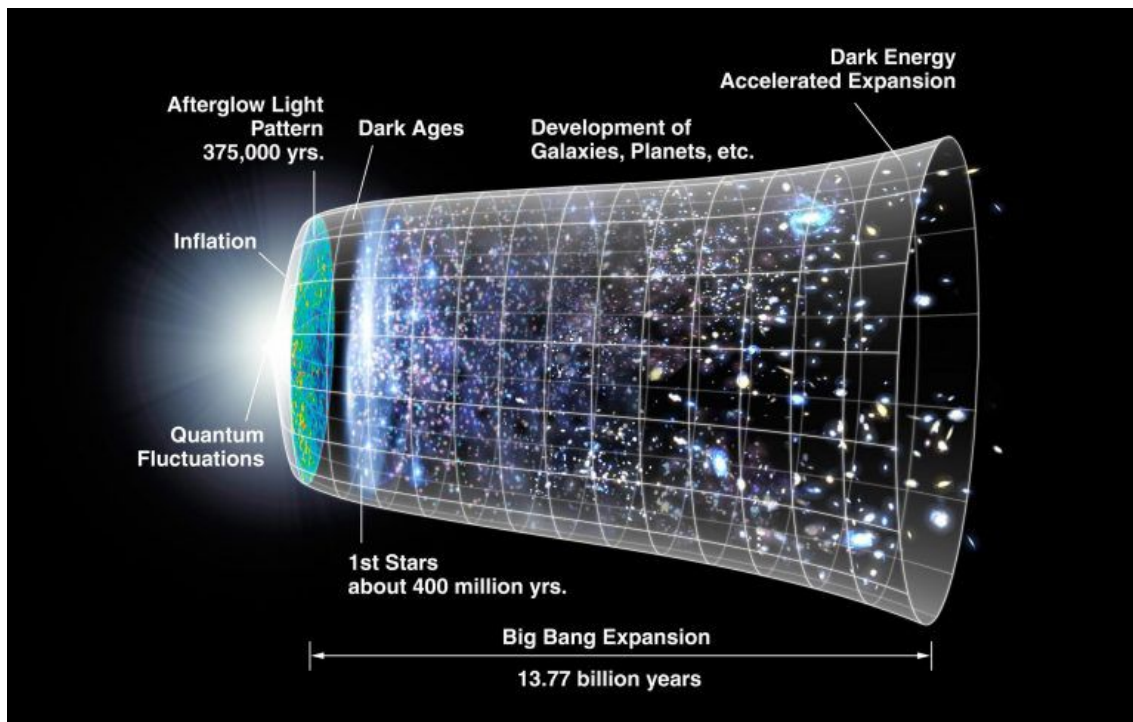


**Figure 2.1.** – A representation of the evolution of the Universe over 13.77 billion years from the Big Bang (left) to the present (right). Credit: NASA/WMAP Science Team.

About 380 000 years after the Big Bang, the Universe had expanded enough so that its density was much lower than earlier. Likewise, the temperature of the Universe had cooled down. A decrease in temperature to around 4 000 K allowed for *recombination*: electrons and protons combine to form neutral atoms of hydrogen. This marked the beginning of the period known as the *Dark Ages* – a name arising from the fact that there were no individual sources of light, like stars, only clouds of neutral hydrogen. The decoupling had two effects. First, photons were free to propagate across the Universe, which was now largely transparent. This period in the Universe's evolution is called the age of *reionization*. Second, the light that was



unleashed at this time is observed today in the microwave domain, and constitutes the Cosmic Microwave Background (CMB). Observations of the CMB provide a wealth of cosmological information, making it one of the main cosmological probes.

From this moment on, ordinary and dark matter (DM) could both react to gravity: denser concentrations of matter (both ordinary and dark) grew denser and more massive. Around 200 to 500 million years after the Big Bang, the distribution of matter in the Universe had produced very dense knots at the intersections of the sheets and filament of ordinary and dark matter known, the Large Scale Structure (LSS) also known as the *cosmic web*. This LSS appears like a huge web shaped by gravity, with most galaxies and galaxy clusters lying along the strands of dark matter. It constitutes the skeleton supporting the later emergence of stars and galaxies. Eventually the densest concentrations gave rise to the first stars, leading to the end of the *Dark Ages*.

The Universe has passed through different eras. After Inflation, and until about 47 000 years after the Big Bang, the Universe was radiation-dominated, and then it became matter-dominated until the Universe was about 10 billion years old. From that time, the Universe has looked much as it does today and it is in the era of Dark Energy domination, in which its expansion is accelerating.

### 2.1.1. General Relativity

The picture we have just presented, as our modern understanding of cosmology, relies on the *Theory of General Relativity* (GR) by Einstein (1915). GR describes the Universe by a four dimensional space-time, which is characterised by its metric tensor  $g_{\mu\nu}$ . The geometry and the energy content of the Universe are interrelated by *Einstein's field equations*

$$R_{\mu\nu} - \frac{R}{2}g_{\mu\nu} = \frac{8\pi G}{c^4}T_{\mu\nu} - \Lambda g_{\mu\nu}. \quad (2.1)$$

Here,  $R_{\mu\nu}$  is the Ricci tensor, which describes the curvature of space-time. Its trace is the Ricci scalar  $R$ . The metric of space-time is  $g_{\mu\nu}$ , while  $T_{\mu\nu}$  is the energy-momentum tensor describing the energy content of the Universe. The Greek indices run over the four components '0' for time and '1, 2, 3' for space. Finally,  $G$  is the Newton's gravitational constant,  $c$  is the speed of light, and  $\Lambda$  is the cosmological constant. The field equations show that the curvature of space-time, represented by the Ricci tensor, is fundamentally linked to the energy and matter content, represented by the energy-momentum tensor. This means that the amount and type of energy in the Universe determines its shape and dynamical evolution.

### 2.1.2. The isotropic and homogeneous Universe

Solving the field equations is, in general, a difficult task, because they form a set of ten coupled non-linear differential equations. However, we can find solutions to Eq. (2.1) if we use the *cosmological principle*. It states that the Universe is spatially isotropic on scales above hundreds of Megaparsecs<sup>1</sup> (Mpc) and that our position in space is not unique at all. The second condition implies that the large-scale Universe is isotropic around any point in space and consequently homogeneous. Actual observations of the CMB (Eisenstein et al. 2011; Planck Collaboration et al. 2020), for instance, confirm the Universe we live in is indeed isotropic (and hence homogeneous). Of course, this is clearly no longer the case at the scales we experience daily.

Assuming the cosmological principle to hold true, the space-time of the Universe is described by the Robertson-Walker metric (Robertson 1935; Walker 1937)

$$ds^2 = -c^2 dt^2 + a^2(t) dl^2, \quad (2.2)$$

where  $t$  is the cosmic time and  $a(t)$  the *scale factor*. This factor describes the dynamics of the Universe. An increasing  $a$  corresponds to an expanding Universe, while a decreasing  $a$  means that the Universe is shrinking. The scale factor is normalised such that today, at  $t_0$ ,  $a(t_0) = 1$ . The line element  $dl^2$  can be decomposed by making use of the comoving distance

$$dl^2 = d\chi^2 + f_K(\chi)^2 (d\theta^2 + \sin^2(\theta)d\phi^2). \quad (2.3)$$

Here,  $\chi$  is the comoving radial distance,  $\theta$  and  $\phi$  are angular coordinates, and  $f_k(\chi)$  is the comoving angular diameter distance, given as

$$f_K(\chi) = \begin{cases} K^{-1/2} \sin(K^{1/2} \chi) & \text{for } K > 0 \text{ (spherical)} \\ \chi & \text{for } K = 0 \text{ (flat)} \\ |K|^{-1/2} \sinh(|K|^{1/2} \chi) & \text{for } K < 0 \text{ (hyperbolic)}. \end{cases}$$

The parameter  $K$  describes the spatial curvature, and so the geometry, of the Universe. The latest cosmological observations (Planck Collaboration et al., 2020) indicate that the curvature of the Universe is flat or close to flat.

Inserting the metric from Eq. (2.2) into Eq. (2.1) and treating the contents of the Universe as a perfect fluid with density  $\rho$ , pressure  $p$  and four-velocity  $u$ , the energy momentum tensor is

$$T_{\mu\nu} = \left( \rho + \frac{p}{c^2} \right) u_\mu u_\nu + p g_{\mu\nu}. \quad (2.4)$$

---

<sup>1</sup>1pc= 3.086 × 10<sup>18</sup> cm.

With these assumptions, the *Friedmann equations* are

$$\left(\frac{\dot{a}}{a}\right)^2 = \frac{8\pi G}{3}\rho - \frac{Kc^2}{a^2} + \frac{\Lambda c^2}{3}, \quad (2.5)$$

and

$$\frac{\ddot{a}}{a} = -\frac{4\pi G}{3}\left(\rho + 3\frac{p}{c^2}\right) + \frac{\Lambda c^2}{3}, \quad (2.6)$$

which describe the dynamics of the Universe and its expansion history. The left-hand side of Eq. (2.5) is the square of the *Hubble parameter*

$$H(t) = \frac{\dot{a}(t)}{a(t)}, \quad (2.7)$$

whose current value is the *Hubble constant*  $H_0$ . By convention, one can also use the dimensionless *Hubble constant*  $h = H_0/(100 \text{ km s}^{-1}\text{Mpc}^{-1})$ .

To understand the time evolution of the scale factor, we still need a relation between the energy density and the pressure, which we call the *equation of state*. In general it is

$$w = \frac{p}{\rho c^2}, \quad (2.8)$$

where all the components can be time-dependent in principle. The equation of state varies according to the different types of energy-matter content in the Universe as follows

$$\begin{aligned} \text{matter : } w_m = 0 &\quad \rightarrow \rho_m \propto a^{-3}, \\ \text{radiation : } w_r = 1/3 &\quad \rightarrow \rho_r \propto a^{-4}, \\ \text{vacuum energy : } w_\Lambda = -1 &\quad \rightarrow \rho_\Lambda = \text{const}, \end{aligned} \quad (2.9)$$

where the dependence of the scale factor on time is obtained by solving the first Friedmann equation (2.5). The total density is given as a sum of the components  $\rho_{\text{tot}} = \rho_m + \rho_r + \rho_\Lambda$ . The critical density required for a flat geometry of the Universe (with curvature parameter  $K = 0$ ) is

$$\rho_{\text{crit}} = \frac{3H_0^2}{8\pi G}. \quad (2.10)$$

This allow to define the dimensionless density parameters

$$\Omega_m = \frac{\rho_m}{\rho_{\text{crit}}}, \quad \Omega_r = \frac{\rho_r}{\rho_{\text{crit}}}, \quad \Omega_b = \frac{\rho_b}{\rho_{\text{crit}}}, \quad \Omega_\Lambda = \frac{\Lambda c^2}{8\pi G \rho_{\text{crit}}}. \quad (2.11)$$

### 2.1.3. Cosmological distances

In Euclidean space it is possible to have a unique definition of distance: it is the length of a line connecting two simultaneous events. In the non-Euclidean space, and in general in GR, there is no unique description of distances, therefore different types of ‘distances’ are used in cosmology, as depicted in Figure 2.2.

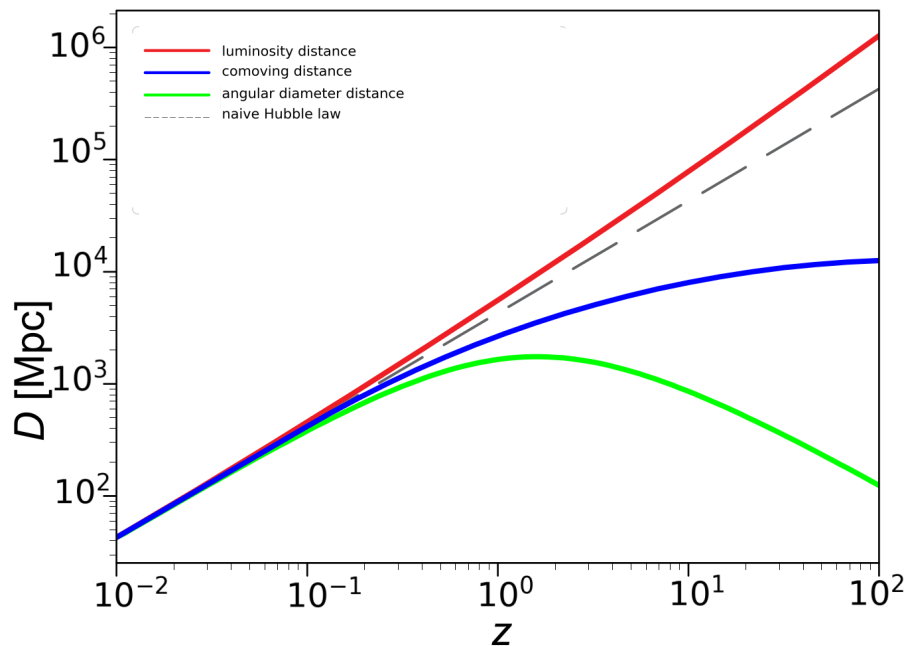


**Figure 2.2.** – Different cosmological distance measures as a function of redshift  $z$ . The distances are computed for a flat  $\Lambda$ CDM model with  $h = 0.7$ ,  $\Omega_m = 0.3$ , and  $\Omega_\Lambda = 0.7$ ; for the naive Hubble law  $H(z) = H_0$  is assumed. In the local Universe, i.e. for  $z \ll 1$ , all distance measures agree, for higher redshifts they diverge with  $D_{\text{ang}} < \chi < D_{\text{Hubble}} < D_{\text{lum}}$ .

#### Comoving distance

A photon travelling towards an observer follows a null geodesic, i.e.  $ds^2 = 0$ . Hence, for a radial light ray with  $d\theta = d\phi = 0$ , Eq. (2.2) reduces to

$$cdt = -a(t)d\chi, \quad (2.12)$$

and we observe the photons from a source at a *comoving distance*

$$\chi(t) = \int_t^{t_0} \frac{cdt'}{a(t')} = \int_{a(t_0)}^{a(t)} \frac{cda}{a^2 H(a)}, \quad (2.13)$$

which relates the comoving distance to  $H(t)$ , and so to the cosmological parameters.

### Cosmological redshift

Like the sound of an ambulance speeding away from the observer is altered by the Doppler effect, the expansion of the Universe causes a change to the wavelength of light that reaches us. We call this change *redshift*: as the space between the distant object and us is expanding, the wavelength of light in the visible domain is shifted towards longer (red) wavelengths. The redshift of a source is defined as

$$z \equiv \frac{\lambda_{\text{obs}} - \lambda_{\text{em}}}{\lambda_{\text{em}}}, \quad (2.14)$$

with the emitted wavelength  $\lambda_{\text{em}}$  and the observed wavelength  $\lambda_{\text{obs}}$  of a photon travelling from the source to the observer. Redshift and scale factor are directly related by

$$a(t) = \frac{1}{1 + z(t)}. \quad (2.15)$$

Making use of the definition of redshift, Eq. (2.13) can be rewritten as

$$\chi(z_1, z_2) = \int_{z_2}^{z_1} \frac{cdz'}{H(z')}, \quad (2.16)$$

which is generally known as the *distance-redshift distance*.

### Angular diameter distance

The *angular diameter distance* relates the physical size of objects (diameter)  $d$  to the observed angular size  $\theta$  on the sky as

$$D_{\text{ang}}(a) = af_K(\chi) = \frac{d}{\theta} \quad (2.17)$$

Due to the geometry of our Universe and its expansion, the diameter distance is not a monotonously increasing function with redshift, but it shows a maximum value at  $z \approx 1.7$  or equivalently  $a \approx 0.4$ . This means that objects with the same physical size appear larger at  $a = 0.3$  than those nearer to us at  $a = 0.4$ .

### Luminosity distance

Another description of distances can be obtained relating the bolometric luminosity  $L$  of an object and the observed bolometric flux  $S$  that decreases with the inverse square of its distance

$$D_{\text{lum}}(z) = \sqrt{\frac{L}{4\pi S}}. \quad (2.18)$$

The *luminosity distance* does not have a maximum value and continues to grow as a function of redshift. Furthermore, the Universe is expanding while photons travel to us, which additionally dilutes the measured flux compared to what we would expect

in a Euclidean space. Hence, luminosity and angular diameter distance are not the same in general. They can be related by

$$D_{\text{lum}}(z) = (1+z)^2 D_{\text{ang}}(z), \quad (2.19)$$

which shows that they agree for  $z \ll 1$ . These distances are not additive, meaning  $D_{\text{ang}}(z_1+z_2) \neq D_{\text{ang}}(z_1)+D_{\text{ang}}(z_2)$  and the same happens for the luminosity distance. According to the problem we are studying, we have to use a particular definition of distance. In weak lensing, since we generally deal with sizes, the angular diameter distance is the most used.

### 2.1.4. The $\Lambda$ CDM Model

The previous subsections provided us with the necessary concepts to define the current standard model of cosmology, the so-called  $\Lambda$ CDM *model*. It assumes that the matter content of the Universe is divided in two different subtypes. *Ordinary matter* is made of baryonic elements (and electrons), the majority of which is found in the form of hydrogen. Observations from the CMB indicate that the baryonic density parameter is  $\Omega_b = 0.0489 \pm 0.0003$  (Planck Collaboration et al., 2020) and so its contribution is only  $\sim 5\%$  of the total content of the Universe. *Dark matter*, although it behaves like baryonic matter as a pressureless fluid, is invisible as it does not interact with electromagnetic radiation, but is detectable via its gravitational force. Dark matter is expected to be non-relativistic, that is, to be Cold Dark Matter (CDM) and it is roughly five times abundant than baryonic matter, i.e.  $\sim 25\%$ . Nowadays, dark matter is believed to be a massive particle that interacts weakly (WIMP), but it has still to be confirmed and other ideas are still a topic of discussion. Together, baryonic and dark matter account for the total matter density  $\rho_m$  and  $\Omega_m = \Omega_b + \Omega_{\text{dm}} = 0.3111 \pm 0.056$  (Planck Collaboration et al., 2020).

Ordinary matter and dark matter govern most of the structure formation in the Universe. Their influence on the structure formation is determined by the mass of an individual dark matter particle. Light particles, referred to as hot dark matter, are free-streaming, which means all small-scale perturbations are erased, and the largest structures form first. On the other hand, a cold dark matter scenario of massive dark matter particles lets small structures, like galaxies, form first and large structures, like galaxy clusters, only emerge later. This is called a *bottom-up* or *hierarchical scenario*.

Next are the relativistic components of the Universe, the majority of which are photons. All particles with zero rest mass as well as massive particles at relativistic energies are considered *radiation*. As the Universe keeps cooling, the number of relativistic particle species declines and radiation only dominates the energy content of the Universe for redshifts  $z > z_{\text{eq}} \sim 5900$ . Today's best estimate is  $\Omega_r \simeq 10^{-5}$

(Planck Collaboration et al., 2020).

The  $\Lambda$ CDM model also assumes that the cosmological constant  $\Lambda$  is non-zero. Recent observational evidence (Riess et al. 1998; Perlmutter et al. 1999) has shown our Universe's expansion has recently (on cosmological scales) started accelerating. The name given to the origin of this acceleration is *dark energy*. Dark energy dominates the total energy of the Universe ( $\simeq 70\%$ ) in the current epoch with  $\Omega_\Lambda = 0.6889 \pm 0.056$  (Planck Collaboration et al., 2020).

Using the definitions in Eq. (2.11), the Friedmann equations (2.5) and (2.6) can be summarized into the more compact form

$$H(a)^2 = H_0^2 [\Omega_r a^{-4} + \Omega_m a^{-3} + (1 - \Omega_r - \Omega_m - \Omega_\Lambda) a^{-2} + \Omega_\Lambda]. \quad (2.20)$$

The values of the density parameters and the Hubble constant are critical in understanding the expansion history of the Universe. According to the Eq. (2.20), the Universe experienced three different expansion epochs. First, for small  $a$  at early times, the Universe was dominated by radiation and the expansion was proportional to  $t^{1/2}$ . With growing  $a$ , the Universe experienced the epoch of matter domination with  $a \propto t^{2/3}$ . During the transition between these two epochs, although the radiation and matter terms evolve at different rates, at the matter-radiation equality time, they became both are equal, and

$$\Omega_r a_{\text{eq}}^{-4} = \Omega_m a_{\text{eq}}^{-3}, \quad (2.21)$$

where  $a_{\text{eq}}$  is the scale factor at the equality time. Today, the Universe is dominated by the cosmological constant and  $a$  is increasing exponentially

$$\Omega_\Lambda > \Omega_m a^{-3}. \quad (2.22)$$

Current measurements indicate that  $\Omega_r + \Omega_m + \Omega_\Lambda = 1$  due to the flatness of our Universe, so the term proportional to  $a^{-2}$  vanishes. Throughout this thesis, we assume  $H_0 = 70 \text{ km s}^{-1} \text{ Mpc}^{-1}$ ,  $\Omega_m = 0.3$ , and  $\Omega_\Lambda = 0.7$  as approximately consistent with Komatsu et al. (2011).

Observations of various cosmological probes, such as the spatial galaxy distribution (Hurtado-Gil et al., 2021), the CMB (e.g. Goldstein et al. 2003; Rebolo et al. 2004; Planck Collaboration et al. 2020), the distances to supernovae type Ia (SNIa) (e.g. Blinnikov et al. 2005), cosmic shear (e.g. Hildebrandt et al. 2017; Secco et al. 2022), or neutral hydrogen observations (e.g. Bharadwaj et al. 2009) support the  $\Lambda$ CDM model. In particular, this model describes the observed accelerated expansion of the Universe (Riess et al. 1998; Perlmutter et al. 1999) and with a small set of parameters describes a large variety of observations. Even though the  $\Lambda$ CDM model is currently the *cosmological standard model*, the values of its parameters are

under debate.

As seen so far, the standard model relies on the two dominant ingredients of the mass-energy content of the Universe: dark matter and dark energy. Neither of these ingredients can be described satisfactorily by our current theories of particle physics and gravity. In particular, measurements of different observables do not yield the same values, suggesting a discrepancy exceeding  $4\sigma$ , which also known as *H0 Tension* (Wagner, 2022). This tension describes the disagreement between the Hubble constant measured with SNIa distances in the local Universe and the value inferred from the CMB (Verde et al., 2019; Riess, 2019). For example, the Planck Collaboration: Aghanim et al. (2019) provided a value of  $H_0 = (67.4 \pm 0.5) \text{ km s}^{-1} \text{ Mpc}^{-1}$  from the CMB, while Riess et al. (2019) measured  $H_0 = (74.03 \pm 1.42) \text{ km s}^{-1} \text{ Mpc}^{-1}$  with SNIa. The main goals of modern observational cosmology are to achieve improved precise measurements of the parameters in the  $\Lambda$ CDM model and to search for deviations from it (see e.g. Amendola et al. 2013, for a review). Consequently, this means to both develop consistent models of cosmic acceleration and to explore optimal ways to connect these models to observations.

## 2.2. The physics of galaxy formation and evolution

The Universe is not homogeneous at all scales. When looking at the night sky we recognise an enormous variety of systems and structures spanning several orders of magnitude in size: from the myriads of stars in the disk of our own galaxy, the Milky Way, to a richness of complex ‘stellar systems’, the galaxies, ranging from compact galaxies of only few kpc in size and  $10^6 - 10^8 M_\odot^2$  in mass, to giant ellipticals with size of the order of 100 kpc and stellar masses of about  $10^{12} M_\odot$ . Moving out to larger distances, galaxies are further assembled in clusters of galaxies, extending for few Mpc, up to large super-clusters and filamentary structures, forming the LSS (see Figure 2.3).

As already said, in the context of  $\Lambda$ CDM, structure forms hierarchically (Peebles, 1978; White & Rees, 1978; White & Frenk, 1991), originating from small adiabatic, as predicted by the cosmic inflation, density fluctuations (Peebles, 1982). As gravity is the driving force in structure formation, overdensities become denser with time, attracting more matter from underdense regions, which in turn get even less dense. Once an overdense region reaches a critical density, it starts to collapse, forming a small halo. These halos are the building blocks where then, the growth of larger structures, like groups and clusters of galaxies, occurs via mergers and accretion. Although  $\Lambda$ CDM is in good agreement with the observed LSS, it does

---

<sup>2</sup> $1 M_\odot = 1.0989 \times 10^{33} \text{ g}$ .



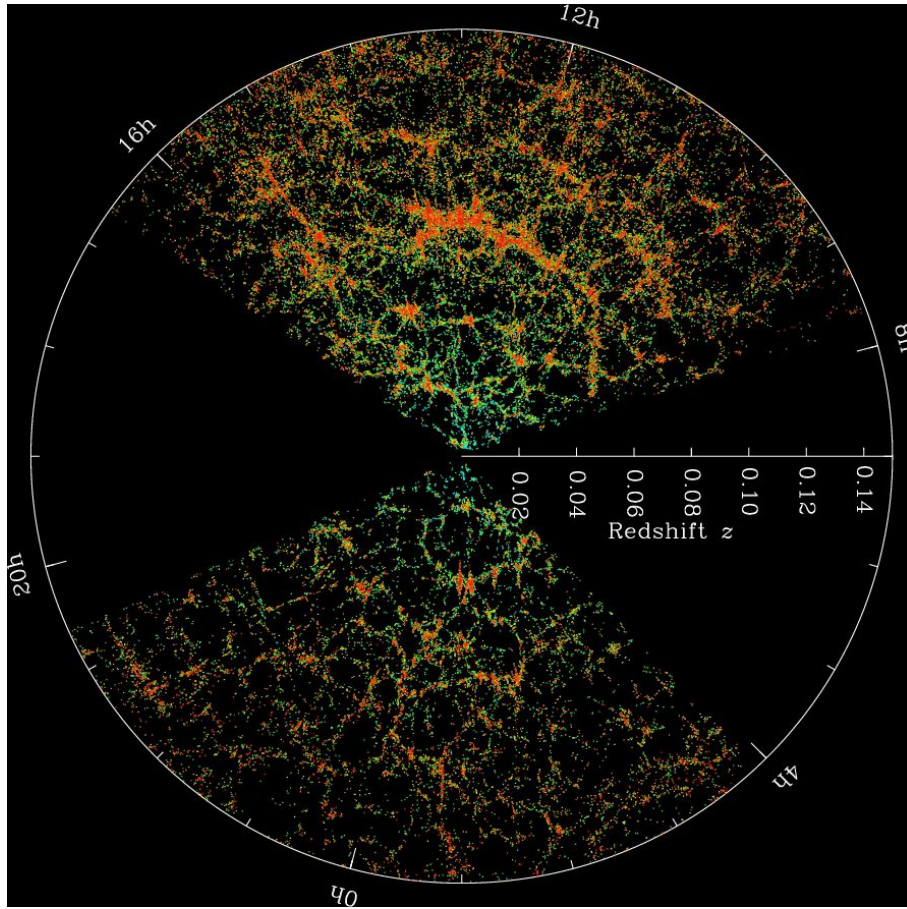


**Figure 2.3.** – Slices through the SDSS 3-dimensional map of the distribution of galaxies obtained by the Sloan Digital Sky Survey (SDSS). Galaxies are colored according to the ages of their stars, with the redder, more strongly clustered points showing galaxies that are made of older stars. It is possible to appreciate that galaxies are not uniformly distributed, but they organize in clusters, walls and filamentary structures, which surround regions of voids. Credit: M. Blanton and SDSS.

not agree with observations on the scales of individual galaxies. The process of evolution of the baryonic matter, such as the star formation (SF) in galaxies, is governed by much more complex physics. In particular, the galaxies we observe today are the result of a complex evolutionary process that depends both on the cosmological paradigm and on the local environment in which they were formed and subsequently evolved.

This topic has largely become a fundamental target of cosmological investigations in the last decade (Katz & Gunn 1991; Springel et al. 2005; Somerville & Davé 2015; Kewley et al. 2019; Wu et al. 2021). In this thesis, we tackle the problem from both a theoretical and an observational point of view, with a particular focus on massive

early-type galaxies. In this chapter we will give an overview on galaxy formation and evolution to lay the foundation for the work presented in Chapter 5.

### 2.2.1. Galaxy classification

Galaxies in the Universe appear in a large variety of shape, sizes, luminosities and colours at different wavelengths. This diversity reflects the differences in the past and present SF activity, gas and dust content, and possibly interactions with the surrounding environment. Galaxies have been classified according to their morphology and properties into the *Hubble sequence* or commonly referred to as *Hubble Tuning Fork*, from elliptical to irregular galaxies, passing through systems with a bulge or a disk component, the latter having different degrees of spiral structures (Hubble, 1926), as shown in Figure 2.4.

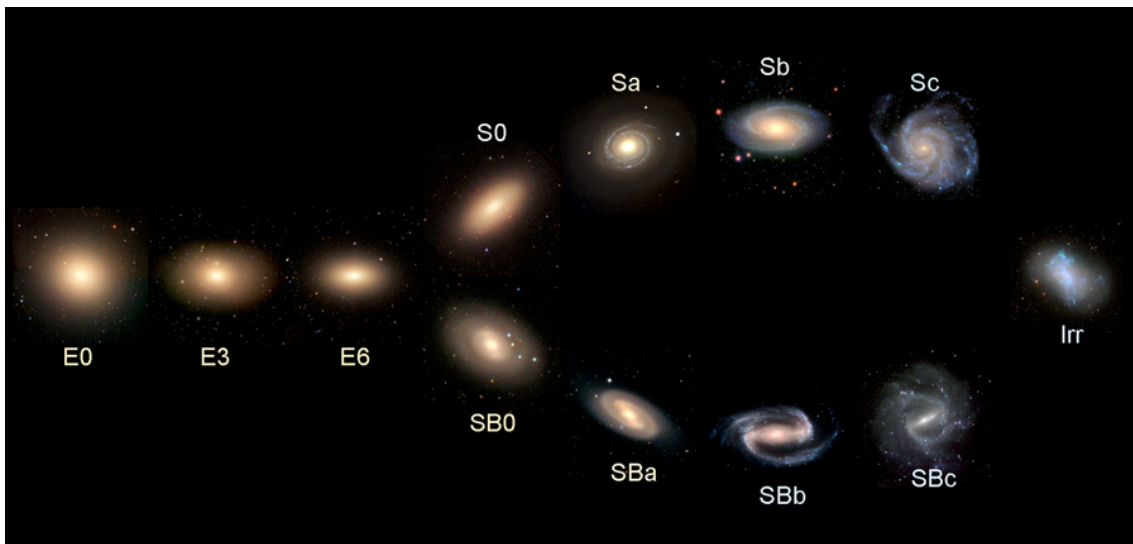


**Figure 2.4.** – The Hubble galaxy classification scheme, also known as the Hubble tuning fork. Image credit: Cosmic Assembly Near-infrared Deep Extragalactic Legacy Survey (CANDELS) collaboration.

On the left hand side of the Hubble tuning fork (Figure 2.4) are the *elliptical galaxies*, which are divided into sub-classes starting with the most spherical objects which have an ellipticity  $\epsilon = 1 - \frac{b}{a} = 0$ , with  $a$  and  $b$  semi-major and semi-minor axis of an ellipse, respectively. Moving towards the right, the ellipticity increases and the galaxies become more flattened. Their light distribution  $I$  as a function of radius  $R$  can be well described by a Sérsic profile (Sérsic, 1963a)

$$I(r(x, y)) = I_e \exp \left\{ -b_n \left[ \left( \frac{r}{R_e} \right)^{1/n} - 1 \right] \right\}, \quad (2.23)$$

where  $I$  is the intensity at position  $(x, y)$ ,  $r$  is the radius from the center that corresponds to  $(x, y)$ ,  $R_e$  is the effective radius, which is equal to the projected half-light radius,  $I_e$  ( $I_e = I(R_e)$ ) is the intensity at the half-light radius and,  $n$  is the Sérsic index which determines the concentration of the light and so, the “steepness” of the profile. The constant  $b_n$  is defined such that  $R_e$  contains half the total flux. The de Vaucouleurs profile (de Vaucouleurs, 1961) is a special case of the Sérsic profile with  $n = 4$ .

Moving further towards the right along the Hubble sequence, one reaches the bifurcation at the ‘S0’ galaxy type. S0 galaxies are a morphologically intermediate type between spiral and elliptical galaxies that contain large-scale disks but do not have prominent spiral arms. They are therefore also called *lenticular galaxies*. The *spiral galaxies*, which occupy the right part of the Hubble sequence, are divided into barred ‘SB’ and non-barred ‘S’ systems. The lower-case letters from ‘a’ to ‘c’ indicate the prominence of the central bulge, the gas content, and the compactness of the spiral arms as illustrated in Figure 2.4. The light distribution of the bulge component, getting less prominent from ‘a’ to ‘c’, can also be described by a Sérsic profile (see Eq. (2.23)), while the light distribution of the disks can be approximated with an exponential profile

$$I(R) = I_0 \exp(-R/R_s), \quad (2.24)$$

with  $I_0$  the central surface brightness and  $R_s$  the disk scale length.

In addition to the types illustrated in the Hubble sequence, there also exist dwarf counterparts. These are much smaller in size but with similar morphological appearance compared to the classical Hubble types. They are denoted with the letter ‘d’: dwarf elliptical (dE), dwarf spheroidal (dSph), and dwarf irregular (dIrr) galaxies. Furthermore, among these galaxies there are some which are extremely compact in size and massive, the Ultra-Compact Massive galaxies (UCMGs). We will focus on them in Section 2.2.6 and we will present a spectroscopic analysis in Chapter 5.

According to Hubble, ellipticals, also labeled as ‘early-type galaxies’ (ETG) evolved into spiral galaxies, also referred to as ‘late-type galaxies’ (LTG). So, his classification was interpreted as an evolutionary sequence. However, we have now gathered enough evidence, from an observational as well as theoretical point of view, that LTGs are more likely to evolve into ETGs than the other way round<sup>3</sup>. Moreover, it became clear that the Hubble fork cannot be used as an evolutionary sequence for galaxies and that other parameters, rather than only morphology have to be used if aiming at constraining the cosmic evolution of galaxies (e.g.

---

<sup>3</sup>Note that overall ETGs are populated by older stars, especially in their central region, see Section 2.5.

kinematics, see the ATLAS<sup>3D</sup> classification in Cappellari et al. 2011).

The color of early-type and late-type galaxies depends on the different stellar types dominating their stellar populations. The colour of a star is directly related to its temperature, which depends in turn on its evolutionary stage dominating its light distribution. The stellar populations of late-type galaxies (irregulars and spirals) are on average dominated by younger stars. Massive young stars have high temperature and therefore emit in the blue wavelength regime. In contrast to this, in the early-type galaxies the SF is ceased and the high-mass stars have cooled and then dead, and the low-mass stars are generally colder, leading to an integrated redder colour than for late type galaxies.

In addition to the age, the metallicity<sup>4</sup> also plays a role in determining the stellar population's colour. The age-metallicity degeneracy (Worthey, 1994) makes it hard to disentangle whether the spectrophotometric properties of an unresolved stellar population are due to its age or metallicity. For example, a single stellar population (SSP, i.e. a coeval population of stars formed instantaneously) with an age of 9 Gyr and solar metallicity ( $[\text{Fe}/\text{H}] \simeq 0$ ) can hardly be distinguished from a 3 Gyr-old population with super-solar metallicity of  $[\text{Fe}/\text{H}] \simeq 0.3$  (Bertone & Chavez, 2011). For star-forming galaxies, the metallicity can be measured in the gas phase using emission line diagnostics of HII regions (e.g. Evans & Dopita 1987; Kewley & Dopita 2002). The gas-phase metallicity indicates the present star-forming gas and is therefore a good probe for star-forming, late-type galaxies. For massive ETGs, instead, where SF is not occurring any longer, one can use stellar absorption lines to infer the metallicity and elemental abundance (e.g.  $\alpha$ -abundance) of the stellar populations (Trager et al., 2000).

### 2.2.2. Physical processes

Many physical processes are commonly included in current models of galaxy formation. In the following we briefly discuss them.

#### Gravity

The main ingredient underlying the galaxy formation is gravity. The shape and amplitude of the primordial power spectrum of density fluctuations depend on the cosmological parameters and the properties of DM. This spectrum determines how many DM halos of a given mass have collapsed due to the gravity at any given time, how they cluster in space, and how quickly these halos grow over cosmic time via merging and accretion. As mentioned at the beginning of Section 2.2, in the  $\Lambda$ CDM paradigm every galaxy forms inside one of these dark halos. When

---

<sup>4</sup>The metallicity is the abundance of elements heavier than hydrogen and helium, measured with respect to the solar abundance.

halos merge, each containing its own central galaxy, gravity and dynamical friction gradually cause the orbits to decay until the galaxies merge. Mergers can have important effects on galaxies, including triggering bursts of SF and accretion onto central super-massive black holes (SMBHs), and transforming galaxy structure and morphology.

### **Star-formation feedback**

Observations show that less than 10% of the total baryon budget today is in the form of stars. However, in the standard model framework we would expect most of the gas to have cooled and formed stars by the present day if we did not consider some sort of feedback suppressing the cooling and the SF. It is now established that many processes associated with massive stars and supernovae (SNe) (e.g., photoheating, photoionization, winds) could contribute to making SF inefficient and driving large-scale winds to reduce the baryon fractions in galaxies (for an overview see Hopkins et al. 2012).

### **Active galactic nucleus feedback and black hole growth**

Observations show that the majority of all spheroid-dominated galaxies (which comprise most of all massive galaxies) contain a SMBH (Kormendy & Ho, 2013). The growth of these black holes releases vast amounts of energy that powers quasars and other weaker active galactic nuclei (AGNs). The energy to feed these BHs must exceed the binding energy of the host galaxy, suggesting that it could have a very significant effect on galaxy formation (Silk & Rees, 1998). In addition, a tiny fraction of this energy, if absorbed by the host galaxy, could halt star formation by heating and ejecting ambient gas (Cattaneo et al., 2009). Observational evidence of feedback associated with AGNs and SMBHs includes high-velocity winds, which may be ejecting the cold inter stellar medium (ISM) from galaxies, and hot bubbles apparently generated by giant radio jets, which may be heating the hot halo gas (Fabian 2012; Heckman & Best 2014).

### **Radiative transfer**

The radiation emitted by stars and AGNs can have an important impact on galaxy formation. Radiation can directly heat gas and can also modify cooling rates (especially for metal-enriched gas) by changing the ionization state of the gas. Moreover, the radiation emitted in different wavelength ranges through scattering by dust can greatly impact the measured total luminosity, color, and observationally determined morphological and structural properties of galaxies (Narayanan et al., 2021).

## **2.2.3. Tools for modeling galaxy formation and evolution**

The most explicit way to model galaxy formation is using numerical hydrodynamic techniques, in which the equations of gravity, hydrodynamics, and thermodynamics

are included to account for DM, gas, and stars. The advantage of these techniques is that, within the limitations of the adopted numerical resolution, one obtains predictions of the density of each of these three components (as well as that of heavy elements) over cosmic time. They also provide estimates for the velocities of the stars and DM, and the temperature of the gas. Thus the structure and kinematics of galaxies as well as their global properties and spatial distribution can be studied in great detail. Hydrodynamical simulations have been carried out with some success (Lee et al. 2021; Vogelsberger et al. 2020; Springel & Hernquist 2003), however they are numerically very costly, given the high resolution required, especially to explore multidimensional parameter spaces.

An alternative and more efficient method for modeling galaxy formation in a cosmological context is provided by semi-analytic models (SAMs), pioneered by White & Rees (1978) and developed by several groups (Baugh 1996; Somerville & Primack 1999; Guo et al. 2011; Henriques et al. 2017; Gabrielpillai et al. 2021). This method does not explicitly solve gas-dynamical equations for particles, but they are replaced with simple, yet physically and observationally motivated prescriptions for star formation and feedback (see Baugh 2006, Benson 2010 for reviews).

Semi-analytic models in the context of hierarchical clustering scenarios can be coupled to population synthesis models (see Section 2.2.5) to predict the luminosities, colours and other observed relation of nearby galaxies. In addition, in SAMs the formation of structure through gravitational instability in an expanding Universe is represented via merger trees. A merger tree records the masses of DM halos and the times at which these progenitor halos merge together to form a larger halo.

### 2.2.4. Two-phase formation model

In the hierarchical paradigm of galaxy formation, massive ETGs assemble in a *two-phase formation* scenario as identified in semi-analytic models of structure formation Abadi et al. (2006) and hydrodynamical cosmological simulations (e.g. Naab et al. 2009b; Oser et al. 2010b). High-redshift observations show that massive red objects have 3 – 5 times smaller sizes than in the local Universe, and thus they are 30 – 100 times denser (Werner et al., 2018). The two-phase formation scenario, so far seems to be the most favoured model to explain the mass assembly and evolution across cosmic time of very massive galaxies.

The two phases are closely related to the concept of the *in-situ* and *accreted/ex-situ* halos, first introduced by Abadi et al. (2006) in order to classify the luminous halos of stars surrounding ETGs. The original position where a given star was made (from gas) compared to the position in the final galaxy, is an important tracer of the size evolution of massive galaxies. We define ‘in-situ’ stars as those stars made

near to the galactic center over an extended time period. They are made from dissipative gas and, for massive systems, probably have relatively high metallicity (Zolotov et al., 2015). On the contrary, the accreted/ex-situ stars are typically made at quite early times as well, outside the virial radius, but added to the parent galaxy late in its evolution. They are added typically at radii larger than the effective radius,  $R > R_e$ , and are expected to be metal poor, since they originated in lower mass, lower metallicity systems (Naab et al., 2009b). The ex-situ stars accrete via an energetically conservative process and their final binding energy is transferred to other phases (gas, stars, and dark matter) rather than simply radiated away (Johansson et al., 2009).

Given this way of envisioning galaxy formation, the two-phase formation scenario of ETGs can be summarised as follows.

**Phase I.** At high redshift ( $2 < z < 6$ ) the assembly of galaxies at all masses is dominated by in-situ star formation fed by cold flows. A first intense and fast dissipative series of processes forms their central gas-rich cores with high stellar mass. These so-called “blue nuggets” form stars in-situ at high rate, and this causes a gradual stellar and halo mass growth (Dekel & Burkert, 2013). Subsequently, the star formation in the central region quenches and the blue nuggets quickly (and passively) evolve into compact “red nuggets” – massive, passive and very compact galaxies with size a factor of  $\sim 4$  smaller than local massive galaxies (Daddi et al. 2005; van Dokkum et al. 2008a). At the present day, these stars appear old and rich of  $\alpha$ -elements.

**Phase II.** From  $z \sim 3$  until the present day, in-situ star formation does not play a significant role anymore. This phase is more time-extended, dominated by mergers and gas inflows. It is responsible for the dramatic structural evolution and size growth (Buitrago et al. 2008, 2018; van Dokkum et al. 2008b; Damjanov et al. 2011; Szomoru et al. 2012). Unfortunately, this “accreted” material, which tends to stay preferentially in the outskirts, overlaps along the line-of-sight, with the spatial and orbital distributions of the in-situ light, that encodes the information about high- $z$  baryonic processes, irreversibly limiting the resolving power (e.g. Naab et al. 2014; Ferré -Mateu et al. 2019). In addition, the metal-poor stars, accreted from smaller stellar system, cause a metallicity gradient.

A sketch of the two-phase model is shown in Figure 2.5.

### 2.2.5. Stellar population synthesis models

Single stars cannot be resolved in distant galaxies, where we can observe only their integrated light. The integrated spectra of galaxies are the results of the

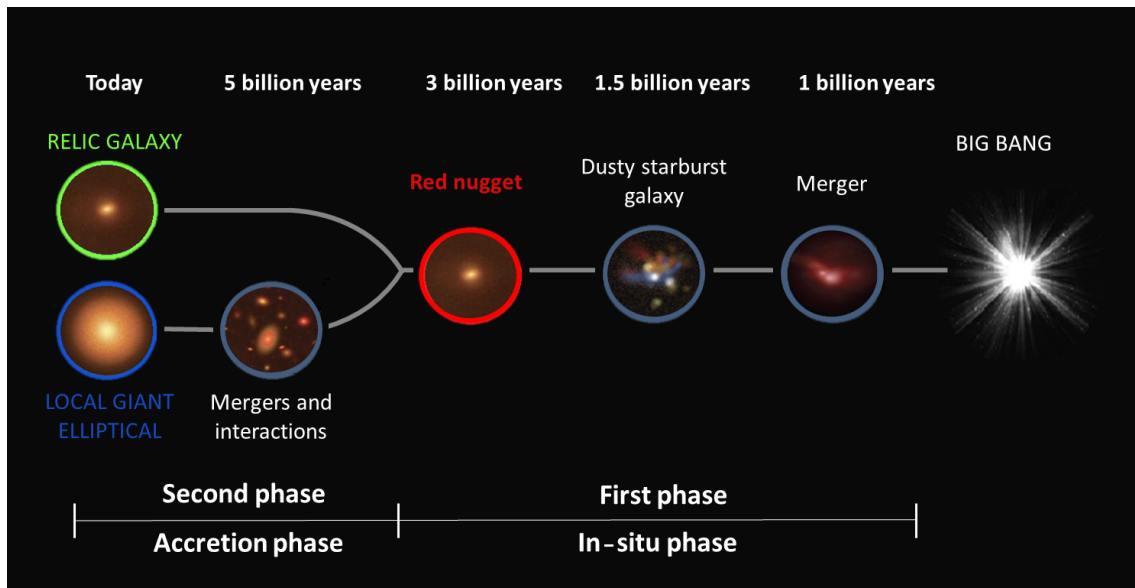


**Figure 2.5.** – The two-phase formation scenario for the mass assembly and cosmic evolution of massive galaxies.

superimposition of different stellar populations. They carry information about the ages and metallicity of the stars in galaxies, and thus on the star formation and chemical enrichment history of the Universe. Stellar population synthesis (SPS) models are the major tool to interpret integrated colours and spectra of galaxies in terms of the physical parameters of their stellar populations (Maraston 1998; Vazdekis 1999; Bruzual & Charlot 2003; Gutkin et al. 2016). This technique is based on the idea that a stellar population with any star formation history can be decomposed into a series of instantaneous starbursts, or “Simple Stellar Populations” (SSP). The only free parameters involved are the star formation rate in the form of isochrones<sup>5</sup>, the initial mass function<sup>6</sup> and, in some cases, the chemical enrichment rate. Thus, using population synthesis models we can describe the time-dependent distribution of stars in the colour-magnitude diagram and derive the integrated spectral evolution of the stellar population.

The spectral energy distribution of a stellar population with star formation rate  $\Psi(t)$  and metallicity  $Z(t)$  can be written as

$$F_{\lambda}(t) = \int_0^t \Psi(t-t') S_{\lambda}(t', Z(t-t')) dt, \quad (2.25)$$

<sup>5</sup>An isochrone specifies the location in the Hertzsprung-Russell (HR) diagram of stars with a common age and metallicity.

<sup>6</sup>The initial mass function is the relative number of stars, as a function of their individual initial mass, that forms during a single star forming episode.



where  $S_\lambda(t', Z(t-t'))$  is the spectral energy distribution (SED) of an SSP of age  $t$  and metallicity  $Z(t-t')$ . The calculation requires a stellar evolution prescription, which gives the theoretical stellar evolutionary tracks of single stars of mass  $m$ , and the stellar spectral libraries, both theoretical stellar atmosphere libraries and observed stellar spectra, in addition to the libraries of individual stellar spectra are necessary to assign spectra to stars in the various evolutionary stages of the isochrone. Finally, the SED of the SSP is obtained by summing the spectra of individual stars along the isochrone.

From the spectral evolution of an SSP from 1 to 13 Gyr, we expect that when the population is young, the spectrum is dominated by short-lived, massive stars emitting in the ultraviolet (UV), below 2000 Å. As time goes by, the most massive stars leave the main sequence and evolve into red giant stars, causing a decrease in the UV light and an increase in the near-infrared (IR) light. After a few Gyrs, red giant stars represent the major contribution to the near-IR emission. From 4 to 13 Gyr the shape of the spectrum from the optical to the near-IR is almost not evolving, because low-mass stars cover a narrow temperature range during their entire evolution.

The spectral evolution is visible also in the strength of stellar absorption lines. In particular, between 0.1 and 1 Gyr there is a marked strengthening of all the Balmer lines (from H $\alpha$  at 6563 Å to the continuum limit at 3646 Å), which are indicative of a recent burst of star formation. Another important spectral feature is the so-called 4000 Å-break caused by the absorption of high energy radiation from metals in stellar atmospheres. This feature is widely used as age indicator, but it shows also a dependence on metallicity at old ages. All these spectral lines, plus other metallic lines associated to Ca, Mg, Fe, continue to evolve even between 4 and 13 Gyr when the shape of the continuum is almost constant. These absorption features are used as a diagnostic of age and abundance of elements typical of active/passive stellar populations.

In order to perform an analysis of galaxy spectra, in this work, we fit population synthesis models based on higher-resolution stellar spectra that cover the entire temperature range and use multi-wavelength photometry of the galaxies in the sample with single burst models from Bruzual & Charlot (2003).

### 2.2.6. Ultra-Compact Massive Galaxies

Ultra-Compact Massive Galaxies (UCMGs) are objects with stellar mass  $M_\star > 8 \times 10^{10} M_\odot$  and effective radius  $R_e < 1.5$  kpc (although sometimes other stellar mass and effective radius ranges are adopted, see Chapter 5). They are clear outliers in the mass-size relation (Shen et al., 2003). They are the perfect candidates to be “relic galaxies”, i.e. high-redshift red nuggets that, given the stochastic nature of

mergers, have slipped through the cosmic time untouched and without accreting any stars from satellites and mergers. These galaxies have assembled early on in time and have somehow missed completely the second phase of the two-phase formation scenario (size growth). They are therefore supposedly made of only the in-situ stellar population and as such they provide a unique opportunity to track the formation of this specific galaxy stellar component, which is mixed with the accreted one in normal massive ETGs. Indeed, very massive, extremely compact systems have been already found at intermediate to low redshifts (Tortora et al. 2018; Spiniello et al. 2020; 2021), also including the local Universe (Ferré-Mateu et al., 2017).

Old UCMGs or relics are the building blocks of today’s giant ellipticals. However, it is not yet clear how these massive, very compact galaxies were formed and, above all, how they evolved into today’s massive ETGs, and this question has significance that goes well beyond the context of the size evolution of quiescent galaxies.

The precise abundance of relics, and even more generally of UCMGs, without any age restriction, at low redshifts is an open issue. In fact, at  $z \leq 0.5$ , a strong disagreement exists between simulations and observations and among observations themselves on the number density of UCMGs and its redshift evolution. In general, simulations predict that the fraction of objects that should survive until the local Universe without undergoing any significant size transformation after the first high- $z$  burst of star formation is about 1 – 15% (e.g. Hopkins et al. 2009; Quilis & Trujillo 2013; Wellons et al. 2016; Furlong et al. 2017). This number highly depends on the physical processes acting during the second phase, and in particular on the relative contribution of major and minor galaxy mergers (e.g. Nipoti et al. 2009b, 2009a; Belli et al. 2014).

More recently, the evolution in redshift of massive red nuggets has been studied using cosmological hydrodynamical simulations, such as Illustris (Flores-Freitas et al., 2022) and EAGLE (Furlong et al., 2017). The number of galaxies that remains untouched after their mass assembly varies substantially, with Illustris predicting a number two times larger (31%) than the one predicted by EAGLE (15%). However, Illustris found that even massive compact galaxies that evolved undisturbed show an increase in mass and size with time, and only one red nugget at high redshift would respect the size threshold to be classified as UCMG also at  $z = 0$ . This means that the different assumptions on which the simulations are based heavily influence the size growth and consequently the evolution of the number density with time. At the lowest redshifts (i.e.,  $z \sim 0.2$ ), simulations predict densities of relics of  $10^{-7} - 10^{-5} \text{ Mpc}^{-3}$ .

From an observational point of view, thanks to the advent of wide-sky deep photometric and/or spectroscopic surveys, it has become possible to scan large portions

of the sky searching for UCMGs at low redshift ( $z < 0.5$ , e.g. Trujillo et al. 2009; Valentinuzzi et al. 2010; Poggianti et al. 2013; Damjanov et al. 2014, 2015; Saulder et al. 2015; Tortora et al. 2016; Baldry et al. 2020). The results are in strong disagreement with each other, as shown in Figure 2.6.

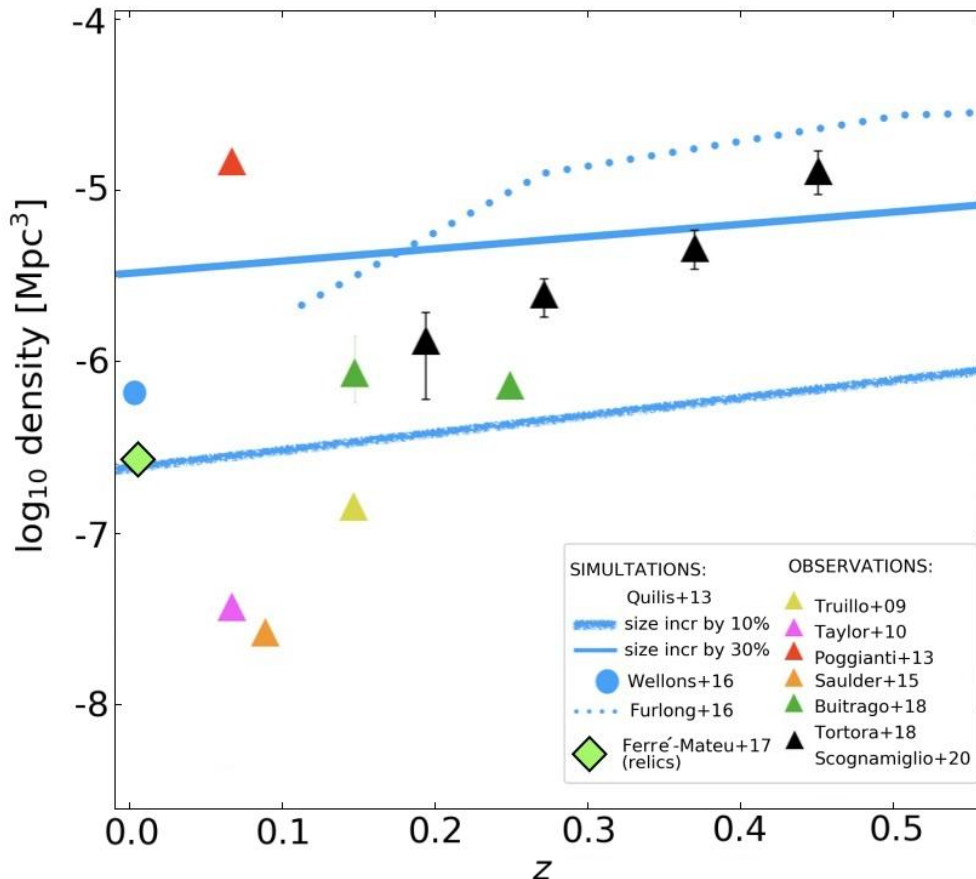


**Figure 2.6.** – UCMGs and relic number densities from  $z \sim 0.54$  to the local universe computed from different observations and simulations, as reported in the legend.

Some works find number densities similar to the ones found at higher redshifts (Valentinuzzi et al. 2010; Poggianti et al. 2013), whereas in the near-by Universe, large sky surveys as the Sloan Digital Sky Survey (SDSS) find a decline of more than three orders of magnitude with respect to the high redshift values (Trujillo et al. 2009; Taylor et al. 2010). Moreover, data from the WINGS survey of near-by clusters (Fasano et al. 2006; Valentinuzzi et al. 2010; Cava et al. 2017) estimate, at  $z \sim 0$ , a number density of two orders of magnitude above the estimates based on the SDSS dataset.

All these results have been obtained for UCMGs in general, without any distinction between younger and older (relics) systems. However, putting constraints on the relic number density is of crucial importance to shed light on the mechanisms regulating the size growth of galaxies. In fact, if relics are absent or very rare in the local Universe, this will be a strong indication that the growth mechanisms of the massive systems require more than merging to produce the observed massive galaxy population. The hypothesis that the number of mergers is much larger than theoretically predicted is excluded as we know that the number of satellites among massive galaxies at all redshifts is over-predicted by those simulations (Quilis & Trujillo 2013; Wellons et al. 2015; Pulsoni et al. 2021). On the other hand, if the relic number density at low- $z$  is comparable to the values measured at high- $z$ , then the number of merger would be lower than theoretically expected. However, one of the possible reasons behind the strong disagreement between the observations could be related to the presence of observational biases due to environmental effects in shaping properties of UCMGs and relics.

### 2.3. Gravitational lensing

Gravitational lensing is a consequence of General Relativity (Einstein, 1936): as photons move along the geodesics of space-time, their trajectories are perturbed by the gravitational potential of massive foreground objects, much like optical lenses do, giving the name to the phenomenon. Its effects are well-understood, and it acts both on baryonic and dark matter, and when the right conditions are met, for instance when the observer, a massive foreground, and a luminous background galaxies are aligned, gravitational lensing can lead to spectacular images. In just over a century, from its first detection, when Dyson et al. (1920) measured its effects during a total solar eclipse, today gravitational lensing has become the arguably most powerful tool to measure the matter content of the Universe and its distribution.

Depending on the observational consequences, gravitational lensing is divided into two main categories. *Strong gravitational lensing* produces multiple images, arcs and even complete rings. Meanwhile, the effects of *weak gravitational lensing* cannot be detected from single background galaxies, but only statistically from an ensemble of coherently lensed background galaxies, this is why it requires statistical methods to be studied. Both applications lead to accurate mass measurements of galaxies, galaxy clusters, and robust estimates of various cosmological parameters.

In the next sections we will concentrate on weak lensing. A recent review of gravitational lensing can be found in Bartelmann (2010).

### 2.3.1. Lens equation

We consider gravitational lensing in the weak-field limit of GR, with the lensing system in Minkowskian space-time. Thus, we assume that the lenses gravitational potential  $\Phi$ , its typical scales  $L$  and intrinsic velocity  $\mathbf{v}$  are all small, so,

$$|\Phi| \ll c^2, \quad L \ll \frac{c}{H_0}, \quad |\mathbf{v}| \ll c. \quad (2.26)$$

Figure 2.7 shows a sketch for a typical gravitational lens system. A background object, the *source*, located in the source plane at an angular diameter distance  $D_s$  from the observer, while the mass concentration, the *lens* (also called the deflector) at a distance  $D_d$ . The distance between the source and the deflector is given by  $D_{ds}$ . The observer sees the light deflected by the mass concentration of the lens (located in the lens plane). An optical axis intersects and is perpendicular to the source and lens planes, connecting the observer and the center of the lens. The source is located in the source plane at position  $\boldsymbol{\eta}$ . The distance in the lens plane between the lens and the intersection of the light ray with the lens plane is given by  $\boldsymbol{\xi}$ ,  $\boldsymbol{\beta}$  is the position that the source would have been observed at without the deflection caused by gravitational lensing, while  $\boldsymbol{\theta}$  is the observed source position. All of the angles can be assumed to be small.

We also assume that the distances between the lens, source and observer are much larger than the size of the lens and that the light rays travel in straight paths and are only deflected in the lens plan, which is known as the Born approximation. Hence, the true position of the source,  $\boldsymbol{\beta}$ , and its observed position on the sky,  $\boldsymbol{\theta}$  are related by a very simple relation, obtained by a geometrical construction. This relation is called the *lens equation* and is written as

$$\boldsymbol{\theta} D_s = \boldsymbol{\beta} D_s + \hat{\boldsymbol{\alpha}} D_{ds}, \quad (2.27)$$

Defining the scaled deflection angle as

$$\boldsymbol{\alpha}(\boldsymbol{\theta}) \equiv \frac{D_{ds}}{D_s} \hat{\boldsymbol{\alpha}}(\boldsymbol{\theta}), \quad (2.28)$$

where  $\hat{\boldsymbol{\alpha}}$  is the true deflection angle, from Eq. (2.27), we obtain

$$\boldsymbol{\beta} = \boldsymbol{\theta} - \boldsymbol{\alpha}(\boldsymbol{\theta}). \quad (2.29)$$

The lens equation (2.29) relates the apparent position of a source galaxy to its true position.

### 2.3.2. Deflection angle and deflection potential

We will first consider the case of a point-like lens of mass  $M$ . Under the assumption that the impact parameter  $\xi = |\boldsymbol{\xi}|$  is much larger than the Schwarzschild radius of

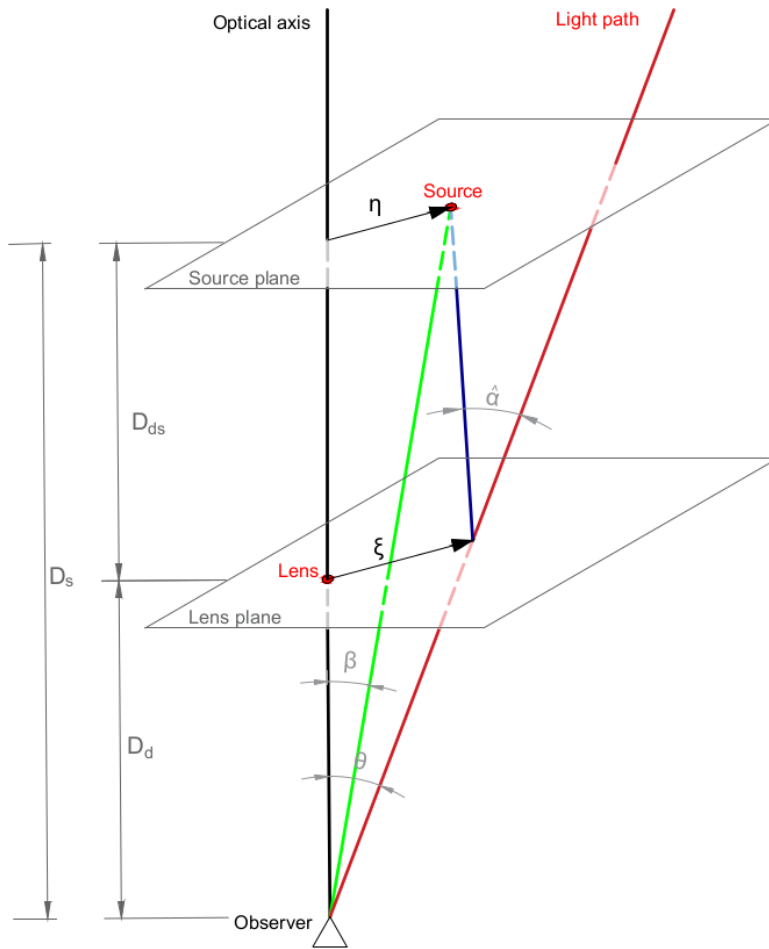


**Figure 2.7.** – Sketch of a gravitational lensing system. The distances  $D_s$ ,  $D_d$ , and  $D_{ds}$  are the angular diameter distances to the source, to the lens, and from the lens to source, respectively.

the lens,  $\xi \gg R_S = 2GMc^{-2}$ , the gravitational field is weak, and GR predicts the true deflection angle to be

$$\hat{\alpha} = \frac{4GM}{c^2 \xi^2} \xi, \quad (2.30)$$

which is twice as large as predicted by Newtonian gravity. For a mass distribution in the lens plane, the total deflection can be calculated as the superposition of deflections given by infinitesimal mass elements

$$\hat{\alpha}(\xi) = \frac{4G}{c^2} \int d^2\xi' \Sigma(\xi') \frac{\xi - \xi'}{|\xi - \xi'|^2}, \quad (2.31)$$

where  $\Sigma(\boldsymbol{\xi}')$  is the *surface mass density* at  $\boldsymbol{\xi}'$  and  $|\boldsymbol{\xi} - \boldsymbol{\xi}'|$  is the impact parameter for  $\Sigma(\boldsymbol{\xi}')$ . We can express the *reduced deflection angle* in terms of the surface mass density and of observable angles as

$$\boldsymbol{\alpha}(\boldsymbol{\theta}) = \frac{1}{\pi} \int d^2\theta' \kappa(\boldsymbol{\theta}') \frac{\boldsymbol{\theta} - \boldsymbol{\theta}'}{|\boldsymbol{\theta} - \boldsymbol{\theta}'|^2}, \quad (2.32)$$

where  $\kappa$  is the *convergence* (or the dimensionless surface mass density), which is given by

$$\kappa(\boldsymbol{\theta}) = \frac{\Sigma(D_d \boldsymbol{\theta})}{\Sigma_{\text{cr}}}. \quad (2.33)$$

The *critical surface mass density*  $\Sigma_{\text{cr}}$  characterizes the lens system and is a function of the angular diameter distances of lens and source

$$\kappa_{\text{cr}} = \frac{c^2}{4\pi G} \frac{D_s}{D_d D_{\text{ds}}}. \quad (2.34)$$

Based on the convergence, a lensing system is called critical. If  $\kappa \geq 1$  somewhere in the mass distribution, then the lens equation has more than one solution<sup>7</sup> and multiple images can be formed from the same source and/or arc-like features and rings. In this case, we are in the strong lensing regime and large distortions occur. For  $\kappa \ll 1$  we are in the weak lensing regime and in this case, the images are typically distorted at the percent level. The difference between large and subtle distortions is phenomenological rather than mathematical, although the surface density of the lens plane is often used as criteria for determining the need to work within a particular regime.

The deflection angle can be expressed as a gradient of a two-dimension scalar *deflection potential*  $\Psi$

$$\boldsymbol{\alpha} = \nabla \Psi(\boldsymbol{\theta}), \quad (2.35)$$

which indicates the strength of the deflection. The deflection potential can also be written in terms of the dimensionless surface mass density

$$\Psi(\boldsymbol{\theta}) = \frac{1}{\pi} \int_{\mathbb{R}^2} d^2\theta' \kappa(\boldsymbol{\theta}') \ln |\boldsymbol{\theta} - \boldsymbol{\theta}'|. \quad (2.36)$$

The deflection potential is the two-dimensional analogue of the three-dimensional Newtonian gravitation potential. The potential and the convergence are therefore related by

$$\nabla^2 \Psi(\boldsymbol{\theta}) = 2\kappa(\boldsymbol{\theta}), \quad (2.37)$$

which represents the Poisson equation for the deflection potential.

<sup>7</sup>Note that  $\kappa \geq 1$  is a sufficient but not necessary condition for multiple images to occur.

### 2.3.3. Image distortions

Gravitational lensing perturbs the path of light as it travels through the Universe, and as a consequence also the original shapes of the galaxies are affected. Furthermore, if the objects are small compared to the scale on which the lens mapping changes considerably, we can describe the image distortion using only a few parameters. In order to investigate the image distortion, let us start considering the lens equation in the following form

$$\boldsymbol{\beta} = \boldsymbol{\theta} - \nabla\Psi(\boldsymbol{\theta}). \quad (2.38)$$

Taking the gradient of Eq. (2.38) and linearizing it, leads to

$$\partial_j\beta_i = \delta_{ij} - \partial_i\partial_j\Psi(\boldsymbol{\theta}) \equiv A_{ij}, \quad (2.39)$$

where  $A$  is the Jacobian of the lensing potential, which describes the distortion of such an extended source. It is given by

$$A_{ij} = \frac{\partial\beta_i}{\partial\theta_j} = \left( \delta_{ij} - \frac{\partial^2\Psi(\boldsymbol{\theta})}{\partial\theta_i\partial\theta_j} \right) = \begin{bmatrix} 1 - \kappa - \gamma_1 & -\gamma_2 \\ -\gamma_2 & 1 - \kappa + \gamma_2 \end{bmatrix} \quad (2.40)$$

where we define the components of *shear*  $\gamma$  as

$$\gamma_1 = \frac{1}{2} \left( \frac{\partial^2}{\partial\theta_1^2} - \frac{\partial^2}{\partial\theta_2^2} \right) \Psi, \quad (2.41)$$

$$\gamma_2 = \frac{1}{2} \frac{\partial^2\Psi}{\partial\theta_1\partial\theta_2}. \quad (2.42)$$

The shear is often parametrized as a single complex number

$$\gamma \equiv \gamma_1 + i\gamma_2 = |\gamma| e^{2i\phi}, \quad (2.43)$$

where  $\phi$  is the position angle, i.e. the angle between the semi-major axis of the ellipse and the  $x$ -axis. As seen, the convergence and the shear can be expressed as derivatives of the deflection potential and they have different effects in the lens mapping. From the last form of the Jacobian one can nicely see that the convergence is responsible for an isotropic change in size of the images while the shear causes also a change in the shape of the images, see Figure 2.8. Furthermore, shear and convergence are related to the *reduced shear*  $g$

$$g = \frac{\gamma}{1 + \kappa} = \frac{\gamma_1 + i\gamma_2}{1 + \kappa}. \quad (2.44)$$

The reduced shear describes the anisotropic distortion of the image shape between the observed image and the intrinsic source galaxy image; actual measurements of



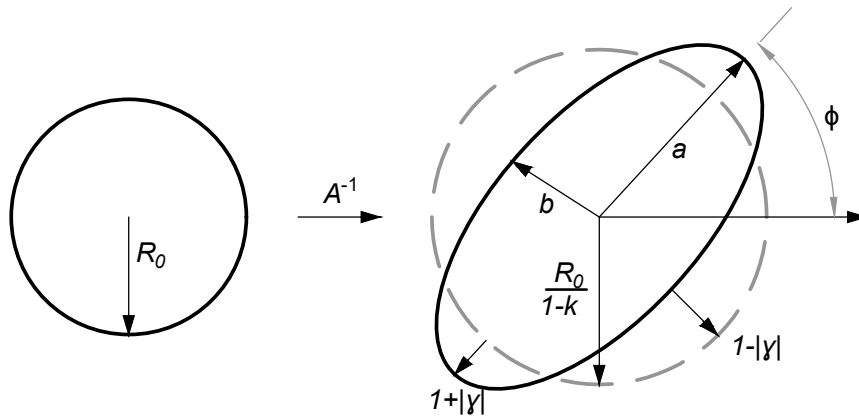


**Figure 2.8.** – Illustration of the first order effect of convergence  $\kappa$  and shear  $\gamma$  on an intrinsically round source with radius  $R_0$ , which is mapped by the inverse Jacobian  $A^{-1}$  onto an ellipse. In the absence of shear, the resulting image is a circle with modified radius, depending on  $\kappa$ . Shear causes an axis ratio different from unity, and the orientation of the resulting ellipse depends on the phase of the shear  $\phi$ .

galaxy shapes in practice give us an estimate of  $g$  rather than  $\gamma$  itself.

Aside from the distortion of the source shape, gravitational lensing also magnifies (or de-magnifies) images. Indeed, Liouville’s theorem states lensing conserves the surface brightness. Due to the shape distortion, however, the observed apparent solid angle  $\omega$  of the image differs from the one in the absence of lensing,  $\omega_0$ . Hence, also the flux  $s$  that we receive, is enhanced or reduced compared to the unlensed flux  $s_0$ . The *magnification factor* is defined as

$$\mu(\boldsymbol{\theta}) = \frac{\omega(\boldsymbol{\theta})}{\omega_0} = \frac{s(\boldsymbol{\theta})}{s_0} = \frac{1}{\det A(\boldsymbol{\theta})} = \frac{1}{(1 - \kappa)^2 - |\gamma|^2}. \quad (2.45)$$

The magnification factor can take both negative and positive values. An infinitesimally small source is therefore dimmed or brightened by a factor of  $|\mu(\boldsymbol{\theta})|$ . While the magnification by gravitational lenses enables the observation of faint sources, which would be undetectable otherwise (see e.g. Richard et al. 2011; Schmidt et al. 2017), it also affects the observed number density of the galaxies, enhancing or reducing the galaxy counts on the sky. So, besides being able to create multiple images of the same source, gravitational lensing also modifies the properties of a source from the point of view of the observer due to differential deflection across light bundles. In particular, the shape of an object can be distorted (sheared) and the observed flux can be changed (magnified).

### 2.3.4. Weak gravitational lensing

In the following, we focus only on weak gravitational lensing where small effects on background galaxies are induced, i.e.  $\kappa \ll 1$  and  $|\gamma| \ll 1$ .

In order to quantify the observed changes in the shape of the source, we start by considering an idealised galaxy with elliptical isophotes and defining the ellipticity as

$$|\epsilon| = \frac{a - b}{a + b}, \quad (2.46)$$

where  $a$  and  $b$  are the sizes of the semi-major and semi-minor axis, respectively. The two ellipticity components are:

$$\epsilon_1 = |\epsilon| \cos 2\phi \quad (2.47)$$

$$\epsilon_2 = |\epsilon| \sin 2\phi, \quad (2.48)$$

with  $\phi$  the angle between the semi-major axis of the ellipse and the  $x$ -axis. Due to weak lensing, the observed ellipticity is composed of the intrinsic ellipticity  $\epsilon^{\text{int}}$  and the reduced shear  $g$ ,

$$\epsilon = \frac{\epsilon^{\text{int}} + g}{1 + g^* \epsilon^{\text{int}}}, \quad (2.49)$$

where we use the asterisk for the complex conjugation. In the weak lensing regime  $g \simeq \gamma$ , so we can in principle estimate the shear directly from the observed ellipticity. However, in this regime the galaxy shapes are only slightly distorted, and the shape distortion is usually smaller (1%) than the intrinsic ellipticity of a galaxy. This means that we cannot study the resulting effect by observing individual galaxies, but we need to carry out a statistical analysis of a large number of them. Assuming the cosmological principle, claiming that the Universe is homogeneous and isotropic, the galaxies are randomly oriented. On the other hand, the distortion coming from lensing will have a preferential direction according to the position of the galaxies with respect to the lens. The observed ellipticity is the sum of the intrinsic ellipticity and the shear,

$$\langle \epsilon^{\text{obs}} \rangle \simeq \langle \epsilon^{\text{int}} \rangle + \langle \gamma \rangle. \quad (2.50)$$

Averaging over many galaxies, the average ellipticity is zero, i.e.,  $\langle \epsilon^{\text{int}} \rangle = 0$ , and we can disentangle intrinsic ellipticity and shear with

$$\langle \epsilon^{\text{obs}} \rangle \simeq \langle \gamma \rangle, \quad (2.51)$$

since their intrinsic ellipticity does not follow a preferential direction. As discussed in Section 2.3.3, round sources are transformed into ellipses. However, galaxies have complex brightness profiles, whether it is because of different components (e.g. a bulge and a disk) of highly different shapes, of spiral arms, or simply, in the case of irregular galaxies, they are only poorly represented by ellipses.

Since gravitational lensing conserves surface brightness, it is convenient to define the ellipticity of a galaxy in terms of its second-order brightness moments

$$Q_{ij} = \frac{\int d^2\theta \theta_i \theta_j I(\boldsymbol{\theta})}{\int d^2\theta I(\boldsymbol{\theta})} \quad i, j \in \{1, 2\}, \quad (2.52)$$

with  $I(\boldsymbol{\theta})$  the surface brightness distribution and  $\boldsymbol{\theta}$  is the center of the galaxy. The latter is chosen such that the first moment of the brightness distribution vanishes

$$\int d^2\theta \boldsymbol{\theta} I(\boldsymbol{\theta}) = 0. \quad (2.53)$$

We can now define the ellipticity of our image  $I$  as

$$\epsilon = \frac{Q_{11} - Q_{22} + 2iQ_{12}}{Q_{11} + Q_{22} + 2(Q_{11}Q_{22} - Q_{12}^2)^{1/2}}. \quad (2.54)$$

This definition can be used for shear measurements as it responds to a lensing shear in a well-defined way (Mandelbaum, 2018).

## 2.4. Measuring weak lensing

In the last three decades, WL has been established as a rich source of cosmological information. Although technically challenging to measure because of the small amplitude of the weak lensing signal, the methodology and observation techniques have advanced enormously.

Sensitive measurements of shear (see e.g. Kilbinger 2015; Mandelbaum 2018, for recent reviews) require the observation of large and deep sky areas with an excellent image quality, together with sophisticated image analysis methods. Only with these two ingredients, one can probe the evolution of structure on large scales as well as the geometry of the Universe, and derive cosmological information. These are the primary goals of large dedicated surveys that will gather data in the near future: the space missions *Euclid*<sup>8</sup> (Laureijs et al. 2011b) and the Nancy Grace Roman Space Telescope<sup>9</sup> (Spergel et al. 2015b) as well as the ground-based Vera C. Rubin Observatory's Legacy Survey of Space and Time<sup>10</sup> (Rubin-LSST; LSST Science Collaboration et al. 2009).

A question naturally arises: *how can we turn what we observe into practical measurements of shapes and galaxy parameters?* Four factors are especially important for this. The desired precision on the measurement of the cosmic shear amplitude

<sup>8</sup>[sci.esa.int/Euclid/](http://sci.esa.int/Euclid/)

<sup>9</sup><https://roman.gsfc.nasa.gov/>

<sup>10</sup><https://www.lsst.org/lsst>

requested by the upcoming surveys requires a very large number of galaxies and their shapes have to be measured with high accuracy. The point-spread function (PSF), which is the combined effect of the imaging system consisting of the atmosphere (for ground-based surveys), telescope optics, and detector, heavily impacts the galaxy images. In particular, the anisotropic part of the PSF creates spurious correlations of galaxy shapes which, if unaccounted, are typically larger than the cosmological shear correlation. Any method of galaxy shape measurement including the removal of PSF effects has to be calibrated, to ensure that measurement biases are small enough compared to the statistical errors. For this, large sets of image simulations must be analysed, where the amount of input shear is controlled. The interpretation of measured shape correlations depends on the redshift distribution of the lensed galaxy sample, thus multiple optical band observations are essential to estimate photometric redshifts.

In this work, we consider only the first three of these factors. We put our effort into understanding if HST-observed galaxy images can in principle be used to emulate *Euclid* observations of sheared galaxy images with real morphology. This requires an investigation of the uncertainties in the HST PSF models, as well as a calibration of shape measurement methods using a large volume of image simulations to correct residual systematic biases in cosmic shear analyses, as described in Chapter 4. Photometric redshifts will be needed only once the procedure will be applied to real HST data, which is out of the scope of this work.

### 2.4.1. Sources of bias and calibration

All the shape measurements method suffer from measurement biases and require a large and representative sample of observed (to account for real morphologies) and/or simulated galaxies to calibrate these biases in order to obtain unbiased estimates of the shear.

In the last decade, large volumes of image simulations have been created in order to test the accuracy in the shear estimates of various shear measurement techniques, such as the Shear TEsting Project (STEP) with the two consecutive blind tests STEP1 (Heymans et al., 2006) and STEP2 (Massey et al. 2007a), the GRavitational lEnsing Accuracy Testing (GREAT), containing GREAT08 (Bridle et al. 2009; Bridle et al. 2010), GREAT10 (Kitching et al. 2011a, Kitching et al. 2012a, Kitching et al. 2013), and GREAT3 (Mandelbaum et al., 2014a). The results have shown that the shear measurement problem is quite complex.

Typically shape measurement methods show residual biases, but these can be calibrated using simulations from the differences between the input and the recovered shear if the simulations resemble the true data sufficiently well. Before going to the

methods we use in this thesis to measure the shapes and the parameters of galaxies, we briefly review some of the main sources of biases affecting shear measurements. *Pixel noise bias* arises from the fact that ellipticity is not a linear function of pixel intensities in the presence of noise and PSF (Hirata et al. 2004; Refregier et al. 2012; Kacprzak et al. 2014). It affects the second-order moment measurements of convolved galaxy images, however some works (Zhang & Komatsu 2011; Bernstein & Armstrong 2014; Viola et al. 2014) have shown that it is possible to reduce it.

Real galaxies usually cannot be easily described by simple analytical profiles. Thus, selecting a model which cannot sufficiently reproduce the galaxy introduces the so-called *model bias* (Bernstein, 2010). Moreover, galaxies have bulge and disc components with different ellipticities. For galaxies with a bulge that is more circular than its disk, the ellipticity is a function of the scale where it is measured (Bernstein 2010; Voigt & Bridle 2010), leading to the *ellipticity gradient*.

Another type of bias is the *selection bias*, which occurs when a galaxy is preferentially selected because of the increasing brightness when its shape is aligned with the PSF distortion or orthogonally-aligned with the shear (Kaiser 2000; Bernstein & Jarvis 2002; Hirata & Seljak 2003). Biases in estimates of shear correlations can be related to intrinsic alignments, which are not caused by gravitational lensing, but by the source gravitational field (Troxel & Ishak, 2015). Although the effects of intrinsic-intrinsic (II) alignment can be reduced by removing pairs of galaxies that are physically close in the measurement of the shear correlation (King & Schneider 2002; Heymans & Heavens 2003), there still remains a residual bias due to the shear-intrinsic (GI) terms. In fact, the GI term has a contribution from gravitational lensing and therefore a scaling with redshift that is very similar to cosmic shear. Nevertheless it is possible to suppress the GI signal, but one can only do so robustly with a substantial loss in cosmological constraining power (Joachimi & Schneider, 2010).

We turn now our attention on another source of bias, which will be investigated in Chapter 4 and is related to the PSF. The observed galaxy images are obtained from telescopes, which means they are not only distorted by gravitational shear. The origins of this distortion are due to various affects. Indeed, in actual measurements, we do not measure directly the moments of the sheared galaxy images, but rather we measure the moments of the galaxy image after the additional convolution with the PSF of the telescope (and atmosphere for ground-based observations).

The observed brightness profile  $I_{\text{obs}}$  is related to the true surface brightness  $I$  of an image by a convolution with the PSF  $P$

$$I_{\text{obs}}(\boldsymbol{\theta}) = \int d\boldsymbol{\vartheta}^2 I(\boldsymbol{\theta} - \boldsymbol{\vartheta}) P(\boldsymbol{\vartheta}), \quad (2.55)$$

which summarises these effects. Space-based observations have a much higher resolution, which is mainly determined by the diffraction limit of the telescope. For ground-based telescopes, the effect of the atmospheric turbulence further contributes to the isotropic blurring. The latter is the main driver for the development of space-based telescopes. Imperfect optics, for instance due to the polishing of the mirrors, coma, chromatic aberrations, astigmatism, field curvature of the telescope optics, and possibly stray light propagating within the instrument also affect the PSF.

In the shape measurement method used in this work, the PSF can be decomposed into isotropic smearing and anisotropic distortions. An anisotropic PSF can be created by astigmatism, field curvature, wrong offsets in the image co-addition, tracking errors, or wind at the telescope site. While isotropic smearing dilutes the signal, an anisotropic PSF can mimic a false shear signal. Thus, it is important for WL measurements to model the convolving PSF and correct for it using stars.

Additional complications arise when the distortions caused by the PSF depend on the observing wavelength (Cypriano et al., 2010). Similarly, high resolution images of galaxies show that their spectral energy distributions (SEDs) vary across the galaxy profile, referred to as the ‘color gradient’ (CG). Then, the distortions due to the chromatic PSF will be different for different points on the galaxy. As a consequence, PSF corrections that are applied assuming a constant SED can lead to systematic bias in the shape measurements, the *color gradient bias*. The bias related to this colour-dependence of the PSF depends on the SED variation within the filter, which is the larger the broader the filter is. In the case of *Euclid*, which has a wide wavelength range for the optical filter, this effect has to be necessarily taken into account (Cypriano et al. 2010; Plazas & Bernstein 2012; Meyers & Burchat 2015). In addition, its observations will require high-quality PSF models for WL measurements.

Other sources of systematics are induced by the detector. A galaxy image will appear on the CCD camera discretised into pixels. Ideally, the size of the pixels is much smaller than the width of the PSF, which is then well sampled. However, the PSF is often poorly sampled, making a proper PSF correction particularly difficult.

The charge transfer efficiency (CTE) of space-based instruments provides another source of image distortion. In contrast to ground-based CCDs, cosmic rays are of particular concern for space-based cameras. These highly energetic particles of extraterrestrial origin deposit energy while passing through the CCD leading to pixels with very high signal. Depending on the angle under which a cosmic ray passes through the chip, its signature in the image can range from only very few neighbouring pixels to long traces of affected pixels, creating chip defects acting as

charge traps. If the image of an object moves across such a trap during parallel read-out transfers, a fraction of its charge will first be trapped and then statistically released during the following read-out steps. This effectively creates charge-trails behind objects, causing an elongation of the objects that is correlated with the read-out direction and the distance from the read-out amplifier. Over time the CTE degrades, increasing the magnitude of this effect (Rhodes et al. 2004; Miralles et al. 2005).

Due to the dependency of this effect on the  $S/N$  and on the shape of the object, PSF models derived from high  $S/N$  stars do not provide a sufficient CTE correction for faint and more extended galaxies. In addition, the effect depends on the number of transfers (position) and sky background, where high sky values fill the traps continuously, reducing the effect of charge trails. Recent analysis (Massey et al, in prep.) shown that the radiation damage has a different effect in the cold environment of space than in the warm environment of a terrestrial laboratory. For this, increasingly accurate models describing the effect of radiation damage are of paramount importance to improve the correction of HST data to be used as input for WL image simulations for *Euclid*.

The Brighter-Fatter effect (BFE) (Guyonnet et al. 2015; Plazas et al. 2018), wherein the size of brighter objects tends to be larger, is particularly relevant to WL and especially PSF modelling, since the latter is typically performed using bright stars. Furthermore, observations are affected by various sources of noise, such as sky background, dark current, photon noise, and read-out electronics, but also image defects like cosmic rays and hot or cold pixels.

In order to achieve accurate scientific results, we have to account for the many effects affecting the galaxy shape, otherwise they can lead to a wrong estimate of the gravitational shear. Furthermore, the intrinsic properties of the galaxy prior to lensing distortion are unknown. This is the reason why simulations are essential to account for all these effects and calibrate them out.

Knowing the input shear  $g^{\text{true}}$  in weak lensing image simulations, one usually fits the recovered shear  $g^{\text{obs}}$  as

$$g_i^{\text{obs}} = (1 + \mu_i)g_i^{\text{true}} + c_i, \quad i = 1, 2, \quad (2.56)$$

for both components of the shear separately. So, shape biases can be characterised to first approximation by a multiplicative component  $\mu$ , and additive term  $c$  (Heymans et al. 2006; Huterer et al. 2006). The aim of the calibration step is to both evaluate and correct for these terms. The typical change in ellipticity caused by gravitational lensing is about a per cent, much smaller than the intrinsic ellipticities of galaxies and also smaller than the typical biases introduced by

instrumental effects. Dominant sources for multiplicative bias include noise bias (Refregier et al., 2012), model bias (e.g. Melchior & Viola 2012; Refregier et al. 2012; Miller et al. 2013; Kacprzak et al. 2014), or the impact of neighbouring objects (Hoekstra et al., 2017; Martinet et al., 2019), and it biases the amplitude of the shear by a factor  $(1 + \mu)$ . The additive bias term  $c$  can, for example, be caused by an insufficient correction for the PSF anisotropy and may lead to spurious correlation in the shapes of galaxies (Massey et al., 2012).

While “Stage III” experiments (i.e., the Dark Energy Survey (DES)) provided shear estimates with  $|\mu|$  at the 1 to 10 percent level (Jarvis et al., 2016), and  $c$  between  $10^{-3}$  and  $10^{-2}$ , “Stage IV” experiments like *Euclid* (Laureijs et al., 2011b), Vera C. Rubin Observatory’s Legacy Survey of Space and Time (Rubin-LSST) (Ivezić et al., 2019), Nancy Grace Roman Space Telescope (Spergel et al., 2015b) require the accuracy of calibrated shapes to be on the order of 0.1% (Amara & Réfrégier, 2008). To match the statistical precision of *Euclid*, systematic shear measurement biases will need to be controlled to an accuracy of  $|\delta\mu| < 2 \times 10^{-4}$  and  $|\delta c| < 5 \times 10^{-5}$  (Cropper et al., 2013).

### 2.4.2. Shape measurements - KSB method

The correction of PSF effects is of paramount importance for weak lensing studies. A correction is in principle possible, if the PSF is properly sampled on the pixel grid and across the image. So, assuming we obtained an appropriate PSF model, we can finally turn to the practical measurement of shapes.

Historically the shape measurements methods fall into two categories: model-fitting and moment-based algorithms. In this thesis, we use the Kaiser, Squires and Broadhurst (KSB) algorithm (Kaiser et al. 1995; Luppino & Kaiser 1997a; Hoekstra et al. 1998), which measures ellipticities of galaxies using weighted second-order moments of the galaxy light distribution, performing a correction for the PSF using the stars in the field. Then the galaxy ellipticities are corrected for smearing and anisotropy. Although new and more modern methods (Huff & Mandelbaum 2017; Tewes et al. 2019; Pujol et al. 2020; Lanusse et al. 2021) have been developed for shear analysis, the KSB method is a widely used weak lensing shape measurement technique, performing quite well for our purposes.

In Section 2.3.4 we defined the ellipticity parameters of galaxies in terms of the second-order brightness moments  $Q_{ij}$  where the integral is done over the entire image plane. For real images the integration has to be replaced by a sum over pixel values and has to be truncated due to neighbouring objects. The ellipticity



of each background galaxy is measured individually, using the weighted quadrupole moments  $Q_{ij}$  of the light in the form of (in analogy with the Eq. (2.52))

$$Q_{ij} = \frac{\int d^2\boldsymbol{\theta} W(\boldsymbol{\theta}) I(\boldsymbol{\theta}) \theta_i \theta_j}{\int d^2\boldsymbol{\theta} W(\boldsymbol{\theta}) I(\boldsymbol{\theta})} \quad i, j \in \{1, 2\}, \quad (2.57)$$

where  $I(\boldsymbol{\theta})$  is the surface brightness and  $W(\boldsymbol{\theta})$  is a weight function which in our case is a Gaussian function with scale length  $r_g$ , which depends on the size of the objects and is determined in the process of object detection. For our study, we choose uniform shear weights.

The two component of the complex ellipticity are defined as

$$\begin{aligned} \epsilon_1^{\text{obs}} &= \frac{1}{Q_{11} + Q_{22}} (Q_{11} - Q_{22}), \\ \epsilon_2^{\text{obs}} &= \frac{1}{Q_{11} + Q_{22}} (2Q_{12}), \end{aligned} \quad (2.58)$$

which correspond to the two axis on which the ellipticity is measured. The first component,  $\epsilon_1$ , is aligned with the direction of the pixel and the second,  $\epsilon_2$ , is diagonal to the pixel.

In KSB, the PSF effects on the ellipticity of a galaxy are approximated as a convolution with a circularly smeared PSF and an anisotropic kernel. This is not fully true for many realistic PSFs, in particular, the HST PSFs used in Chapter 4. But it can be used as an approximation (Hoekstra et al., 1998) and we can test how this affects the results using simulations (see Section 4.6).

We can describe the anisotropic component of the PSF, which can only be estimated using stars, as

$$p_\mu = (P^{\text{sm}*})_{\mu\alpha}^{-1} \epsilon_\alpha^{*\text{obs}}, \quad (2.59)$$

with  $\epsilon_\alpha^{*\text{obs}}$  the measured ellipticity and  $P^{\text{sm}*}$  the smear polarisability tensor of stars (indicated with the asterisk) (Kaiser & Squires, 1993).

The PSF anisotropy-corrected ellipticity of galaxies can then be defined as

$$\epsilon_\alpha^{\text{cor}} = \epsilon_\alpha^{\text{obs}} - P_{\alpha\beta}^{\text{sm}} p_\beta, \quad (2.60)$$

where  $P_{\alpha\beta}^{\text{sm}}$  is the smear polarisability tensor, which describes the sensitivity of the galaxy to the smearing caused by the PSF.

To account for the isotropic effect of the PSF and the weight function, we write the intrinsic ellipticity  $\epsilon^s$  and the gravitational shear  $\gamma$  as follows

$$\epsilon_\alpha^{\text{cor}} = \epsilon_\alpha^s + P_{\alpha\beta}^g \gamma_\beta. \quad (2.61)$$

The pre-seeing shear polarisability tensor,  $P_{\alpha\beta}^g$ , is defined as

$$P_{\alpha\beta}^g = P_{\alpha\beta}^{\text{sh}} - P_{\alpha\gamma}^{\text{sm}} \left[ (P^{\text{sm}*})_{\gamma\delta}^{-1} P_{\delta\beta}^{\text{sh}*} \right], \quad (2.62)$$

where  $P_{\alpha\beta}^{\text{sh}}$  is the shear polarisability tensor defined in Hoekstra et al. (1998), which measures the response of galaxy ellipticity to shear in the absence of PSF effects, and  $P_{\alpha\gamma}^{\text{sm}*}$  and  $P_{\alpha\gamma}^{\text{sh}*}$  are the stellar smear and shear polarisability tensors, respectively.

We can now define the fully corrected ellipticity, which is our KSB shear estimator as

$$\epsilon_a = (P^g)_{\alpha\beta}^{-1} \left[ \epsilon_\beta^{\text{obs}} - P_{\alpha\mu}^{\text{sm}} p_\mu \right]. \quad (2.63)$$

In the weak lensing regime,  $\kappa \ll 1$  we have

$$\langle \epsilon_\alpha \rangle = g \simeq \gamma, \quad (2.64)$$

which is an unbiased estimator for the reduced gravitational shear, assuming the intrinsic ellipticity are randomly orientated.

### 2.4.3. Parameter measurements - Galaxy model fits

As an approximation, we use to simulated our galaxy a Sérsic profile (Eq. (2.23)). Thus, we employ the Astropy `EllipSersic2D` model to model them and a least-squares method, i.e. the Levenberg–Marquardt algorithm, to estimate the main galaxy parameters, such as the total flux  $F$ , the half-light radius  $R_e$  and, the Sérsic index  $n$ . More details are reported in Chapter 4.

# CHAPTER 3

---

## The surveys

---

*“The universe as astronomy reveals it is very vast. How much there may be beyond what our telescopes show, we cannot tell; but what we can know is of unimaginable immensity.”*

- Bertrand Russell, *Sceptical Essays*

This thesis relies both on simulations of optical data from space-based telescopes and real ground-based optical observations. Weak lensing studies require not only deep and high resolution observations to detect faint background galaxies with high signal-to-noise ratio, but also a wide sky coverage to maximise the number of observed galaxies. These requirements are best satisfied by a space-based telescope such as *Euclid* and the *Hubble* Space Telescope (HST). On the other hand, follow-up observations that aim to spectroscopically confirm the nature of galaxies can very well be obtained with ground-based telescopes, such as, the Isaac Newton Telescope (INT) and the Telescopio Nazionale Galileo (TNG).

In this section, we will summarise relevant properties of these instruments and some key aspects relevant for the works presented in Chapters 4 and 5.

### 3.1. Space-based telescopes

The performance of a testing environment employing HST data as input images to calibrate weak lensing shape measurements for *Euclid* can be estimated using image simulations of both telescopes, we will review, as will be further explained in Chapter 5. In the following, we will describe both telescopes and relevant surveys.

### 3.1.1. The *Euclid* mission

*Euclid* is a medium-class ESA mission, part of its “Cosmic Vision” program, with a launch planned (at time of writing) on a Ariane 62 rocket in May of 2023. The space-borne observatory will have a nominal lifetime of 6 years and it will carry out its observations from the L2 Sun-Earth Lagrange point. Figure 3.1 shows the *Euclid*’s payload and service modules.



**Figure 3.1.** – The *Euclid* spacecraft with its payload and service modules. Credit: ESA.

The main science objectives of *Euclid* are understanding the distribution of dark matter and the nature of dark energy in the Universe. This will be achieved through the use of two main cosmological probes: weak gravitational lensing (WL) and Baryonic Acoustic Oscillations (BAO), which are wiggle patterns, imprinted in the clustering of galaxies on large scales. In order to maximize the yield of its two main probes, as both WL and galaxy clustering rely on the measurement of a large number of objects, *Euclid* aims to observe as much of the sky as possible. It will perform a Wide Survey (WS), which covers  $\lesssim 15\,000$  deg<sup>2</sup> of extragalactic sky at a depth to observe  $\sim 30$  galaxies per arcmin<sup>2</sup>, corresponding to a detection limit of  $10\sigma$  for moderately extended sources at  $m_{\text{AB}} = 24.5$ . In addition, it will repeatedly observe the three *Euclid* Deep Fields (EDFs, dubbed EDF North, EDF South and EDF Fornax) in order to go deeper and probe the high-redshift Universe (which will also be useful for WL, especially calibration; see e.g. Martinet et al. 2019). Although *Euclid* is primarily designed as a tool to quantify the various components of the Universe in detail, it will provide important insight into many fields of astrophysics, from galaxies and active galactic nuclei (AGN) evolution to extra-solar planets, going through the study of supernovae and transients.

The *Euclid* spacecraft is made up of the *payload module*, comprising the telescope, the instruments and some of the data processing electronics, and the *service module*, which contains the satellite systems, see Figure 3.1. The telescope is a 1.2 m on-axis 3-mirror Korsch, providing a field of view (FOV) of  $0.79 \times 1.16$  deg<sup>2</sup>. The two instruments on board are the wide-band visible imager (VIS), and the Near Infrared Spectrometer and Photometer (NISIP), which can operate simultaneously by using a dichroic to split the incident light. While NISIP will perform both imaging photometry to provide photometric redshifts and slitless spectroscopy to obtain spectroscopic redshifts, VIS will acquire high quality images to carry out the weak lensing galaxy shear measurements.

In this work we are interested in the VIS instrument, thus we now turn our attention to it. In fact, to emulate *Euclid*-like observations, we adapt the technical parameters of our image simulations to mimic the planned design and specifications of *Euclid*'s VIS instrument, and we employ a narrow and under-sampled *Euclid*-like PSF. More details are provided in Chapter 4.

The VIS focal plane is made up of a mosaic of  $6 \times 6$  CCDs, each of them comprising  $4096 \times 4132$  pixels, and its associated Read Out Electronics units (ROE). The pixel scale is of about 0.1 arcsec, leading to a very wide FOV of about  $0.700 \times 0.778$  deg<sup>2</sup> (Scaramella et al., 2022). For comparison, the FOV of the HST's ACS instrument, we will describe in the next section, is about 180 times smaller. Despite this, it produced the best space-based WL catalogs to date, thus the VIS instrument can only do better. The wide wavelength range spans most of the optical

domain, from 550 to 920 nm. This, however, comes at the cost of needing to handle the chromatic variations of the PSF (Cypriano et al. 2010; Eriksen & Hoekstra 2018).

The VIS instrument consists of several units, which we list here.

#### **VIS Focal Plane Assembly (VI-FPA VIS)**

It detects the visible light for imaging purpose.

#### **VIS Shutter Close (VI-SU)**

The shutter prevents direct light from falling onto the CCDs during the closed phase while allowing the fine guidance sensors to be exposed to light continuously.

#### **VIS Calibration Unit (VI-CU)**

The calibration unit is designed to obtain flat fields of the focal plane array for calibration. This structure encloses a 12-LEDs panel illuminating a diffusing panel inside an integrating sphere.

#### **Control and Data Processing Unit (VI-CDPU)**

It controls the instrument and compresses the scientific data before transfer to the payload mass memory, thus it represents the interface spacecraft for data handling.

#### **Power and Mechanism Control Unit (VI-PMCU)**

It controls the instrument mechanisms and calibration units.

#### **Flight Harness (VI-FH)**

It connects the units and the electronics.

The main role of the visible imaging is to measure galaxy shapes and hence, the shear induced by weak gravitational lensing. This is achieved through the analysis of a large sample of galaxies, from which the matter maps can be reconstructed as a function of distance, to a high level of precision. Then, constraints on the cosmological parameters can be derived using observable real quantities such as the shear-shear correlation functions (Simon, P. et al. 2004; Pires et al. 2020).

The design conceived for *Euclid*, its survey and the analysis, ensuring top-level science requirements, make *Euclid* one of the most powerful space mission and one of the best next-generation dark energy experiment in terms of precision and accuracy. This implies that some important features must be met, such as the high image quality and PSF stability, the accessibility to near infrared wavelengths, and a homogeneous survey of the extra-galactic sky with a minimum of sources of potential systematic effects. These requirements led to the choice for the size of the FOV of the detectors and the size of the telescope. Furthermore, going to

space offers the following two advantages: escaping atmospheric turbulence, which provides a stable and small PSF and infrared observations obtaining photo- $z$ s to significantly higher redshifts than from the ground. It is primarily relevant that the space-based NIR images are much deeper than ground-based ones because of lower NIR background. In addition, providing images of excellent quality means not only that the PSF must be acceptable, but its characteristics must also be known very precisely at any point over the FOV and for any observation. Indeed, telescope and survey are optimised for PSF stability, especially by allowing only for small variations in the solar aspect angle (Scaramella et al., 2022).

### 3.1.2. The *Hubble* Space Telescope

Launched in April 1990, the *Hubble* Space Telescope (HST) is a 2.4 meter  $f/24$  Ritchey–Chretien Cassegrain telescope, still in operation. Orbiting high above the Earth, in a low Earth orbit, the HST has a clear view of the Universe free from the blurring and absorbing effects of the atmosphere. This provides high-resolution imaging in optical, near-infrared and, ultraviolet wave bands. For these latter, the light is absorbed by the atmosphere and visible only from space. In addition, space-based observations have a lower sky background, which in combination with the high resolution enable very deep observations. For weak lensing study, being in space provides the great advantage to resolve a high number density of galaxies, allowing accurate WL shape measurements at small angular scales.

The telescope was designed to be visited periodically by astronauts, who brought new instruments and technology during its 20 years. HST's current suite of instruments includes the Wide Field Camera 3 (WFC3), the Cosmic Origins Spectrograph (COS), the Advanced Camera for Surveys (ACS), the Space Telescope Imaging Spectrograph (STIS) and the Fine Guidance Sensors (FGS). Figure 3.2 depicts the HST's control and support systems and the instruments.

We are interested in simulating galaxies such as those observed by ACS/WFC, since it is the most effective HST camera in the optical in terms of FOV and throughput. The ACS instrument consists of three independent channels:

#### **Wide Field Channel (ACS/WFC)**

It consists of two  $2048 \times 4096$  pixel thinned, backside-illuminated CCDs, with  $\sim 0.05$  arcseconds per pixel and a FOV of  $202 \times 202$  arcseconds. The wavelength range covered spans from  $\sim 3700 \text{ \AA}$  to  $11000 \text{ \AA}$ .

#### **High Resolution Channel (ACS/HRC)**

It is a  $1024 \times 1024$  pixel thinned, backside-illuminated CCD, with  $\sim 0.028 \times 0.025$

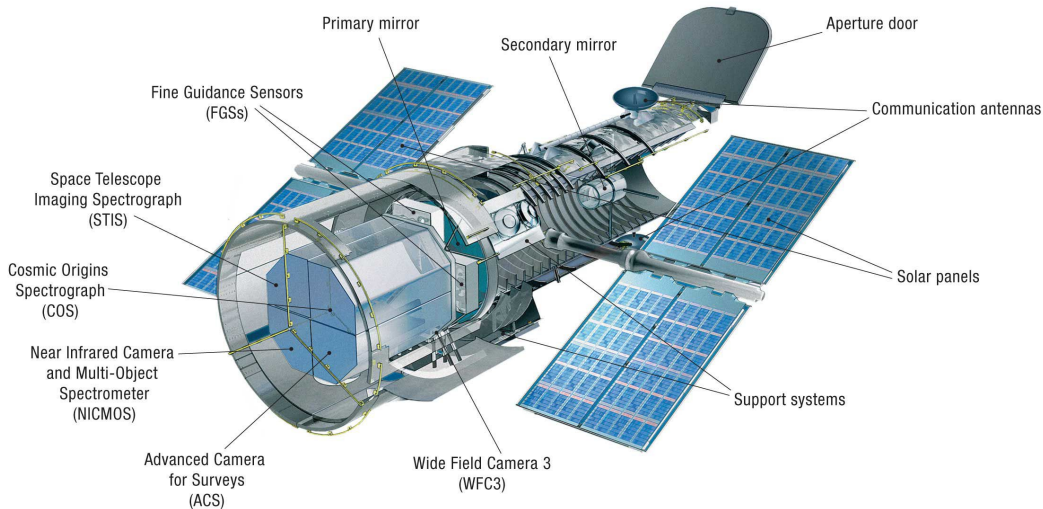


**Figure 3.2.** – The HST’s control and support systems and the instruments. Credit: Hubble-site.

arcseconds per pixel, with a FOV of  $29 \times 26$  arcsecond, with a spectral response from  $\sim 2000 \text{ \AA}$  to  $11000 \text{ \AA}$ . It is no longer operational since 2007.

#### Solar Blind Channel (ACS/SBC)

It is a detector CsI Multi-Anode Micro-channel Array (MAMA), with  $1024 \times 1024$  pixels and FOV of  $35 \times 31$  arcseconds. This instrument provides photon-counting UV imaging capability, operating in the far-UV range from  $1150 \text{ \AA}$  to  $1700 \text{ \AA}$ .

The instrument dedicated for WL measurements is the ACS Wide Field Channel detector, as it provides the largest FOV of  $202'' \times 202''$  and highest sensitivity in optical bands of all HST cameras, in combination with relatively good sampling, enabling accurate shape measurements. In Figure 3.3, the projected position of the WFC FOV relative to the optical axis and the other cameras is shown. For further details the reader is referred to Ryon (2022).

The WFC shares two filter wheels with the HRC, allowing the use of the following filters for the WFC: F435W, F475W, F502N, F550M, F555W, F606W, F625W, F658N, F660N, F775W, F814W, F850LP, and the grism G800L. In order to test the use of HST archive data, we will start simulating galaxies in F606W and F814W filters, which correspond to the wavelength range of *Euclid*/VIS. We also generate HST PSF models with TinyTim (Krist, 1993), accounting for all the characteristics of the ACS (see Chapter 4). The WFC camera has two CCD chips, usually denoted as WFC1 and WFC2, where WFC1 is located at higher  $Y$  positions



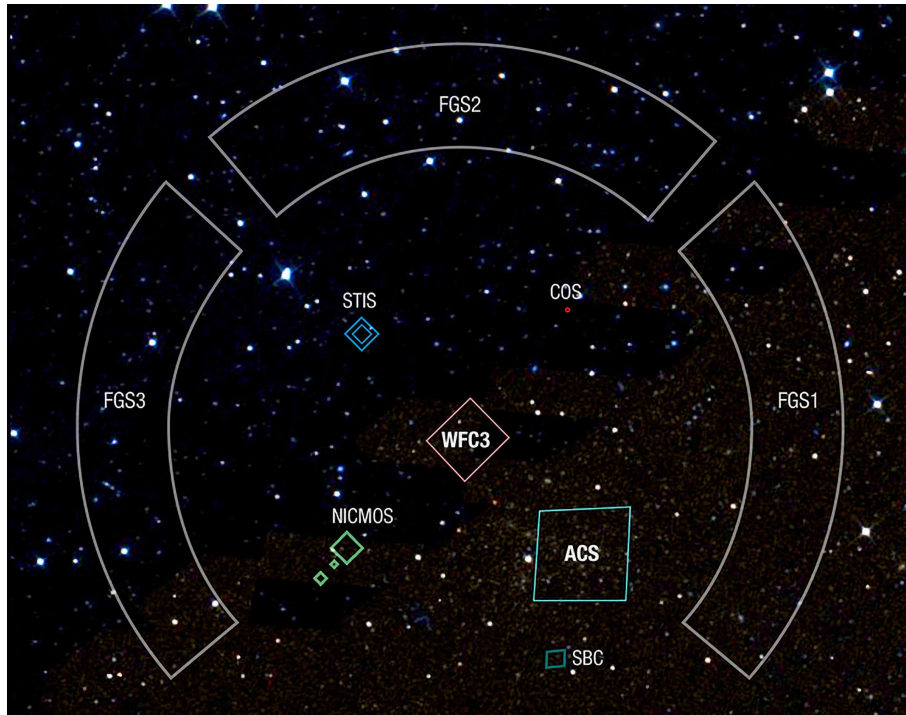


**Figure 3.3.** – The HST field-of-view, where the ACS/WFC CCDs have a stretched shape due to the strong geometric distortion. Credit: Hubblesite.

in the composite image and at about 200 to 500 arcseconds from the optical axis of the telescope. Thus, the focal surface is tilted with respect to the optical axis, creating a strong geometric distortion. The pixel scale is smaller along the radial direction from the optical axis than along the tangential direction. Thus, the square pixels are projected onto trapezoids of varying area across the field. Similarly to the single pixels, the whole WFC FOV is stretched along the direction tangential to the optical axis relative to the radial direction, which approximately coincides with the diagonal from the upper left corner of WFC1 to the lower right corner of WFC2. This results into a projected angle of the  $x$ -/ $y$ -detector axes on the sky of  $\sim 85$  degrees.

Accurate calibration and proper correction are essential for a WL analysis due to various reasons. In order to co-add dithered images and avoid any local residual shift, they need to be mapped to a distortion-free coordinate system. In case of dithers, objects do no longer line up correctly everywhere in the FOV when stacking without removing camera distortion. An incorrect mapping would result in a degradation of the image PSF, contaminating the shear estimates. Furthermore, the varying pixel scale across the FOV influences the flux measurement of compact sources. Finally geometric distortions influence the shape and position of objects

leading to wrong shear measurements.

## 3.2. Ground-based telescopes

In Chapter 5 we present a spectroscopic follow-up analysis of 33 objects. Twenty-nine objects are extracted from a photometrically selected sample of 1221 UCMG candidates, while the remaining 4 come from the data sample assembled in Tortora et al. 2016 (T16 henceforth).

Data have been collected in the years 2017 and 2018 during three separate observing runs, two carried out with the 3.6m Telescopio Nazionale Galileo (TNG), and one using the 2.54m Isaac Newton Telescope (INT), both located at Roque de los Muchachos Observatory (Canary Islands).

In the following sections, we discuss the instrumental and observational setup for the two different instrumentation as well as the data reduction steps.

### 3.2.1. Telescopio Nazionale Galileo

The other 20 spectra of UCMG candidates have been collected using the Device Optimized for the Low RESolution (DOLORES) spectrograph mounted on the 3.5m Telescopio Nazionale Galileo (TNG), in Figure 3.4, during 6 nights in 2017 and 2018 (PI: N.R. Napolitano, ID: A34TAC\_22 and A36TAC\_20). The instrument has a  $2k \times 2k$  CCD detector with a pixel scale of 0.252 arcsec/pixel. The observations for both subsamples have been carried out with the LR-B grism with dispersion of 2.52 Å/pixel and resolution of 585 (calculated for a slit width of 1 arcsec), covering the wavelength range from 4000 to 8000 Å. As in the previous case, we have obtained from 1 to 5 single exposures per target, each with exposure time ranging between 600 and 1200 seconds. Following T18, the DOLORES 2D spectra have been flat-fielded, sky-subtracted and wavelength calibrated using the HgNe arc lamps. Then, the 1D spectra have been extracted by integrating over the source spatial profile (see Figures 2, 3 and 4 in the Appendix A).

### 3.2.2. Isaac Newton Telescope

Data on 13 luminous UCMG candidates have been obtained with the IDS spectrograph during 6 nights at the Isaac Newton Telescope (INT) telescope, shown in Figure 3.5, in visitor mode (PI: C. Tortora, ID: 17AN005). The observations have been carried on with the RED+2 detector and the low resolution grating R400V, covering the wavelength range from 4000 to 8000 Å. The spectra have been acquired with long-slits of 1.6 arcsec or 2 arcsec width, providing a spectral resolution



**Figure 3.4.** – The Telescopio Nazionale Galileo dome. Credit: Isaac Newton group of telescope, IAC.

of  $\Delta\lambda/\lambda = 560$ , a dispersion of  $1.55 \text{ \AA}/\text{pixel}$ , and a pixel scale of  $0.33 \text{ arcsec}/\text{pixel}$ . The average seeing during the observing run was  $\text{FWHM} \sim 1.5 \text{ arcsec}$ , the single exposure time ranged between 600 and 1200 seconds and from 1 up to 5 single exposures have been obtained per target, depending on their magnitudes.

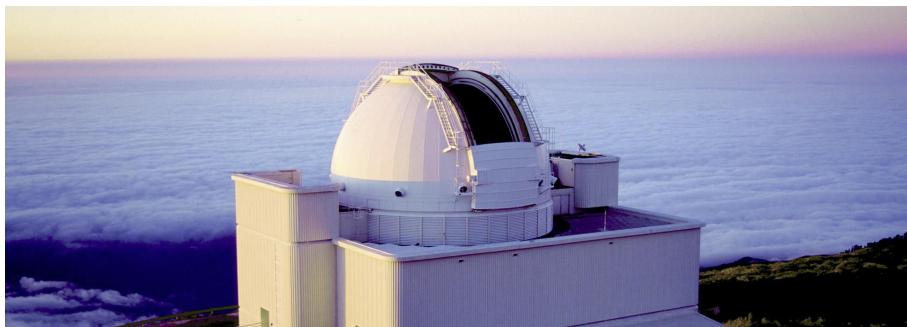


**Figure 3.5.** – The Isaac Newton Telescope dome. Credit: Instituto de Astrofísica de Canarias (IAC).

### 3.2.3. Data reduction

Data reduction has been performed using IRAF<sup>1</sup> image processing packages. In the follow, we summarize the main data reduction steps.

#### Data pre-reduction

The goal of image pre-reduction is to correct two types of errors in the CCD data: additive and multiplicative errors, which add to the values of pixels and multiply the value in a pixel, respectively.

Additive errors arise from two primary sources: bias offset and dark current. There are two types of calibration images that might be used to correct these additive errors: bias and dark frames. A *bias frame* is essentially an exposure with zero seconds exposure time. It is used to correct for the bias offset, which is added on purpose to ensure that the signal always remains positive even in the presence of noise fluctuations. Typically, the median<sup>2</sup> of around ten bias frames (*master bias*) is subtracted from the scientific frame. A *dark frame* is simply an image taken with the camera shutter closed, for the same exposure length as the exposure it is meant to correct. CCDs are affected by thermal noise generating free electrons. Since the effect is temperature-dependent, cooling is an efficient way to reduce the problem. However, the remaining excess charge from thermal noise can be accounted for with a dark frame. After subtraction of the master bias from all the dark frames and their normalization, the median of around ten dark frames (*master dark*) is subtracted from the scientific frame to remove the dark current signature.

Multiplicative errors can arise from several sources: differences in quantum efficiency, illumination differences (vignetting), and dust halos (also called dust ‘doughnuts’). All of these represent a difference in sensitivity from pixel to pixel in the chip thus, the values of pixels with a lower sensitivity need to be scaled up to larger values to match more sensitive pixels. To correct this, we take a calibration image called a *flat field*. The flat is simply an image of an evenly illuminated field (usually a white spot on the inside of the dome) or it is obtained by observing the twilight sky. Around ten flat frames are median combined and then normalised, in order to obtain a normalized<sup>3</sup> flat in which most pixels are near to a value of one.

---

<sup>1</sup>IRAF is distributed by the National Optical Astronomy Observatories, which is operated by the Associated Universities for Research in Astronomy, Inc. under cooperative agreement with the National Science Foundation.

<sup>2</sup>The median is more robust than the mean and, thus less sensitive to outliers in the data. This is why it is preferable to use the median.

<sup>3</sup>Note that in case of twilight flats, they need to be scaled to a common value before combining them. This is particularly important if the flats are twilight flats in which the average image value typically changes significantly as the images are being taken.

For calibration, the scientific frames are divided by this master flat frame.

### **Wavelength calibration**

To get the wavelength associated with each pixel, we use a reference spectrum for which we know the position of the spectral features. The choice for the reference depends on the wavelength range we want to observe, because we want many evenly spread lines, that are easy to identify. We use as a comparison spectra of CuAr+CuNe or HgNe lamps acquired for each observing night. Then we use the IRAF IDENTIFY task to identify all the features. Then, we fit a function to the identified lines, providing a relation between the line position on the detector and the wavelength.

### **Sky subtraction**

In addition to receiving light from our target, the CCD also collects radiation from the background sky, as well as from undetected objects, moonlight, and potential urban light pollution. This background level must be subtracted from each pre-processed science frames in order to solely measure the flux of the source. Thus, a sky spectrum has been extracted from the outer edges of the slit, and subtracted from each row of the two dimensional spectra using the IRAF task BACKGROUND in the TWODSPEC.LONGSLIT package.

### **From 2D to 1D spectra**

The sky-subtracted frames have been co-added to averaged 2D spectra and then the 1D spectra have been obtained extracting and summing up the lines from the long slit spectrum with higher  $S/N$  using the task SCOPY (see Figures 2, 3 and 4 in the Appendix A). These final spectra will be used to derive the spectroscopic redshifts and the velocity dispersions, as explained in Section 5.3.2.

For our analysis, we zoom-in the wavelength region  $3\,800 - 5\,500 \text{ \AA}$ , where we can find the main stellar absorption features we are interested in. Above all, the H and K lines of the CaI doublet, are very clear features in spectra of ETGs. The G-band is also prominent in most of the spectra, as it is typical for passive galaxies (Wang et al. 2018). For most of the galaxies Mg and Fe lines are also strong in our spectra, further confirming the passive nature of the candidates. Other intrinsically weaker features (i.e. CN 3883 band,  $H_\alpha$ ,  $H_\gamma$ ), are visible only in spectra with higher  $S/N$ .



## CHAPTER 4

---

# Weak lensing image simulations for *Euclid* using HST-emulated data

---

*“And the whole is greater than the part.”*

- Euclid, *Elements*

**On the use of HST images as input for weak lensing image simulations  
for *Euclid***

*D. Scognamiglio, T. Schrabback, M. Tewes, B. Gillis, H. Hoekstra et al.,*  
in preparation

### Overview

Given their high resolution, *Hubble* Space Telescope (HST)-observed galaxy images can in principle be used to emulate *Euclid* observations of sheared galaxy images with real morphology.

In this chapter we aim to test this procedure using simulations and investigate if uncertainties in the HST point-spread function (PSF) models introduce significant biases in the weak lensing shear calibration. We use simplified galaxy models to simulate both HST and *Euclid* observations. We then “euclidize” our HST simulations, and compare the result with the directly simulated *Euclid*-like images. For this we use the Kaiser-Squires-Broadhurst (KSB) shape measurement algorithm and galaxy model fits. We also conduct an in-depth analysis of the accuracy of TinyTim HST PSF models using star fields observed in the F606W and F814W

filters.

The research presented in this chapter is currently being finalised and to be submitted to the refereed journal *Astronomy & Astrophysics*. The author (myself) set-up the simulations and carried out the following analysis, under the supervision of Dr. T. Schrabback and Dr. M. Tewes. The original code for the creation of the TinyTim PSF models was provided by Dr. B. Gillis, but it has been adapted for this work by myself. The other co-authors have contributed several helpful discussions and advice on different, specific steps of this study.

### 4.1. Motivation

In Section 2.4, we have seen that the measurements of the correlation between galaxy shapes, referred to as shear (see e.g. Kilbinger 2015, Mandelbaum 2018, for recent reviews) can be used to probe the statistical properties of the mass distribution and to probe the evolution of structure on large scales as well as the geometry of the Universe. Obtaining such constraints is a primary goal of large dedicated surveys that will gather data in the near future: the space missions *Euclid*<sup>1</sup> (Laureijs et al., 2011a) and the *Nancy Grace Roman* Space Telescope<sup>2</sup> (Spergel et al., 2015a) as well as the ground-based *Vera C. Rubin* Observatory's Legacy Survey of Space and Time<sup>3</sup> (*Rubin*-LSST; Ivezić et al. 2019).

In this work, we focus on the *Euclid* mission, which will survey 15 000 deg<sup>2</sup> of the sky in the optical and near-infrared, aiming to obtain unprecedented weak lensing constraints on the large-scale structure (LSS) of the Universe. *Euclid* is optimised for weak lensing measurements by providing optimal conditions for accurate galaxy shape measurements. This is possible thanks to the stable observing conditions and high spatial resolution achieved by being in space, as well as its design. The latter minimises any corrections for the inevitable blurring caused by the Point-Spread Function (PSF) and the stability allows the PSF to be known accurately as a function of time, position and wavelength across the field of view. *Euclid* has a wide field of view of 0.54 deg<sup>2</sup> with a broad optical band pass (VIS), covering approximately the range 550 – 920 nm, to maximize the number of observed galaxies. However, the observations will be still compromised by some factors. For example, the PSF, with which the observed galaxies are convolved, depends on the wavelength, and thus on the spectral energy distribution (SED) in the observed frame. Hence, an incorrect estimate of the wavelength-dependent model for the PSF and/or the galaxy SED biases the shear estimate (Cypriano et al., 2010; Eriksen

---

<sup>1</sup>[sci.esa.int/Euclid/](https://sci.esa.int/Euclid/)

<sup>2</sup><https://roman.gsfc.nasa.gov/>

<sup>3</sup><https://www.lsst.org/lsst>



& Hoekstra, 2018). In addition, the SED of a galaxy typically varies spatially, generating ‘colour gradients’ (CG) bias (Voigt et al., 2012; Semboloni et al., 2013; Er et al., 2018; Kamath et al., 2019). The bias depends on the width of the filter that is used (Semboloni et al., 2013). Consequently, CG bias is expected to be particularly relevant for *Euclid* because of its wide pass-band (Laureijs et al., 2011a).

The *Hubble* Space Telescope (HST) archive data, with its high spatial resolution and filters covering the *Euclid* band-pass, is the most suitable data-set to calibrate *Euclid* shear measurements against CG bias. We can use HST images of representative galaxy sample *Euclid* will observe in order to accurately calibrate the shear measurement biases. In addition, a sufficient number of galaxies has been observed to calibrate the bias with the precision required to achieve *Euclid*’s science objectives (Semboloni et al., 2013).

Multi-band HST galaxy images, together with the supporting PSF models, can be used for *Euclid* calibrations via two approaches. In the first approach, models are fit to the galaxies providing distributions of galaxy parameters. These can be used as input distributions for image simulations based on parametric galaxy models, (e.g. Hoekstra et al. 2017; Kannawadi et al. 2019; Hernández-Martín et al. 2020). In the second approach, HST postage stamps are directly used as input to the image simulations to render fully realistic morphologies (Mandelbaum et al. 2012, 2015; Rowe et al. 2015).

In this manuscript we focus on the second approach, and investigate the use of HST galaxy images to generate emulated *Euclid* observations of galaxies, with a known artificial weak lensing shear. This “euclidization”, as we name the procedure, of the HST image implies in particular a change in resolution and depth. More precisely, the euclidization consists of deconvolving the HST galaxy images by the HST PSF, adding some artificial shear, convolving with the *Euclid* PSF, adjustments to the pixel noise and flux scaling, and resampling. In order to test the procedure and quantify the impact of uncertainties in the HST data (in particular regarding the PSF model), we apply the procedure to simulated input galaxies. For these we vary properties such as the half-light radius  $R_e$ , Sérsic index  $n$ , and Signal-to-Noise ratio ( $S/N$ ).

Our testing environment consists of creating *Euclidized* galaxy images, through the euclidization setup, in which the emulated HST galaxy image is deconvolved for the HST PSF, sheared, and reconvolved with the *Euclid* PSF, followed by a noise symmetrization, flux rescaling and addition of further noise (see the bottom branch of Figure 4.1), making use of emulated HST-like galaxy images as input and, compare them to ‘directly’ emulated *Euclid*-like images. In addition to this approach, recently, Lanusse et al. (2021) have proposed an alternative method

where machine learning is used to produce *Euclid*-like images with no shear. For both branches of the Figure 4.1, we then compare shear measurement biases, which should be identical if the euclidization procedure emulates sheared galaxy images correctly.

Given the importance of the HST PSF model for the euclidization procedure, we also carry out an in-depth analysis of the accuracy of TinyTim PSF models for HST/ACS using star fields observed in filters F606W and F814W, extending the work done in Gillis et al. (2020). We finally investigate the accuracy of recovering the focus in a the regime of low stellar density.

This chapter is structured as follows. In Section 4.2 we review the formalism of the WL shear measurement biases behind our analysis. In Section 4.3 we describe the testing environment, while in Section 4.4 we discuss the size of the galaxy sample. The two methods for the galaxy shape and properties parameters measurements are described in Section 4.5. We present the different tests and our findings in Section 4.6. In Section 4.7 we report our investigation of the accuracy of the TinyTim PSF models for HST. We then summarize our results and discuss their significance in Section 4.8.

## 4.2. Shear measurement formalism

In the WL limit ( $|g| \ll 1$ , with  $g$  the reduced shear, which in the following we refer to as shear for simplicity), for a given galaxy of intrinsic ellipticity  $\epsilon^{\text{int}}$  and having undergone a lensing-induced shear  $g$ , the observed ellipticity is the sum of the intrinsic ellipticity and the shear

$$\epsilon_i^{\text{obs}} = \epsilon_i^{\text{int}} + g_i, \quad i = 1, 2. \quad (4.1)$$

Assuming random intrinsic ellipticity orientations and averaging over a large set of objects we have  $\langle \epsilon^{\text{obs}} \rangle = \langle g \rangle$ , since  $\langle \epsilon^{\text{int}} \rangle = 0$ . The dispersion of the observed ellipticity is  $\sigma(\epsilon^{\text{obs}}) \simeq \sqrt{\sigma^2(\epsilon^{\text{int}}) + \sigma_m^2}$ , which has contributions from both the intrinsic ellipticity dispersion  $\sigma(\epsilon^{\text{int}}) = \sigma(\epsilon^{\text{obs}} - g)$  of the galaxy sample and measurement noise  $\sigma_m$  (e.g. Hoekstra et al. 2000, Leauthaud et al. 2007, Schrabback et al. 2018). The intrinsic ellipticity dispersion is the dominant term by an order of magnitude.

Systematic biases affect the measurement of galaxy ellipticity. To control these systematic errors, any shear measurement method needs to be calibrated through simulations to quantify possible differences between the input and the recovered shear. Analyses distinguish between additive bias  $c$ , which can for example be caused by an insufficient correction for the PSF anisotropy and may lead to spurious correlation in the shapes of galaxies (Massey et al., 2012), and multiplicative bias  $\mu$ .

Dominant sources for multiplicative bias include noise bias (Refregier et al., 2012), model bias (e.g. Melchior & Viola 2012; Refregier et al. 2012; Miller et al. 2013; Kacprzak et al. 2014), or the impact of neighbouring objects (Hoekstra et al., 2017; Martinet et al., 2019), and it biases the amplitude of the shear by a factor  $(1 + \mu)$ . Thus, knowing the input shear  $g^{\text{true}}$  in weak lensing image simulations, one usually fits the recovered shear  $g^{\text{obs}}$  as

$$g_i^{\text{obs}} = (1 + \mu_i)g_i^{\text{true}} + c_i, \quad i = 1, 2, \quad (4.2)$$

for both components of the shear separately. The typical change in ellipticity caused by gravitational lensing is about a per cent, much smaller than the intrinsic ellipticities of galaxies and also smaller than the typical biases introduced by instrumental effects.

### 4.3. Simulation and analysis setup

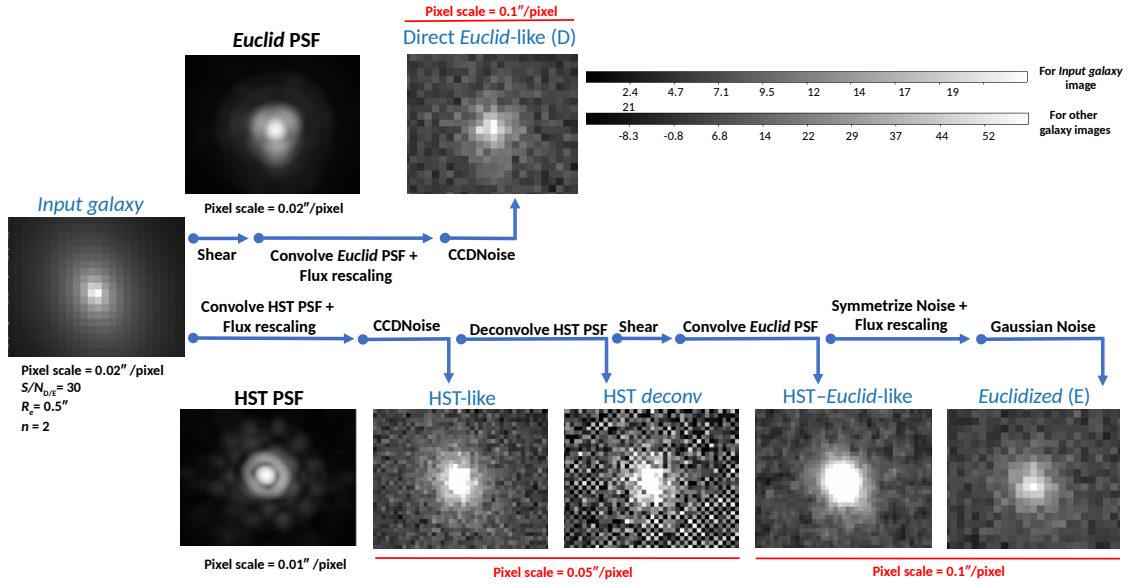


**Figure 4.1.** – Illustration of the testing environment to create Direct *Euclid*-like (D) images to be compared with *Euclidized* (E) images. See the text in Section 4.3 for details.

To quantify the uncertainties for the use of HST images as input for WL image simulations, we build a testing environment, which employs simulated data that approximately resemble the properties of HST/ACS and *Euclid*/VIS observations. We generate galaxy image simulations with the freely available GALSIM software<sup>4</sup>

<sup>4</sup><https://github.com/GalSim-developers/GalSim>

(Rowe et al., 2015).

In the following, we describe the steps of the testing environment featured in Figure 4.1.

### Input galaxy

As input for our simulations, we model the galaxy light profile with a single component Sérsic model (Sérsic, 1963b)

$$I(R) = I_e \exp\left(-b_n \left[\left(R/R_e\right)^{1/n} - 1\right]\right), \quad (4.3)$$

with the half-light radius  $R_e$ , the intensity at that radius  $I_e$  and the parameter  $b_n \approx 2n - 1/3$ , where  $n$  is the Sérsic index.

We create postage stamp images of isolated galaxies of size  $512 \times 512$  pixels and a pixel scale of  $0''.02$  or  $0''.04$  (depending on the test we are carrying out, see Section 4.6). This large postage stamp size avoids any problems due to the dilation of the galaxies during later steps of the procedure. We arbitrarily assign an initial flux of 10 000 ADU to the mock galaxy. The flux will be rescaled later according to the HST and *Euclid* telescopes properties, in order to have four different values for the  $S/N$ , from 10 to 40 with a step of 10, which we compute using the CCD equation (Howell, 1989) as detailed in the appending Section 4.9. To probe the sensitivity of our analysis to intrinsic galaxy properties, we conduct the analysis for a range of half-light radii  $R_e ['] \in \{0.2, 0.3, 0.4, 0.5, 0.6, 0.7\}$  and Sérsic indices  $n \in \{1, 2, 3\}$ .

We assign to the galaxies the intrinsic ellipticity components  $\epsilon_1$  and  $\epsilon_2$  drawn from a Gaussian distribution with mean  $\mu = 0$  and dispersion  $\sigma = 0.3$ , but excluding galaxies with very high ellipticities  $|\epsilon| > 0.7$ . We then apply a random shift to the galaxy position with a uniform distribution from  $-0.05$  to  $0.05$  arcsec in both axes to have a small random displacement with respect to the pixel centre, as it occurs for real data. Then, for each galaxy we create a second galaxy, which is identical but orthogonally oriented, to mitigate the intrinsic shape noise (see Section 4.4 for more details).

At this point, two versions of the same mock galaxy are drawn in order to be simulated as Direct *Euclid*-like observations (hereafter D) and *Euclidized* image (hereafter E), as shown in the Figure 4.1, with the following steps:

### Direct *Euclid*-like

The *Input galaxy* pair is sheared by a value taken from a discrete uniform distribution in the range from  $-0.06$  to  $0.06$  with a step of  $0.004$ , using the GALSIM function

`galsim.lens` without magnification. Sheared galaxy images are convolved with the *Euclid*-like PSF. We employ an example VIS model PSF, which was computed with the `SHE_PSFtoolkit` from a realistic simulation of galaxy SEDs using the Empirical Galaxy Generator (EGG) (Schreiber et al., 2017), at the center of the field of view assuming a physical model of the telescope. This PSF model is sampled on a grid of  $0''.02/\text{pixel}$ , that is a five times finer sampled than the native VIS pixel scale.

The flux of the galaxy is then empirically rescaled so that its measured  $S/N$  statistically reaches the desired value, given the simulated *Euclid* conditions. We apply noise in our simulations using the `GALSIM` function `CCDNoise`, which includes Poisson shot noise from the source and the sky background, and Gaussian read-out noise. We use a sky level  $m_{\text{sky}} = 22.35 \text{ mag arcsec}^{-2}$  (Refregier et al., 2010). This value is computed as

$$F_{\text{sky}} = \frac{t_{\text{exp}}}{\text{gain}} 10^{-0.4(m_{\text{sky}} - \text{ZP})} l^2, \quad (4.4)$$

where we assume an exposure time  $t_{\text{exp}}$  for *Euclid* of 1695 s, corresponding to the co-addition of three single exposures of 565 s each (Laureijs et al., 2011a). While *Euclid* will take four exposures, a large fraction of the survey will only be covered by three exposures given the chip gaps, justifying this assumption. The CCD gain is set to  $\text{gain} = 3.1 \text{ e}^-/\text{ADU}$  (Niemi et al., 2015), the read-out noise  $\text{ron} = 4.2 \text{ e}^-$  (Cropper et al., 2016). We set the instrumental Zero-Point  $\text{ZP} = 24.6 \text{ mag}$  (Tewes et al., 2019) and the pixel size  $l = 0''.1$  (Laureijs et al., 2011a). Once the noise is applied, we obtain the “Direct *Euclid*-like” image, D.

The bottom branch of the diagram in Figure 4.1 illustrates how the *Euclidized* image is obtained.

### HST-like

The same *Input galaxy* pair is now convolved with the HST PSF created with `TinyTim` (see Section 4.7 and appending Section 4.10 for a detailed analysis). The flux is rescaled to take into account the properties of the *Hubble* Space Telescope and finally CCD noise is added in order to create HST-like images. For the HST observations we assume an exposure time of 1000 s and a  $S/N$  twice the value of the Direct *Euclid*-like galaxy to represent the difference in the mirror size between the two telescopes. The CCD gain is set to  $\text{gain} = 2.0 \text{ e}^-/\text{ADU}$ , the read-out noise is  $\text{ron} = 5.0 \text{ e}^-$ . We set the sky background to an average value of  $m_{\text{sky}} = 22.5 \text{ mag arcsec}^{-2}$  and the Zero-Point  $\text{ZP}_{\text{F814W}} = 25.9 \text{ mag}$ <sup>5</sup> for F814W. We also simulated HST observations in the F606W filter, with  $\text{ZP}_{\text{F606W}} = 26.5 \text{ mag}$ .

<sup>5</sup>This information is available in the “Advanced Camera for Surveys Instrument Handbook” from [https://www.stsci.edu/itt/review/ihb\\_cy15/ACS/ACS\\_ihb.pdf](https://www.stsci.edu/itt/review/ihb_cy15/ACS/ACS_ihb.pdf)

### ***HST deconv***

In the following steps we perform a “reconvolution” process as described in Rowe et al. (2015). We deconvolve the *HST*-like images by the *HST* PSF using the GALSIM class `galsim.Deconvolution`, which is based on a division in Fourier space. To analyse the impact of *HST* PSF model uncertainties, we may use a different PSF for this deconvolution step than for the prior convolution (see Section 4.6.4).

### ***HST–Euclid-like***

We add shear to the *HST deconv* images and convolve them with the *Euclid* PSF.

### ***Euclidized***

The images resulting from the convolution with the *Euclid* PSF carry correlated noise. As part of the euclidization, we attempt to compensate for the effect of this correlated noise by an isotropization. The isotropization (or symmetrization) of this noise enforces a four-fold symmetry, introducing minimal extra noise through the GALSIM function `symmetrizeImage`. After rescaling the flux, in order to match the noise level of the ‘direct’ branch, some extra Gaussian noise is added to the stamp. In this step we neglect the Poisson noise term from the photon counts of the sources, since the scope of this extra noise is just to provide a match between the  $S/N$  of the output images. At this point, we obtain the “*Euclidized*” image, E, that can be compared with the “Direct *Euclid-like*” images, D, and analyzed in exactly same manner.

Our test procedure does not include detection and deblending steps, as we simulate images of isolated galaxies. As a result of this simplification, we do not suffer from the object detection bias discussed in Sheldon et al. (2020) and Hoekstra et al. (2021). In the scope of this work, we only test the euclidization of simple Sérsic profile galaxies.

## **4.4. Simulation size and shape noise cancellation**

To match the statistical precision of *Euclid*, systematic shear measurement biases will need to be controlled to an accuracy of  $|\delta\mu| < 2 \times 10^{-4}$  and  $|\delta c| < 5 \times 10^{-5}$  (Cropper et al., 2013). For this purpose, the sources of statistical uncertainty can be overcome by averaging over large numbers of galaxies given by (e.g., Mandelbaum 2018, Conti et al. 2017)

$$N_{\text{gal}} = \left( \frac{\sigma_\epsilon}{|\delta\mu||\gamma|} \right)^2, \quad (4.5)$$

where in this study,  $\sigma_\epsilon = 0.3$  is the dispersion of galaxy ellipticities and  $|\gamma|$  is the shear modulus applied in our simulations. For a shear modulus of 0.03 on average, we need  $2.5 \times 10^9$  galaxies to constrain the multiplicative bias to  $|\delta\mu| < 2 \times 10^{-4}$ .

In order to reduce the required simulation volume, we employ shape noise cancellation (Nakajima & Bernstein 2007; Massey et al. 2007b; Mandelbaum et al. 2014b). Here, for each simulated galaxy a second galaxy is also simulated, for which the intrinsic ellipticity has been rotated by 90 degrees. This also ensures that the covariance of the two outputs (both employing the same intrinsic ellipticity) does not affect the results<sup>6</sup>. Note that alternative approaches have been proposed to reduce simulation volumina, such as measurements of the shear response for individual galaxies (Pujol et al., 2018) and pixel noise cancellation (Martinet et al., 2019).

For this work we use an approximate number of galaxies of the order of  $\sim 10^7$  galaxies for each setting (including the rotated galaxies). For the upcoming journal paper we plan to expand this to approximately  $\sim 10^8$  galaxies. The latter number is sufficient to reach an accuracy on the multiplicative bias of  $\sim 10^{-3}$  (see Section 4.6.3), which will allow us to estimate bias differences at the *Euclid* requirement level. Moreover, the size of our sample is of the same order of magnitude as the one used in Martinet et al. (2019).

## 4.5. Galaxy property measurements

At this analysis step we perform the galaxy shape and parameter measurements on the Direct *Euclid*-like and *Euclidized* images, in order to check the accuracy of the euclidization. As comparison metrics we use two approaches: measuring the biases in the shear recovery using KSB galaxy shape measurements (see Section 4.5.1; also Kaiser et al. 1995; Luppino & Kaiser 1997b; Hoekstra et al. 1998) and estimating galaxy parameters from a galaxy model fit (see Section 4.5.2).

### 4.5.1. KSB measurements

The galaxy shapes are measured using the `galsim.hsm.EstimateShear`<sup>7</sup> function with KSB as desired method for PSF correction. This implementation requires the PSF and galaxy images to share the same pixel scale. However, the *Euclid*

<sup>6</sup>We verified that we obtain consistent results regarding the multiplicative bias difference when directly fitting the difference of the shear estimates versus separately fitting multiplicative biases for both outputs and computing the difference.

<sup>7</sup>The GALSIM KSB algorithm is a specific implementation of the KSB method (Kaiser et al. 1995; Luppino & Kaiser 1997b), as described in Appendix C of Hirata & Seljak (2003).

PSF is actually created up-sampled by a factor 5 (nearest neighbor interpolation<sup>8</sup>) with respect to the native pixel scale so to not lose relevant details. In order to use this method, in the tests described in Section 4.6, we choose either to up-sample the galaxy image to  $0''.02$  or use a pixel scale of  $0''.04$  for each step of the procedure, according to what we want to investigate. Furthermore, in the cases where we up-sample the galaxy images from  $0''.1$  to  $0''.02$  before running KSB, we also convolve the *Euclid* PSF model with a 2D top-hat profile of  $0''.1 \times 0''.1$ . The underlying reason is related to the fact that observations done with large pixels lead to a loss of resolution. If we artificially super-sample an image with pixels  $0''.1$  to  $0''.02$  we do not recover that loss in resolution. When applying the KSB method, the specified PSF must contain all the convolutive effects that were applied to the galaxy image after the latter is sheared in space. This includes the loss of resolution from diffraction by the telescope optics (which is captured by a super-sampled PSF model), but also the loss of resolution due to the pixellation by the detector array, in the present case not captured by the super-sampled PSF model. A way to take this into account is to include a pixel convolution before applying the KSB method, avoiding to propagate errors to the KSB shape measurements.

The KSB method measures the moments of the surface-brightness distribution of stars and galaxies to infer PSF-corrected estimates of galaxy ellipticities. It parametrizes galaxies according to their weighted quadrupole moments and describes the PSF as a small but highly anisotropic distortion convolved with a large circularly symmetric function. Furthermore, all the tests we present in Section 4.6 use unit shear weights. With these assumptions, the KSB method returns a per-object estimate of the shear components  $g_1$  and  $g_2$ . We use the Weighted Least Square (WLS) fit of the model described in Eq. (4.2) to measure shear bias. We recover the multiplicative bias term  $\mu_i^j$  and additive bias term  $c_i^j$  for both components  $i \in \{1, 2\}$  of the shear and both images  $j \in \{E, D\}$ , as the slope and intercept values of the fitting<sup>9</sup> and their standard deviation (SD). We also calculate the differences  $\mu_1^D - \mu_1^E$  and  $c_1^D - c_1^E$  and their SD, using Gaussian error propagation.

The KSB method is computationally fast but, in some cases, its implementation fails to compute the shapes of certain objects, or returns ellipticity estimates with an absolute value bigger than 1. This is because the algorithm is not robust to noise or highly elliptical galaxies and therefore does not always converge to a solution. In our analysis, this occurs especially at lower  $S/N$  or for large input ellipticities  $|\epsilon| \gtrsim 0.7$ . For this reason, we reject galaxies with  $|g| > 1$ . On average, for the different tests we performed, this results in the removal of a small fraction of galaxies from our initial sample, see Table 4.1. For more details, we refer to Section 4.6. It is worth

---

<sup>8</sup>Each pixel's flux is split (uniformly) into  $n_x \times n_y$  smaller pixels, with  $n_x$  and  $n_y$  the number of sub-pixels in the  $x$  and  $y$  direction, respectively, for each original pixel.

<sup>9</sup>We fit generically  $y = bx + c$ , with  $b = 1 + \mu$  and  $c = c$  of Eq. (4.2).



noting that the objective of this study is not to obtain a tight absolute calibration of this algorithm. We rather want to test the euclidization procedure by investigating the relative bias difference between the two branches and estimate the correction to apply to real data in shear measurement analysis.

### 4.5.2. Galaxy model fit

To obtain an alternative comparison metric, we fit two-dimensional elliptical Sérsic models to the PSF-convolved output galaxy images D and E of the two branches of the testing environment, which we then compare to each other. Employing the `Astropy EllipSersic2D` model<sup>10</sup> galaxies are modelled with a single Sérsic profile (see Eq. (2.23)) and the following parameters:

- `r_eff`: Effective (half-light) radius ( $R_e$ );
- `n`: Sérsic index, corresponds to  $n$ ;
- `amplitude`: Surface brightness at `r_eff` ( $I_e$ );
- `x_0` and `y_0`: Center  $x$  and  $y$  position ( $x_0, y_0$ );
- `ellip`: Ellipticity of the profile, corresponds to  $\text{ellip} = 1 - \frac{b}{a}$ , with  $a$  and  $b$  are the unit length of the semi-major axis and of the semi-minor axis, respectively;
- `theta`: Rotation angle in radians, counterclockwise from the positive  $x$ -axis ( $\theta$ ).

These parameters are estimated directly from the galaxy postage stamp, although one can provide initial guesses for them. Note that this model intentionally omits the PSF. The purpose of this fit is solely to compare the shape of galaxies as simulated in the D and E images.

We set the postage stamp dimensions to  $512 \times 512$  pixels, a large image size in order to include the flux without encountering any image edge effects in the galaxy properties measurement. However, the fit to estimate the galaxy parameters is performed using the Levenberg-Marquardt algorithm (LMA) within a smaller region, which is computed following the procedure described in the appending Section 4.9, containing an elliptical aperture that extends out to three half-light radii of the galaxy. This allows us to save computational time since the postage stamp will be much smaller than the original  $512 \times 512$  pixels.

---

<sup>10</sup>We adjusted the default major and minor axis as follows  $a = R_e / \sqrt{(1 - |g|)/(1 + |g|)}$  and  $b = R_e \times \sqrt{(1 - |g|)/(1 + |g|)}$  in order to have a match between the different definitions in `Astropy` and `GALSIM`.

**Table 4.1.** – Summary of the tests presented in this chapter. We report the number of galaxies NR for each  $S/N$ , the failure rate of the KSB method averaged on the four  $S/N$  and the pixel scales for the output images D and E.

Test	NR [ $10^6$ ]	Failure rate [%]		Pixel scale ["]	
		D	E	D	E
I	3.8	4.9	4.6	0.1	0.1
I (Gauss. PSF)	3.8	4.4	4.1	0.1	0.1
I ( $10 \times S/N_{HST}$ )	3.8	4.9	4.0	0.1	0.1
II	3.7	5.9	6.4	0.04	0.04
III	3.8	4.9	4.9	0.1	0.05/0.1
III (F606W)	3.8	4.8	4.7	0.1	0.05/0.1
III (No Sym)	3.8	4.8	5.0	0.1	0.05/0.1
III (fixnoise)	3.8	4.9	5.3	0.1	0.05/0.1
III (PSF stack)	3.8	4.9	4.7	0.1	0.05/0.1
IV	3.8	4.7	5.1	0.04	0.04
IV (rotat.)	3.8	4.7	5.1	0.04	0.04
V ( $n = 1$ )	7.2	5.6	5.8	0.04	0.04
V ( $n = 2$ )	7.4	2.2	2.2	0.04	0.04
V ( $n = 3$ )	7.5	1.6	1.5	0.04	0.04

In our analysis we discard unreliable fit results (no convergence or Sérsic index  $n$  outside of the range  $[0.1, 6.0]$ ). To further reduce run-time, we perform the fit only on a smaller sample of galaxies and some configurations of our pipeline. This is discussed further in the next section.

## 4.6. Tests and results

In this section, we proceed by testing our proposed euclidization procedure (and variants) under different conditions in order to investigate its accuracy. If not mentioned otherwise, we focus on simulated images using a PSF for HST/ACS in the F814W filter. An overview of the different tests is given in Table 4.1.

### 4.6.1. Test I: Native pixel scales

In the first test we employ the testing environment using the native pixel scales of  $0''.05$  and  $0''.1$  for the simulated HST/ACS and *Euclid*/VIS images, respectively, starting with an *Input galaxy* with a pixel scale of  $0''.02$  arcsec. This approach is illustrated in Figure 4.1. Hence, the two outputs images D and E are drawn with the native *Euclid*/VIS pixel scale of  $0''.1$ . However, for the computation of galaxy shapes using the KSB method, the two galaxies are up-sampled by a factor 5, in order to compute the KSB moments consistently from the PSF image and galaxy

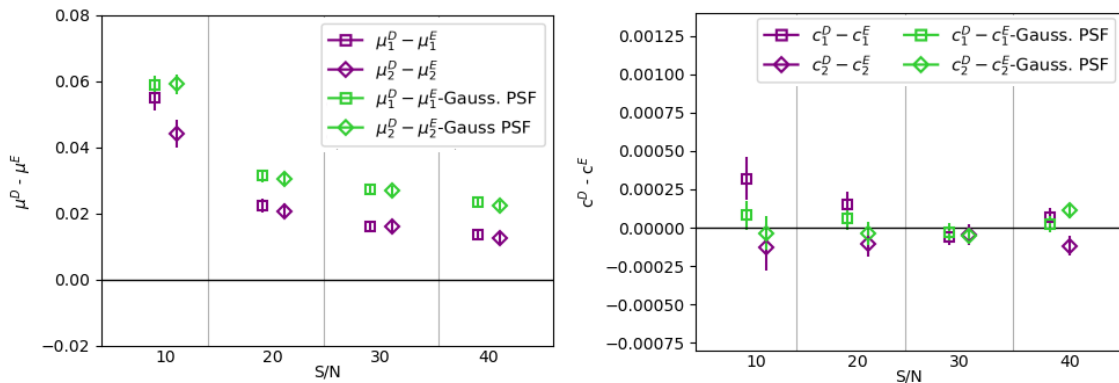


**Figure 4.2.** – Multiplicative (left) and additive (right) shear bias differences obtained employing a *Euclid*/VIS pixel scale of  $0''.1$  (Section 4.6.1). We also report the results employing a Gaussian PSF instead of the *Euclid* PSF (labelled as ‘Gauss PSF’). The data points show the bias obtained from the fit with the error-bars indicating  $1\sigma$  uncertainties for  $\text{NR} \simeq 3.8 \times 10^6$  galaxies for each  $S/N$ .

postage stamp with a fine pixel scale of  $0''.02$ . The number of galaxies (NR) for each sample of D and E galaxies and for each  $S/N$  and the KSB failure rates, are reported in Table 4.1.

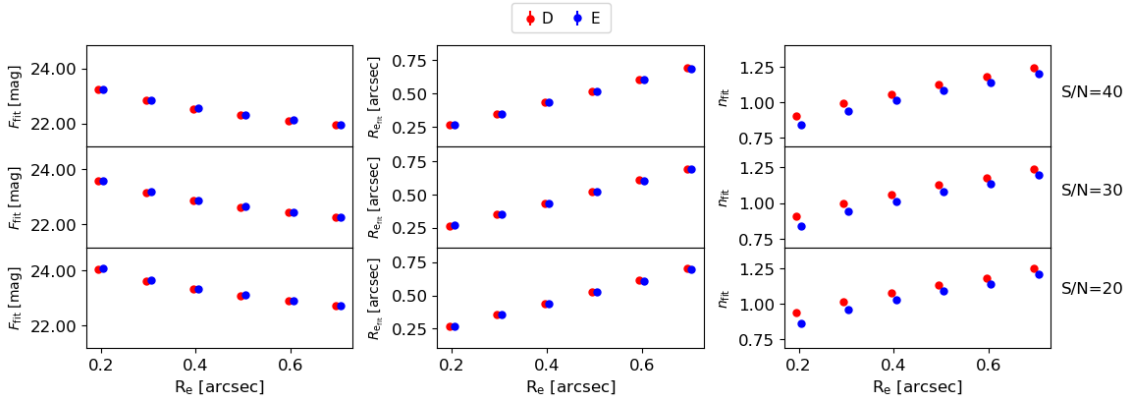
Figure 4.2 shows the multiplicative and additive bias differences ( $\Delta\mu$  and  $\Delta c$ ) between the two outputs, for four different values of  $S/N$ . The  $\Delta\mu$  increases at  $S/N = 10$ , with  $\Delta\mu = 0.04963 \pm 0.00010$  averaged over both shear components. For comparison, when averaging over the analyses with  $S/N \geq 20$ , we find  $\Delta\mu = 0.01683 \pm 0.00019$ . In contrast, the difference of the additive biases is consistent with zero. This is also the case for most of the other scenarios we explore. Therefore, we will only discuss it explicitly in cases where we find significant non-zero additive bias differences.

Clearly the significant percent-level  $\Delta\mu$  bias differences obtained with this first configuration are beyond any accuracy requirements on the euclidization procedure. To test if the *Euclid* PSF shape (but not the size) can have an impact on the bias difference, we repeat the analysis with a circular Gaussian PSF. The width of this Gaussian is set by  $\sigma = 0''.07$ , corresponding to the best fit to the detailed *Euclid* PSF. This Gaussian PSF is sampled with a pixel scale of  $0''.02$ , as before. The results are shown in Figure 4.2 as well. The multiplicative bias difference is slightly increased, by 0.01 on average. There is no significant difference for the additive bias, which remains consistent within the error with the default setup.

We also present the results from the galaxy model fit in Figure 4.3. The figure shows the average recovered fit parameters: the half-light radius  $R_{\text{fit}}$ , the flux  $F_{\text{fit}}$ , and the

Sérsic index  $n_{\text{fit}}$ , as a function of the input half-light radius, for three different values of the  $S/N$ . We find a good agreement between D and E for the half-light radius and the flux. This is not the case for  $n_{\text{fit}}$  for which we obtain slightly but consistently lower estimates in E than D. This suggests that the *Euclidized* galaxy images E are slightly less centrally peaked than the Direct *Euclid*-like images D, likely reflecting the origin for the difference in the multiplicative bias estimates. Note that it is not surprising that the recovered  $n_{\text{fit}}$  are generally lower than the input  $n$  given that the employed model fit does not correct for the smoothing impact of the PSF.

**Figure 4.3.** – Results from the galaxy model fits for Test I (see Section 4.6.1) using the native HST/ACS and *Euclid*/VIS pixel scales, for  $NR \simeq \times 10^4$ . The fitted parameters  $R_{\text{e,fit}}$  [arcsec],  $F_{\text{fit}}$  [mag], and  $n_{\text{fit}}$  are shown as a function of the input  $R_e$  in arcsec for both the output galaxies D and E and for three values of the  $S/N$ . The data points are the average over the number of galaxies in each sample. The error bars, representing the  $1\sigma$  uncertainty on the mean, are smaller than the size of the points, thus are not visible.



To identify the origin of the multiplicative bias difference and the shift in the recovered Sérsic index, we now test if these discrepancies are related to the noise level of the HST images. We increase the  $S/N$  of the emulated HST galaxy images by a factor 10, representing the use of much deeper HST data for the euclidization. This increase in  $S/N$  leads to a reduction of the (averaged) bias difference to  $\Delta\mu \simeq 0.0086 \pm 0.0006$ , as shown in Figure 4.4. The multiplicative bias difference does not vanish completely, but it remains constant for all the  $S/N$ . Note that as the following sections show, an increase of HST depth is not mandatory for a bias-free euclidization.

#### 4.6.2. Test II: Finer pixel scale

To analyse the impact of sampling on the euclidization, we perform an experiment where we deliberately set both the HST and the *Euclid*/VIS pixel scale to  $0''.04$ , instead of the native values. This value is close to the native HST/ACS pixel scale

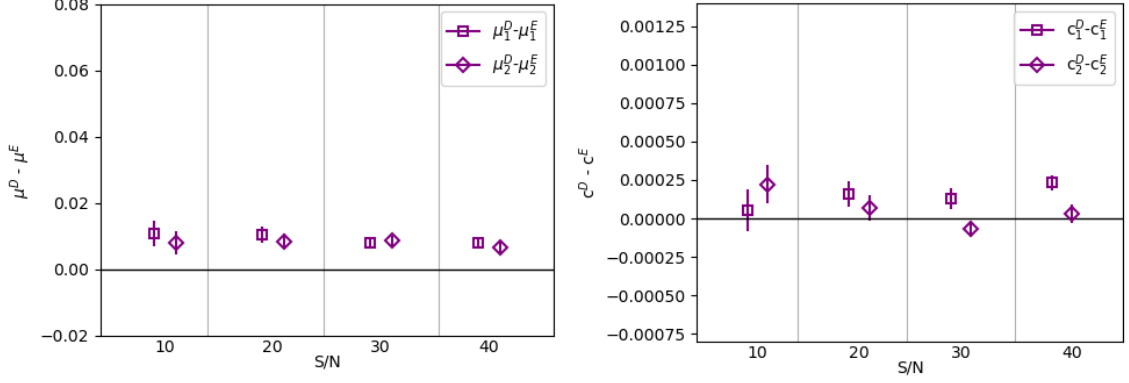


**Figure 4.4.** – Multiplicative (left) and additive (right) shear bias differences obtained employing a *Euclid*/VIS pixel scale of  $0''.1$  and increasing the  $S/N$  of the HST-like images by a factor 10 (Section 4.6.1). The data points show the bias obtained from the fit with the error-bars indicating  $1\sigma$  uncertainties for  $NR \simeq 3.8 \times 10^6$  galaxies for each  $S/N$ .

but a bit finer (e.g. matching the sampling of HST/UVIS). We therefore need to up-sample the output galaxies by a factor 2 immediately prior to running KSB, to match the sampling of the PSF, and also convolve this PSF by a  $0''.04$ -wide tophat pixel profile. In Table 4.1 are reported the NR of each sample of E and D galaxies for each  $S/N$  value and the averaged failure rates.

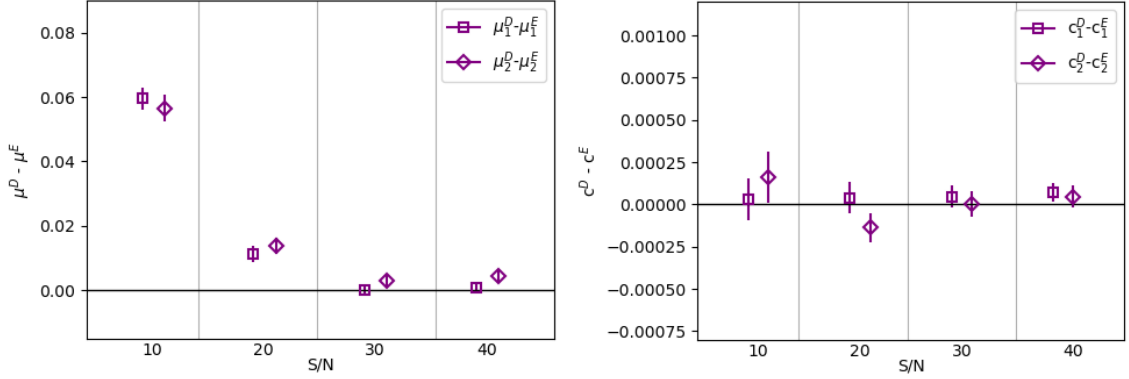


**Figure 4.5.** – Multiplicative (left) and additive (right) shear bias differences obtained when deliberately using a pixel scale of  $0''.04$  (Section 4.6.2). The data points show the bias obtained from the fit with the error-bars indicating  $1\sigma$  uncertainties for  $NR \simeq 3.7 \times 10^6$  galaxies for each  $S/N$ .

As shown in Figure 4.5, we find that the finer sampling reduces the  $\mu$  bias at higher VIS  $S/N$  ( $\geq 10$ ), to  $\Delta\mu \simeq 0.0056 \pm 0.0002$ . The combination of finer sampling and deeper HST images could be a solution to recover the accuracy on the  $\mu$  bias we desire. While for the  $c$  bias difference, there is no impact and they are in agreement

with what we have found in the previous test.

We carry on the galaxy model fit on samples of  $\simeq 10^4$  galaxies for each  $S/N$ . We find a good agreement in size and flux between the D and E galaxies. We cannot claim the same for  $n_{\text{fit}}$ , as performing the fit reveals discrepancies in the fitted Sérsic index comparable to those of Figure 4.3.

### 4.6.3. Test III: Hybrid approach with a pixel scale of $0''.05$ and binning of the Euclidized images

Using the native pixel scales yields a high multiplicative bias difference, while using a finer pixel scale leads to a substantial increase in the data volume and computational effort. In order to mitigate the biases, we now test a hybrid approach which employs finer pixels for some intermediate steps of the actual euclidization of E, while still producing E (and D) images at the native VIS pixel scale of  $0''.1$ . More precisely, compared to the setup of Test I shown in Figure 4.1, the symmetrization of the noise and the flux rescaling now happen at a pixel scale of  $0''.05$ . Only after these steps, the final *Euclidized* image is obtained by binning  $2 \times 2$  to reach the  $0''.1$  pixel scale.

As done for Test I, both the D and E images are sub-sampled by a factor 5 for the measurement of the KSB moments. We report the NR of each sample of E and D galaxies for each  $S/N$  value and the averaged failure rates in Table 4.1. Figure 4.6 shows that using this approach the  $\Delta\mu$  decrease to the  $0.0038 \pm 0.0005$  level, on average. Comparing Figures 4.5 and 4.6,  $\Delta\mu$  is reduced at  $S/N = 10$  in Figure 4.6, but at  $S/N = 40$  it turns negative. It is worth noticing that the strength of this strategy is the balance between the use of native pixel scales and the accuracy of the calibration. This would reduce both the data volume and the computational time since we do not need to use finer pixel scale for all the steps of the procedure.

#### Influence of HST PSF size

As the influence of sampling issues is likely related to the PSF size, which can smooth the galaxy differently, we repeat the experiment using a different and slightly narrower HST PSF from the F606W filter instead of F814W. In this case, both the convolution and the deconvolution in the bottom branch of Figure 4.1 are performed with the same F606W filter PSF.

The results are shown in Figure 4.6 as well, and they are labelled as ‘F606W’.

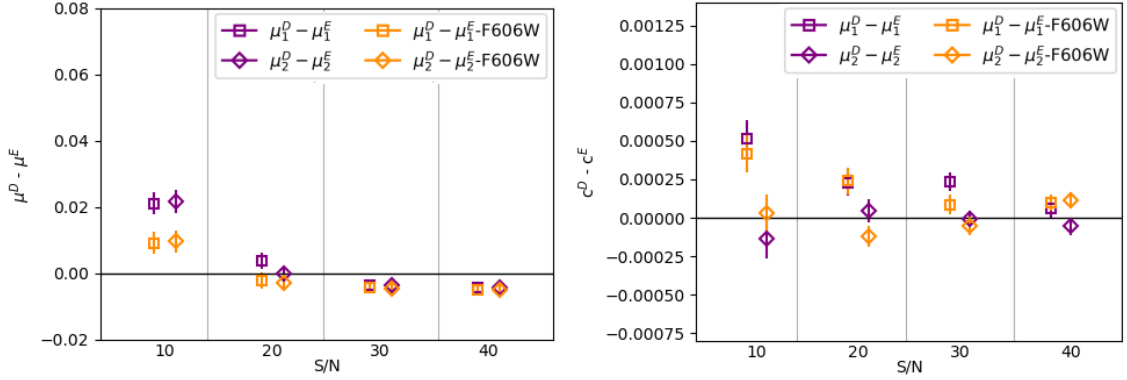


**Figure 4.6.** – Multiplicative (left) and additive (right) shear bias differences obtained when using a pixel scale of  $0''.1$  for D and a pixel scale of  $0''.05$  that we re-bin to  $0''.1$  for E (Section 4.6.3). We also report the results employing a TinyTim PSF model in the filter F606W (labelled as ‘F606W’), for the same number of galaxies NR (Section 4.6.3). The data points show the bias obtained from the fit with the error-bars indicating  $1\sigma$  uncertainties for  $NR \simeq 3.8 \times 10^6$  galaxies for each  $S/N$ .

### Influence of the correlated noise

In addition to the case where we apply the noise symmetrization, we also employ two alternative approaches regarding the noise correlation introduced in the initial steps of the euclidization procedure: one in which we do not apply any noise symmetrization (referred to as ‘No Sym’) and the other, we refer to as ‘fixnoise’, following Sheldon & Huff (2017). The latter correction is also designed to statistically cancel the effects of correlated noise. For each image that passes through the convolution-shearing-deconvolution steps, we generate a random noise field and apply the same operations, but using a shear with the opposite sign. We then add this noise image in real space to our galaxy image. This would result in an approximation for the galaxy image without correlated noise.

The results in Figure 4.7 show that the suppression of the noise symmetrization slightly decreases the multiplicative bias difference, compared to Figure 4.6 using the HST/PSF in the F814W filter. On average, the multiplicative bias difference changes by  $\sim 1\%$  between the two approaches, reported in Figure 4.6. A possible explanation is that the symmetrized images may still have some residual correlated noise, despite the addition of the extra Gaussian noise. The suppression of the noise symmetrization does not have a big impact on the additive bias difference. In addition, the  $c$  bias calibration can be carried out also used directly real images (e.g. Heymans et al. 2012).

In Figure 4.7, we also report the case using the ‘fixnoise’. There is no major improvement compared to the cases with/without noise symmetrization, with the mul-

multiplicative bias difference being consistent with zero only at higher  $S/N$ . On the contrary, the  $\Delta\mu$  increases by  $\sim 2\%$  at  $S/N = 10$ , making this method not so efficient for our procedure.

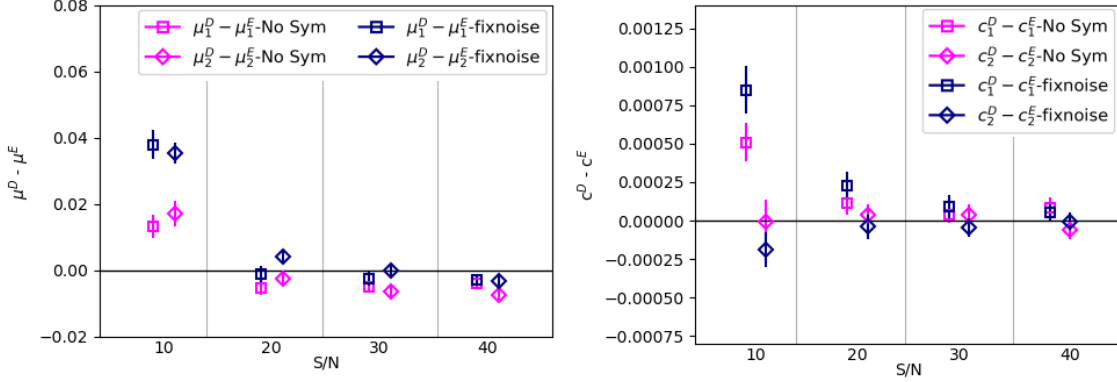


**Figure 4.7.** – Multiplicative (left) and additive (right) shear bias differences obtained when using a pixel scale of  $0''.1$  for D and a pixel scale of  $0''.05$  that we re-bin to  $0''.1$  for E (Section 4.6.3). We report the results for the case without applying any noise symmetrization (labelled as ‘No Sym’) and the approach by Sheldon & Huff (2017) (labelled as ‘fixnoise’). The data points show the bias obtained from the fit with the error-bars indicating  $1\sigma$  uncertainties for  $NR \simeq 3.8 \times 10^6$  galaxies for each  $S/N$ .

#### 4.6.4. Test IV: Different HST PSF models

In order to evaluate the impact of the HST PSF model uncertainties on the use of HST images, we analyze a setup where we employ moderately different HST PSF models for the convolution and the deconvolution in the bottom branch of Figure 4.1. We probe the sensitivity to PSF uncertainties in two setups.

In the first setup, we consider two TinyTim PSF models in filter F814W, which we create at different positions  $(x, y) = (1088, 488)$  and  $(64, 64)$  and foci of  $3.1$  and  $1.5 \mu\text{m}$ . The difference between these models is at a similar level as typical systematic uncertainties of the PSF model (see Section 4.7). Therefore, their use allows us to gauge the approximate level of the impact of systematic HST PSF model errors on the euclidization setup. In this test we employ a similar setup to the one described in Section 4.6.2 using a pixel scale of  $0''.04$  for each step of the procedure and the *Euclid* PSF is directly passed to the KSB method with a pixel scale of  $0''.04$ . The number of galaxies for each  $S/N$  and the failure rates are reported in Table 4.1. The results now show a substantial  $c$  bias difference between D and E (see the top right panel of Figure 4.8). The  $\mu$  bias difference behaves similarly as in Section 4.6.2. This test suggests that typical ACS PSF model uncertainties have little impact on the  $\mu$  bias calibration, but could signifi-



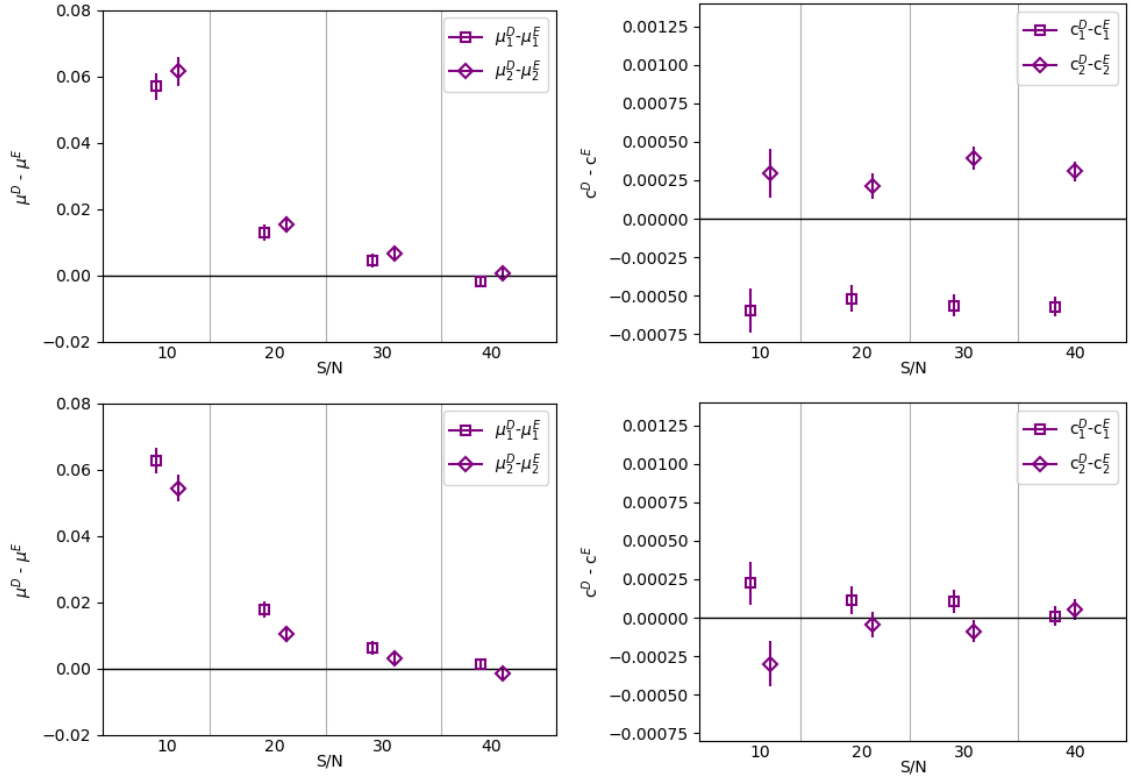


**Figure 4.8.** – Multiplicative (left) and additive (right) shear bias differences obtained when using two different HST TinyTim PSF models for *HST conv* and *HST deconv* and a pixel scale of  $0''.04$  (upper panels). The lower panels show the results applying an extra rotation after the deconvolution. The data points show the bias obtained from the fit with the error-bars indicating  $1\sigma$  uncertainties for  $\text{NR} \simeq 3.8 \times 10^6$  galaxies for each  $S/N$ .

cantly affect the  $c$  bias calibration, in agreement with Semboloni et al. (2013) as well.

To avoid this  $c$  bias issue, we propose to add an extra random rotation within the euclidization procedure after the deconvolution for the HST PSF and prior to the application of the shear. In order to keep the shape noise cancellation, the *Input galaxy* pair must be rotated by the same random rotation angle, drawn from a uniform distribution of values between 0 and 180 degrees. As shown in the bottom panels of Figure 4.8, this indeed sufficiently suppresses the  $c$  bias difference, and therefore the issue. We do report in Table 4.1 the number of galaxies and the failure rates for this test although these values are the same as for the test without the rotation of the galaxy.

It is worth bearing in mind that when we will use real HST data, the *Input galaxy* for the euclidization setup will correspond to the *HST conv* images of Figure 4.1. In this case, the extra rotation will be included not only to decorrelate the analysis

from the *HST* PSF anisotropy residuals, but also because we have a finite number of *HST* galaxies. Indeed, for each galaxy we want to be able to generate output galaxies with all kind of rotations to optimise our analysis.

In the second setup, we use for the convolution and the deconvolution in the bottom branch of Figure 4.1, an average star stack and an average model stack, respectively, as a PSF model. We obtain these stack as results from the pipeline presented in Gillis et al. (2020). Figure 4.9 shows that the multiplicative bias difference is in agreement with what we found in the previous hybrid approaches. Thus, although there is the presence of residuals between the model and the star stacks (see Section 4.7.1), this do not affect the galaxy measurements. The additive bias difference is consistent between the two components.

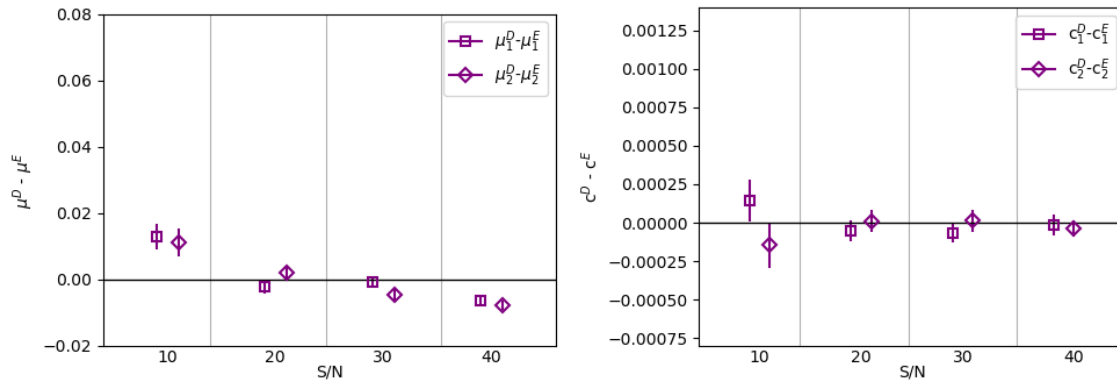


**Figure 4.9.** – Multiplicative (left) and additive (right) shear bias differences obtained when using a pixel scale of  $0''.1$  for D and a pixel scale of  $0''.05$  that we re-bin to  $0''.1$  for E. We have employed in the euclidization procedure as PSF models a star stack for the convolution and a model stack for the deconvolution (Section 4.6.4). The data points show the bias obtained from the fit with the error-bars indicating  $1\sigma$  uncertainties for  $NR \simeq 3.8 \times 10^6$  galaxies for each  $S/N$ .

#### 4.6.5. Test V: Truncation radius for the input galaxies

Background noise makes the faint outer parts of galaxy brightness profiles undetectable. As shown by Hoekstra et al. (2017), shape measurement biases may depend significantly on these external regions of a galaxy. For example, a potential outer truncation of the brightness profiles would affect shape calibrations at a level relevant for experiments such as *Euclid*. Given the presence of noise it is difficult to quantify such a potential outer truncation radius accurately. This introduces systematic uncertainties in shear calibrations that use model galaxies described by analytic brightness profiles, or that rely on simulated galaxy images in some way.

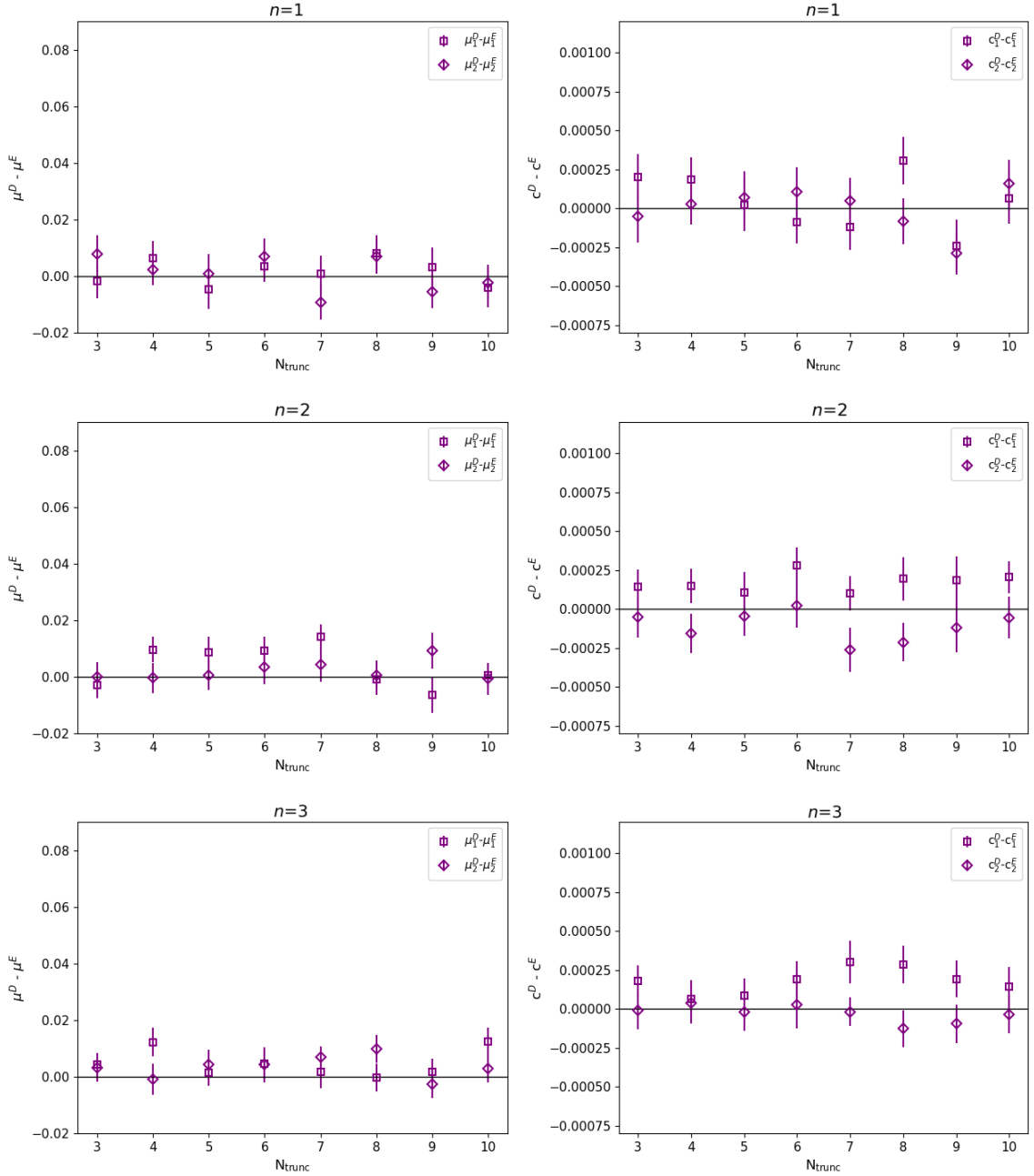


**Figure 4.10.** – Multiplicative (left) and additive (right) shear bias differences obtained when using a truncation radius for the input galaxies and a pixel scale of  $0''.04$ . In each row, the results for a specified Sérsic index  $n$  are shown. The data points show the bias obtained from the fit with the error-bars indicating  $1\sigma$  uncertainties for  $\text{NR} \simeq 7.3 \times 10^6$  galaxies for  $S/N = 30$ .

In this subsection we investigate if calibration simulations based on HST postage stamps (rather than analytic galaxy models) avoid this issue. For this, we employ

the testing environment, using simulated input galaxies that have different truncation indices  $N_{\text{trunc}} = R_{\text{trunc}}/R_e$ , which we vary in the range  $[3, 10]$  at one unit increments. Figure 4.10 shows that multiplicative bias differences are indeed independent of  $N_{\text{trunc}}$ . Thus, the euclidization setup yields an accurate multiplicative bias calibration independent of what the true galaxy truncation radius may be. In Figure 4.10 we see a disagreement between the additive bias components for some  $N_{\text{trunc}}$ , which is worth to be further investigated. Nevertheless also here no clear dependence on  $N_{\text{trunc}}$  is detected.

For this test we restrict our analysis to  $R_e["] \in \{0.3, 0.4, 0.5, 0.6, 0.7\}$  and  $-0.04 < g_1(g_2) < 0.04$ . The whole testing environment uses a pixel scale of  $0''.04$ . The number of galaxies and the failure rates are reported in Table 4.1.

## 4.7. Analysis of the accuracy of the TinyTim PSF model for HST

Assuming galaxies are randomly oriented intrinsically, their measured ellipticities provide unbiased estimates of the shear if observational and instrumental effects are accurately corrected for. These include the convolution of an image with the PSF of the telescope, the geometrical distortion of an image, which is particularly relevant in the ACS camera due to its location off of the optical axis of HST, and the CTI during the CCD readout (Massey, 2010). In addition, the ACS PSF is known to vary temporally, due to thermal fluctuations during the orbit causing variations in telescope focus (Lallo et al. 2006; Rhodes et al. 2007).

In order to apply accurate corrections for the impact of the PSF, a good PSF model is needed in the first place. Building up on earlier work (Rhodes et al., 2007; Gillis et al., 2020) we further investigate the accuracy of HST/ACS PSF models computed using TinyTim (Krist et al., 2011). In addition to direct WL measurements based on HST observations (e.g. Massey et al. 2007a), such models are needed when using HST observations of galaxies as input for WL image simulations, as discussed in this chapter. For the purpose of deconvolving the HST-observed galaxy shapes from the PSF in the euclidization (see Figure 4.1), we must accurately know the shape of the PSF at the position of the object and at the time of the observation. The latter makes the things even more complicated: the PSF, indeed, changes over time because the HST goes in and (slightly) out of focus during each orbit around the Earth. The cycle is like a slow breathing of the entire telescope barrel: it cools and contracts when it passes through the Earth's shadow, then warms and expands as it emerges back into sunlight (Lallo et al., 2006; Rhodes et al., 2007). These cyclical expansion and contraction alter the distance between the primary and secondary mirrors, which corresponds to an adjustment of focus, altering the

PSF size and shape. So, this influence of the PSF will affect the observed ellipticities.

Errors in the size of the PSF model will lead to multiplicative biases, while errors in the PSF model shape introduce additive biases (Paulin-Henriksson et al., 2008). To this end, in Section 4.7.1, we focus on the creation and investigation of the accuracy of TinyTim PSF models for the HST/ACS using dense stellar fields in the F814W filter, in addition to the F606W filter, which was already investigated in Gillis et al. (2020). The aim is to quantify the impact on the testing environment results. Additional analyses on the TinyTim PSF models in the regime of low stellar densities, as in the galaxy fields, are reported in Section 4.7.2. In addition, in the appending Section 4.16 we compare TinyTim based estimates of the HST telescope focus in stellar fields to the first coefficient in the Principal Component Analysis (PCA) of ACS PSF variations by Schrabback et al. (2010; 2018).

### 4.7.1. Generation and analysis of TinyTim PSF models

To generate HST/ACS PSF models, we use TinyTim (Krist et al., 2011), a standard tool to for generating model PSFs for the HST. Gillis et al. (2020) conducted an in-depth analysis of the accuracy of TinyTim PSF models for HST/ACS images taken in the F606W filter by comparing them to stellar images in observations of star fields. While accounting for the PSF dependence on position and telescope focus, this analysis revealed significant residual differences between the models and stars. They therefore computed an updated set of HST PSF Zernike coefficients from the star field observations, which allowed them to reduce, but not completely remove these residuals. In the same line, we extend the wavelength analysis also to images in filter F814W.

The methodology of Gillis et al. (2020) is computationally expensive as it creates an individual TinyTim PSF model for every star of the analysis. In the present work, we choose instead to pre-compute TinyTim models on a grid of positions and focus parameters, and query this database for the nearest pre-computed neighbor to every observed star. We subdivide the images of each chip ( $4096 \times 2048$  pixels) into  $128 \times 128$  cells each, and the focus is computed in the range  $-10 \mu\text{m}$  to  $8.5 \mu\text{m}$  (exceeding the range of expected variations, see Gillis et al. 2020) in steps of  $0.1 \mu\text{m}$ . TinyTim generates finely up-sampled models with a subsampling factor of 8, not accounting for the convolution with a charge diffusion kernel. This factor is large enough to allow us to shift the PSF model to adequately match the proper subpixel center for any star.

Since the TinyTim PSF models using the default parameters fail to adequately characterize the observed PSF, we use the refined best-fit estimates of higher-order Zernike coefficients from Gillis et al. (2020). These coefficients characterise the

optics of the telescope, e.g., the focus offset corresponds to the fourth Zernike polynomial's coefficient. For this analysis, we fit our gridded pre-computed PSF models

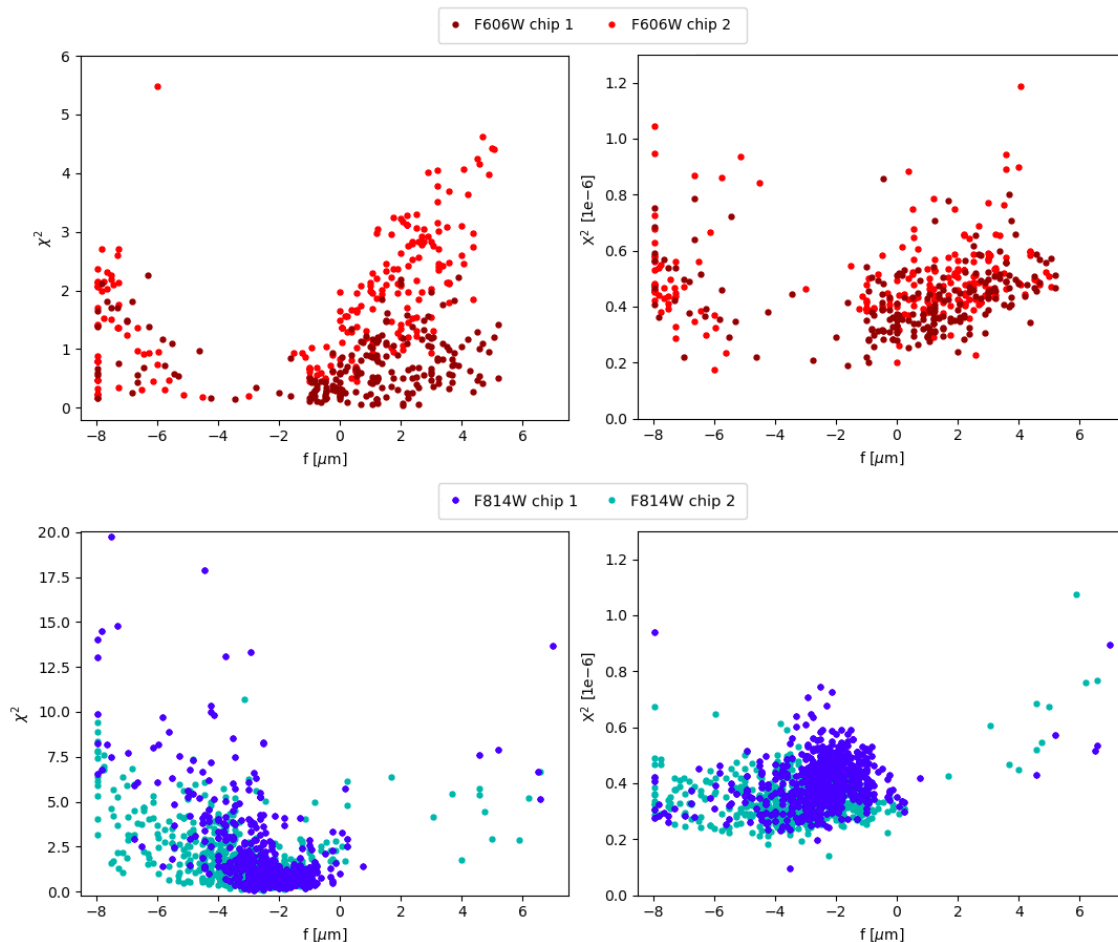


**Figure 4.11.** – The statistical parameter  $\chi^2$  (on the left) and the quality-of-fit parameter  $X^2$  (on the right) for each filter and chip plotted against the best-fit focus value of each of 205 star fields in F606W filter and 645 star fields in F814W filter.

to stars in a set of *HST*/*ACS* star fields described in Schrabback et al. (2018), which comprise 205 star fields exposures observed in F606W and 645 observed in F814W. Compared to the computation of a PSF model for each individual star, the computation of model PSFs on a grid yields a substantial speed-up, while yielding consistent focus estimates (with a difference of the order of  $10^{-4}\mu\text{m}$ ). Each observed star is compared to the models from the corresponding cell, in terms of a particular statistic  $X^2$  of the fitting residuals. This statistic is based on high-order moments of the PSF fitting residuals, which explicitly summarizes the effect of PSF model mismatch on shear measurements (for details see Gillis et al., 2020). Thus, the best-fit focus corresponds to the value which minimizes the  $X^2$ . In addition, we also compute a  $\chi^2$  based on the quadrupole moments of the brightness of the PSF

as detailed in Gillis et al. (2020).

We show the resulting  $\chi^2$  and  $X^2$  for all star fields as a function of the best fit focus in Figure 4.11. Overall, the range of  $\chi^2$  and  $X^2$  is similar for both filters, suggesting that the refined Zernike coefficients from Gillis et al. (2020) perform similarly well for F606W (on which they were calibrated) and F814W. However, we note that the F606W observations show a broader scatter in the recovered best-fit focus. We suspect that this mostly reflects a different range in typical observing conditions of the F814W and F606W star fields.

For illustration we also show the stack of the model PSFs for one F606W and one F814W example star field in Figure 4.12, as well as the stack of the residuals between the models and observed stars. The figure illustrates the case with background noise, estimated as the standard deviation of the image by sampling pixels around the edge, and the case without background noise. For both filters the residuals are at a moderate level, but detected with high significance.

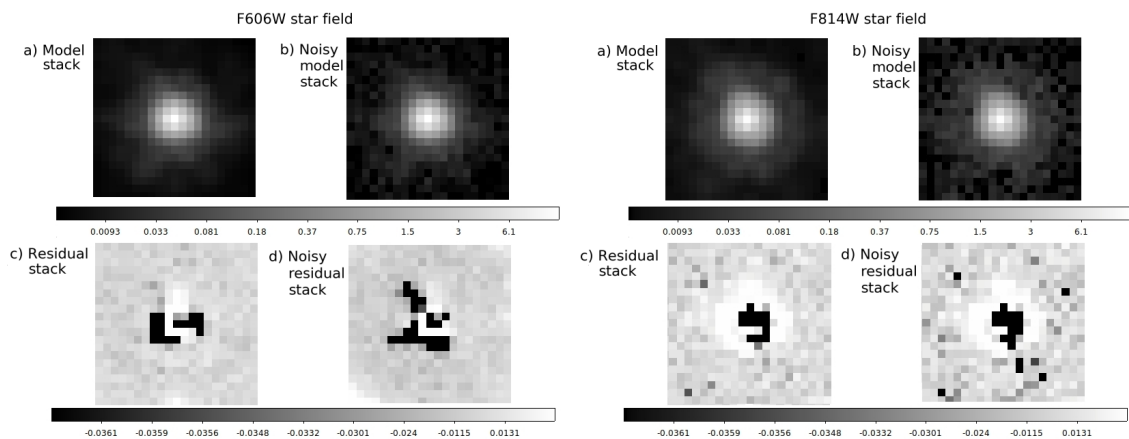


**Figure 4.12.** – TinyTim PSF model stacks without background noise a) and with background noise b) and the residual images without noise c) and with noise d) for a star field in F606W (left) and in F814W (right) filter.

#### 4.7.2. Low stellar density regime

To investigate the dependency of the recovery precision of the telescope focus on the number of available stars in a galaxy field, we create random subsamples of stars in the star fields, from which the focus is refitted. For each star field and for a range of numbers of stars within  $[5, 90]$ , we employ 30 independent random subsamples. The stars selected have magnitudes in the range  $[22, 25]$ , sizes (in pixels) in the range  $[0.8, 5.0]$ , and a minimum value for the  $S/N$  of 50. In addition, the objects have to be separated from each other by at least 1 pixel and have as minimum

value for the SEXtractor (Bertin & Arnouts, 1996a) parameter CLASS\_STAR of 0.95 (with 0 for a galaxy and 1 for a star).

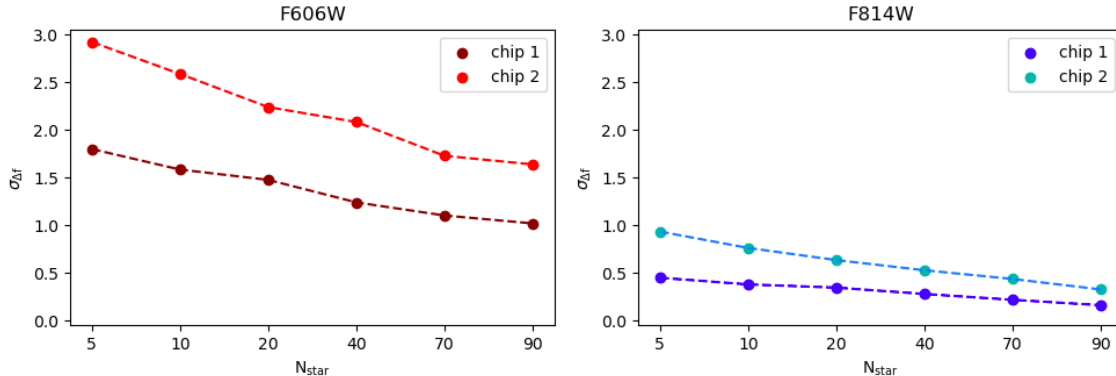


**Figure 4.13.** – Standard deviation ( $\sigma_{\Delta f}$ ) of the difference between the recovered focus using bootstrapped star subsamples containing  $N_{\text{star}}$  stars and the focus estimated using the full sample, for different sizes of the bootstrap sample for F606W and F814W and for both chips 1 and 2.

Figure 4.13 shows the standard deviation ( $\sigma_{\Delta f}$ ) of the difference between the recovered focus using bootstrapped star subsamples and the focus estimated using the full sample of stars, for different sizes of the bootstrap sample for F606W and F814W and for both chips 1 and 2. In this analysis we consider star fields having at least 90 stars in order to be able to include the same number of fields<sup>11</sup> in each subsample.

In table 4.2 we report the mean focus offset as difference between the mean focus value obtained considering a subsample of  $N_{\text{stars}}$  stars and the focus accounting for the full sample of stars in the star fields and their standard deviation (SD). As we expect, the greater the number of stars considered, the smaller the error in the focus estimation.

The large residual in the model increases the scatter when we consider small subsamples of stars. In particular, the F606W PSF models do not fit both the core and the wings well, resulting in inaccurate focus values, with a maximum  $\sigma_{\Delta f}$  of  $\sim 3 \mu\text{m}$ . The problems could be due to the presence of unresolved binary stars in our sample. Indeed, it should increase the observed size of the PSF, biasing the model to a focus value which provides a larger size, meaning the best-fit focus will be pulled away from a correct value. The same behaviour is also found in Gillis et al. (2020), who show that for F606W star fields the algorithm generally finds the

<sup>11</sup>The original sets of 645 star fields in F814W and 245 star fields in F606W are reduced by 33% for F814W chip 1, 11% for F814W chip 2, and 3.4% for F606W chip 1 and 6.3% for F606W chip 2. Thus, the final samples we plot in Figure 4.13 consist of 434, 573, 198, and 192 star fields, respectively.



**Table 4.2.** – Mean focus offset, calculated as the difference between the mean focus value obtained considering a subsample of  $N_{\text{stars}}$  stars (first column) and the focus estimated from the full sample of stars in the star fields and the SD on the difference, for the filter F606W and F814W in both chips 1 and 2 (from second to fourth column).

$N_{\text{stars}}$	$\bar{f} - f_{\text{full sample}} \pm \sigma_{\bar{f} - f_{\text{full sample}}} [\mu\text{m}]$			
	F606W chip 1	F606W chip 2	F814W chip 1	F814W chip 2
5	$0.06 \pm 1.80$	$-0.15 \pm 2.92$	$0.01 \pm 0.45$	$0.22 \pm 0.93$
10	$0.23 \pm 1.58$	$-0.05 \pm 2.59$	$-0.007 \pm 0.380$	$0.11 \pm 0.76$
20	$0.23 \pm 1.48$	$0.02 \pm 2.24$	$-0.03 \pm 0.35$	$0.06 \pm 0.63$
40	$0.17 \pm 1.24$	$0.15 \pm 2.08$	$-0.03 \pm 0.28$	$0.01 \pm 0.53$
70	$0.11 \pm 1.10$	$0.17 \pm 1.73$	$-0.01 \pm 0.22$	$-0.004 \pm 0.437$
90	$0.12 \pm 1.02$	$0.12 \pm 1.64$	$-0.007 \pm 0.162$	$-0.01 \pm 0.32$

best solution to the focus at larger focus offset values. Another hypothesis could be the blending, causing the detection of a single but bigger in size stars if the field is crowded. From the visual inspection of the star fields, we note indeed, that many images are crowded star fields, especially for the F606W filter, while some observations in F814W include star fields with globular clusters. Those fields are the same which avoid the focus range of  $-8$  to  $-2 \mu\text{m}$  in the comparison between the focus values and the principal component coefficients in the appending section 4.10.2. We note that combining the two chips, for F606W, even if we consider  $N_{\text{star}} = 90$  stars we can recover the focus value with an accuracy of  $\sigma_{\Delta f} \simeq 2.7 \mu\text{m}$ . For the F814W filter, we can obtain the focus value with less than  $1 \mu\text{m}$  uncertainty with  $N_{\text{star}} = 5$  stars.

## 4.8. Summary and conclusions

Next generation experiments, such as *Euclid*, are poised to revolutionize our understanding of dark matter and dark energy using weak gravitational lensing measurements, thanks to their large sky coverage, wavelength coverage, and high spatial resolution. Before exploiting real data, simulations are of paramount importance to investigate the impact of systematic effects and mitigate them in order to then estimate cosmological parameters.

In this chapter we present the preparation of a testing environment, which is used to propagate the impact of uncertainties regarding the use of HST data for the generation of *Euclid* weak lensing calibration image simulations. Using simulated data we have demonstrated that the euclidization procedure can provide accurate

shear calibrations if one avoids sampling related issues via an at least initial super-sampling of the emulated *Euclid*/VIS images. Moreover, we carried out an analysis of the accuracy of the TinyTim PSF models for HST/ACS, investigating also the regime of lower stellar density for the star fields.

Our main findings and conclusions can be summarized as follows. We have:

- found that when using the native *Euclid*/VIS and HST/ACS pixel scales in the euclidization setup, a difference in the multiplicative bias estimates between outputs D and E of  $\Delta\mu \simeq 0.01683 \pm 0.000019$  occurs at  $S/N \geq 20$ , when employing the KSB method to estimate galaxy shapes. This value increases to  $\Delta\mu \simeq 0.04963 \pm 0.00010$  at  $S/N = 10$ . In addition, we have shown that the galaxy model fits retrieve consistent estimates for the half-light radii and for the fluxes for the samples of galaxies in the D and E outputs but not for the Sérsic indices. If we use a Gaussian PSF instead of the original *Euclid*, the averaged multiplicative bias difference increases by 0.01 on average. Furthermore, we found that increasing the HST  $S/N$  ratio by a factor 10, the multiplicative bias difference decreases to  $\Delta\mu \simeq 0.0086 \pm 0.0006$ ;
- shown that using a finer pixel scale decreases the multiplicative bias difference, and again, the use of deeper HST-like images improves the bias calibration, attaining a  $\Delta\mu \simeq 0.0056 \pm 0.0002$ , if we exclude galaxies with  $S/N=10$ . Also in this case, the galaxy model fit provides a good agreement between the parameters of D and E galaxies, but not for  $n$ ;
- tested a hybrid approach for the euclidization setup in which the E images are initially created using a finer pixel scale of  $0''.05$  arsec and then re-binned to the native *Euclid*/VIS pixel scale of  $0''.1$ . In this setup the multiplicative bias difference is reduced to  $\Delta\mu \simeq 0.0038 \pm 0.0005$ . This indicates that the issue is caused by the limited sampling provided at the native VIS pixel scale within the euclidization procedure. The strength of this mitigation strategy is the balance between the use of native pixel scales and the accuracy of the calibration. In addition, we perform this test also simulating galaxies in the F606W filter, obtaining a negative value for the multiplicative bias difference of  $\Delta\mu \simeq -0.0007 \pm 0.0005$ ;
- performed the test III modifying the procedure to mitigate the correlated noise bias in the euclidization. We tested the procedure without applying any noise symmetrization, resulting in a decrease by  $\Delta\mu$  of  $\sim 1\%$  compared to the default approach (with the symmetrization). We also followed the Sheldon & Huff (2017) approach using a ‘fixednoise’ field as correction, obtaining no major improvements compared to the cases with/without noise symmetrization but a  $\Delta\mu$  converging to zero at higher  $S/N$ ;

- found that the HST/ACS PSF model uncertainties can lead to significant biases in the shear calibration, as demonstrated by our use of two slightly different PSF models in the convolution and deconvolution steps within the euclidization setup. We have demonstrated that resulting additive shape measurement bias differences can be mitigated via the introduction of an extra rotation after the deconvolution for the ACS PSF;
- shown that the accuracy of the euclidization setup is not degraded if input galaxies with truncated brightness profiles are used. Weak lensing image simulations that use actual galaxy postage stamps as input should therefore yield accurate bias calibrations independent of the true truncation radii of galaxy brightness profiles;
- extended the work from Gillis et al. (2020), who recalibrated TinyTim PSF models for HST/ACS in the F606W filter and tested their accuracy, to an analysis of star field observations in the F814W filter, finding a similar level of accuracy for the models. We have found that the F606W images show a broader scatter in the recovered best-fit focus compared to the images in the F814W filter. Such additional F814W PSF models will be needed in future applications of the euclidization setup that aim to also emulate color-dependent effects from the combination of F606W and F814W observations. Moreover, we have tested the TinyTim PSF model recovery in scenarios where only few stars are available to constrain the focus. We have found that for the F606W filter even with 90 stars the focus value is inaccurate ( $\Delta f \simeq 0.12 \pm 1.02$  for chip 1 and  $\Delta f \simeq 0.12 \pm 1.64$  for chip 2), while for the F814W filter we obtain a  $\sigma_{\Delta f} < 1 \mu\text{m}$  already using 5 stars;
- compared TinyTim focus estimates to the leading coefficient in the PSF principal component analysis from Schrabback et al. (2010; 2018), finding an approximately linear relation in most of the coefficient range, but strong deviations at extreme focus values (see the appending Section 4.10.2).

Although our simulations do not include all the features of real data and do not rely on more advanced methods for galaxy simulations (Lanusse et al., 2021), we can conclude that shear biases can be mitigated. The testing environment, in which we have employed emulated HST-like images, can be used to estimate, and thus to calibrate, biases for *Euclid*. Given limited computing resources we have estimated biases to a sub-percent level ( $\simeq 0.4\%$ ) in our analysis. For the actual *Euclid* calibrations this will need to be reduced in the future to the  $\Delta\mu < 0.02\%$  level using larger sets of simulations.

## 4.9. Appendix A: Signal-to-Noise ratio estimation

Given an initial value for the flux of the *Input galaxy* pair, we tune each step of the testing environment such that the output galaxies have certain measured  $S/N$  values, according to the CCD equation (Howell, 1989):

$$S/N = \frac{F_{\text{gain}}}{\sqrt{F_{\text{gain}} + a^2 \pi \left(\frac{R_e}{l}\right)^2 (F_{\text{sky}} \text{gain} + \text{ron}^2)}}, \quad (4.6)$$

where  $F$ [ADU] is the flux of the galaxy,  $\text{gain}[e^-/\text{ADU}]$  is the gain,  $a$  is a multiplicative factor related to the aperture,  $R_e$ [arcsec] the half-light radius,  $l$ [arcsec] the pixel size,  $F_{\text{sky}}[\text{mag}/\text{arcsec}^2]$  the sky background flux and  $\text{ron}[e^-]$  is the read-out noise. In particular, since we want to emulate Direct *Euclid*-like and *Euclidized* images, we use parameter values that match expectations for *Euclid*, as reported in Section 4.3. We consider in our analysis the following input values of  $S/N = 10, 20, 30$ , and 40.

To estimate the  $S/N$ , we choose an elliptical aperture with a radius three times ( $a = 3$ ) the mock half-light radius of the *Input galaxy*,  $R_e$ . The factor 3 is chosen as compromise between obtaining a ‘true’ total magnitude and precision (Kaiser et al., 1995). Once all the steps of the procedure are taken, to verify that the simulated images have the correct  $S/N$ , we calculate the output  $S/N_{\text{measured}}$  using two different methods.

**Photutils Aperture.** Using the Astropy Photutils package (Bradley et al., 2020), we consider an optimal elliptical aperture and calculate the  $S/N_{\text{measured}}$  within it as the ratio between the `kron_flux` and its `error kron_fluxerr`. This method overestimates the lowest  $S/N$  and underestimates the highest  $S/N$ . Furthermore, the estimates of the  $S/N_{\text{measured}}$  have a strong dependency on the half-light radius  $R_e$  and the Sérsic index  $n$ . In particular, the  $S/N_{\text{measured}}$  for galaxies with extreme values of both parameters, e.g.,  $R_e = 0''.2$  and  $n = 3.0$  or  $R_e = 0''.7$  and  $n = 3.0$ , are far off the input  $S/N_{\text{measured}}$  (see e.g., the bottom panels in Figure 4.14).

We verify also the impact of the dilatation of the input galaxy due to the PSF after the convolutions. In this case, the radius of the aperture is  $R_{\text{e\_apert}} = 3 \times \sqrt{R_e^2 + R_{\text{e\_PSF}}^2}$ , where  $R_{\text{e\_PSF}} = 0.085$  arcsec, corresponding to half of the Full-Width-at-Half-Maximum (FWHM) of the *Euclid* PSF (Cropper et al., 2016). We note that its maximum impact is  $\sim 4\%$  for  $R_e = 0''.2$  and  $n = 2$ . The impact decreases to a minimum value of  $\sim 0.4\%$  for  $R_e = 0''.7$  and  $n = 3$ , regardless of the input  $S/N$  and the output E or D. Given the minor impact we decided to not take  $R_{\text{e\_PSF}}$  into account in the CCD equation.

**Elliptical aperture.** As a validation, we also estimate the  $S/N$  creating a circular aperture with a radius of three times  $R_e$  and drawing it as an `Image` with `GALSIM`. In order to transform the circular aperture into an elliptical one, we first interpolate the image using `galsim.InterpolatedImage`, second we assign the two components for the ellipticity  $g_1$  and  $g_2$ , and then we randomly shift the center position and apply the shear, assigning the same values we give to the *Input galaxy*. The  $S/N_{\text{measured}}$  is calculated within this aperture, where the signal is the sum of the pixel values in the aperture, and the noise is calculate in a stripe of one thousand pixels near the bottom part of the image as the variance in those pixels.

The results are shown in Figure 4.14, illustrating in the left panel the  $S/N_{\text{measured}}$  using a customized aperture and, in the right panel, the results for the  $S/N_{\text{measured}}$  estimate from *Photutils*, as a function of the half-light radius  $R_e$ , for D, HST-like and E. We report the results only for the intermediate Sérsic index  $n = 2$  for small ( $\text{NR} \sim 5.8 \times 10^4$ ) samples of galaxies with  $S/N = 30$ . We designed the HST-like observations to have a  $S/N$  that is approximately twice as high as the  $S/N$  for the D and E images, consistent with the recovered values. The  $S/N_{\text{measured}}$  estimates computed using the elliptical apertures have a weaker dependence on  $R_e$  (see Figure 4.14), which is why we regard this method as our default approach for  $S/N$  computation.

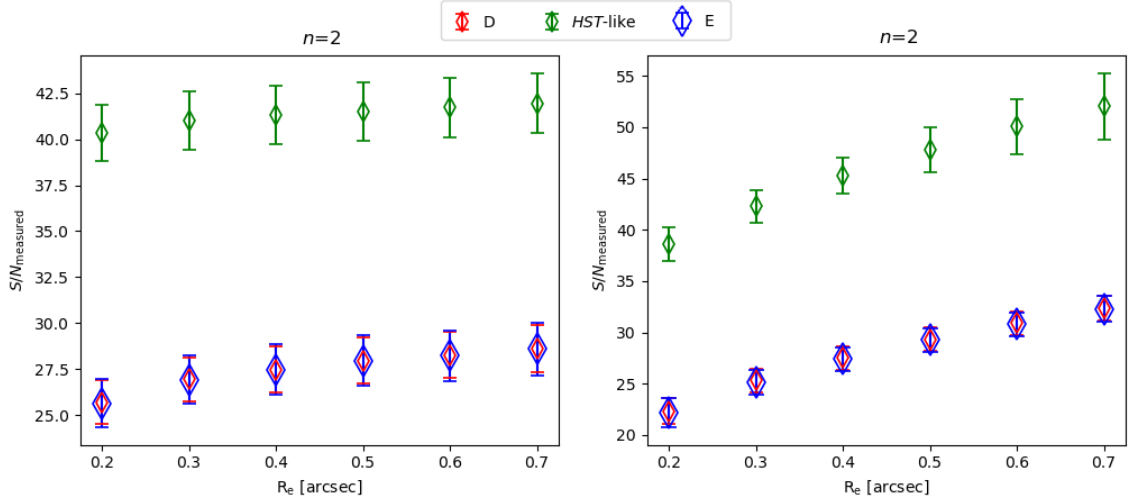


**Figure 4.14.** – Comparison between the measured  $S/N_{\text{measured}}$  estimated within a customized aperture (left) and with *Photutils* (right) for D, HST-like, and E as a function of the half-light radius  $R_e$  for an input  $S/N = 30$ . We only report the results for  $n = 2$  and for  $\text{NR} \simeq 5.8 \times 10^4$  galaxies. The data points are the mean and the error-bar is  $1\sigma$  SD.

## 4.10. Appendix B: On the TinyTim PSF models

In this appendix we describe additional details regarding the analysis of the TinyTim PSF models.

### 4.10.1. Quality of fit parameters for TinyTim PSF models

Gillis et al. (2020) define and investigate different quantities regarding the accuracy of PSF model fits for weak lensing analyses. In particular, they define  $X^2$  as:

$$X^2 = \sum_k Z_k^2, \quad (4.7)$$

which is the sum over the set of the following eights  $Z_k^2$  values<sup>12</sup>:

$$\begin{aligned} Z_x^{2(-)} &\simeq \sum_{i=0}^N \left( Q_{x,\text{star},i}^{(-)} - Q_{x,\text{model},i}^{(-)} \right)^4, \\ Z_y^{2(-)} &\simeq \sum_{i=0}^N \left( Q_{y,\text{star},i}^{(-)} - Q_{y,\text{model},i}^{(-)} \right)^4, \\ Z_+^{2(\pm)} &\simeq \sum_{i=0}^N \left( Q_{+,\text{star},i}^{(\pm)} - Q_{+,\text{model},i}^{(\pm)} \right)^2, \\ Z_x^{2(\pm)} &\simeq \sum_{i=0}^N \left( Q_{x,\text{star},i}^{(\pm)} - Q_{x,\text{model},i}^{(\pm)} \right)^2, \\ Z_s^{2(\pm)} &\simeq \sum_{i=0}^N \left( Q_{s,\text{star},i}^{(\pm)} - Q_{s,\text{model},i}^{(\pm)} \right)^2, \end{aligned} \quad (4.8)$$

where the  $Q$  are the different quality of fit parameters, each of them related a particular feature of the PSF.

In order to further investigate the PSF model imperfections, in each panel of Figure 4.15 we depict the behaviour of each  $Q$  parameter as a function of the best focus value. The top panels show  $Q_{x\_diff\_diff}$  and  $Q_{y\_diff\_diff}$ , which are related to the position of the centroid.  $Q_{plus\_diff\_diff}$  and  $Q_{plus\_sum\_diff}$  are the diagonal terms of the moments matrix of the PSF,  $Q_{cross\_diff\_diff}$  and  $Q_{cross\_sum\_diff}$  are the other two off-diagonal terms of the matrix,  $Q_{size\_diff\_diff}$  and  $Q_{size\_sum\_diff}$  are related to the size estimator. The final  $\_diff$  in each of these labels means that the variable expresses the difference between the value for the model and data, averaged over all stars. The ‘ $\_sum$ ’ or ‘ $\_diff$ ’ in the middle refers to whether it is the (+) or (-) value, respectively, as given in Eqs. (4.8). We show the results of images for both filters F814W and F606W and both chips 1 and 2.

---

<sup>12</sup>Here we use “ $Z_k^2$ ” as a shorthand for the set of eight parameters.

In the case of perfectly calibrated PSF models we would expect that these parameters should only show some mild scatter (due to noise) around zero. Instead, some of them show significant, in parts focus dependent deviations from zero. This was already shown by Gillis et al. (2020) for F606W, and is similarly confirmed by our analysis for F814W. In contrast to F606W, the performance is more similar for both chips for F814W, except for `Qsize_sum_diff` (see the bottom right panel of Figure 4.15), for which chip 2 performs significantly better than chip 1.

In the second and third row panels of Figure 4.15, we also see for the filter F606W images, a gap between the values of chip 1 and chip 2. The parameters `Q_plus` and `Q_cross` are related to the mean square contribution of the PSF shape inaccuracies to the first additive component of the shear bias. This discrepancy could be related to the temperature variations and gradients distorting the image plane in ways that are not accounted for by the TinyTim model. The difference between the two chips might be considered to be due to the fact that there is a vertical offset between them of about  $0.5 \mu\text{m}$  (Gillis et al., 2020). This effect was also noticed by others (Cox & Niemi, 2011), who attributed it to most likely being due to differences in spherical aberration and charge diffusion between the two chips. But we find this to be an insufficient explanation. Further analysis conducted by Gillis et al. (2020) shows that sometimes the model PSFs match the sizes of the observed PSF on average, but there is very large scatter in this relationship. This suggests that a possible explanation for these discrepancies might be that there is an additional spatial variation in the PSF that is not accounted for in the model.

#### 4.10.2. Relation between principal component coefficients and focus values

As an alternative approach to investigate the TinyTim PSF model accuracy, we use the star fields to calibrate a relation between the TinyTim focus estimates and the first coefficient in the Principal Component Analysis (PCA) of PSF variations from previous analyses of the same star fields conducted by Schrabback et al. (2010; 2018).

Figure 4.16 shows that these quantities correlate tightly in an approximately linear relation within most of the range of the first principal coefficient. However, for the filter F814W, substantial residuals occur for focus values around  $\sim -4 \mu\text{m}$ , corresponding to the regime showing a bimodal focus distribution in the left panel of Figure 4.16. For the filter F606W, in the right panel of Figure 4.16, some strongly negative focus values are clearly off. This seems to be especially the case for fields where both chips get very different focus estimates. These large discrepancies indicate the limitation of the recalibrated TinyTim models in this regime, since the focus value should be similar for both chips. We also see that this problem occurs more often for F606W than for F814W.

#### 4. Weak lensing image simulations for *Euclid* using *HST*-emulated data

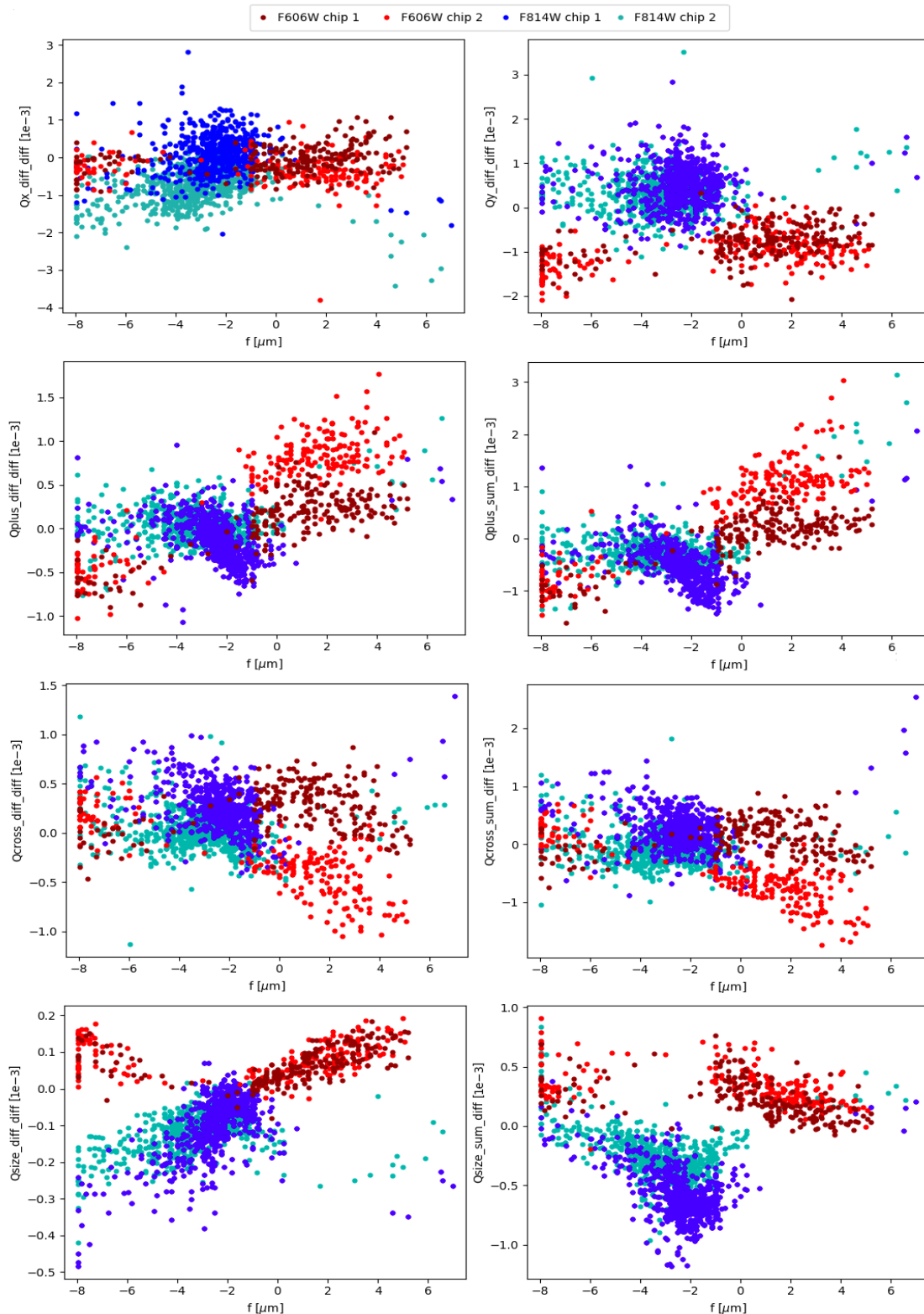


**Figure 4.15.** – The best-fit focus values plotted against each component of the quality-of-fit parameter  $Q$  for the filters F814W and F606W and both chips 1 and 2. In the ideal case of a perfect PSF model we should see a flat trend around zero. Some parameters exhibit a clearly different behaviour between chips 1 and 2 for the filter F606W.



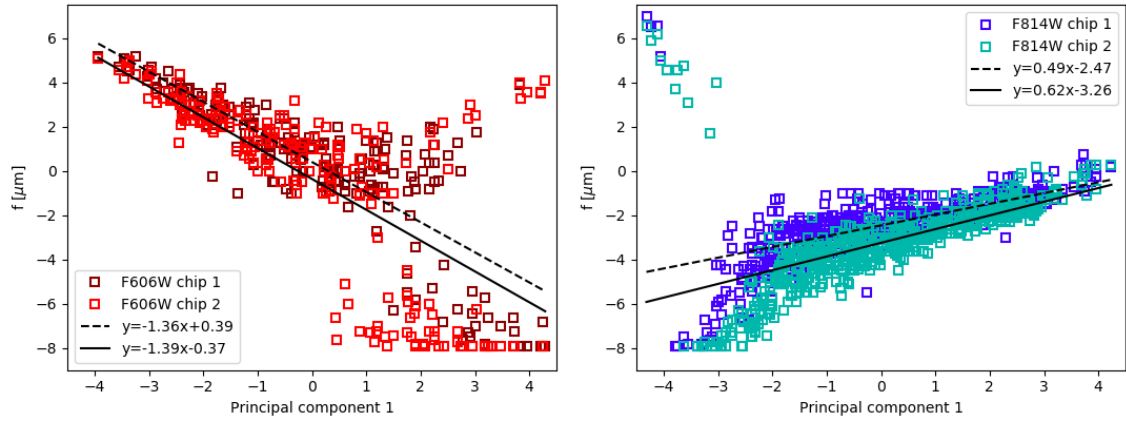


**Figure 4.16.** – The best-fit focus offset values plotted against the first Principal Component coefficients for 205 star fields in the F606W filter (left panel) and 640 star fields in the F814W filter (right panel) and for both chips 1 and 2. The dashed and the solid lines indicate the fit lines to the data points for chip 1 and chip 2, respectively, which we also report in the legend.



## CHAPTER 5

---

# Ultra-Compact Massive Galaxies within the Kilo Degree Survey

---

*“Everything dies, from the smallest blade of grass to the biggest galaxy.”*

- Stephen R. Donaldson, *Unknown source*

### **Building the largest spectroscopic sample of ultra-compact massive galaxies with the Kilo Degree Survey**

*D. Scognamiglio, C. Tortora, M. Spavone, C. Spiniello, N. R. Napolitano, G. D’Ago, F. La Barbera, F. Getman, N. Roy, M. Raj, M. Radovich, M. Brescia, S. Cavuoti, L. V. E. Koopmans, K. H. Kuijken, G. Longo, C. E. Petrillo*  
The Astrophysical Journal, (2020), 893, 4, DOI: 10.3847/1538-4357/ab7db3

### **Overview**

In this chapter, we present a spectroscopic analysis of 33 new candidates at redshifts  $0.15 \lesssim z \lesssim 0.5$  and confirm 19 of them as UCMGs, based on their nominal spectroscopically inferred  $M_*$  and  $R_e$ . The addition of these 19 newly confirmed objects to our previous finding allows us to fully assess the systematics on the system selection and to finally reduce the number density uncertainties. Moreover, putting together the results from our current and past observational campaigns, we build the largest sample of UCMGs ever collected.

This chapter reproduces the work published in The Astrophysical Journal in 2020. The paper Scognamiglio et al. 2020 is provided in its integrity in original form in

the Appendix A. The data reduction and the following analysis for the spectroscopic confirmation of the objects have been performed by the author (myself). Dr. C. Tortora performed the observations, Dr. N. Roj provided me the photometric catalogs of the UCMG candidates. Dr. M. Spavone supervised the data reduction. The contribution of the other co-authors amounted to help in data analysis and in the interpretation of the results and helpful advice and input to improve the work.

## 5.1. Motivation

In Section 2.2.6, we have seen that since the situation in the local Universe is very complex and different studies report contrasting results. Thus, finding and characterizing these galaxies at different redshifts is a crucial and a very valuable way to disentangle between possible physical scenarios driving the formation and size-evolution of galaxies.

In recent years different works have contributed to the census of UCMGs in wide-field surveys at these redshifts (Tortora et al. 2016, 2018 (hereafter T18); Charbonnier et al. 2017; Buitrago & Ferreras 2019). In particular, within the Kilo Degree Survey (KiDS) collaboration, we have undertaken a systematic search for UCMGs in the intermediate redshift range with the aim of building a large spectroscopically-confirmed sample that will allow us to systematically search for relic galaxies.

After identification of the candidates, spectroscopic validation is necessary to obtain precise spectroscopic redshifts and confirm the compactness and large masses of the systems. In this work we therefore continue the study started in T18 and we present spectroscopic observations for 33 new KiDS UCMG candidates selected from a sample of  $\sim 1000$  candidates (hereafter UCMG\_FULL sample). This study represents a further step forward to our final goal, which is to unequivocally prove that a fraction of the red and dead nuggets, which formed at  $z > 2$ , evolved undisturbed and passively into local “relics”. In particular, to be classified as relics, the objects have to be spectroscopically validated UCMGs and to have a very old stellar populations (e.g.,  $t \gtrsim 10$  Gyrs). We make significant progress on the first part of the story, building the largest sample of spectroscopically confirmed UCMGs at  $z < 0.5$ . Then, with spectra with resolution and signal-to-noise high enough to constrain the stellar age, it will be possible to really disentangle relics from younger UCMGs (see Spiniello et al. 2021).

The layout of this chapter is as follows. In Section 5.2, we briefly describe the different KiDS samples of high signal-to-noise ratio ( $S/N$ ) galaxies and the selection of the objects we followed-up spectroscopically. In Section 5.3 we give an overview

of the observations, the spectroscopic redshift and velocity dispersion calculation procedures. In Section 5.4, we discuss the main results, i.e. the number density as a function of redshift and the impact of systematics on these number densities. We also derive a tentative relation between the stellar mass and the velocity dispersion at the effective radius of our sample of UCMGs, compared with a sample of normalized elliptical galaxies at similar masses and redshifts. Finally, in Section 5.5, we summarize our findings and discuss the conclusion.

## 5.2. Sample definition

As a baseline sample of our search, we use the data included in the third Data Release of KiDS (KiDS-DR3) presented in de Jong et al. (2017), which as a unique image quality, consisting of 440 survey tiles ( $\approx 333 \text{ deg}^2$ , after masking). The galaxy data sample is described in the next Section 5.2.1.

### 5.2.1. Galaxy data sample

From the KiDS multi-band source catalog (de Jong et al. 2015, 2017), we built a catalog of  $\sim 5$  million galaxies (La Barbera et al. 2008) within KiDS-DR3, using SExtractor (Bertin & Arnouts 1996b), selected according their integrated optical photometry, structural parameters, galaxy classification and, stellar masses. We also cross-match this sample with overlapping spectroscopic surveys catalogs to obtain spectroscopic redshifts for the objects in common. In addition, the photometric redshifts are derived with the Multi Layer Perceptron with Quasi Newton Algorithm (MLPQNA) method (see, Brescia et al. 2013, 2014; Cavuoti et al. 2015).

We use the above dataset, that we name `KiDS_FULL`, to collect a complete set of photometrically selected UCMGs, using criteria as described in the next section. Moreover, in order to check what galaxies had already literature spectroscopy, we cross-match the `KiDS_FULL` with publicly available spectroscopic samples and define the so-called `KiDS_SPEC` sample, which comprises all galaxies from our complete photometric sample with known spectroscopic redshifts.

### 5.2.2. ucmgs selection and our sample

To select the UCMG candidates, we use the same criteria reported in T16 and T18:

1. *Massiveness*: A Chabrier-IMF based stellar mass of  $M_\star > 8 \times 10^{10} M_\odot$  (Trujillo et al. 2009; T16, T18);
2. *Compactness*: A circularized effective radius  $R_e < 1.5 \text{ kpc}$  (T18);

3. *Best-fit structural parameters*: A reduced  $\chi^2 < 1.5$  in  $g$ -,  $r$ - and  $i$ - filters (La Barbera et al. 2010), and further criteria to control the quality of the fit, as  $\Theta_e > 0''.05$ ,  $q > 0.1$  and  $n > 0.5$ ;
4. *Star/Galaxy separation*: A discrimination between stars and galaxies using the  $g - J$  vs.  $J - K_s$  plane to minimize the overlap of sources with the typical stellar locus.

Our final sample consists of 33 UCMG candidates with  $\text{MAG\_AUTO\_r} \lesssim 20.5$  and  $z_{\text{phot}} \lesssim 0.45$ .

Following the previous papers of this series (T16 and T18), we adopt rather stringent criteria on the sizes and masses to select only the most extreme (and rare) UCMGs. The large variety of definitions and assumptions used in other literature studies leads to a “definition bias”. However, the threshold on the stellar mass and the effective radius and the assumption of the shape of the stellar Initial Mass Function (IMF) compared to the one of other studies have a negligible impact on our selection.

### 5.3. Spectroscopic analysis

Once we have a large sample of UCMG candidates, the next step is its spectroscopical confirmation. In other terms, a spectroscopic confirmation of their photometric redshifts is crucial to confirm them as UCMGs, since both compactness and massiveness are originally based on the  $z_{\text{phot}}$  associated with the photometric sample.

Data of the 33 objects have been acquired in the years 2017 and 2018 during three separate runs, two carried out with the 3.6m Telescopio Nazionale Galileo (TNG), and one using the 2.54m Isaac Newton Telescope (INT), both located at Roque de los Muchachos Observatory (Canary Islands). We thus divide our sample into three sub-groups, according to the observing run they belong to: UCMG\_INT\_2017, UCMG\_TNG\_2017 and UCMG\_TNG\_2018.

#### 5.3.1. Spectroscopic signal-to-noise ratio determination

For each object we calculate the signal-to-noise ratio ( $S/N_{\text{spec}}$ ) of the integrated spectra from the flux under the assumptions that the noise is uncorrelated in wavelength bins spaced two pixels apart and that it is approximately Gaussian distributed. We mark that these signal-to-noise ratio estimates are calculated over a rather blue wavelength range, whereas the light of early-type galaxies is expected to be strong in redder regions. Thus, they have to be interpreted as a lower limit for the whole spectrum. This arises clearly from the comparison of these  $S/N_{\text{spec}}$  with the ones we will describe in the next section, which are computed, for each galaxy, over

the region used for the kinematic fit and are systematically larger. Both of them will be used in Section 5.4.4 as one of the proxy of the reliability of the velocity dispersion ( $\sigma$ ) measurements.

### 5.3.2. Redshift and velocity dispersion measurements

Redshift and velocity dispersion values have been measured with the Optimised Modelling of Early-type Galaxy Aperture Kinematics pipeline (OMEGA-K, D’Ago et al. 2018), a Python wrapper based on the Penalized Pixel-Fitting code (PPXF, Cappellari 2017). In addition to the 33 new UCMG candidates presented, we also apply the same kinematics procedure to the 28 UCMG candidates from T18. Once the observed spectra and the template libraries are ingested, OMEGA-K performs 257 fits on each spectrum. As a result, it automatically retrieves an optimal pixel mask and noise level ( $1\sigma$  noise spectrum) for the observed spectrum, and a robust estimate of the galaxy kinematics together with its uncertainties.

Given the high uncertainties, we separate the UCMGs into two groups, “high-quality” (*HQ*) and “low-quality” (*LQ*), based on the following criteria: the success rate (SR) defined as the ratio between the number of accepted fits over the total 257 attempts, the spectral  $S/N$  calculated on a common wavelength range covered by all the spectra (see Section 5.3.1) and the  $(S/N)_{\text{O-K}}$  from the OMEGA-K pipeline (calculated over different wavelength ranges for different spectra). We then classify as *HQ* objects as those above the following limits:  $\text{SR} = 0.3$ ,  $S/N_{\text{spec}} = 3.5$  and  $(S/N)_{\text{O-K}} = 6.5/\text{px}$ . In Figure 5.1 we show two examples of the PPXF fit obtained by OMEGA-K on the spectra of two different objects from the sample of the 33 UCMG candidates for which we obtain new spectroscopy in this work.

## 5.4. Results

In the following sections we discuss the main findings and their implications.

### 5.4.1. ucmgs validation

A small variation in  $z_{\text{phot}}$  can induce variations in  $R_e$  and  $M_*$  large enough to bring them outside the limits of our definition of UCMG. The agreement between the spectroscopic and the photometric redshifts can be quantified using the following quantity

$$\Delta z \equiv \frac{z_{\text{spec}} - z_{\text{phot}}}{1 + z_{\text{spec}}}, \quad (5.1)$$

and we interpret the scatter as the standard deviation of  $\Delta z$ , and bias as the absolute value of the mean of  $\Delta z$ . We find a bias of 0.0008 and a scatter of 0.0516

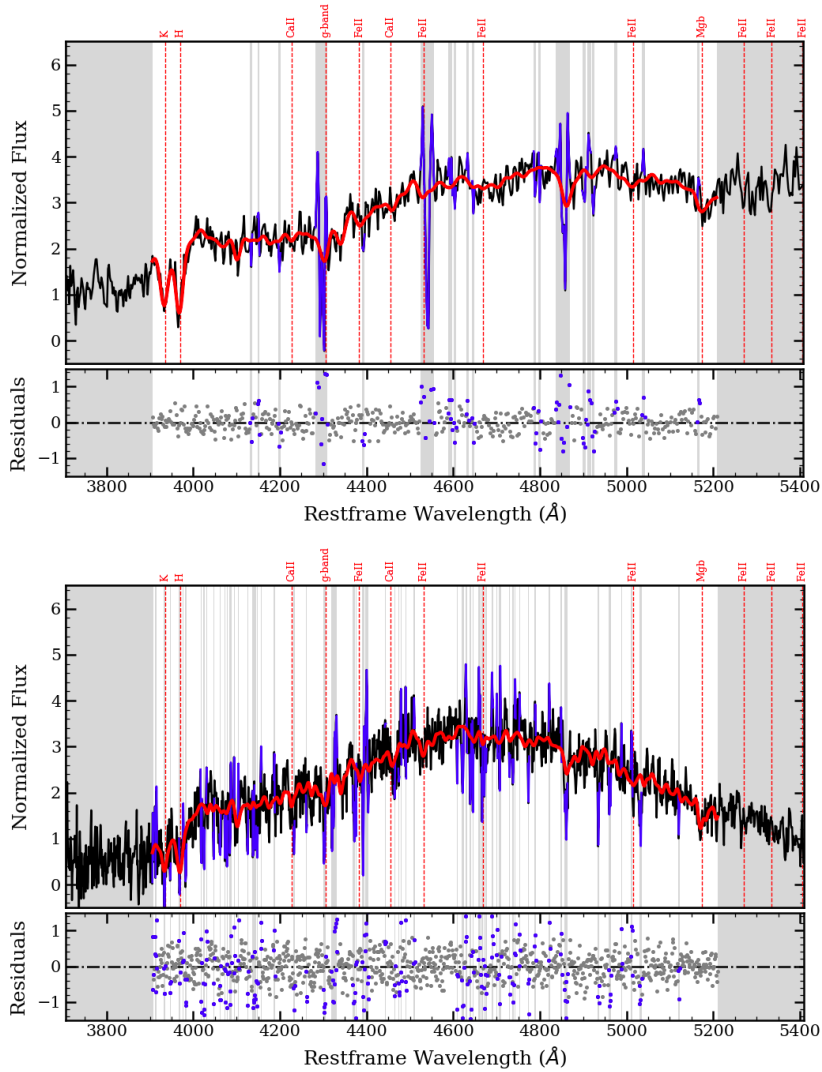


**Figure 5.1.** – Two examples of PXP fits obtained with OMEGA-K on the spectra of two different UCMGs, one of the best  $HQ$  system and one of the worse  $LQ$  system, thus representative of the whole sample, observed with two different telescopes. For each panel we plot the galaxy spectrum in black, the best template fit in red and the regions excluded from the fit as blue lines. We note that the fit is performed only outside the gray shaded regions. Finally, we highlight stellar absorption lines in red and show the residuals of the plot below each panel.

for our 33 systems and the distribution of the new redshifts is generally consistent with what found using the full sample of galaxies included in KiDS-DR3.

Using the new obtained the spectroscopic redshifts and a slightly different mass setup compared to T18, we re-calculate both  $R_e$  and  $M_*$  for the final sample of 61 UCMG candidates. We confirm as UCMGs 37 out of 61 UCMG candidates, with a



success rate of 60%. A very important point to stress here is that we simply use the face values and include/exclude galaxies on the basis of the resulting nominal size and mass values. This will allow us to not propagate the error on the photometric and spectroscopic redshifts into masses and sizes errors, also simplifying the analysis of the systematics, we will discuss in the next Section 5.4.3. Tables 5.1 and 5.2 lists key quantities of the 61 UCMG candidates from our spectroscopic analysis.

### 5.4.2. Contamination and incompleteness

One of the main goals of our spectroscopic campaigns is to quantify the impact of systematics on the UCMG photometric selection. Because of the uncertain photometric redshifts, the candidate selection includes “contaminants” (or false-positives), i.e., galaxies which are selected as UCMGs according to their photometric redshifts, but would not result ultra-compact and massive when recalculating the masses on the basis of the more accurate spectroscopic redshift values (see T16 and T18) and “missed” systems (or false-negatives), i.e., those galaxies which are not selected as UCMGs according to their photometric redshifts, but would be selected using the spectroscopic values instead (i.e., they are real UCMGs that our selection excluded).

To estimate the fraction of contaminants, we use UCMG samples selected using the photometric redshifts, but for which we have also spectroscopic redshifts available from the literature. The correction factor for the number counts is defined as  $\mathcal{I}_F/\mathcal{C}_F$ , with  $\mathcal{I}_F$  the difference between the number of UCMG candidates using  $z_{\text{spec}}$  and  $z_{\text{phot}}$  and  $\mathcal{C}_F$  the inverse of the success rate discussed in the previous subsection. In conclusion, we find that the true number counts for UCMGs at  $z < 0.5$  would be  $\sim 15\%$  higher than the values one would find in a photometrically selected sample, on average in the whole redshift range we consider here.

### 5.4.3. ucmg number counts

Taking into account the two systematic effects discussed in Section 5.4.2, we correct the number counts of the 1221 candidates in UCMG\_FULL, in each single redshift bin to minimize the errors on number counts. Figure 5.2 shows a decrease of number counts with cosmic time, from  $\sim 9 \times 10^{-6}$  Mpc $^{-3}$  at  $z \sim 0.5$ , to  $\sim 10^{-6}$ , Mpc $^{-3}$  at  $z \sim 0.15$ . The number of UCMGs decreases by a factor of  $\sim 9$  in about 3 Gyr, consistent with the one found in T18 (see lower panel of Figure 5.2).

The comparison with other works shows a paucity of UCMGs at  $z < 0.15$  and this is in disagreement with the current hierarchical paradigm of galaxy formation, where some relic systems at  $z \sim 0$  are actually expected to be found. In addition, we do not report in Figure 5.2 the results obtained in Charbonnier et al. (2017) and Buitrago

## 5. Ultra-Compact Massive Galaxies within the Kilo Degree Survey

**Table 5.1.** – Results of the spectroscopic analysis of the objects belonging to the three observational runs presented here: UCMG\_INT\_2017, UCMG\_TNG\_2017, UCMG\_TNG\_2018. The columns from left to right list: the galaxy ID, the photometric redshift, the measured spectroscopic redshift with its error, the corrected velocity dispersion to the effective radius in  $\text{km s}^{-1}$ , the equivalent circular aperture in arcsec. Finally, in the final five columns, we also report the success rate, the signal-to-noise ratio per pixel calculated in the range 3600 – 4600 Å, the signal-to-noise ratio per pixel calculated over the region used for the fit by OMEGA-K, the quality level of the velocity dispersion estimates, and the spectral validation response: “Y” if the candidate is a confirmed UCMG, (i.e.  $\log_{10}(M_*/M_\odot) > 10.9$  and  $R_e < 1.5$  kpc), “N” if it is not.

ID	$z_{\text{phot}}$	$z_{\text{spec}} \pm \Delta z_{\text{spec}}$	$\sigma_e$	SR	$(S/N)_{\text{spec}}$	$(S/N)_{\text{O-K}}$	Quality level	Spec. Valid.
1	0.28	$0.2696 \pm 0.0002$	211	0.62	1.99	6.13	LQ	Y
2	0.26	$0.3158 \pm 0.0002$	210	0.77	3.21	5.69	LQ	Y
3	0.26	$0.2995 \pm 0.0003$	291	0.79	2.50	6.19	LQ	N
4	0.45	$0.3084 \pm 0.0005$	281	0.3	2.18	4.23	LQ	N
5	0.37	$0.4401 \pm 0.0003$	161	0.07	4.00	6.87	LQ	Y
6	0.22	$0.2988 \pm 0.0002$	217	0.75	2.42	7.27	LQ	N
7	0.23	$0.3221 \pm 0.0002$	224	0.15	2.96	6.71	LQ	Y
8	0.24	$0.2976 \pm 0.0002$	257	0.59	3.06	6.31	LQ	N
9	0.34	$0.2915 \pm 0.0001$	251	0.21	4.07	6.04	LQ	N
10	0.32	$0.359 \pm 0.0004$	293	0.12	2.00	2.05	LQ	Y
11	0.24	$0.2797 \pm 0.0003$	286	0.85	1.40	4.58	LQ	Y
12	0.28	$0.3312 \pm 0.0002$	218	0.73	2.70	6.76	LQ	Y
13	0.23	$0.2668 \pm 0.0007$	274	0.23	1.77	2.89	LQ	N
14	0.35	$0.2946 \pm 0.0003$	369	0.66	2.01	3.97	LQ	Y
15	0.27	$0.2974 \pm 0.0002$	451	0.69	6.90	13.25	HQ	Y
16	0.33	$0.3594 \pm 0.0001$	292	0.84	6.87	14.32	HQ	Y
17	0.33	$0.2656 \pm 0.0006$	347	0.43	1.95	8.20	LQ	Y
18	0.32	$0.1586 \pm 0.0002$	276	0.70	2.93	12.76	LQ	N
19	0.3	$0.3281 \pm 0.0002$	251	0.3	2.97	6.27	LQ	N
20	0.3	$0.2728 \pm 0.0003$	361	0.21	2.85	5.58	LQ	Y
21	0.33	$0.2523 \pm 0.0003$	366	0.85	2.62	9.93	LQ	N
22	0.28	$0.2719 \pm 0.0002$	413	0.66	5.91	12.72	HQ	N
23	0.25	$0.2971 \pm 0.0002$	443	0.79	6.18	17.38	HQ	Y
24	0.33	$0.3491 \pm 0.0002$	215	0.23	5.79	11.15	LQ	Y
25	0.28	$0.2703 \pm 0.0002$	298	0.91	6.80	18.11	HQ	Y
26	0.32	$0.1984 \pm 0.0002$	316	0.89	3.96	17.92	HQ	N
27	0.33	$0.2843 \pm 0.0002$	267	0.91	5.08	15.85	HQ	N
28	0.33	$0.4203 \pm 0.0002$	191	0.02	6.59	11.69	LQ	Y
29	0.29	$0.3116 \pm 0.0002$	177	0.52	7.74	15.65	HQ	Y
30	0.39	$0.2994 \pm 0.0002$	319	1.00	8.53	24.59	HQ	N
31	0.41	$0.4655 \pm 0.0001$	280	0.98	9.18	18.13	HQ	Y
32	0.29	$0.3382 \pm 0.0003$	301	0.88	3.51	9.73	HQ	N
33	0.43	$0.4028 \pm 0.0003$	335	0.84	4.96	9.16	HQ	Y

& Ferreras (2019), since these authors use less restrictive size criterion. However, including these results, we would have a perfect agreement with number densities reported in Charbonnier et al. (2017) in terms of normalization and evolution with redshift. Furthermore, our number counts present an evolution with redshift steeper

**Table 5.2.** – Same as Table 5.1, but for the samples UCMG\_TNG\_T18 and UCMG\_NTT\_T18.

ID	$z_{\text{phot}}$	$z_{\text{spec}} \pm \Delta z_{\text{spec}}$	$\sigma_e$	SR	$(S/N)_{\text{spec}}$	$(S/N)_{\text{O-K}}$	Quality level	Spec. Valid.
34	0.29	$0.3705 \pm 0.0001$	392	0.98	15.05	22.41	<i>HQ</i>	<i>N</i>
35	0.22	$0.2175 \pm 0.0004$	446	0.31	7.68	14.62	<i>HQ</i>	<i>Y</i>
36	0.35	$0.4078 \pm 0.0002$	412	0.93	6.70	14.33	<i>HQ</i>	<i>Y</i>
37	0.31	$0.3341 \pm 0.0002$	242	0.92	7.84	17.82	<i>HQ</i>	<i>N</i>
38	0.42	$0.3988 \pm 0.0003$	448	0.75	5.33	12.67	<i>HQ</i>	<i>Y</i>
39	0.36	$0.319 \pm 0.0004$	245	0.82	4.14	10.2	<i>HQ</i>	<i>N</i>
40	0.2	$0.3019 \pm 0.0002$	464	0.73	2.09	6.75	<i>LQ</i>	<i>Y</i>
41	0.35	$0.3853 \pm 0.0001$	223	0.98	3.69	10.92	<i>HQ</i>	<i>N</i>
42	0.28	$0.2367 \pm 0.0003$	235	1.00	2.38	9.30	<i>LQ</i>	<i>N</i>
43	0.29	$0.2801 \pm 0.0001$	214	0.94	2.77	9.55	<i>LQ</i>	<i>Y</i>
44	0.31	$0.2789 \pm 0.0001$	235	1.00	3.67	12.46	<i>HQ</i>	<i>N</i>
45	0.27	$0.2888 \pm 0.0001$	216	0.94	3.09	9.30	<i>LQ</i>	<i>Y</i>
46	0.31	$0.3618 \pm 0.0053$	196	0.09	1.39	4.08	<i>LQ</i>	<i>Y</i>
47	0.25	$0.2622 \pm 0.0003$	363	0.99	2.31	7.65	<i>LQ</i>	<i>Y</i>
48	0.27	$0.2949 \pm 0.0003$	295	1.00	3.79	10.53	<i>HQ</i>	<i>Y</i>
49	0.28	$0.2974 \pm 0.0001$	149	0.58	3.54	10.01	<i>HQ</i>	<i>Y</i>
50	0.29	$0.3188 \pm 0.0001$	408	0.96	3.88	11.85	<i>HQ</i>	<i>Y</i>
51	0.34	$0.3151 \pm 0.0001$	166	0.66	3.82	11.69	<i>HQ</i>	<i>N</i>
52	0.22	$0.2124 \pm 0.0001$	265	1.00	1.64	9.19	<i>LQ</i>	<i>N</i>
53	0.25	$0.2578 \pm 0.0002$	194	0.68	2.37	9.73	<i>LQ</i>	<i>Y</i>
54	0.34	$0.3024 \pm 0.0009$	226	0.7	1.97	4.14	<i>LQ</i>	<i>Y</i>
55	0.31	$0.3667 \pm 0.0001$	262	1.00	4.99	13.1	<i>HQ</i>	<i>Y</i>
56	0.32	$0.407 \pm 0.0001$	342	1.00	4.82	10.6	<i>HQ</i>	<i>Y</i>
57	0.33	$0.2612 \pm 0.0001$	233	0.99	3.00	10.88	<i>LQ</i>	<i>N</i>
58	0.27	$0.2818 \pm 0.0002$	227	0.92	2.41	7.38	<i>LQ</i>	<i>N</i>
59	0.23	$0.2889 \pm 0.0002$	221	0.95	2.80	9.99	<i>LQ</i>	<i>Y</i>
60	0.34	$0.3393 \pm 0.0001$	167	0.73	4.59	10.78	<i>HQ</i>	<i>Y</i>
61	0.31	$0.2889 \pm 0.0001$	236	1.00	2.47	8.67	<i>LQ</i>	<i>Y</i>

than predictions from simulations, being consistent with the most (less) efficient (in terms of merging occurrence) model predictions from Guo et al. (2011, 2013) at low (high) redshifts. It is worth noticing that the validation of a larger sample of confirmed objects allows us to reduce the error budget from cosmic variance and Poisson noise of 5 – 25%, in the four redshift bins.

#### 5.4.4. Relationship between stellar mass and velocity dispersion

The location of UCMGs on a mass-velocity dispersion diagram is deeply related the assembly of baryons and dark matter. Thus, it can provide important constraints on our understanding of the formation and evolution of these systems, but also on the intrinsic properties of UCMGs (Saulder et al. 2015).

Given the compact sizes of UCMGs, the virial theorem predicts larger velocity dispersions with respect to normal-sized galaxies of similar mass. In this section, we report the preliminary results for the 37 confirmed UCMGs. Figure 5.3 shows

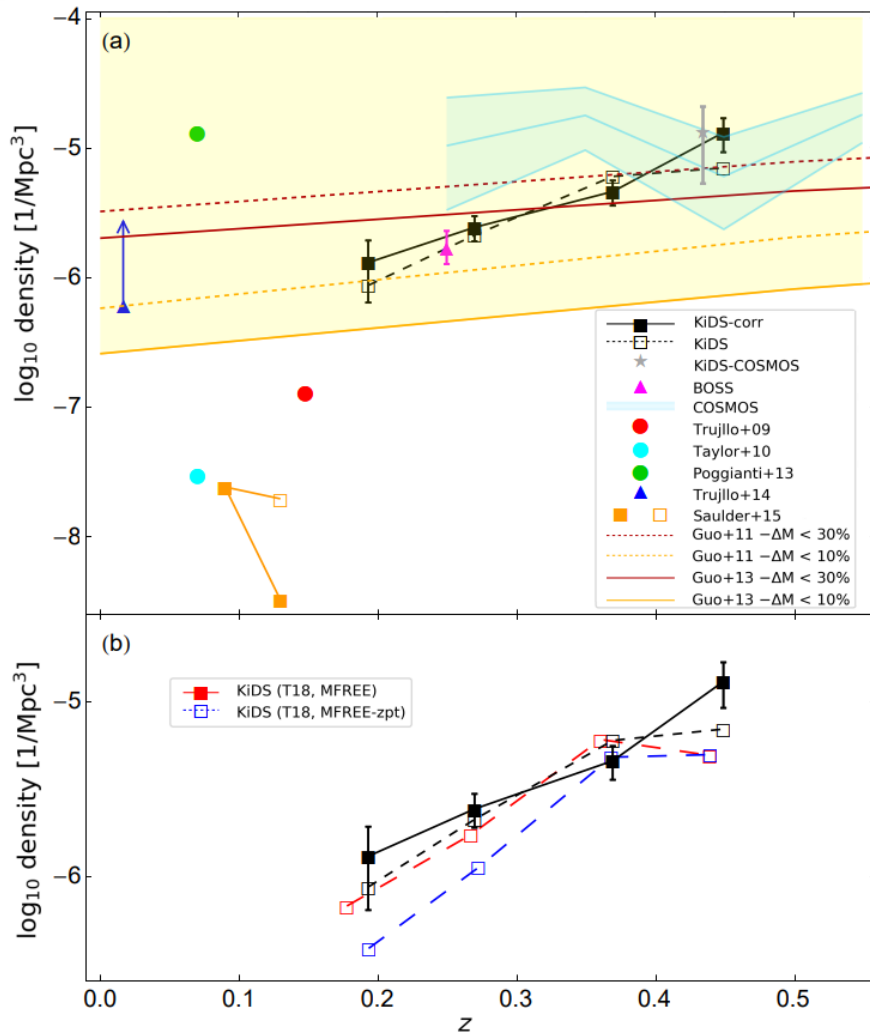


**Figure 5.2.** – *Panel a.* Filled (open) black squares, with solid (dashed) line, quoted as KiDS-corr(KiDS) in the legend, plot the number density after (before) correction for systematics, for the selected sample assuming reference masses. Error bars denote  $1\sigma$  uncertainties, taking into account Poisson noise, cosmic variance and errors on  $M_*$  and  $R_e$  (see the text for more details). The gray star is for the UCMG candidates at  $z < 0.5$  found in the tile KIDS\_150.1\_2.2 centered on COSMOS field. Other colored symbols are number density obtained from other papers, as described in the caption. *Panel b.* Number counts obtained here are compared with those presented in T18, named MFREE and MFREE-zpt, see the text for more details.

that the UCMGs have systematically larger velocity dispersions at any fixed mass compared to a sample of normal-sized ETGs derived from SDSS-III/BOSS (Baryon Oscillation Spectroscopic Survey) Data Release 10<sup>1</sup> (DR10, Ahn et al. 2014). This offset appears especially above  $\log M_*/M_\odot = 11.05$  and for *HQ* objects.

<sup>1</sup>The data catalogs are available from [http://www.sdss3.org/dr10/spectro/galaxy\\_portsmouth.php](http://www.sdss3.org/dr10/spectro/galaxy_portsmouth.php)

Speculative explanations of this offset are the presence of a massive black hole at the center of the galaxy (e.g. van den Bosch et al. 2012, 2015; Ferré-Mateu et al. 2017) which might influence the kinematics in the innermost region and the IMF which is different in very massive galaxies from a universal Milky Way-like IMF.

We aim at consolidating this result with a larger number of systems, to increase the statistics, and using spectroscopic data of better quality, in order to have more robust velocity dispersion estimates. With new and better spectroscopic, data we will also be able to constrain the age of the systems, which is the crucial ingredient to identify the relics among the confirmed UCMGs.

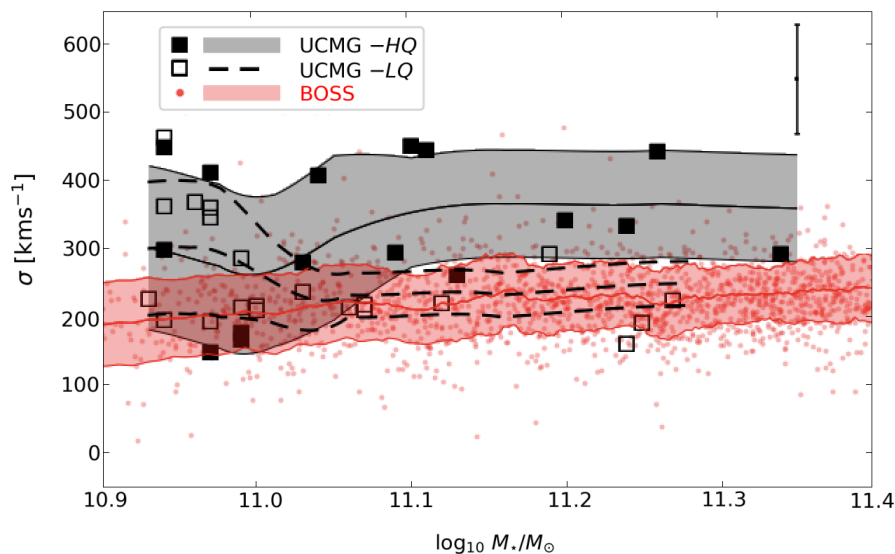


**Figure 5.3.** – Distribution on the  $M_*$  –  $\sigma$  plane for the 37 confirmed UCMGs compared with a sample of elliptical galaxies (red symbols) from the BOSS survey. Filled squared symbols are UCMGs classified as high quality ( $HQ$ ), with spectra that satisfy at the same time the three conditions  $SR \geq 0.3$ ,  $S/N_{\text{spec}} \geq 3.5$  and  $(S/N)_{O-K} \geq 6.5$ . Empty squares are instead classified as low-quality ( $LQ$ ) since their spectra do not satisfy one or more of the aforementioned criteria. For each sample, running means and  $1\sigma$  scatter are overplotted. In the top-right corner we show the mean error bar for the UCMG velocity dispersions. For both UCMGs and the sample of ellipticals, velocity dispersions are calculated within 1 effective radius, as explained in the text.

## 5.5. Conclusions

The existence of ultra-compact massive galaxies (UCMGs) at  $z < 1$  and their evolution up to the local Universe challenges the currently accepted galaxy formation models. In the effort of “bridging the gap” between the high redshift red nuggets and the local relics, in this work we have:

- spectroscopically followed up a sample of 33 UCMG candidates at redshifts  $0.15 \lesssim z \lesssim 0.5$ , found in  $333 \text{ deg}^2$  of KiDS. We have also provided a summary on how the galaxies have been photometrically selected;
- obtained the spectroscopic redshift and velocity dispersion values for these objects and for the 28 objects already presented in T18. To this purpose, we have used the Optimised Modelling of Early-type Galaxy Aperture Kinematics pipeline (OMEGA-K, D'Ago et al., in prep.);
- confirmed as UCMGs 37 out of 61 candidates, implying a success rate of 60%;
- quantified the effect of contamination and incompleteness due to the difference in redshift between the photometric and spectroscopic values. We have found that the true number counts for UCMGs at  $z < 0.5$  is  $\sim 15$  per cent higher than the values found in a photometrically selected sample;
- obtained the UCMG number counts, after correcting them with the incompleteness and the contamination factors. We have confirmed the clear decrease of the number counts with the cosmic time already found in T18, from  $\sim 9 \times 10^{-6} \text{ Mpc}^{-3}$  at  $z \sim 0.5$ , to  $\sim 10^{-6} \text{ Mpc}^{-3}$  at  $z \sim 0.15$ ,  $\sim 9$  times less in about 3 Gyr;
- shown the distribution of the 37 confirmed UCMGs in the  $M_\star - \sigma$  plane, comparing them with a sample of normal-sized elliptical galaxies from the BOSS Survey. On average, we found larger values for UCMGs compared to regular ETGs of same mass. This result, in agreement with what expected from the evolution of massive and compact galaxies, is for now speculative but it will be checked again once new, high resolution spectroscopy (already awarded) will be obtained.

In the future, we plan to continue to enlarge the sample of spectroscopically confirmed UCMGs at low and intermediate redshifts, based on photometric candidates from the KiDS survey. In addition, thanks to already awarded spectroscopic data with much higher  $S/N$ , which will allow us to perform a detailed stellar population analysis, we will separate relics from younger UCMGs. In this way, we will be able to confirm the two-phase formation scenario proposed for the mass assembly of massive/giant ETGs (Oser et al., 2010a).

## CHAPTER 6

---

### Summary and Conclusions

---

*“An ending is only happening because at some point it was a beginning.”*

- Craig D. Lounsbrough, *An Intimate Collision: Encounters with Life and Jesus*

In this chapter, I summarise the key results and give the future perspectives for the individual science work undertaken in this manuscript.

#### **6.1. Weak lensing analysis for *Euclid* using HST images as input for simulations**

In modern weak-lensing surveys, the common approach to correct for residual systematic biases in the shear is to calibrate shape measurement methods using simulations. In particular, this work focuses on building a test environment to test if *Hubble* Space Telescope (HST)-observed galaxy images can be used to emulate *Euclid* observations. We use simplified galaxy models to simulate both HST and *Euclid* observations. We then “euclidize” our HST simulations (E images, hereafter), and compare the result with the directly simulated *Euclid*-like images or D images. After setting up the procedure, we applied it using different conditions, such as different pixel scales, different correlated noise corrections and PSFs in order to investigate what can introduce significant biases in the weak lensing shear calibration.

An important result of our analysis is that the multiplicative bias difference converges to zero at high  $S/N$  (where noise-related biases are expected to be small) in the case of the fine pixel sampling ( $0''.04$ ). At the same  $S/N$  this degrades when using the native VIS pixel scale. This suggests that sampling related issues can significantly affect the euclidization procedure. On the other hand, we generally observe an increase in multiplicative bias differences towards lower  $S/N$ , suggesting that the corrections for the impact of noise that we apply within the euclidization procedure are insufficient and require further investigation. Interestingly, our hybrid approach seems to suffer less from this issue, but unfortunately it leads to a slight bias difference with opposite sign at high  $S/N$ .

Furthermore, for the native and finer pixel scales tests, we also estimated the main parameters, such as  $F$ ,  $R_e$  and  $n$ . The galaxy model fits retrieved consistent estimates for the half-light radii and for the fluxes for the samples of galaxies in the D and E outputs, but not for the Sérsic indices. This hints that the euclidized galaxy images E are slightly less centrally peaked than the Direct *Euclid*-like images D, likely reflecting the origin for the difference in the multiplicative bias estimates.

We also found that the HST/ACS PSF model uncertainties can lead to significant biases in the shear calibrations. However, the resulting additive shape measurement biases can be mitigated via the introduction of an extra rotation after the deconvolution for the ACS PSF. In addition, we have shown that there is no degradation in the shear bias estimates when using a truncation radius for the input galaxies.

The analyses of the recalibrated TinyTim PSF models for HST/ACS revealed that the F606W images show a broader scatter in the recovered best-fit focus compared to the images in F814W filter, although the optical parameters were recalibrated on F606W images. This inaccuracy is also reflected in the TinyTim PSF model recovery in scenarios where only few stars are available to constrain the focus. Finally, from the comparison between the TinyTim focus estimates and the leading coefficient in the PSF principal component analysis from Schrabback et al. (2010; 2018), we found an approximately linear relation in most of the coefficient range, but strong deviations at extreme focus values.

### Outlook

In the future, the testing environment could be used to propagate the impact of other potential inaccuracies in the HST data processing, such as residuals from the correction for charge transfer inefficiency (Massey 2010, 2014). However, we expect that their impact is likely small compared to the PSF model uncertainties, and can therefore likely be neglected. Furthermore, the additional F814W PSF models



which we have created, as well as the ones for the F606W filter, will be needed in future applications of the euclidization setup that aim to emulate color-dependent effects from the combination of F606W and F814W observations.

Regarding the testing environment, the current capabilities of the GALSIM software package already allow for the simulation of galaxies with much higher fidelity to the real sky compared to our present work. We stress it has been the aim of our work to test this procedure using simulations and investigate if uncertainties in the HST PSF model introduce significant biases in the weak lensing shear calibration for *Euclid* rather than provide a finalized pipeline.

We plan to perform an additional test for the correction of correlated noise. The noise in astronomical images is typically a combination of Poisson noise on the pixel counts plus other sources of noise that are Gaussian (e.g., read noise). For the faint galaxies that dominate weak lensing measurements, the noise is largely uncorrelated between pixels such as the noise can commonly be modeled as stationary on the scale of galaxy images, at least for the faint galaxies that dominate weak lensing measurements (Gurvich & Mandelbaum, 2016). This means that the dispersion of the sum over the pixel values scales as the root square of the number of pixels multiplied by the dispersion computed from single pixel values. However, some types of image processing, e.g. convolution and deconvolution can induce noise correlations between neighbouring pixels. Thus, if the noise estimate is computed from an individual pixel, the correlations are neglected and the noise estimate could be smaller. Following Hartlap et al. (2009), we will estimate the effective influence of the noise correlations before applying the extra Gaussian noise to the images. This allow us to calculate the value, if any, by which we over-estimate the  $S/N$  and account for it in our procedure.

Remaining issues of significant concern include biases resulting from shear estimation for low-resolution and/or low Signal-to-Noise Ratio ( $< 10$ ) galaxies, object detection and selection, color gradient, and deblending. We expect future work to extend this method to deal with the complexities inherent in real data.

## 6.2. Spectroscopic analysis of Ultra-Compact Massive Galaxies within the Kilo Degree Survey

Scanning a wide portion of the night sky, in combination with the multi-band photometric coverage, high image quality, excellent spatial resolution and seeing, the Kilo Degree Survey (KiDS) provides a unique opportunity to study the properties of ultra-compact massive galaxies (UCMGs). In particular, the oldest UCMGs or relics play a key role in our understanding of galaxy formation and evolution, sitting in

the transition region between the two different phases of the so-called ‘two-phase’ formation scenario. They are believed to have missed the channels of galaxy size growth and are therefore unique objects to shed light on the mechanism that regulates the mass accretion history of the most massive galaxies in our Universe. These systems are unfortunately very rare and their number density is sensitive to the different assumptions and ingredients used to calculate it (e.g. Naab et al. 2009a; Oser et al. 2010b; Quilis & Trujillo 2013; Zolotov et al. 2015; Wellons et al. 2016; Pulsoni et al. 2021).

In Chapter 5, following the selection criteria on the mass and the size from Quilis & Trujillo (2013), we presented our analysis of 33 new selected UCMGs candidates at redshift  $0.15 \lesssim z \lesssim 0.5$ . Thanks to our multi-site and multi-telescope spectroscopic observational campaign, we confirmed many candidates. In fact, we assemble a sample of 57 UCMGs, allowing us to build the largest spectroscopic sample (at the time of writing) of spectroscopically confirmed UCMGs at intermediate redshifts. The spectra showed clear spectral absorption features typical of an old stellar population, such as Ca-H, Ca-K, Balmer lines ( $H_\delta$ ,  $H_\gamma$  and  $H_\beta$ ), Mgb, and Fe lines.

Using the Optimised Modelling of Early-type Galaxy Aperture Kinematics pipeline (OMEGA-K), we measured the spectroscopic redshifts. To these ones we added the redshifts measured from observations at the TNG and the NTT presented in T18. We found that most of the objects are in good agreement with the 1-to-1 relation with a parent sample of galaxies with SDSS and GAMA spectroscopy. With the spectroscopic redshifts, we re-calculated the masses and the effective radii and we confirmed 19 out of 33 as UCMGs. This comparison allowed us to estimate all the sources of systematics in the search of UCMGs in a photometric survey such as KiDS. This survey, although provides precise photometric redshifts, is still unavoidably prone to systematics induced by small differences between the true spectroscopic redshift and the more uncertain photometric value. We found a success rate of 58% to confirm a candidate as an UCMGs, in good agreement with the one reported in T18. In addition, using the newest mass setup, we have confirmed 18 out of 27 UCMGs from T18, corresponding to a success rate of 67%. Thus, in total, we confirmed as UCMGs 37 out of 61 candidates, implying a success rate of 60%. With a tolerance up to  $3\sigma$  on the effective radii and stellar masses inferred from the spectroscopic redshifts, the number of confirmed UCMGs rises to 57 out of 61 UCMGs candidates, which means a success rate of  $\sim 93\%$ .

Since an inaccurate redshift induces a change in both the size and stellar mass, our large sample provided a unique chance to quantify the systematics. For this purpose, we quantified the effects of contamination and incompleteness due to the redshift errors via the contamination factor,  $\mathcal{C}_F$ , and the incompleteness factor,  $\mathcal{I}_F$ , and used them to correct the final number counts of UCMGs. We found that the true number counts for UCMGs at  $z < 0.5$  is  $\sim 15$  per cent higher than the values found

in a photometrically selected sample, corroborating the fact that a spectroscopic campaign is of paramount importance. We also investigated the UCMG number counts across the last 5 Gyr, finding a steep decrease with cosmic time of a factor 9 in less than 3 Gyr. Besides the dependency of the number density on the criteria used to select these objects, the decrease should suggest a size-dependent evolution of the number count of ETGs, with the smallest and most massive galaxies progressively reducing their number (e.g. Carollo et al. 2013; Cassata et al. 2013).

We finally presented a preliminary distribution of the 37 confirmed UCMGs in the  $M_\star - \sigma$  plane. Despite the large uncertainties on the velocity dispersion measurements, due to the low signal-to-noise ratio of the spectra, we found tentative evidence suggesting that the UCMGs have larger values compared to regular ETGs of the same mass. This result is in agreement with what is expected from the evolution of massive and compact galaxies and what we found with high resolution spectroscopy from X-Shooter spectrograph (XSH) at the VLT in Spiniello et al. (2021).

### Future directions

The present analysis improves, in terms of numbers, covered area, and analysis the one performed in Tortora et al. (2018). Beyond these improvements, we recently propose with an observational program to assess whether a correlation exists between UCMGs star formation history (SFH), their structural and photometric parameters, and the local environment they inhabit, as already hinted by the literature (Tortora et al., 2020). Disentangling the role of internal processes and the environment (including the role of mergers) is crucial for understanding the formation and evolution of galaxies. Although significant work has gone from both an observational and a theoretical point of view, there is still a poor understanding of the role of the environment in shaping properties of UCMGs and relics, and of the specific physical processes through which the environment operates leaving these objects so compact and dense, leading to contrasting results (Stringer et al. 2015 vs. Tortora et al. 2020). Furthermore, within the INSPIRE Project (“INvestigating Stellar Population In RElics”, PI: C.Spiniello) (Spiniello et al. 2020, 2021), we have found hints regarding a “degree of relicness”, in the sense that some of the morphological and stellar characteristics of the relics might be more or less extreme in different environments.

Aiming to understand if the relic and UCMG structural properties and the degree of relicness could be correlated to the local environment in which these galaxies live, we have started the ‘Characterizing the environment of Relic and Ultra-Compact Massive galaxies’ (CHARTER) pilot program (PIs: D. Scognamiglio & C. Tortora,

A44TAC\_11). We have selected four UCMGs from the INSPIRE DR1, visible at the TNG, with different SFHs and environment (fields vs. clusters), although similar integrated ages, masses, sizes, structural parameters (axis ratio and Sérsic index, computed from the *gri*-band KiDS images). Our goal is to measure redshifts for a large number of galaxies in the proximity of four UCMGs from the INSPIRE sample with different degree of relicness. A definitive characterization of the environment for these objects is however still missing, since the cluster selection is based on photometric redshifts, and can potentially miss low-mass clusters or groups. Thus, the spectroscopic redshifts planned with this program ( $\sim 12$  hrs), are crucial to confirm the presence of groups or clusters around these galaxies.

Looking forward, there is much to be learned about galaxy formation and evolution in the local as well as in the distant Universe in the coming years, both from an observational and theoretical perspective. The advent of new and powerful telescopes, such as the Nancy Grace Roman Space Telescope (Spergel et al., 2015b), Vera C. Rubin Observatory (Ivezić et al., 2019) and *Euclid* (Laureijs et al., 2011b) will give us an unprecedented deeper look at the galaxies, covering wide sky areas at different wavelengths, delivering data at an unprecedented precision and, providing additional observational evidence to inspire theoretical work. Similarly, advances in numerical techniques and computational power promise to give us additional flexibility to study problems which were previously inaccessible. There are many questions still remaining, but with these instruments and, especially their synergy, we will be able to discover many more aspects of how the galaxies form and evolve across the cosmic time.

# Appendix



## APPENDIX A

---

### UCMGs in KiDS Paper

---

The paper *Scognamiglio et al. 2020, The Astrophysical Journal (2020), 893, 4* is reproduced below in its original form with permission by IOP Publishing for the American Astronomical Society.



# Building the Largest Spectroscopic Sample of Ultracompact Massive Galaxies with the Kilo Degree Survey

Diana Scognamiglio<sup>1,2</sup>, Crescenzo Tortora<sup>3</sup>, Marilena Spavone<sup>1</sup>, Chiara Spiniello<sup>1,4</sup>, Nicola R. Napolitano<sup>1,5</sup>, Giuseppe D’Ago<sup>6</sup>, Francesco La Barbera<sup>1</sup>, Fedor Getman<sup>1</sup>, Nivya Roy<sup>5</sup>, Maria Angela Raj<sup>1</sup>, Mario Radovich<sup>7</sup>, Massimo Brescia<sup>1</sup>, Stefano Cavuoti<sup>1,8</sup>, Léon V. E. Koopmans<sup>9</sup>, Konrad H. Kuijken<sup>10</sup>, Giuseppe Longo<sup>8</sup>, and Carlo E. Petrillo<sup>9</sup>

<sup>1</sup> INAF—Osservatorio Astronomico di Capodimonte, Salita Moiarillo 16, I-80131—Napoli, Italy; [napolitano@mail.sysu.edu.cn](mailto:napolitano@mail.sysu.edu.cn), [dianasco@astro.uni-bonn.de](mailto:dianasco@astro.uni-bonn.de)

<sup>2</sup> Argelander-Institut für Astronomie, Auf dem Hügel 71, D-53121—Bonn, Germany

<sup>3</sup> INAF—Osservatorio Astronomico di Arcetri, L.go E. Fermi 5, I-50125—Firenze, Italy

<sup>4</sup> European Southern Observatory, Karl-Schwarzschild-Str. 2, D-85748—Garching, Germany

<sup>5</sup> School of Physics and Astronomy, Sun Yat-sen University Zhuhai Campus, Daxue Road 2, 519082—Tangjia, Zhuhai, Guangdong, People’s Republic of China

<sup>6</sup> Instituto de Astrofísica Pontificia Universidad Católica de Chile, Avenida Vicuña Mackenna, 4860—Santiago, Chile

<sup>7</sup> INAF—Osservatorio Astronomico di Padova, Vicolo Osservatorio 5, I-35122—Padova, Italy

<sup>8</sup> Dipartimento di Scienze Fisiche, Università di Napoli Federico II, Compl. Univ. Monte S. Angelo, I-80126—Napoli, Italy

<sup>9</sup> Kapteyn Astronomical Institute, University of Groningen, P.O. Box 800, 9700 AV—Groningen, The Netherlands

<sup>10</sup> Leiden Observatory, Leiden University, P.O. Box 9513, 2300 RA—Leiden, The Netherlands

Received 2019 July 28; revised 2020 February 29; accepted 2020 March 5; published 2020 April 8

## Abstract

Ultracompact massive galaxies (UCMGs), i.e., galaxies with stellar masses  $M_* > 8 \times 10^{10} M_\odot$  and effective radii  $R_e < 1.5$  kpc, are very rare systems, in particular at low and intermediate redshifts. Their origin as well as their number density across cosmic time are still under scrutiny, especially because of the paucity of spectroscopically confirmed samples. We have started a systematic census of UCMG candidates within the ESO Kilo Degree Survey, together with a large spectroscopic follow-up campaign to build the largest possible sample of confirmed UCMGs. This is the third paper of the series and the second based on the spectroscopic follow-up program. Here, we present photometrical and structural parameters of 33 new candidates at redshifts  $0.15 \lesssim z \lesssim 0.5$  and confirm 19 of them as UCMGs, based on their nominal spectroscopically inferred  $M_*$  and  $R_e$ . This corresponds to a success rate of  $\sim 58\%$ , nicely consistent with our previous findings. The addition of these 19 newly confirmed objects allows us to fully assess the systematics on the system selection—and to finally reduce the number density uncertainties. Moreover, putting together the results from our current and past observational campaigns and some literature data, we build the largest sample of UCMGs ever collected, comprising 92 spectroscopically confirmed objects at  $0.1 \lesssim z \lesssim 0.5$ . This number raises to 116, allowing for a  $3\sigma$  tolerance on the  $M_*$  and  $R_e$  thresholds for the UCMG definition. For all these galaxies, we have estimated the velocity dispersion values at the effective radii, which have been used to derive a preliminary mass–velocity dispersion correlation.

*Unified Astronomy Thesaurus concepts:* [Early-type galaxies \(429\)](#); [Galaxy formation \(595\)](#); [Galaxy mergers \(608\)](#); [Spectroscopy \(1558\)](#); [Galaxy counts \(588\)](#); [Galaxy kinematics \(602\)](#)

## 1. Introduction

The discovery that massive, quiescent galaxies at redshift  $z > 2$  are extremely compact with respect to their local counterparts (Daddi et al. 2005; Trujillo et al. 2006; Damjanov et al. 2009, 2011; van Dokkum et al. 2010) has opened a new line of investigation within the context of galaxy formation and evolution. In particular, the strong galaxy size growth (Daddi et al. 2005; Trujillo et al. 2006) needed to account for the difference in compactness from high- to low- $z$  finds its best explanation in the so-called two-phase formation model (Oser et al. 2010). First of all, massive and very compact gas-rich disk objects are created due to dissipative inflows of gas. These so-called “blue nuggets” form stars *in situ* at high rate, and this causes a gradual stellar and halo mass growth (Dekel & Burkert 2014). Subsequently, the star formation in the central region quenches and the blue nuggets quickly (and passively) evolve into compact “red nuggets.”

In many cases, the masses of these high- $z$  red nuggets are similar to those of local giant elliptical galaxies, which indicates that almost all the mass is assembled during this first formation phase. However, their sizes are only about a fifth of the size of local ellipticals of similar mass (Werner et al. 2018). Thus, during the second phase of this scenario, at lower redshifts, red nuggets undergo dry mergers with lower-mass galaxies, growing in size (but only slightly increasing their masses) and becoming, over billions of years, present-day ETGs.

Nevertheless, given the stochastic nature of mergers, a small fraction of the red nuggets slips through the cosmic time untouched and without accreting any stars from satellites and mergers: the so-called “relics” (Ferré-Mateu et al. 2017). These galaxies have assembled early on in time and have somehow completely missed the size growth. They are therefore supposedly made of only an *in situ* stellar population, and as such they provide a unique opportunity to track the formation of this specific galaxy stellar component—which is mixed with the accreted one in normal massive ETGs.

Indeed, very massive, extremely compact systems have been already found at intermediate to low redshifts, also including the local universe (Trujillo et al. 2009, 2014; Taylor et al. 2010;



Original content from this work may be used under the terms of the [Creative Commons Attribution 4.0 licence](#). Any further distribution of this work must maintain attribution to the author(s) and the title of the work, journal citation and DOI.



Valentinuzzi et al. 2010; Shih & Stockton 2011; Läscher et al. 2013; Poggianti et al. 2013a, 2013b; Hsu et al. 2014; Stockton et al. 2014; Damjanov et al. 2015a, 2015b; Ferré-Mateu et al. 2015; Saulder et al. 2015; Stringer et al. 2015; Yıldırım et al. 2015; Wellons et al. 2016; Gargiulo et al. 2016; Tortora et al. 2016, 2018b; Charbonnier et al. 2017; Beasley et al. 2018; Buitrago et al. 2018). Ultracompact Massive Galaxies (UCMGs hereafter), defined here as objects with stellar mass  $M_* > 8 \times 10^{10} M_\odot$  and effective radius  $R_e < 1.5$  kpc (although sometimes other stellar mass and effective radius ranges are adopted; see Section 2) are the best relic candidates.

The precise abundance of relics—and even more generally of UCMGs—without any age restriction, at low redshifts, is an open issue. In fact, at  $z \lesssim 0.5$ , a strong disagreement exists between simulations and observations—as well as among observations themselves—on the number density of UCMGs and its redshift evolution. From a theoretical point of view, simulations predict that the fraction of objects that survive without undergoing any significant transformation since  $z \sim 2$  is about 1–10% (Hopkins et al. 2009; Quilis & Trujillo 2013), and at the lowest redshifts (i.e.,  $z \lesssim 0.2$ ), they predict densities of relics of  $10^{-7}$ – $10^{-5}$   $\text{Mpc}^{-3}$ . This is in agreement with the lower limit given by NGC 1277, the first discovered local ( $z \sim 0.02$ ) compact galaxy with old stellar population, which is the first prototype of a local “relic” of high- $z$  nuggets (Trujillo et al. 2014), and the most updated estimate of  $6 \times 10^{-7}$   $\text{Mpc}^{-3}$  set by Ferré-Mateu et al. (2017), who report the discovery of two new confirmed, local “relics.” In the nearby universe, large sky surveys as the Sloan Digital Sky Survey (SDSS<sup>11</sup>) show a sharp decline in compact galaxy number density of more than three orders of magnitude below the high-redshift values (Trujillo et al. 2009; Taylor et al. 2010). In contrast, Poggianti et al. (2013a, 2013b) suggest that the abundance of low-redshift compact systems might be even comparable with the number density at high redshift. Moreover, data from the WINGS survey of nearby clusters (Fasano et al. 2006; Valentinuzzi et al. 2010) estimate, at  $z \sim 0$ , a number density of two orders of magnitude above the estimates based on the SDSS data set.

Because the situation in the local universe is very complex and different studies report contrasting results, it is crucial to increase the UCMG number statistics in the range  $0.1 \lesssim z \lesssim 0.5$ , where these systems should be more common. In recent years, different works have contributed to the census of UCMGs in wide-field surveys at these redshifts (Tortora et al. 2016, 2018b; Charbonnier et al. 2017; Buitrago et al. 2018). In particular, within the Kilo Degree Survey (KiDS; see Section 2) collaboration, we have undertaken a systematic search for UCMGs in the intermediate-redshift range with the aim of building a large spectroscopically confirmed sample. In the first paper of the series (Tortora et al. 2016, hereafter T16), we collected a sample of  $\lesssim 100$  candidates in the first  $\sim 156$   $\text{deg}^2$  of KiDS (corresponding to an effective area of  $\sim 107$   $\text{deg}^2$ , after masking). In the second paper (Tortora et al. 2018b, hereafter T18), we updated the analysis and extended the study to the third KiDS Data Release (KiDS-DR3). We have collected a sample of  $\sim 1000$  candidates, building the largest sample of UCMG candidates at  $z < 0.5$  assembled to date over the largest sky area (333  $\text{deg}^2$ ).

It is worth noticing that nearly all of the previously published findings on these peculiar objects are based on photometric

samples. However, after identification of the candidates, spectroscopic validation is necessary to obtain precise spectroscopic redshifts and confirm the compactness of the systems. Thus, in T18 we presented the first such spectroscopic validation, with data obtained at Telescopio Nazionale Galileo (TNG) and at the New Technology Telescope (NTT).

In this third paper of the series, we therefore continue the work started in T18 to spectroscopically validate UCMGs and derive their “true”<sup>12</sup> number densities at intermediate redshifts. In particular, we present here spectroscopic observations for 33 new KiDS UCMG candidates and add to these all the spectroscopic confirmed UCMGs publicly available in the literature to update the UCMG number density distribution, already presented in T18, at redshift  $0.15 < z < 0.5$ . Finally, we also obtain and present here the velocity dispersion measurements ( $\sigma$ ) for the new 33 UCMGs and for the 28 UCMGs from T18. Finally, we present a preliminary correlation between stellar mass and velocity dispersion of these rare objects, with the aim of starting to fully characterize the properties of these systems.

This paper represents a further step forward to our final goal, which is to unequivocally prove that a fraction of the red and dead nuggets, which formed at  $z > 2$ , evolved undisturbed and passively into local “relics.” In particular, to be classified as such, the objects have to: 1) be spectroscopically validated UCMGs, and 2) have very old stellar populations (e.g., assuming a formation redshift  $z_{\text{phot}} \gtrsim 2$ , the stellar population age needs to be  $t \gtrsim 10$  Gyr). Because we do not derive stellar ages, this paper makes significant progress only on the first part of the full story, as not all the confirmed UCMGs satisfy a stringent criterion on its stellar age. We are confident that most of our confirmed UCMGs will likely be old, as we showed in T18 that most of the candidates presented very red optical and near-infrared colors. Moreover, in the spectra we present here (see Section 3), we find spectral features typical of passive stellar population. However, only with higher resolution and high signal-to-noise (S/N) spectra, which would allow us to perform an in-depth stellar population analysis, will it be possible to really disentangle relics from younger UCMGs. The detailed stellar population analysis is also particularly important, as a fraction of our UCMGs also shows some hint of recent star formation or of younger stellar population. This has been already seen in other samples (Trujillo et al. 2009; Ferré-Mateu et al. 2012; Poggianti et al. 2013b; Damjanov et al. 2015a, 2015b; Buitrago et al. 2018), but it is not necessarily in contrast with the predictions from galaxy assembly simulations (see, e.g., Wellons et al. 2015). In fact, they find that ultracompact systems host accretion events, but still keep their bulk of stellar population old and the compact structure almost unaltered. Hence, higher-quality spectroscopical data will be mandatory to perform a multipopulation analysis and possibly confirm also this scenario.

The layout of the paper is as follows. In Section 2, we briefly describe the KiDS sample of high S/N galaxies, the subsample of our photometrically selected UCMGs, the objects we followed up spectroscopically, and the impact of the selection criteria we use. In Section 3, we give an overview on observations and data reduction, and we discuss the spectroscopic redshift and velocity dispersion calculation procedures. In Section 4, we discuss the main results, i.e., the number density as a function of redshift and the impact of systematics

<sup>11</sup> <https://www.sdss.org/>

<sup>12</sup> By the word “true,” we mean here the number density obtained with a spectroscopically confirmed sample.

on these number densities. We also derive a tentative relation between the stellar mass and the velocity dispersion at the effective radius of our sample of UCMGs, compared with a sample of normal-sized elliptical galaxies at similar masses and redshifts. Finally, in Section 5, we summarize our findings and discuss future perspectives. In the Appendix, we report the final validated UCMGs catalog, where some redshifts come from our spectroscopic program and others from the literature. For all galaxies, we give structural parameters in the  $g$ ,  $r$ ,  $i$ , bands and the  $u$ ,  $g$ ,  $r$ ,  $i$ , aperture photometry from KiDS.

Throughout the paper, we assume  $H_0 = 70 \text{ km s}^{-1} \text{ Mpc}^{-1}$ ,  $\Omega_m = 0.3$ , and  $\Omega_\Lambda = 0.7$  (Komatsu et al. 2011).

## 2. Sample Definition

KiDS is one of the ESO public wide-area surveys (1350 deg<sup>2</sup> in total) being carried out with the VLT Survey Telescope (VST; Capaccioli & Schipani 2011). It provides imaging data with unique image quality (pixel scale of 0.21/pixel and a median  $r$ -band seeing of 0''65) and baseline ( $ugri$  in optical +  $ZYJHK$  if combined with VIKING (Edge & Sutherland 2014; Wright et al. 2019)). These features make the data very suitable for measuring structural parameters of galaxies, including very compact systems, up to  $z \sim 0.5$  (Roy et al. 2018; T16; T18). Both image quality and baseline are very important for the selection of UCMGs, as they allow us to mitigate systematics that might have plagued previous analyses from the ground.

As baseline sample of our search, we use the data included in the third Data Release of KiDS (KiDS-DR3) presented in de Jong et al. (2017), consisting of 440 survey tiles ( $\approx 333 \text{ deg}^2$ , after masking). The galaxy data sample is described next in Section 2.1.

### 2.1. Galaxy Data Sample

From the KiDS multiband source catalog (de Jong et al. 2015, 2017), we built a catalog of  $\sim 5$  million galaxies (La Barbera et al. 2008) within KiDS-DR3, using SExtractor (Bertin & Arnouts 1996). Since we mainly follow the same selection procedure of T16 and T18, we refer the interested reader to those papers for more general details. Here, we only list relevant physical quantities for the galaxies in the catalog, explaining how we obtain them and highlighting the novelty of the setup we use in the stellar mass calculation:

1. *Integrated optical photometry.* We use aperture magnitudes  $\text{MAGAP}_6$ , measured within circular apertures of 6'' diameter, Kron-like  $\text{MAG\_AUTO}$  as the total magnitude, and Gaussian Aperture and PSF (GAaP) magnitudes,  $\text{MAG\_GAaP}$  (de Jong et al. 2017), in each of the four optical bands ( $ugri$ ).
2. *Structural parameters.* Surface photometry is performed using the 2DPHOT environment (La Barbera et al. 2008), which fits galaxy images with a 2D Sérsic model. The model also includes a constant background and assumes elliptical isophotes. In order to take the galaxies best-fitted and remove those systems with a clear sign of spiral arms, we put a threshold on the goodness of the fit, only selecting  $\chi^2 < 1.5$ . We also calculate a modified version,  $\chi'^2$ , which includes only the central image pixels, which are generally more often affected by these substructures. The 2DPHOT model fitting provides the following parameters: average surface brightness  $\mu_e$ , major-axis effective radius  $\Theta_{e,\text{maj}}$ , Sérsic index  $n$ , total magnitude  $m_S$ ,

axial ratio  $q$ , and position angle. In this analysis, we use the circularized effective radius  $\Theta_e$ , defined as  $\Theta_e = \Theta_{e,\text{maj}} \sqrt{q}$ . Effective radius is then converted to the physical scale value  $R_e$  using the measured (photometric and/or spectroscopic) redshift. Only galaxies with  $r$ -band  $(S/N)_r \equiv 1/\text{MAGERR\_AUTO}_r > 50$ , where  $\text{MAGERR\_AUTO}_r$  is the error on the  $r$ -band  $\text{MAG\_AUTO}$ , are kept for the next analysis (La Barbera et al. 2008, 2010; Roy et al. 2018; T16; T18).

3. *Photometric redshifts.* Redshifts are determined with the Multi Layer Perceptron with Quasi Newton Algorithm (MLPQNA) method (Brescia et al. 2013, 2014; Cavuoti et al. 2015a), and presented in Cavuoti et al. (2015b, 2017), which we refer to for all details.
4. *Spectroscopic redshifts.* We cross-match our KiDS catalog with overlapping spectroscopic surveys to obtain spectroscopic redshifts for the objects in common, i.e., the KiDS\_SPEC sample. We use redshifts from the Sloan Digital Sky Survey Data Release 9 (SDSS-DR9; Ahn et al. 2012, 2014), Galaxy And Mass Assembly Data Release 2 (GAMA-DR2; Driver et al. 2011), and 2dFLenS (Blake et al. 2016).
5. *Stellar masses.* We run lephare (Arnouts et al. 1999; Ilbert et al. 2006) to estimate stellar masses. This software performs a simple  $\chi^2$  fitting between the stellar population synthesis (SPS) theoretical models and the data. In order to minimize the degeneracy between colors and stellar population parameters, we fix the redshift, either using the  $z_{\text{phot}}$  or  $z_{\text{spec}}$ , depending on the availability and the sample under exam. It is evident that, when a  $z_{\text{spec}}$  is obtained for a UCMG candidate, the stellar mass needs to be re-estimated because the “true” redshift might produce a different mass that needs to be checked against the criteria to confirm the UCMG nature (see next section). Since the UCMG candidates sample analyzed in this paper has been collected using a slightly different spectral library with respect to the sample presented in T18, we use a partially different setup to estimate stellar masses. As in T18, we fit multiwavelength photometry of the galaxies in the sample with single-burst models from Bruzual & Charlot (2003, hereafter BC03). However, here we further constrain the parameter space, forcing metallicities and ages to vary in the range  $0.2 \leq Z/Z_\odot \leq 2.5$  and  $3 \leq t \leq t_{\text{max}}$  Gyr, respectively. The maximum age,  $t_{\text{max}}$ , is set by the age of the universe at the redshift of the galaxy, with a maximum value of 13 Gyr at  $z = 0$ . The age cutoff of 3 Gyr is meant to minimize the probability of underestimating the stellar mass by obtaining an age that is too young, following Maraston et al. (2013). Then, as in T18, we adopt a Chabrier (2001) IMF and the observed  $ugri$  magnitudes  $\text{MAGAP}_6$  (and related  $1\sigma$  uncertainties  $\delta u$ ,  $\delta g$ ,  $\delta r$ , and  $\delta i$ ), which are corrected for Galactic extinction using the map in Schlafly & Finkbeiner (2011). In order to correct the  $M_*$  outcomes of lephare for missing flux, we use the total magnitudes derived from the Sérsic fitting and the formula

$$\log_{10} M_* = \log_{10} M_*^{\text{lephare}} + 0.4 \times (\text{MAGAP}_6 - m_S), \quad (1)$$

where  $\log_{10} M_*^{\text{lephare}}$  is the output of lephare. We consider calibration errors on the photometric zero-point  $\delta_{zp} \equiv (\delta u_{zp}, \delta g_{zp}, \delta r_{zp}, \delta i_{zp}) = (0.075, 0.074, 0.029, 0.055)$ ,

quadratically added to the SExtractor magnitude errors (see T18).

6. *Galaxy classification.* Using lephare, we also fit the observed magnitudes with the set of 66 empirical spectral templates used in Ilbert et al. (2006), in order to determine a qualitative galaxy classification. The set is based on different templates resembling spectra of “Elliptical,” “Spiral,” and “Starburst” galaxies.

We use the above data set, which we name KiDS\_FULL, to collect a complete set of photometrically selected UCMGs, using criteria as described in the next section.

Moreover, in order to check what galaxies already have literature spectroscopy, we cross-match the KiDS\_FULL with publicly available spectroscopic samples and define the so-called KiDS\_SPEC sample, which comprises all galaxies from our complete photometric sample with known spectroscopic redshifts.

## 2.2. UCMGs Selection and Our Sample

To select the UCMG candidates, we use the same criteria reported in T16 and T18:

1. *Massiveness:* A Chabrier-IMF-based stellar mass of  $M_* > 8 \times 10^{10} M_\odot$  (Trujillo et al. 2009; T16, T18);
2. *Compactness:* A circularized effective radius  $R_e < 1.5$  kpc (T18);
3. *Best-fit structural parameters:* A reduced  $\chi^2 < 1.5$  in  $g$ -,  $r$ -, and  $i$ -filters (La Barbera et al. 2010), and further criteria to control the quality of the fit, as  $\Theta_e > 0''.05$ ,  $q > 0.1$ , and  $n > 0.5$ ;
4. *Star/Galaxy separation:* A discrimination between stars and galaxies using the  $g-J$  versus  $J-Ks$  plane to minimize the overlap of sources with the typical stellar locus (see, e.g., Figure 1 in T16).

Further details about the above criteria to select UCMGs from both KiDS\_FULL and KiDS\_SPEC can be found in T16 and T18. In the following, we refer to the *photometrically selected* and the *spectroscopically selected* samples as the ones where  $M_*$  and  $R_e$  are calculated using  $z_{\text{phot}}$  or  $z_{\text{spec}}$ , respectively.<sup>13</sup>

After applying all the requirements, we end up with the following samples at  $z < 0.5$ :

1. UCMG\_FULL: a photometrically selected sample of 1221 UCMG candidates<sup>14</sup> (1256 before the color-color cut) extracted from KiDS\_FULL;
2. UCMG\_SPEC: a spectroscopically selected sample of 55 UCMGs, selected from the KiDS\_SPEC sample, for which stellar masses and radii have been computed using the spectroscopic redshifts;
3. UCMG\_PHOT\_SPEC: a sample of 50 photometrically selected UCMG candidates that have spectroscopic redshift available from literature. Practically speaking, these

galaxies have been extracted from KiDS\_SPEC, but they were determined to be UCMG on the basis of their  $z_{\text{phot}}$ .

In the UCMG\_FULL sample, which provides the most statistically significant characterization of our UCMG candidates, the objects are brighter than  $r \sim 21$ . Most of them are located at  $z_{\text{phot}} > 0.3$ , with a median redshift of  $z_{\text{phot}} = 0.41$ . Median values of 20.4 and 11 dex are found for the extinction corrected  $r$ -band MAG\_AUTO and  $\log_{10}(M_*/M_\odot)$ . More than 97 percent of the UCMG\_FULL candidates have KiDS photometry consistent with “Elliptical” templates in Ilbert et al. (2006), and they have very red colors in the optical-NIR color-color plane. The  $R_e < 1.5$  kpc constraint corresponds to  $\Theta_e \lesssim 0''.4$ , and the medians for these parameters are  $R_e = 1.22$  kpc and  $\Theta_e = 0''.23$ , respectively. The range of the values for axis ratio and Sérsic index is wide, but their distributions are peaked around values of  $q \sim 0.4$  and  $n \sim 4$ , with median values of 0.47 and 4.6, respectively.

## 2.3. The Impact of Selection Criteria

Following the previous papers of this series (T16 and T18), we adopt rather stringent criteria on the sizes and masses to select only the most extreme (and rare) UCMGs. However, there is a large variety of definitions used in other literature studies. Until there is a consensus, the comparison among different analyses will be prone to a “definition bias.” Here in this section, we evaluate the impact of different definitions on our UCMG\_FULL sample (see also a detailed discussion in T18). For instance, keeping the threshold on the stellar mass unchanged and releasing the constraints on the size, such as  $R_e < 2$  kpc and  $< 3$  kpc, the respective numbers of candidates (before color-color cut) would increase to 3430 and 12,472. If instead the mass threshold were decreased from  $\log_{10}(M_*/M_\odot) = 10.9$  to 10.7, the number of selected galaxies within UCMG\_FULL would not change by more than 3%, i.e., the size criterion is the one with greater impact upon the UCMG definition. Besides the threshold in size and mass, another important assumption that might significantly impact our selection is the shape of the stellar Initial Mass Function (IMF). Here, we assume a universal Chabrier IMF for all the galaxies, despite recent claims for a bottom-heavier IMF in more massive ETGs (e.g., Cappellari et al. 2012; Conroy & van Dokkum 2012; Spiniello et al. 2012, 2014, 2015; La Barbera et al. 2013; Tortora et al. 2013). This choice has been made to compare our results with other results published in the literature, all assuming a Chabrier IMF. If a Salpeter IMF were to be used instead, more coherently with predictions for compact and massive systems (Martín-Navarro et al. 2015; Ferré-Mateu et al. 2017), then keeping the massiveness and compactness criteria unchanged, we would retrieve 1291 UCMGs instead of 1256. Thus, the IMF slope also has a negligible impact on our selection.

## 3. Spectroscopic Observations

Having obtained a large sample of UCMG candidates, the natural next step is their spectroscopic confirmation. In other terms, a spectroscopic confirmation of their photometric redshifts is crucial to confirm them as UCMGs, because both compactness and massiveness are originally based on the  $z_{\text{phot}}$  associated to the photometric sample. In this work, we present the spectroscopic follow-up of 33 objects. Twenty-nine candidates are extracted from UCMG\_FULL, while the remaining four come from the data

<sup>13</sup> When the spectroscopic redshift becomes available for a given UCMG candidate, one has to recompute both the  $R_e$  in kpc (which obviously scales with the true redshift) and the stellar mass (see Section 2.1) to check that the criteria of compactness and massiveness hold.

<sup>14</sup> In T18, we collected 995 photometrically selected candidates (1000 before the color-color cut), which is different from the number of 1221 found here. The difference between these numbers is related to the different sets of masses adopted in T18 and in the present paper. We will discuss the impact of the mass assumption later in the paper, showing the effect on the number density evolution.

**Table 1**  
Integrated Photometry for the 33 UCMG Candidates Observed within Our Spectroscopic Program

ID	Name	MAG_AUTO_r	$u_6''$	$g_6''$	$r_6''$	$i_6''$	$z_{\text{phot}}$
Observation date: 2017 March		Instrument: INT/IDS					
1	KIDS J085700.29-010844.55	19.21	$22.70 \pm 0.21$	$20.74 \pm 0.01$	$19.22 \pm 0.003$	$18.71 \pm 0.01$	0.28
2	KIDS J111108.43+003207.00	19.05	$22.49 \pm 0.14$	$20.46 \pm 0.01$	$19.04 \pm 0.003$	$18.61 \pm 0.006$	0.26
3	KIDS J111447.86+003903.71	19.00	$22.35 \pm 0.12$	$20.47 \pm 0.01$	$19.03 \pm 0.003$	$18.57 \pm 0.009$	0.26
4	KIDS J111504.01+005101.16	19.21	$20.43 \pm 0.02$	$19.92 \pm 0.006$	$19.24 \pm 0.003$	$19.01 \pm 0.014$	0.45
5	KIDS J111750.31+003647.35	19.13	$22.80 \pm 0.19$	$20.74 \pm 0.01$	$19.12 \pm 0.003$	$18.69 \pm 0.01$	0.37
6	KIDS J122009.53-024141.88	18.69	$21.93 \pm 0.1$	$20.02 \pm 0.007$	$18.71 \pm 0.002$	$18.19 \pm 0.006$	0.22
7	KIDS J122639.96-011138.08	18.59	$22.15 \pm 0.11$	$20.06 \pm 0.008$	$18.63 \pm 0.003$	$18.21 \pm 0.008$	0.23
8	KIDS J122815.38-015356.06	18.84	$22.17 \pm 0.1$	$20.26 \pm 0.008$	$18.84 \pm 0.003$	$18.37 \pm 0.008$	0.24
9	KIDS J140127.77+020509.13	19.04	$21.47 \pm 0.06$	$20.23 \pm 0.007$	$19.01 \pm 0.003$	$18.65 \pm 0.007$	0.34
10	KIDS J141120.06+023342.62	18.85	$22.72 \pm 0.17$	$20.47 \pm 0.01$	$18.83 \pm 0.003$	$18.39 \pm 0.007$	0.32
11	KIDS J145700.42+024502.06	18.62	$22.17 \pm 0.13$	$19.95 \pm 0.008$	$18.67 \pm 0.002$	$18.23 \pm 0.007$	0.24
12	KIDS J150309.55+001318.10	18.99	$22.59 \pm 0.19$	$20.47 \pm 0.01$	$19.02 \pm 0.003$	$18.67 \pm 0.007$	0.28
13	KIDS J152844.81-000912.86	18.56	$22.91 \pm 0.25$	$19.98 \pm 0.01$	$18.59 \pm 0.002$	$18.20 \pm 0.005$	0.23
Observation date: 2017 March		Instrument: TNG/DOLORES					
14	KIDS J084239.97+005923.71	19.63	$22.95 \pm 1.76$	$21.14 \pm 0.12$	$19.58 \pm 0.04$	$19.02 \pm 0.08$	0.35
15	KIDS J090412.45-001819.75	19.11	$22.51 \pm 0.95$	$20.58 \pm 0.07$	$19.13 \pm 0.02$	$18.66 \pm 0.02$	0.27
16	KIDS J091704.84-012319.65	19.21	$22.87 \pm 1.03$	$20.84 \pm 0.08$	$19.20 \pm 0.02$	$18.65 \pm 0.02$	0.33
17	KIDS J104051.66+005626.73	19.52	$23.27 \pm 0.29$	$20.97 \pm 0.02$	$19.54 \pm 0.005$	$18.52 \pm 0.01$	0.33
18	KIDS J114800.92+023753.02	19.41	$23.13 \pm 0.33$	$20.54 \pm 0.01$	$19.41 \pm 0.005$	$18.61 \pm 0.009$	0.32
19	KIDS J120203.17+025105.56	19.43	$22.57 \pm 0.18$	$20.95 \pm 0.02$	$19.41 \pm 0.005$	$18.95 \pm 0.01$	0.30
20	KIDS J121856.54+023241.69	19.23	$22.75 \pm 0.17$	$20.79 \pm 0.01$	$19.23 \pm 0.004$	$18.70 \pm 0.008$	0.30
21	KIDS J140257.62+011730.39	19.96	$23.31 \pm 0.48$	$21.33 \pm 0.02$	$19.94 \pm 0.008$	$19.44 \pm 0.02$	0.33
22	KIDS J145656.68+002007.41	19.46	$22.99 \pm 0.23$	$20.84 \pm 0.02$	$19.43 \pm 0.005$	$18.94 \pm 0.006$	0.28
23	KIDS J145948.65-024036.57	18.57	$21.96 \pm 0.88$	$19.92 \pm 0.05$	$18.58 \pm 0.02$	$18.10 \pm 0.04$	0.25
24	KIDS J152700.54-002359.09	19.64	$24.54 \pm 1.45$	$21.19 \pm 0.03$	$19.62 \pm 0.006$	$19.12 \pm 0.01$	0.33
Observation date: 2018 March		Instrument: TNG/DOLORES					
25	KIDS J083807.31+005256.58	19.29	$22.48 \pm 0.14$	$20.66 \pm 0.01$	$19.29 \pm 0.004$	$18.75 \pm 0.009$	0.28
26	KIDS J084412.25-005850.00	19.67	$22.76 \pm 0.22$	$21.16 \pm 0.02$	$19.64 \pm 0.006$	$19.10 \pm 0.015$	0.32
27	KIDS J084413.29+014847.59	19.78	$23.01 \pm 0.32$	$21.22 \pm 0.02$	$19.75 \pm 0.008$	$19.21 \pm 0.014$	0.33
28	KIDS J090933.87+014532.21	19.55	$23.13 \pm 0.35$	$21.14 \pm 0.02$	$19.51 \pm 0.005$	$18.98 \pm 0.01$	0.33
29	KIDS J092030.99+012635.38	19.52	$22.70 \pm 0.19$	$20.96 \pm 0.02$	$19.51 \pm 0.005$	$19.04 \pm 0.015$	0.29
30	KIDS J092407.03-000350.69	19.87	$24.06 \pm 0.55$	$21.48 \pm 0.02$	$19.84 \pm 0.005$	$19.20 \pm 0.012$	0.39
31	KIDS J103951.25+002402.34	19.63	$22.41 \pm 0.15$	$20.66 \pm 0.01$	$19.62 \pm 0.006$	$18.70 \pm 0.013$	0.41
32	KIDS J145721.54-014009.02	19.43	$23.12 \pm 0.35$	$21.03 \pm 0.02$	$19.47 \pm 0.004$	$18.97 \pm 0.014$	0.29
33	KIDS J152706.54-001223.64	19.67	$23.92 \pm 0.73$	$21.39 \pm 0.03$	$19.68 \pm 0.006$	$19.08 \pm 0.01$	0.43

**Note.** For each subgroup of UCMG candidates, 13 in UCMG\_INT\_2017, 11 in UCMG\_TNG\_2017, and nine in UCMG\_TNG\_2018, from left to right, we give: (a) progressive ID number; (b) KIDS identification name; (c)  $r$ -band KiDS MAG\_AUTO; (d)–(g)  $u$ -,  $g$ -,  $r$ - and  $i$ -band KiDS magnitudes measured in an aperture of  $6''$  of diameter with  $1\sigma$  errors; (h) photometric redshift from machine learning. Within each subsample, the galaxies are ordered by R.A. All of the magnitudes have been corrected for galactic extinction using the maps of Schlafly & Finkbeiner (2011). More details are provided in Section 2.

sample assembled in T16,<sup>15</sup> The basic photometric properties of these 33 objects are reported in Table 1. The structural parameters and the  $r$ -band 2D fit outputs derived from 2DPHOT are reported in Table 2, and the fits themselves are showed in Figure 1.<sup>16</sup>

<sup>15</sup> The sample in T16 was assembled in early 2015, applying the same criteria listed in Section 2.2. It consisted of a mixture of the 149 survey tiles from KiDS-DR1/2 (de Jong et al. 2015) and a few other tiles that have been part of subsequent releases. Although this data sample and the KiDS\_FULL one are partially overlapping in terms of sky coverage, they differ in the photometry, structural parameter values, and photometric redshifts.

<sup>16</sup> The  $r$ -band KIDS images sometimes seem to suggest some stripping or interactions with other systems. However, the majority of the spectra are typical of a passive, old stellar population. Moreover, we also note that according to the simulations presented in Wellons et al. (2016), compact galaxies can undertake a variety of evolutionary paths, including some interaction with a close-by companion, without changing their compactness.

Data have been collected in the years 2017 and 2018 during three separate runs, two carried out with the 3.6 m Telescopio Nazionale Galileo (TNG) and one using the 2.54 m Isaac Newton Telescope (INT), both located at Roque de los Muchachos Observatory (Canary Islands). We thus divide our sample into three subgroups, according to the observing run they belong to: UCMG\_INT\_2017, UCMG\_TNG\_2017, and UCMG\_TNG\_2018. They consist of 13, 11, and 9 UCMG candidates, respectively, with  $\text{MAG\_AUTO\_r} \lesssim 20.5$  and  $z_{\text{phot}} \lesssim 0.45$ .

In the following sections, we discuss the instrumental and observational setup as well as the data reduction steps for the two different instrumentation. We then describe the S/N determination as well as the redshift and velocity dispersion calculation, obtained with the new Optimized Modeling of Early-type Galaxy Aperture Kinematics pipeline (OMEGA-K; G. D’Ago et al. 2020, in preparation).

**Table 2**  
Structural Parameters Derived Running 2DPHOT on  $g$ -,  $r$ -, and  $i$ -bands

ID	g-band							r-band							i-band						
	$\Theta_c$	$R_c$	$n$	$q$	$\chi^2$	$\chi'^2$	S/N	$\Theta_c$	$R_c$	$n$	$q$	$\chi^2$	$\chi'^2$	S/N	$\Theta_c$	$R_c$	$n$	$q$	$\chi^2$	$\chi'^2$	S/N
1	0.32	1.36	2.94	0.31	1.01	0.92	81	0.37	1.55	2.33	0.33	1.02	0.98	81	0.34	1.43	4.04	0.33	1.01	1.01	98
2	0.40	1.60	3.31	0.74	1.02	0.96	100	0.28	1.11	5.54	0.76	1.02	1.07	100	0.31	1.23	5.83	0.77	1.02	1.02	161
3	0.36	1.45	4.56	0.25	0.99	1.02	94	0.26	1.06	6.08	0.26	1.03	1.20	94	0.34	1.36	4.93	0.24	1.00	1.00	108
4	0.06	0.32	2.96	0.71	1.00	1.02	148	0.06	0.35	6.32	0.87	1.03	1.12	148	0.10	0.55	5.57	0.73	0.97	0.97	62
5	0.16	0.84	7.10	0.81	1.01	0.99	90	0.14	0.71	6.83	0.87	1.07	1.08	90	0.14	0.70	6.00	0.73	1.00	1.00	108
6	0.43	1.52	1.52	0.29	1.02	0.94	134	0.35	1.23	2.15	0.26	1.02	1.16	134	0.41	1.44	2.11	0.31	0.99	0.99	148
7	0.22	0.82	8.46	0.57	1.02	1.07	118	0.31	1.12	7.53	0.68	1.03	1.28	118	0.36	1.32	2.87	0.61	1.00	1.00	123
8	0.39	1.48	2.96	0.53	1.03	0.98	125	0.36	1.36	2.68	0.54	1.03	1.19	125	0.35	1.34	2.87	0.56	1.05	1.05	128
9	0.20	0.97	4.95	0.79	1.04	1.02	161	0.24	1.14	5.19	0.83	1.04	1.20	161	0.22	1.04	5.30	0.72	0.99	0.99	166
10	0.40	1.10	2.49	0.30	1.00	1.01	97	0.21	0.97	2.97	0.30	1.15	1.20	97	0.21	0.98	2.83	0.31	0.99	1.02	156
11	0.39	1.47	7.86	0.51	1.00	0.91	104	0.27	1.02	6.71	0.42	1.04	1.23	377	0.34	1.31	8.40	0.49	0.99	0.99	129
12	0.32	1.37	6.08	0.48	1.00	1.03	79	0.31	1.30	7.16	0.56	1.07	1.14	283	0.30	1.27	6.93	0.52	1.02	0.93	132
13	0.28	1.61	3.94	0.36	1.00	1.07	135	0.39	1.45	4.24	0.77	1.04	1.19	421	0.41	1.50	5.33	0.77	1.01	0.88	175
14	0.28	1.37	2.22	0.12	1.03	0.94	53	0.23	1.12	3.27	0.29	1.00	1.07	158	0.28	1.40	3.38	0.41	0.98	0.91	105
15	0.43	1.77	4.82	0.32	1.00	1.20	70	0.27	1.13	2.69	0.36	1.04	1.15	297	0.21	0.87	4.37	0.33	1.00	0.99	244
16	0.28	1.35	3.05	0.32	1.02	1.08	70	0.24	1.14	3.03	0.41	1.04	1.18	252	0.27	1.28	4.12	0.41	1.02	1.03	219
17	0.36	1.71	4.57	0.36	1.00	0.93	58	0.31	1.46	6.10	0.38	1.02	1.01	58	0.31	1.47	4.35	0.36	0.99	0.99	91
18	0.27	1.25	2.09	0.58	1.00	0.95	93	0.29	1.36	2.83	0.58	1.03	1.04	93	0.26	1.22	2.75	0.56	1.05	1.05	114
19	0.31	1.38	6.47	0.99	1.04	1.01	59	0.29	1.29	9.54	0.89	1.03	1.09	59	0.36	1.58	5.24	0.87	1.01	1.01	111
20	0.31	1.37	2.05	0.19	1.03	0.93	82	0.33	1.46	2.75	0.30	1.02	1.00	82	0.26	1.15	3.13	0.26	1.03	1.03	132
21	0.17	0.81	6.43	0.44	1.01	0.96	52	0.11	0.50	8.05	0.46	1.03	1.12	52	0.19	0.90	4.08	0.58	1.03	1.03	70
22	0.25	1.04	2.48	0.10	1.04	1.12	74	0.12	0.50	5.60	0.20	1.03	1.11	74	0.11	0.45	5.53	0.31	1.03	1.03	184
23	0.27	1.07	6.15	0.30	1.04	1.39	110	0.31	1.22	4.34	0.30	1.04	2.78	110	0.66	2.57	8.19	0.04	1.00	1.02	146
24	0.39	1.85	10.02	0.94	1.01	1.07	42	0.14	0.67	8.83	0.75	1.01	1.16	42	0.22	1.07	9.16	0.68	1.02	1.02	73
25	0.31	1.30	4.08	0.41	0.99	0.92	84	0.35	1.49	4.02	0.45	1.03	1.06	84	0.30	1.27	3.08	0.40	1.03	0.87	106
26	0.27	1.28	2.00	0.32	1.01	1.01	58	0.29	1.36	2.69	0.36	1.04	1.15	58	0.27	1.26	4.37	0.33	1.02	0.99	75
27	0.32	1.51	6.83	0.44	1.00	0.98	51	0.23	1.11	4.36	0.52	0.98	0.90	51	0.26	1.26	6.56	0.49	1.01	0.94	78
28	0.26	1.24	1.74	0.36	1.03	1.04	55	0.24	1.14	2.66	0.48	1.08	1.28	55	0.22	1.03	3.08	0.43	1.01	0.99	109
29	0.35	1.50	5.72	0.65	1.02	1.04	51	0.33	1.42	6.92	0.68	1.01	0.96	51	0.27	1.17	8.25	0.73	1.01	0.94	70
30	0.18	0.95	6.19	0.25	1.00	0.99	50	0.26	1.39	2.82	0.32	1.00	1.05	50	0.26	1.35	2.66	0.34	1.02	0.95	95
31	0.25	1.37	6.14	0.76	1.03	0.99	85	0.23	1.26	5.59	0.80	1.02	1.00	85	0.27	1.47	2.13	0.80	0.99	0.92	83
32	0.69	3.04	4.60	0.60	1.00	1.00	55	0.34	1.50	8.29	0.53	1.01	1.14	55	0.34	1.48	4.36	0.52	1.01	0.95	63
33	0.23	1.30	5.77	0.18	1.04	1.04	36	0.27	1.49	5.46	0.25	1.02	1.05	36	0.23	1.29	6.43	0.23	0.99	0.92	75

**Note.** For each band, we give: (a) circularized effective radius  $\Theta_c$ , measured in arcsec, (b) circularized effective radius  $R_c$ , measured in kpc (calculated using  $z_{\text{phot}}$  values listed in Table 1), (c) Sérsic index  $n$ , (d) axis ratio  $q$ , (e)  $\chi^2$  of the surface photometry fit, (f)  $\chi'^2$  of the surface photometry fit including only central pixels, and (g) the signal-to-noise ratio S/N of the photometric images, defined as the inverse of the error on MAG\_AUTO.

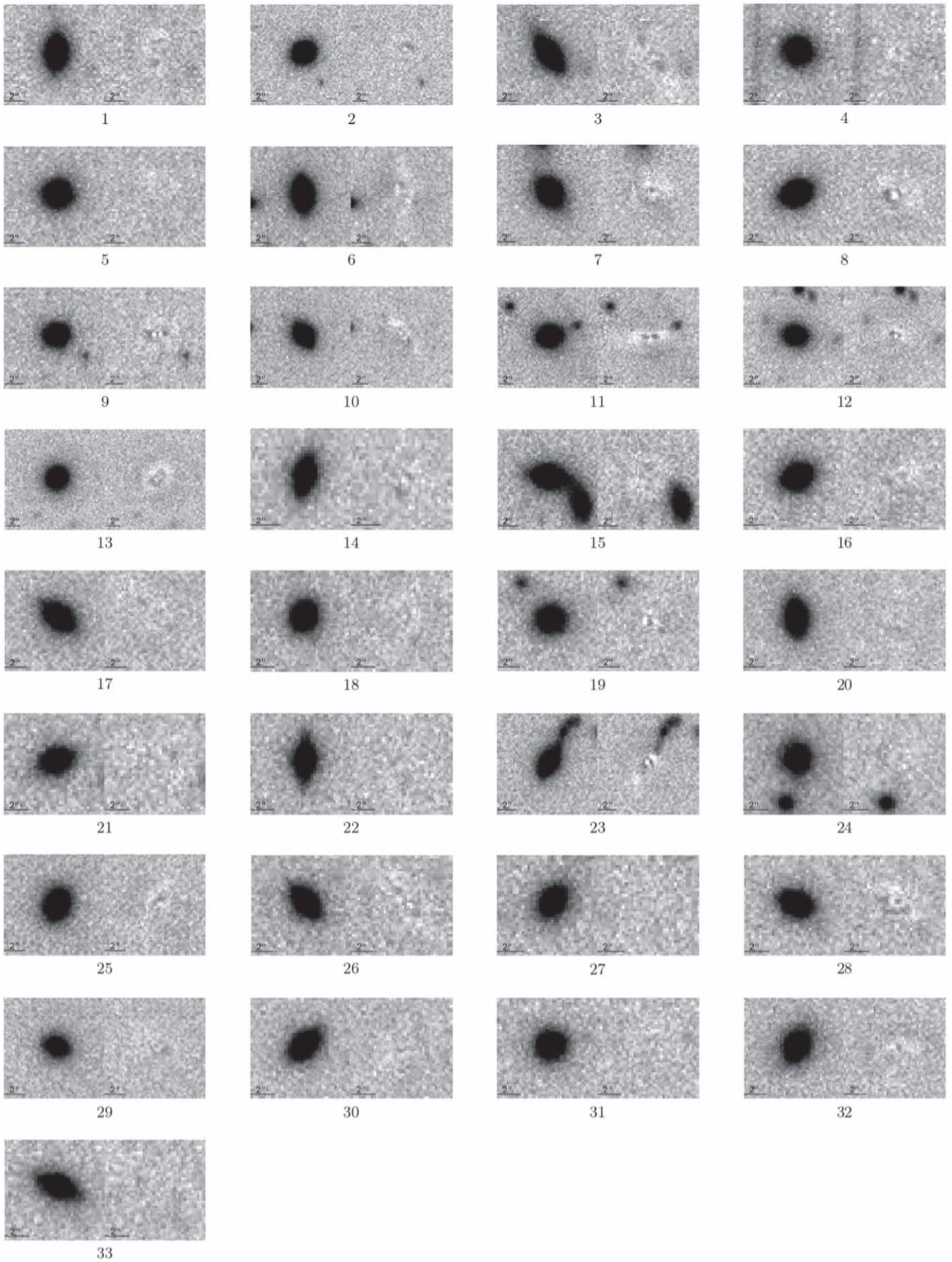


**Figure 1.** Two-dimensional fit output from the 2DPHOT procedure on the 33 UCMG candidates for which we obtained new spectroscopic data. For each UCMG, the left panel shows the original  $r$ -band image and the right panel shows the residual after the subtraction of the 2D single Sérsic PSF convolved model. We also indicate the scale of  $2''$  in the panels.

### 3.1. INT Spectroscopy

Data on 13 luminous UCMG candidates belonging to the UCMG\_INT\_2017 sample have been obtained with the IDS spectrograph during six nights at the INT telescope, in visitor mode (PI: C. Tortora, ID: 17AN005). The observations have been carried out with the RED+2 detector and the low-resolution grating R400V, covering the wavelength range from 4000 to 8000 Å. The spectra have been acquired with long slits of 1''6 or 2'' width, providing a spectral resolution of  $\Delta\lambda/\lambda = 560$ , a dispersion of 1.55 Å pixel<sup>-1</sup>, and a pixel scale of 0.''33 pixel<sup>-1</sup>. The average seeing during the observing run was FWHM  $\sim 1.''5$ , the single exposure time ranged between 600 and 1200 s, and from one up to five single exposures have been obtained per target, depending on their magnitudes.

Data reduction has been performed using IRAF<sup>17</sup> image processing packages. The main data reduction steps include dark subtraction, flat-fielding correction, and sky subtraction. The wavelength calibration has been performed by means of comparison spectra of CuAr+CuNe lamps acquired for each observing night using the IDENTIFY task. A sky spectrum has been extracted from the outer edges of the slit, and subtracted from each row of the two-dimensional spectra using the IRAF task BACKGROUND in the TWODSPEC.LONGSLIT package. The sky-subtracted frames have been coadded to averaged 2D spectra, and then the 1D spectra—which have been used to derive the spectroscopic redshifts—have been obtained by extracting and summing up the lines with higher S/N using the task SCOPY.

The 1D reduced spectra are showed in Figure 2. They are plotted in rest-frame wavelength from  $\sim 3600$  to  $\sim 5600$  Å and units of normalized flux (each spectrum has been divided by its median). The spectra are vertically shifted for better visualization. Vertical red dotted lines show absorption spectral features typical of an old stellar population.

### 3.2. TNG Spectroscopy

The 20 spectra of UCMG candidates in the UCMG\_TNG\_2017 and UCMG\_TNG\_2018 samples have been collected using the Device Optimized for the Low RESolution (DOLORES) spectrograph mounted on the 3.5 m TNG, during six nights in 2017 and 2018 (PI: N.R. Napolitano, ID: A34TAC\_22 and A36TAC\_20). The instrument has a 2k × 2k CCD detector with a pixel scale of 0.''252 pixel<sup>-1</sup>. The observations for both subsamples have been carried out with the LR-B grism with dispersion of 2.52 Å pixel<sup>-1</sup> and resolution of 585 (calculated for a slit width of 1''), covering the wavelength range from 4000 to 8000 Å. As in the previous case, we have obtained from one to five single exposures per target, each with exposure time ranging between 600 and 1200 s. Following T18, the DOLORES 2D spectra have been flat-fielded, sky-subtracted, and wavelength-calibrated using the HgNe arc lamps. Then, the 1D spectra have been extracted by integrating over the source spatial profile. All these procedures have been performed using the same standard IRAF tasks as explained in Section 3.1. The TNG spectra are showed in Figures 3 and 4, using the same units and scale of Figure 2. Similarly to the previous case, the

<sup>17</sup> IRAF is distributed by the National Optical Astronomy Observatories, which is operated by the Associated Universities for Research in Astronomy, Inc., under cooperative agreement with the National Science Foundation.

main stellar absorption features are highlighted with vertical red dotted lines.

### 3.3. Spectroscopic S/N Determination

To calculate the S/N ( $S/N_{\text{spec}}$ ) of the integrated spectra, we use the IDL code DER\_SNR.<sup>18</sup> The code estimates the derived S/N from the flux under the assumptions that the noise is uncorrelated in wavelength bins spaced two pixels apart and that it is approximately Gaussian-distributed. The biggest advantages of using this code are that it is very simple and robust, and above all, it computes the S/N from the data alone. In fact, the noise is calculated directly from the flux using the following equation:

$$N = \frac{1.482602}{\sqrt{6} \times \langle |2S(i) - S(i-2) - S(i+2)| \rangle}, \quad (2)$$

where  $S$  is the signal (taken to be the flux of the continuum level) and the index  $i$  runs over the pixels. The “ $\langle \rangle$ ” symbol indicates a median calculation done over all the nonzero pixels in the restframe wavelength range 3600–4600 Å, which is the common wavelength range for all the spectra, including the T18 ones (in the next section, we also determine the velocity dispersion for the latter). We note that these S/N estimates have to be interpreted as lower limits for the whole spectrum, since they are calculated over a rather blue wavelength range, whereas the light of early-type galaxies is expected to be strong in redder regions. This arises clearly from the comparison of these  $S/N_{\text{spec}}$  with the ones we will describe in the next section; those are computed for each galaxy, over the region used for the kinematic fit, and are systematically larger. Both of them will be used in Section 4.4 as one of the proxies for the reliability of the velocity dispersion ( $\sigma$ ) measurements.

### 3.4. Redshift and Velocity Dispersion Measurements

Redshift and velocity dispersion values have been measured with the OMEGA-K; pipeline (D’Ago et al. 2018), a Python wrapper based on the Penalized Pixel-Fitting code (PPXF; Cappellari 2017).

OMEGA-K comprises a graphical user interface (PPGUI, written by G. D’Ago and to be distributed soon) that allows the user to visualize and inspect the observed spectrum in order to easily set the PPXF fitting parameters (i.e., template libraries, noise level, polynomials, fit wavelength range, and custom pixel masks). We use PPGUI to rest-frame the spectra and obtain a first guess of the redshift, initially based on the  $z_{\text{phot}}$ .

The aim of OMEGA-K is to automatically retrieve an optimal pixel mask and noise level ( $1\sigma$  noise spectrum) for the observed spectrum, and to find a robust estimate of the galaxy kinematics together with its uncertainties by randomizing the initial condition for PPXF and running it hundreds of times on the same observed spectrum, to which a Gaussian noise is randomly added.

As templates for the fitting, we use a selection of 156 MILES simple single stellar population (SSP) models from

<sup>18</sup> The code is written by Felix Stoehr and published on the ST-ECF Newsletter, Issue num. 42. The software is available here: [www.stecf.org/software/ASTROsoft/DER\\_SNR/](http://www.stecf.org/software/ASTROsoft/DER_SNR/); the Newsletter can be found here: [www.space Telescope.org/about/further\\_information/stecfnewsletters/hst\\_stecf\\_0042/](http://www.space Telescope.org/about/further_information/stecfnewsletters/hst_stecf_0042/).

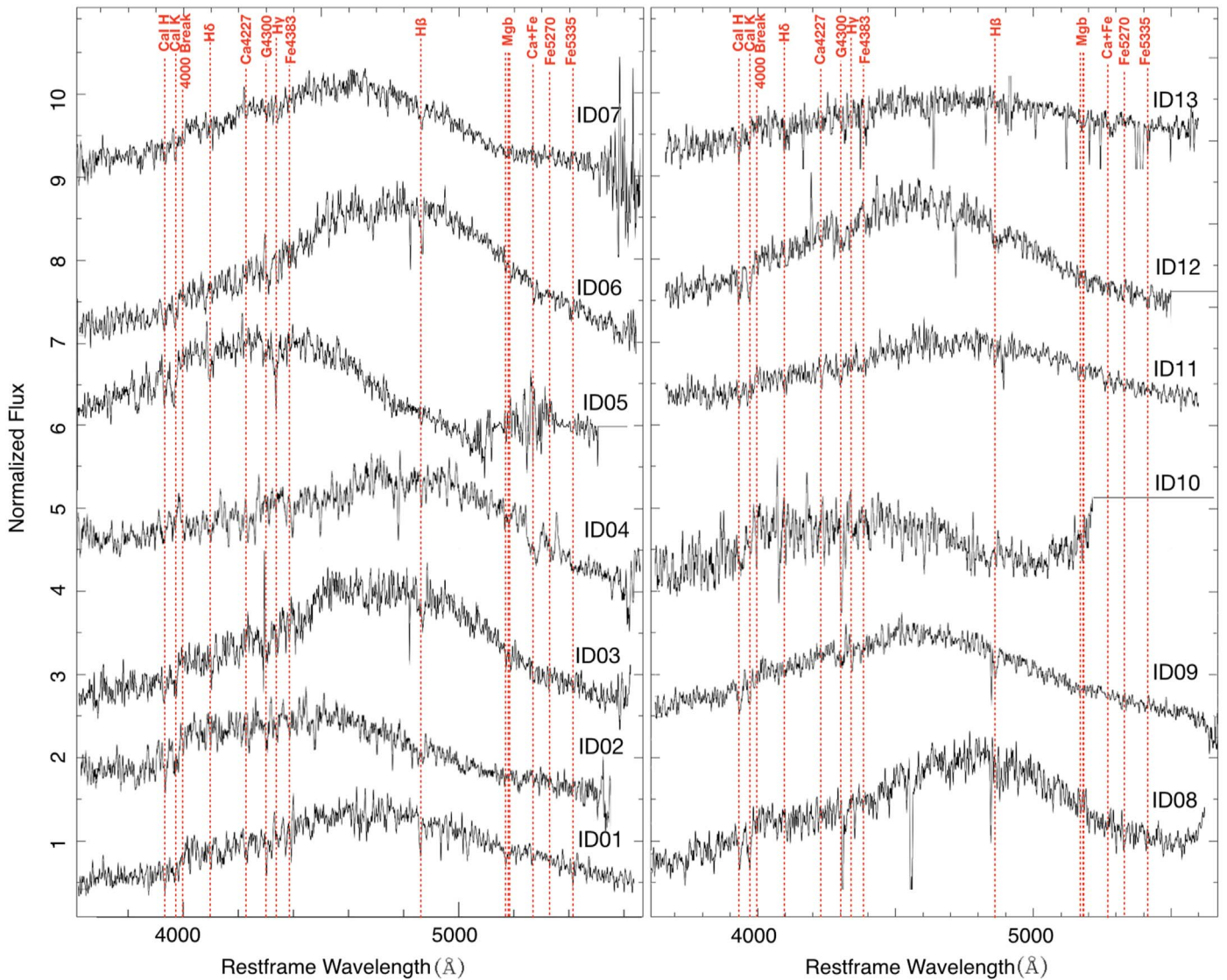


**Figure 2.** Spectra of the 13 candidates observed in our spectroscopic campaign with INT (UCMG\_INT\_2017), for which we obtain a spectroscopic redshift estimation. The spectra are plotted in ascending order of ID, which is reported above each corresponding spectrum and refers to the IDs in Table 3. We only show the wavelength region that was used to derive the redshift and to compute the velocity dispersion. This region includes some of the most common stellar absorption lines, such as Ca–H, Ca–K, Balmer lines ( $H_\delta$ ,  $H_\gamma$  and  $H_\beta$ ), Mg b, and Fe lines. The spectra are plotted in rest-frame wavelength, in units of normalized flux (each spectrum has been divided by its median), and they are vertically shifted for better visualization. In some cases, when the red part of the spectrum was particularly noisy, we cut it out to improve the figure layout.

Vazdekis et al. (2010), covering a wide range of metallicities ( $0.02 \leq Z/Z_\odot \leq 1.58$ ) and ages (between 3 and 13 Gyr). We also perform the fitting using single stars (268 empirical stars from MILES library, uniformly sampling effective temperature, metallicity, and surface gravity of the full catalog of templates) and also including templates with ages  $< 3$  Gyr.

The results do not change and are always consistent within the errors, demonstrating that the choice of the templates does not influence the fitting results.<sup>19</sup> Finally, an additive polynomial is also applied in order to take into account possible template shape and continuum mismatches and correct for imperfect sky subtraction or scattered light.

<sup>19</sup> We note that the stellar templates are used only to infer the kinematics, i.e., to measure the shift and the broadening of the stellar absorption lines. Given the low S/N of our spectra, we do not perform any spectroscopic stellar population analysis.

For a general description of the OMEGA-K pipeline, we refer the reader to abovementioned reference (see also D’Ago et al. 2018) and G. D’Ago et al. (2020, in preparation). Here, we list the main steps of the OMEGA-K run specifically adopted for this work on a single observed spectrum.

1. The observed spectrum and the template libraries are ingested.
2. The optimal  $1\sigma$  noise spectrum and pixel mask are automatically tuned.
3. A series of 256 Monte Carlo resamplings of the observed spectrum using a random Gaussian noise from the  $1\sigma$  noise spectrum are produced.
4. Another 256 sets of initial guesses (for the redshift and the velocity dispersion) and of fitting parameters (additive polynomial degree, number of momenta of the line-of-sight velocity distribution to be fitted, and random shift of



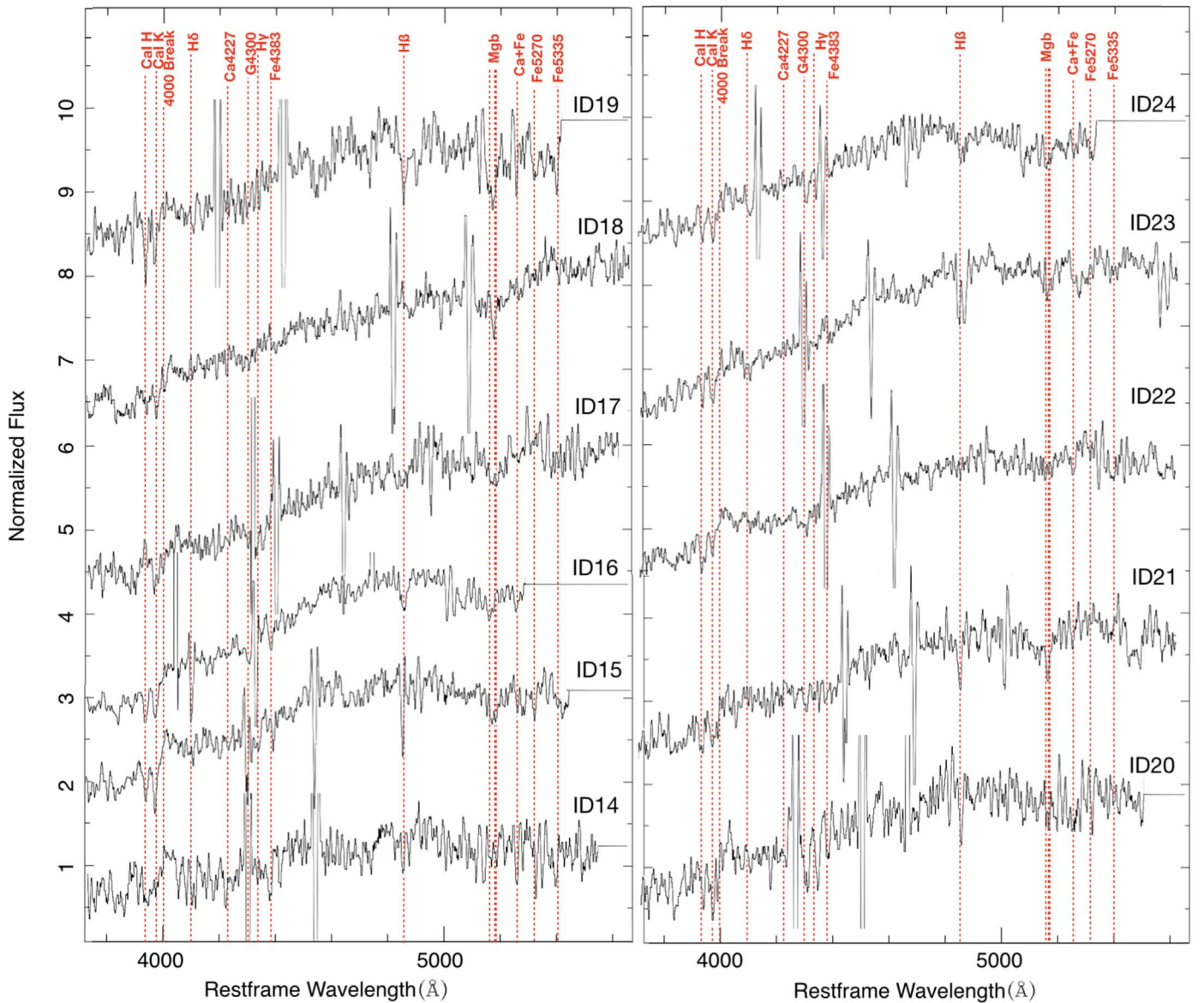


**Figure 3.** Same as Figure 2, but for the 11 candidates observed in our spectroscopic campaign with TNG (UCMG\_TNG\_2017), for which we obtain a spectroscopic redshift estimation.

the fitting wavelength range) are produced in order to allow for a complete bootstrap approach within the parameter space, and to avoid internal biases in the pipeline.

5. The 256 PPXF runs are performed in parallel, and the results from each run are stored (outliers and too noisy reproductions of the observed spectra are automatically discarded).
6. The final redshift and velocity dispersion for each observed spectrum, together with their error, are defined as the mean and the standard deviation of the result distribution from the accepted fits.

Among the 257 fits performed on each spectrum (256 from the OMEGA-K bootstrap stage, plus the fit on the original observed spectrum), we discard the ones for which the best fit fails to converge or the measured kinematics is unrealistically low or unrealistically high. As the lower and upper limits on the

velocity, we choose thresholds of 110 and 500  $\text{km s}^{-1}$ , respectively. The low limit is slightly smaller than the typical velocity scale of the instrument, which we measure to be  $\sim 120 \text{ km s}^{-1}$ . On the other hand, we used 500  $\text{km s}^{-1}$  as a high upper limit in order to incorporate any possible source of uncertainty related to the pipeline, without artificially reducing the errors on our estimates.

We define the success rate (SR) as the ratio between the number of accepted fits over the total 257 attempts.

Finally, OMEGA-K derives a mean spectrum of the accepted fits and performs a measurement of the S/N on its residuals ( $(S/N)_{O-K}$ ). D’Ago et al. (2018) showed—using mock data, a large sample of SDSS spectra, and the entire GAMA DR3 spectroscopic database—that kinematics values with  $SR > 65\%$  and  $(S/N)_{O-K} > 5/\text{px}$  can be considered totally reliable. This S/N ratio is also consistent with what found in Hopkins et al. (2013 and references therein).

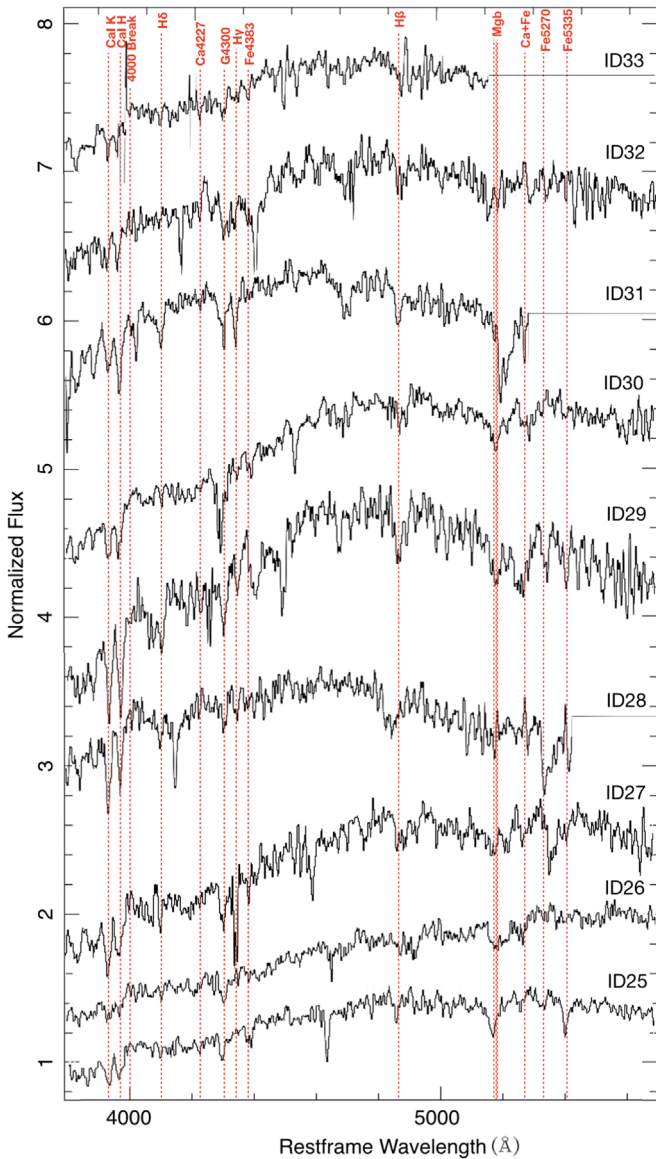


**Figure 4.** Same as Figure 2, but for the nine candidates observed in our spectroscopic campaign with TNG (UCMG\_TNG\_2018), for which we obtain a spectroscopic redshift estimation.

Unfortunately, the uncertainties on our measures are very large. To assess the effect of such large errors on our findings, we separate the UCMGs into two groups: those with “high-quality” (HQ) velocity dispersion measurements and those with “low-quality” (LQ) ones. For this purpose, we use a combination of three quality criteria: the aforementioned SR, the spectral S/N calculated on a common wavelength range covered by all the spectra (see Section 3.3), and the  $(S/N)_{O-K}$  from the OMEGA-K pipeline (calculated over different wavelength ranges for different spectra). We visually inspect the spectra and their fit one by one, in order to set reliable thresholds for these criteria. We set up the following lower limits for quality:  $SR = 0.3$ ,  $S/N_{\text{spec}} = 3.5$ , and  $(S/N)_{O-K} = 6.5/\text{px}$ . We then classify the ones above these limits as HQ objects.

In Figure 5, we show two examples of the ppxf fit obtained with OMEGA-K on the spectra of two different objects from the sample of the 33 UCMG candidates for which we obtain new

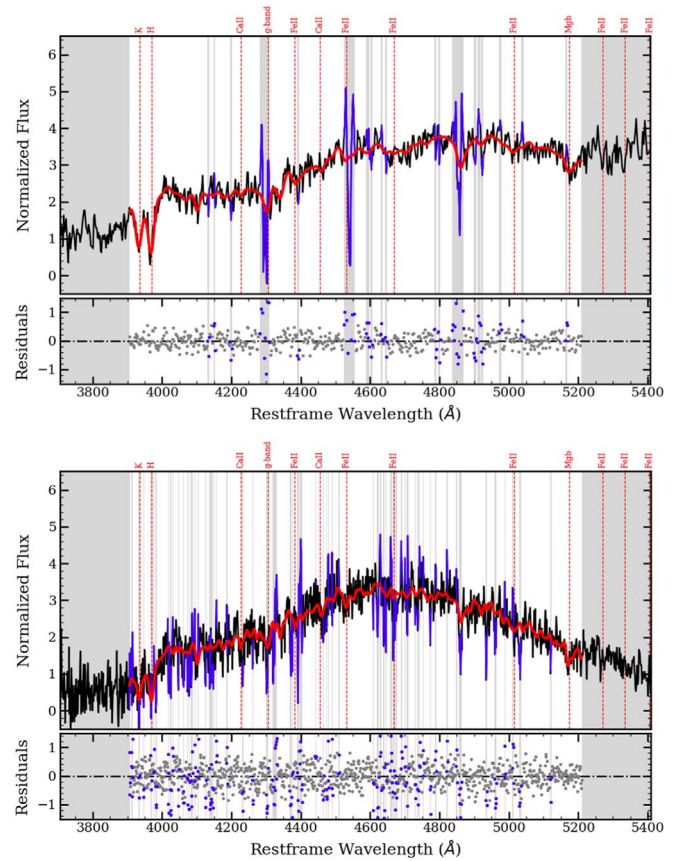


**Figure 5.** Two examples of ppxf fits obtained with OMEGA-K on the spectra of two different UCMGs, one of the best HQ system and one of the worst LQ system, which hence are representative of the whole sample, observed with two different telescopes. For each panel, we plot the galaxy spectrum in black, the best template fit in red, and the regions excluded from the fit as blue lines. We note that the fit is performed only outside the gray shaded regions. Finally, we highlight stellar absorption lines in red and show the residuals of the plot below each panel.

spectroscopy in this paper. These two spectra are representative of the full sample, as they have been observed with two different instruments and one is classified as HQ while the other as LQ. The upper panel shows the galaxy KIDS J090412.45–001819.75 (ID = 15), from the UCMG\_TNG\_2017 sample, which is classified as HQ and has a large velocity dispersion ( $\sigma = 412 \pm 81 \text{ km s}^{-1}$ ). The lower panel instead shows the spectrum of the galaxy KIDS J085700.29–010844.55 (ID = 1), which belongs to UCMG\_INT\_2017. This object, classified as LQ, has a relatively lower velocity dispersion ( $\sigma = 187 \pm 85 \text{ km s}^{-1}$ ) and is one of the worse cases with very low spectral S/N.

In addition to the 33 new UCMG candidates presented in this paper, we also apply the same kinematics procedure to the 28 UCMG candidates from T18, 6 observed with TNG and 22 with NTT, which we refer to as the UCMG\_TNG\_T18 and UCMG\_NTT\_T18 samples, respectively.

In general, the velocity dispersion values from OMEGA-K are derived from 1D spectra using various slit widths and extracted using different numbers of pixels along the slit length. This means that the velocity dispersion values are computed integrating light in apertures with different sizes. The ranges of aperture and slit widths for the 33 new objects presented here and the 28 UCMG candidates from T18 are  $1''.8\text{--}3''.2$  and  $1''.2\text{--}2''$ , respectively. This is not an ideal situation

**Table 3**

Results of the Fitting Procedure on the Spectra Belonging to the Three Observational Runs Presented Here: UCMG\_INT\_2017, UCMG\_TNG\_2017, UCMG\_TNG\_2018

ID	$z_{\text{phot}}$	$z_{\text{spec}} \pm \Delta z_{\text{spec}}$	$\sigma \pm \Delta\sigma$	$\sigma_e$	Aperture	SR	$(S/N)_{\text{spec}}$	$(S/N)_{\text{O-K}}$	Quality Level
1	0.28	$0.2696 \pm 0.0002$	$197 \pm 85$	211	0.97	0.62	1.99	6.13	LQ
2	0.26	$0.3158 \pm 0.0002$	$195 \pm 52$	210	0.97	0.77	3.21	5.69	LQ
3	0.26	$0.2995 \pm 0.0003$	$268 \pm 76$	291	1.21	0.79	2.50	6.19	LQ
4	0.45	$0.3084 \pm 0.0005$	$234 \pm 86$	281	0.97	0.30	2.18	4.23	LQ
5	0.37	$0.4401 \pm 0.0003$	$142 \pm 33$	161	0.97	0.07	4.00	6.87	LQ
6	0.22	$0.2988 \pm 0.0002$	$202 \pm 48$	217	1.21	0.75	2.42	7.27	LQ
7	0.23	$0.3221 \pm 0.0002$	$208 \pm 84$	224	0.97	0.15	2.96	6.71	LQ
8	0.24	$0.2976 \pm 0.0002$	$241 \pm 100$	257	0.97	0.59	3.06	6.31	LQ
9	0.34	$0.2915 \pm 0.0001$	$227 \pm 84$	251	0.97	0.21	4.07	6.04	LQ
10	0.32	$0.3590 \pm 0.0004$	$265 \pm 100$	293	0.97	0.12	2.00	2.05	LQ
11	0.24	$0.2797 \pm 0.0003$	$260 \pm 94$	286	0.97	0.85	1.40	4.58	LQ
12	0.28	$0.3312 \pm 0.0002$	$202 \pm 59$	218	0.97	0.73	2.70	6.76	LQ
13	0.23	$0.2668 \pm 0.0007$	$259 \pm 113$	274	0.97	0.23	1.77	2.89	LQ
14	0.35	$0.2946 \pm 0.0003$	$340 \pm 99$	369	0.94	0.66	2.01	3.97	LQ
15	0.27	$0.2974 \pm 0.0002$	$412 \pm 81$	451	1.07	0.69	6.90	13.25	HQ
16	0.33	$0.3594 \pm 0.0001$	$268 \pm 84$	292	1.01	0.84	6.87	14.32	HQ
17	0.33	$0.2656 \pm 0.0006$	$321 \pm 93$	347	1.01	0.43	1.95	8.20	LQ
18	0.32	$0.1586 \pm 0.0002$	$253 \pm 92$	276	1.01	0.70	2.93	12.76	LQ
19	0.30	$0.3281 \pm 0.0002$	$230 \pm 91$	251	1.18	0.30	2.97	6.27	LQ
20	0.30	$0.2728 \pm 0.0003$	$331 \pm 92$	361	1.12	0.21	2.85	5.58	LQ
21	0.33	$0.2523 \pm 0.0003$	$323 \pm 95$	366	1.12	0.85	2.62	9.93	LQ
22	0.28	$0.2719 \pm 0.0002$	$355 \pm 99$	413	1.18	0.66	5.91	12.72	HQ
23	0.25	$0.2971 \pm 0.0002$	$407 \pm 56$	443	1.12	0.79	6.18	17.38	HQ
24	0.33	$0.3491 \pm 0.0002$	$194 \pm 64$	215	1.07	0.23	5.79	11.15	LQ
25	0.28	$0.2703 \pm 0.0002$	$274 \pm 57$	298	1.12	0.91	6.80	18.11	HQ
26	0.32	$0.1984 \pm 0.0002$	$287 \pm 57$	316	1.18	0.89	3.96	17.92	HQ
27	0.33	$0.2843 \pm 0.0002$	$241 \pm 53$	267	1.23	0.91	5.08	15.85	HQ
28	0.33	$0.4203 \pm 0.0002$	$172 \pm 63$	191	1.18	0.02	6.59	11.69	LQ
29	0.29	$0.3116 \pm 0.0002$	$164 \pm 39$	177	1.01	0.52	7.74	15.65	HQ
30	0.39	$0.2994 \pm 0.0002$	$289 \pm 52$	319	1.12	1.00	8.53	24.59	HQ
31	0.41	$0.4655 \pm 0.0001$	$253 \pm 57$	280	1.18	0.98	9.18	18.13	HQ
32	0.29	$0.3382 \pm 0.0003$	$277 \pm 85$	301	1.18	0.88	3.51	9.73	HQ
33	0.43	$0.4028 \pm 0.0003$	$299 \pm 91$	335	1.28	0.84	4.96	9.16	HQ

**Notes.** Columns from left to right list: the galaxy ID, the photometric redshift, the measured spectroscopic redshift with its error, the measured velocity dispersion in  $\text{km s}^{-1}$  with its error, the corrected velocity dispersion to the effective radius, and the equivalent circular aperture in arcsec. In the final four columns, we also report the success rate, the signal-to-noise ratio per pixel calculated in the range 3600–4600 Å, the signal-to-noise ratio per pixel calculated over the region used for the fit by OMEGA-K, and the quality level of the velocity dispersion estimates, based on these three quality parameters.

if we want to compare velocity dispersion values among different systems and use these measurements to derive scaling relations. We will come back to this specific topic in Section 4.4. Briefly, in order to make the estimates uniform and correct the velocity dispersion values for the different apertures, we first convert the rectangular aperture adopted to extract the UCMG 1D spectra to an equivalent circular aperture of radius  $R = 1.025\sqrt{(\delta x \delta y / \pi)}$ , where  $\delta x$  and  $\delta y$  are the width and length used to extract the spectrum.<sup>20</sup> Then, we use the average velocity dispersion profile in Cappellari et al. (2006) to extrapolate this equivalent velocity dispersion to the effective radius.

Tables 3 and 4 list the results of the fitting procedure for our sample and that of T18. We report the measured spectroscopic redshifts and the velocity dispersion values, each with associated error, the velocity dispersion values corrected to the effective radii ( $\sigma_e$ ), and the equivalent circular apertures for the whole sample of 61 UCMGs. We also present the photometric redshifts to provide a direct comparison with the

spectroscopic ones. Finally, the four following columns indicate the three parameters we use to split the sample in HQ and LQ, and the resulting classification for each object.

In addition, we correct the value of the spectroscopic redshift for the object with ID number 46 (corresponding to ID 13 in T18) with respect to the wrong one reported in T18. Although this changes the value of  $R_e$ , the result of the spectroscopic validation remains unchanged and the galaxy is still a confirmed UCMG. The 28 galaxies from T18 are reported in the same order as the previous paper, but continue the numeration (in terms of ID) of this paper.

#### 4. Results

Although the photometric redshifts generally reproduce quite well the spectroscopic ones (Figure 6), small variations in  $z_{\text{phot}}$  can induce variations in  $R_e$  and  $M_*$  large enough to bring them outside the limits for our definition of UCMG (i.e., it might happen that  $R_e > 1.5 \text{ kpc}$  and/or  $M_* < 8 \times 10^{10} M_\odot$ ). Thus, having obtained the spectroscopic redshifts, we are now able to recalculate both  $R_e$  and  $M_*$ , and find how many candidates are still ultracompact and massive according to our definition.

<sup>20</sup> The same formula was adopted in Tortora et al. (2014), but reported with a typo in the printed copy of the paper.

**Table 4**  
Same as Table 3, but for Samples UCMG\_TNG\_T18 and UCMG\_NTT\_T18

ID	$z_{\text{phot}}$	$z_{\text{spec}} \pm \Delta z_{\text{spec}}$	$\sigma \pm \Delta\sigma$	$\sigma_e$	Aperture	SR	$(S/N)_{\text{spec}}$	$(S/N)_{\text{O-K}}$	Quality Level
34	0.29	$0.3705 \pm 0.0001$	$361 \pm 63$	392	1.12	0.98	15.05	22.41	HQ
35	0.22	$0.2175 \pm 0.0004$	$404 \pm 101$	446	1.59	0.31	7.68	14.62	HQ
36	0.35	$0.4078 \pm 0.0002$	$366 \pm 79$	412	1.33	0.93	6.70	14.33	HQ
37	0.31	$0.3341 \pm 0.0002$	$218 \pm 54$	242	1.12	0.92	7.84	17.82	HQ
38	0.42	$0.3988 \pm 0.0003$	$390 \pm 71$	448	1.01	0.75	5.33	12.67	HQ
39	0.36	$0.3190 \pm 0.0004$	$226 \pm 65$	245	1.01	0.82	4.14	10.20	HQ
40	0.20	$0.3019 \pm 0.0002$	$432 \pm 41$	464	0.69	0.73	2.09	6.75	LQ
41	0.35	$0.3853 \pm 0.0001$	$211 \pm 40$	223	0.69	0.98	3.69	10.92	HQ
42	0.28	$0.2367 \pm 0.0003$	$225 \pm 34$	235	0.69	1.00	2.38	9.30	LQ
43	0.29	$0.2801 \pm 0.0001$	$196 \pm 39$	214	0.69	0.94	2.77	9.55	LQ
44	0.31	$0.2789 \pm 0.0001$	$218 \pm 34$	235	0.69	1.00	3.67	12.46	HQ
45	0.27	$0.2888 \pm 0.0001$	$195 \pm 46$	216	0.69	0.94	3.09	9.30	LQ
46	0.31	$0.3618 \pm 0.0053$	$181 \pm 68$	196	0.69	0.09	1.39	4.08	LQ
47	0.25	$0.2622 \pm 0.0003$	$340 \pm 53$	363	0.69	0.99	2.31	7.65	LQ
48	0.27	$0.2949 \pm 0.0003$	$280 \pm 50$	295	0.69	1.00	3.79	10.53	HQ
49	0.28	$0.2974 \pm 0.0001$	$142 \pm 22$	149	0.69	0.58	3.54	10.01	HQ
50	0.29	$0.3188 \pm 0.0001$	$387 \pm 63$	408	0.69	0.96	3.88	11.85	HQ
51	0.34	$0.3151 \pm 0.0001$	$154 \pm 29$	166	0.69	0.66	3.82	11.69	HQ
52	0.22	$0.2124 \pm 0.0001$	$252 \pm 43$	265	0.69	1.00	1.64	9.19	LQ
53	0.25	$0.2578 \pm 0.0002$	$183 \pm 48$	194	0.69	0.68	2.37	9.73	LQ
54	0.34	$0.3024 \pm 0.0009$	$214 \pm 66$	226	0.69	0.70	1.97	4.14	LQ
55	0.31	$0.3667 \pm 0.0001$	$244 \pm 30$	262	0.69	1.00	4.99	13.10	HQ
56	0.32	$0.4070 \pm 0.0001$	$322 \pm 54$	342	0.69	1.00	4.82	10.60	HQ
57	0.33	$0.2612 \pm 0.0001$	$219 \pm 44$	233	0.69	0.99	3.00	10.88	LQ
58	0.27	$0.2818 \pm 0.0002$	$218 \pm 64$	227	0.69	0.92	2.41	7.38	LQ
59	0.23	$0.2889 \pm 0.0002$	$209 \pm 52$	221	0.69	0.95	2.80	9.99	LQ
60	0.34	$0.3393 \pm 0.0001$	$155 \pm 30$	167	0.69	0.73	4.59	10.78	HQ
61	0.31	$0.2889 \pm 0.0001$	$220 \pm 33$	236	0.69	1.00	2.47	8.67	LQ

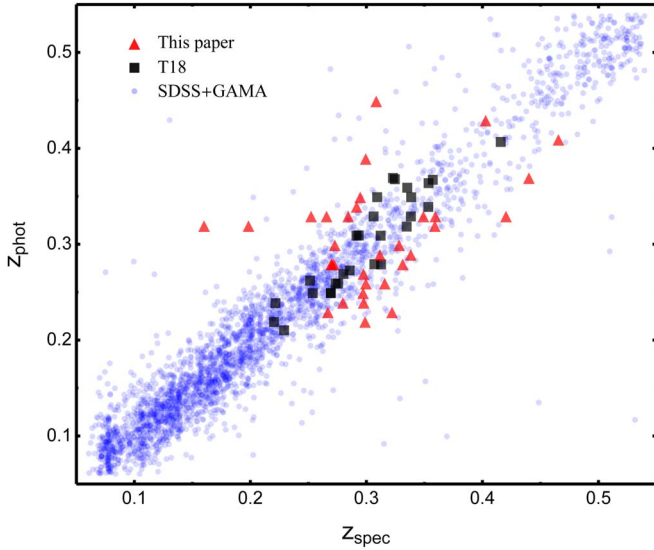


**Figure 6.** Spectroscopic vs. photometric redshifts. Red triangles are for the new sample of 33 UCMG candidates analyzed in this paper with redshifts measured from observations at INT and TNG. Black squares are relative to the set of 28 UCMG KiDS candidates with redshifts measured from observations at TNG and NTT presented in T18. Blue points are for a parent sample of galaxies with SDSS and GAMA spectroscopy (extracted from KiDS\_SPEC), used by Cavuoti et al. (2015b) as a test set for the validation of the photometric redshift determination. We find a good agreement with the one-to-one relation for most of the objects in all of the data sets.

Following the analysis of T18, in the next subsections we study the SR of our selection and systematics in UCMG abundances. We then quantify the UCMG number counts,

comparing our new results with the ones in the literature. We finally show where the final sample of spectroscopically confirmed objects (i.e., the ones presented in T18 plus the ones presented here) is located on the  $M_*$ - $\sigma$  plane, in order to establish some basis for future analysis of the scaling relation.

#### 4.1. UCMGs Validation

In Figure 6, we compare the spectroscopic redshifts measured for the candidates of this paper with the photometric redshift values (red triangles). The results are also compared with the 28 UCMG from T18 (black squares) and with a sample of galaxies with SDSS and GAMA spectroscopy (blue points) from KiDS-DR2 (Cavuoti et al. 2015b). As one can clearly see from the figure, the distribution of the new redshifts is generally consistent with that found using the full sample of galaxies included in KiDS-DR3, on average reproducing well the spectroscopic redshifts.

The agreement on the redshifts can be better quantified by using statistical indicators (Cavuoti et al. 2015b; T18). Following the analysis of T18, we define this quantity as

$$\Delta z \equiv \frac{z_{\text{spec}} - z_{\text{phot}}}{1 + z_{\text{spec}}}, \quad (3)$$

then we interpret the scatter as the standard deviation of  $\Delta z$ , and bias as the absolute value of the mean of  $\Delta z$ . We find a bias of 0.0008 and a scatter of 0.0516 for our 33 systems. These estimates show a larger scatter of the new sample with respect to the sample of galaxies in T18, for which we found a bias of 0.0045 and a standard deviation of 0.028.

**Table 5**

Photometric and Spectroscopic Parameters (Redshifts, Median Effective Radii in kpc and Stellar Masses) for the Validation of the New Samples: UCMG\_INT\_2017, UCMG\_TNG\_2017, and UCMG\_TNG\_2018

ID	$z$		$R_e$		$\log_{10}(M_*/M_\odot)$		Spec. Valid.
	phot	spec	phot	spec	phot	spec	
1	0.28	0.27	1.43	1.39	11.03	11.00	Y
2	0.26	0.32	1.23	1.43	10.94	11.07	Y
3	0.26	0.30	1.36	1.51	10.92	11.21	N
4	0.45	0.31	0.35	0.28	11.29	10.83	N
5	0.37	0.44	0.71	0.79	11.32	11.24	Y
6	0.22	0.30	1.44	1.81	10.93	11.20	N
7	0.23	0.32	1.12	1.42	10.92	11.27	Y
8	0.24	0.30	1.36	1.60	10.93	11.06	N
9	0.34	0.29	1.04	0.94	10.92	10.73	N
10	0.32	0.36	0.98	1.06	11.21	11.19	Y
11	0.24	0.28	1.31	0.96	10.98	10.99	Y
12	0.28	0.33	1.30	1.45	10.95	11.07	Y
13	0.23	0.27	1.50	1.69	11.03	11.03	N
14	0.35	0.29	1.37	1.20	11.08	10.96	Y
15	0.27	0.30	1.13	1.22	11.08	11.10	Y
16	0.33	0.36	1.28	1.36	11.25	11.34	Y
17	0.33	0.27	1.47	1.28	11.16	10.97	Y
18	0.32	0.16	1.25	0.74	10.98	10.61	N
19	0.30	0.33	1.38	1.47	11.01	10.83	N
20	0.30	0.27	1.37	1.27	10.95	10.97	Y
21	0.33	0.25	0.81	0.67	10.99	10.82	N
22	0.28	0.27	0.50	0.49	11.01	10.85	N
23	0.25	0.30	1.22	1.39	11.12	11.26	Y
24	0.33	0.35	1.07	1.11	11.01	11.06	Y
25	0.28	0.27	1.30	1.27	10.97	10.94	Y
26	0.32	0.20	1.28	0.90	10.92	10.46	N
27	0.33	0.28	1.26	1.12	10.97	10.85	N
28	0.33	0.42	1.14	1.32	11.00	11.25	Y
29	0.29	0.31	1.42	1.49	10.99	10.99	Y
30	0.39	0.30	1.35	1.14	11.02	10.78	N
31	0.41	0.47	1.37	1.49	10.93	11.03	Y
32	0.29	0.34	1.48	1.65	11.06	11.18	N
33	0.43	0.40	1.30	1.24	11.31	11.24	Y

**Note.** The last column indicates the spectral validation response: “Y” if the candidate is a confirmed UCMG, (i.e.,  $\log_{10}(M_*/M_\odot) > 10.9$  and  $R_e < 1.5$  kpc), and “N” if it is not.

Since we use a new stellar mass calculation setup with respect to the one in T18, we recalculate sizes and masses, with both  $z_{\text{phot}}$  and  $z_{\text{spec}}$  for the final, total, spectroscopic sample of 61 systems. The results are provided in Tables 5 and 6, where we also report, in the last column, the UCMGs spectral validation.

Using the face values for masses and sizes inferred from the spectroscopic redshifts, we confirm as UCMGs 19 out of 33 new UCMG candidates. This corresponds to an SR of 58%, a number that is fully consistent with the 50–60% estimate found in T18. Moreover, using the new mass setup, 27 out of the 28 objects of T18 are still UCMG candidates according to the mass selection using the photometric redshift values, and 18 are spectroscopically confirmed UCMGs. This corresponds to an SR of 67%. In total, we confirmed 37 out of 61 UCMGs, with an SR of 60%. Considering only the new 19/33 confirmed UCMGs, we find a bias of 0.016 and a scatter of 0.037 in the  $z_{\text{phot}}-z_{\text{spec}}$  plot. This reflects the expectation that the objects with a larger

**Table 6**

Same as Table 5, but for the UCMG\_TNG\_T18 and UCMG\_NTT\_T18 Samples

ID	$z$		$R_e$		$\log_{10}(M_*/M_\odot)$		Spec. Valid.
	phot	spec	phot	spec	phot	spec	
34	0.29	0.37	1.43	1.68	10.97	11.35	N
35	0.22	0.22	1.28	1.27	11.12	11.11	Y
36	0.35	0.41	1.09	1.19	10.92	10.97	Y
37	0.31	0.33	1.06	1.10	10.73	10.80	N
38	0.42	0.40	0.67	0.66	10.98	10.94	Y
39	0.36	0.32	1.46	1.36	10.99	10.87	N
40	0.2	0.30	1.11	1.06	10.94	10.94	Y
41	0.35	0.39	1.45	1.54	11.37	11.43	N
42	0.28	0.24	1.47	1.32	10.91	10.84	N
43	0.29	0.28	0.81	0.80	11.01	10.99	Y
44	0.31	0.28	1.01	0.95	11.01	10.77	N
45	0.27	0.29	0.62	0.65	10.99	11.00	Y
46	0.31	0.36	0.92	1.01	10.95	10.94	Y
47	0.25	0.26	1.02	1.04	10.97	10.94	Y
48	0.27	0.29	1.29	1.36	11.04	11.09	Y
49	0.28	0.30	1.36	1.42	10.91	10.97	Y
50	0.29	0.32	1.36	1.43	11.02	11.04	Y
51	0.34	0.32	1.04	0.99	10.98	10.89	N
52	0.22	0.21	1.11	1.08	10.96	10.70	N
53	0.25	0.26	1.15	1.16	10.95	10.97	Y
54	0.34	0.30	1.47	1.37	11.03	10.93	Y
55	0.31	0.37	1.10	1.24	10.96	11.13	Y
56	0.32	0.41	1.29	1.50	11.22	11.20	Y
57	0.33	0.26	1.27	1.07	10.96	10.81	N
58	0.27	0.28	1.49	1.54	11.00	11.04	N
59	0.23	0.29	1.10	1.30	10.94	11.12	Y
60	0.34	0.34	1.05	1.05	10.99	10.99	Y
61	0.31	0.29	1.08	1.03	11.09	11.03	Y

scatter after the validation do not qualify as compact and massive anymore, according to our formal definition.

A very important point to stress here is that, in the validation process, we do not propagate the error on the photometric and spectroscopic redshifts into masses and sizes errors. We simply use the face values and include/exclude galaxies on the basis of the resulting nominal size and mass values. This might lead us to lose some galaxies at the edges, but it simplifies the analysis of the systematics—as is necessary to correct the number density (see Section 4.3). If we take into account the average statistical  $1\sigma$ -level uncertainties for the measured effective radii and the stellar masses calculated in T18 (see the paper), i.e.,  $\delta R_e \sim 20\%$  and  $\delta \log_{10}(M_*/M_\odot) \sim 0.15$ , we confirm as UCMGs 57 out of 61 UCMG candidates ( $\sim 93\%$ ). If we consider, instead, the  $3\sigma$ -level uncertainties, all the candidates are statistically consistent with the UCMG definition. In the following, we analyze the systematics considering the face values for  $R_e$  and  $M_*$  in the selection.

#### 4.2. Contamination and Incompleteness

One of the main aims of our spectroscopic campaigns is to quantify the impact of systematics on the UCMG photometric selection. Because of the uncertain photometric redshifts, the candidate selection: (1) includes “contaminants” (or false positives), i.e., galaxies that are selected as UCMGs according to their photometric redshifts, but would not be considered ultracompact and massive when recalculating the masses on the basis of the more accurate spectroscopic redshift values (see T16 and T18), and (2) “missed” systems (or false negatives),

i.e., those galaxies that are not selected as UCMGs according to their photometric redshifts, but would be selected using the spectroscopic values instead (i.e., they are real UCMGs that our selection excluded). Thus, following T18, we define the *contamination factor*,  $C_F$ , as the inverse of the SR discussed in the previous subsection, to account for the number of “contaminants” and the *incompleteness factor*,  $\mathcal{I}_F$ , as the difference between the number of UCMG candidates using  $z_{\text{spec}}$  and  $z_{\text{phot}}$ , to estimate the incompleteness of the sample, i.e., quantifying the number of “missing” objects.

In this section, we only report the average values for these factors across the full redshift range. We use different values calculated in different redshift bins to correct the abundances presented in Section 4.3. To estimate the fraction of contaminants, we need UCMG samples selected using the photometric redshifts, but for which we also have spectroscopic redshifts available. Thus, we evaluate  $C_F$  using three different photometrically selected samples with  $z_{\text{phot}} < 0.5$ :

- the new sample of 33 UCMG candidates presented in this paper and discussed in Section 3;
- the 27 (out of 28) UCMG candidates from T18 that satisfy the new mass and size selection based on  $z_{\text{phot}}$ , using the new setup for stellar masses adopted here;
- the sample of 50 photometrically selected galaxies introduced in Section 2.2, UCMG\_PHOT\_SPEC with measured spectroscopic redshifts from SDSS, GAMA, and 2dFLenS, similar to the one presented in T18 but selected with the new mass setup.

For (a), the new sample of UCMGs presented in this paper, we obtain a  $C_F = 1.72$  (corresponding to an SR of 58%; see Section 4.1). Considering the samples in (b) and (c), we find  $C_F = 1.50$  and 1.72, respectively. Joining these three samples, we collect a sample of 110 UCMG candidates, of which 68 have been validated after spectroscopy, implying a cumulative SR of 62% or  $C_F = 1.62$ .

To quantify how many real UCMGs are missing from the photometric selection (incompleteness), we need to use objects with spectroscopic redshifts available from the literature. Thus, to determine  $\mathcal{I}_F$ , we use UCMG\_SPEC: the sample of spectroscopically validated UCMGs with spectroscopic redshifts from SDSS, GAMA, and 2dFLenS. This sample updates and complements the one already presented in T18 (Tables C1 and C2) and consists of 54 galaxies between  $0.15 < z < 0.5$ . The basic photometric and structural parameters for these UCMGs in the spectroscopically selected sample are given in the Appendix. Only 29 out of 54 galaxies, i.e., 54%, would have been selected as candidates using  $z_{\text{phot}}$  instead of  $z_{\text{spec}}$ , which corresponds to  $\mathcal{I}_F = 1.86$ .

Having estimated contaminants and incompleteness, we can now obtain the correction factor for the number counts, as  $\mathcal{I}_F/C_F$ . In conclusion, we find that the true number counts for UCMGs at  $z < 0.5$  would be  $\sim 15\%$  higher than the values one would find in a photometrically selected sample, on average. This is valid for the whole redshift range we consider here. In the next section, we instead calculate a correction in each single redshift bin, to minimize the errors on number counts.

#### 4.3. UCMG Number Counts

UCMG number counts are calculated following the procedure outlined in T18. For completeness, we report here some details.

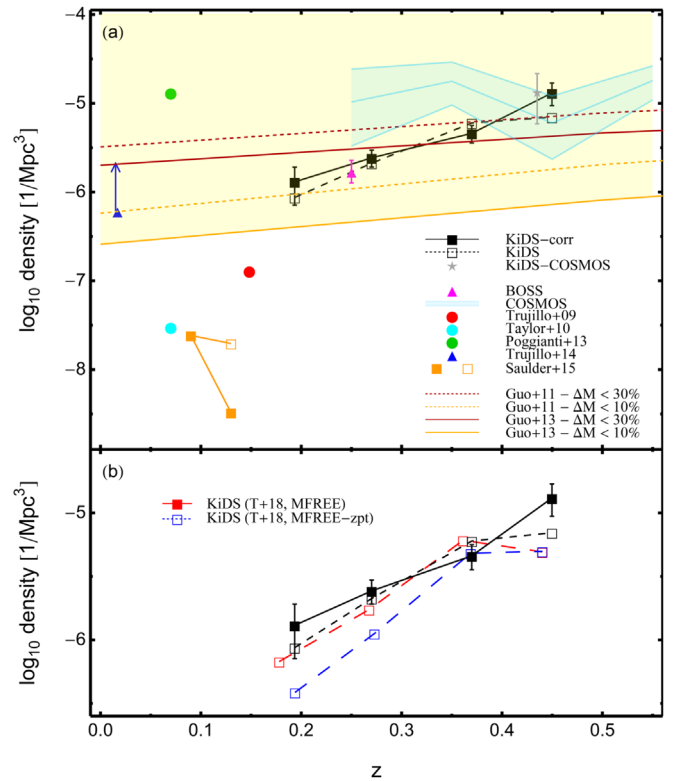


**Figure 7.** Panel (a): Filled (open) black squares, with a solid (dashed) line, referred to as KiDS-corr(KiDS) in the legend, plot the number density after (before) correction for systematics, for the selected sample assuming reference masses. Error bars denote  $1\sigma$  uncertainties, taking into account Poisson noise, cosmic variance, and errors on  $M_*$  and  $R_e$  (see the text for more details). Gray star is for the UCMG candidates at  $z < 0.5$  found in the tile KIDS\_150.1\_2.2, centered on the COSMOS field. Other colored symbols indicate number densities obtained from other papers, as described in the caption. Panel (b): Number counts obtained here are compared with those presented in T18, named MFREE and MFREE-zpt; see the text for more details.

Taking into account the two systematic effects discussed in Section 4.2, we correct the number counts of the 1221 candidates in UCMG\_FULL. In Figure 7, we plot the uncorrected and corrected counts as open squares/dashed line and filled squares/solid lines, respectively. We bin galaxies in four redshift bins ( $z \in (0.15, 0.2)$ ,  $(0.2, 0.3)$ ,  $(0.3, 0.4)$ ,  $(0.4, 0.5)$ ), and normalize to the comoving volume corresponding to the observed KiDS effective sky area of  $333 \text{ deg}^2$  (see T18 for further details). The errors on number counts take into account fluctuations due to Poisson noise, as well as those due to large-scale structure, i.e., the cosmic variance.<sup>21</sup> For this calculation, we use the number of spectroscopically validated UCMGs in each redshift bin. The uncertainties in stellar mass and effective radius measurements are also included in the error budget (as discussed in T18). The number density expectation for the KiDS tile centered on the COSMOS field is also plotted as a gray star. Increasing the number of confirmed objects, thanks to the validation presented in this paper, we are able to reduce the error budget from cosmic variance and Poisson noise to 5–25% in the four redshift bins.

The final result is fully consistent with the one found in T18 and shows a decrease of number counts with cosmic time, from  $\sim 9 \times 10^{-6} \text{ Mpc}^{-3}$  at  $z \sim 0.5$ , to  $\sim 10^{-6} \text{ Mpc}^{-3}$  at  $z \sim 0.15$ .

<sup>21</sup> These sources of errors are calculated according to Trenti & Stiavelli (2008).

The number of UCMGs decreases by a factor of  $\sim 9$  in about 3 Gyr.

Following T18, we also compare our findings to lower-redshift analyses (Trujillo et al. 2009, 2014; Taylor et al. 2010; Poggianti et al. 2013a; Saulder et al. 2015), as well as to other intermediate-redshifts studies (Damjanov et al. 2014, BOSS; Damjanov et al. 2015a, COSMOS). The reader is referred to T18 for a more detailed comparison between the different literature results and a detailed discussion on the impact of the different thresholds and selection criteria that different publications have used. In particular, we do not plot here the results obtained in Charbonnier et al. (2017) and Buitrago et al. (2018), because those authors use a less restrictive size criterion ( $R_e < 2$  kpc). However, including those results, we would have a perfect agreement with the number densities reported in Charbonnier et al. (2017), in terms of normalization and evolution with redshift.

Finally, we also make a comparison with the results presented in Quilis & Trujillo (2013), who have determined the evolution of the number counts of compact galaxies from semi-analytical models, based on the Millennium  $N$ -body simulations by Guo et al. (2011, 2013). They define “relic compacts” as those galaxies with mass changing less than 10–30%, from  $z \sim 2$ . The redshift evolution predicted by these simulations is milder than that obtained with our data, which are in agreement with COSMOS selection at  $z \sim 0.5$  instead (Damjanov et al. 2015a), and with the most recent number density determination in the local environment made by Trujillo et al. (2014).

In the bottom panel of Figure 7, we directly compare our uncorrected and corrected (for systematics) counts with those found in T18, where we used two different setups for the stellar mass derivation, both of them without any constraints on ages and metallicity (which we instead set here in this paper, as described in Section 2.1). In particular, the MFREE masses (red lines and points in the plot) do not include zero-point calibration errors, while MFREE-zpt ones (blue points) do include such contributions. Our results are in a good agreement with the reference T18 results assuming MFREE, and consistent within  $2\sigma$  with the T18 results assuming MFREE-zpt.

It is important to remark that, in Figure 7, we obtain number counts for all the UCMGs—without any distinction between relics (old stellar population) and nonrelics (young stellar population). Unfortunately, the spectra obtained here and in our previous runs (T18) do not reach a signal-to-noise high enough to allow us to perform an in-depth stellar population analysis. This is, however, a *conditio sine qua non* to isolate these compact and massive galaxies, whose stellar population is as old as the universe and has been formed *in situ* during the first phase of the two-phase formation scenario (Oser et al. 2010). We will thus postpone this more detailed analysis and the redefinition of the obtained number densities to a future publication, where we will remove the nonrelic contaminants thanks to spectroscopic stellar population modeling.

#### 4.4. Relationship between Stellar Mass and Velocity Dispersion

The correlation between luminosity (or stellar mass) and velocity dispersion in elliptical galaxies is a well-established scaling relation (Faber & Jackson 1976; Hyde & Bernardi 2009).

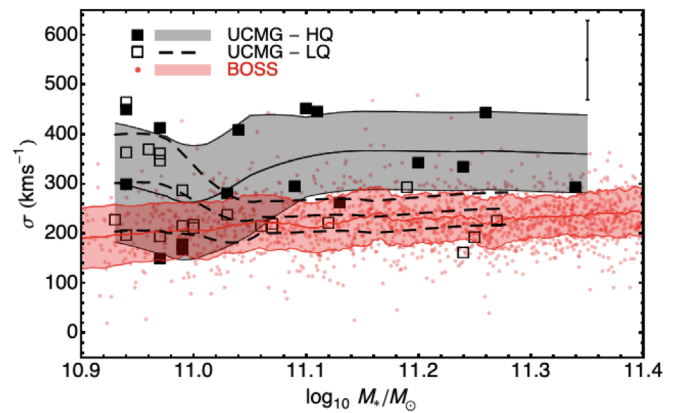


**Figure 8.** Distribution on the  $M_*$ – $\sigma$  plane for the 37 confirmed UCMGs compared with a sample of elliptical galaxies (red symbols) from the BOSS survey. Filled square symbols are UCMGs classified as HQ, with spectra that simultaneously satisfy the three conditions  $SR \geq 0.3$ ,  $S/N_{\text{spec}} \geq 3.5$ , and  $(S/N)_{O-K} \geq 6.5$ . Empty squares are instead classified as LQ because their spectra do not satisfy one or more of the aforementioned criteria. For each sample, running means and  $1\sigma$  scatter are overplotted. In the top right corner, we show the mean error bar for the UCMG velocity dispersions. For both UCMGs and the sample of ellipticals, velocity dispersions are calculated within one effective radius, as explained in the text.

The location of UCMGs in a mass–velocity dispersion diagram ( $M_*$ – $\sigma$ ) can give remarkable insights regarding their intrinsic properties (Saulder et al. 2015). Indeed, given the compact sizes of UCMGs, the virial theorem predicts larger velocity dispersions with respect to normal-sized galaxies of similar mass. This has also been directly confirmed with deep spectroscopy of a handful of these objects at high redshift (van Dokkum et al. 2009; Toft et al. 2012) and of the three local relics (Ferré-Mateu et al. 2017). Therefore, UCMGs should segregate in this parameter space, having a mass–velocity dispersion correlation different from that of normal-sized galaxies. Further, because this  $M_*$ – $\sigma$  relation is intimately connected to the assembly of baryons and dark matter, it can also provide important constraints on our understanding of the formation and evolution of these systems. This might be particularly important in the specific case of relics.

In this section, we present a preliminary result on the  $M_*$ – $\sigma$  relation, based on the velocity dispersion measurements presented in Section 3.4.

In Figure 8, we plot the  $M_*$ – $\sigma$  distribution of the 37<sup>22</sup> confirmed UCMGs (squared symbols).

For comparison, we overplot a sample of normal-sized ETGs (red small dots) analyzed in Tortora et al. (2018a) and derived from SDSS-III/BOSS (Baryon Oscillation Spectroscopic Survey) Data Release 10<sup>23</sup> (DR10; Ahn et al. 2014). We restrict the BOSS sample to the redshift range  $0.15 \lesssim z \lesssim 0.5$ , in order to provide a direct comparison with the sample of UCMGs. For these systems, in Tortora et al. (2018a) we have derived stellar masses using the same setup adopted in this paper, while the velocity dispersion values were originally measured in a circular aperture of radius  $1''$ .

The distribution of all the confirmed UCMGs presents a large scatter, which is mainly the consequence of the large errors on the velocity dispersion values (see typical error bars in top right

<sup>22</sup> We have a total of 19 confirmed systems from the three new spectroscopic runs, and 18 from the runs presented in T18 and confirmed on the basis of the new mass-calculation setup.

<sup>23</sup> The data catalogs are available from [http://www.sdss3.org/dr10/spectro/galaxy\\_portsmouth.php](http://www.sdss3.org/dr10/spectro/galaxy_portsmouth.php).

corner of the figure). We plot with full squares UCMGs classified in the HQ group, and open squares represent the ones belonging to the LQ group, according to the definition given in Section 3.4.

Finally, in order to highlight significant patterns in this figure, we also plot the running mean and  $1\sigma$  scatter for the UCMGs and BOSS galaxies. The running means obtained from the UCMGs in the HQ subsample (i.e., the gray shaded region in the figure) and that obtained for all the normal-sized BOSS galaxies (i.e., red region) differ significantly. The UCMGs have systematically larger velocity dispersions at any fixed mass, especially above  $\log M_*/M_\odot = 11.05$ , and this result is consistent with other studies of high- $z$  systems (van Dokkum et al. 2009; Toft et al. 2012) and local massive relics (Ferré-Mateu et al. 2017). The offset almost disappears when including the LQ UCMGs—which, at least for larger masses, are scattered toward lower  $\sigma$  and are consistent with the normal ETG distribution within the (large) errors.

We consider the offset between BOSS and HQ UCMGs robust and statistically significant, although we anticipate that with better data we will be able to improve the measurement errors and also increase the size of the sample. Nevertheless, taking these finding at face value, one can speculate about possible explanations for this offset. The first possibility is that more compact massive galaxies host a more massive black hole (e.g., van den Bosch et al. 2012, 2015; Ferré-Mateu et al. 2017), which might influence the kinematics in the innermost region. Another possibility is that the IMF in very massive galaxies can be different from a universal Milky Way–like IMF. However, whereas the bottom-heavy IMF for larger galaxies is restricted only in the very central region ( $\sim 0.2\text{--}0.3R_e$ ), the IMF for relics is heavier than Salpeter everywhere up to few effective radii. One physical scenario able to explain this difference would be that only the *in situ* stars formed during the first phase of the assembly of massive ETGs form with a dwarf-rich IMF, while accreted stars (only present in normal-sized ETGs) form with a standard IMF (Chabrier et al. 2014).

We will investigate these possibilities in a dedicated paper, already in preparation. There, we will compare these (and new) measurements with theoretically motivated predictions, including more than one galaxy formation recipe. We will check whether the  $M_*\text{--}\sigma$  relation preserves the footprints of the stellar and dark assembly of these systems, trying to quantify the dynamical contribution of a central supermassive black hole and a bottom-heavy IMF.

In conclusion, given the large uncertainties on the velocity dispersion measurements and the fact that we cannot yet distinguish between relics and non-relics, we provide here only some preliminary speculative explanations. In the future, we aim at consolidating this result with a larger number of systems, to increase the statistics. We also intend to use spectroscopic data of better quality, in order to have more robust velocity dispersion estimates. With new, better spectroscopic data, we will also be able to constrain the age of the systems, which is the crucial ingredient to identify relics among the confirmed UCMGs.

## 5. Conclusions

The existence of UCMGs at  $z < 1$  and their evolution up to the local universe challenges the currently accepted galaxy formation models. In an effort to “bridge the gap” between the

high-redshift red nuggets and the local relics, we have started a census of UCMGs at intermediate redshifts. In particular, in the first paper of this series (Tortora et al. 2016), we have demonstrated that the high image quality, the large area covered, the excellent spatial resolution, and the exquisite seeing of the KiDS make this survey perfect to find UCMG candidates. In the second paper (Tortora et al. 2018b), we have started a multisite and multitelescope spectroscopic observational campaign to confirm as many candidates as possible, with the final goal of building the largest spectroscopically confirmed sample of UCMGs in the redshift range  $0.15 \lesssim z \lesssim 0.5$ .

In this third paper of the series, we have continued in this direction and accomplished the following.

1. We have spectroscopically followed up a sample of 33 UCMG candidates at redshifts  $0.15 \lesssim z \lesssim 0.5$ , found in  $333 \text{ deg}^2$  of KiDS. We have provided details on how the galaxies have been photometrically selected and discussed the spectroscopic campaign on the INT and TNG telescopes, including also the main data reduction steps for each instrument.
2. We have obtained the spectroscopic redshift and velocity dispersion values for these objects, and for the 28 objects already presented in T18. To this purpose, we have used the Optimized Modeling of Early-type Galaxy Aperture Kinematics pipeline (OMEGA-K; G. D’Ago et al. 2020, in preparation).
3. We have confirmed 19 out of 33 as UCMGs, with the newly spectroscopically based masses and effective radii. This translates into a SR of 58%, in good agreement with the one reported in T18. In addition, using the new mass setup, we have confirmed 18 out of 27 UCMGs from T18, corresponding to a SR of 67%. One galaxy from T18 did not qualify as UCMG candidate when recomputing its mass with the newly defined setup. Thus, in total, we confirm as UCMGs 37 out of 61 candidates, implying an SR of 60%. Allowing a tolerance at the  $1\sigma$  level ( $3\sigma$  level) on the effective radii and stellar masses inferred from the spectroscopic redshifts, we confirm as UCMGs 57 (61) out of 61 UCMG candidates, with an SR of  $\sim 93\%$  (100%).
4. We have quantified the effect of contamination and incompleteness due to the difference in redshift between the photometric and spectroscopic values. We have found that the true number counts for UCMGs at  $z < 0.5$  is  $\sim 15\%$  higher than the values found in a photometrically selected sample.
5. We have obtained the UCMG number counts, after correcting them with the incompleteness and the contamination factors, as well as their evolution with redshift in the range  $0.15 < z < 0.5$ . We have also compared our results with those obtained in T18, using a different setup for the mass inference, and with the ones in the literature. We have confirmed the clear decrease of the number counts with the cosmic time already found in T18: from  $\sim 9 \times 10^{-6} \text{ Mpc}^{-3}$  at  $z \sim 0.5$ , to  $\sim 10^{-6} \text{ Mpc}^{-3}$  at  $z \sim 0.15$ ,  $\sim 9$  times less in about 3 Gyr.
6. We have shown the distribution of the 37 confirmed UCMGs in the  $M_*\text{--}\sigma$  plane. We have corrected the sigma values to a common aperture of one effective radius, in order to compare the UCMGs distribution with that of a sample of normal-sized ellipticals from the BOSS Survey.



Despite the large uncertainties on the velocity dispersion measurements, due to the low signal-to-noise of the spectra, we found tentative evidence suggesting that the UCMGs have larger values compared to regular ETGs of same mass. This seems to be statistically significant, at least for the HQ sample and large masses. This preliminary result, in agreement with that expected from the evolution of massive and compact galaxies, will be checked again once new, higher-resolution spectroscopy (already awarded) has been obtained.

After KiDS has been completed, we expect to at least double the number of confirmed UCMGs, and thus reduce by a factor  $\sim 40\%$  the uncertainties on the number counts, while keeping the systematics under full control.

In the future, we also plan to continue to enlarge the sample of spectroscopically confirmed UCMGs at low and intermediate redshifts, based on photometric candidates from the KiDS survey. Moreover, thanks to already awarded spectroscopic data with much higher S/N, which will allow us to perform a detailed stellar population analysis, we will separate relics from younger UCMGs. With the higher signal-to-noise spectra that we will soon have at our disposal, we aim to unambiguously demonstrate that the majority of the objects in our sample are indeed red and dead, as already indicated by their photometric colors, and that they have formed their baryonic matter early on in cosmic time, with a fast and “bursty” star formation episode. In this way, we will be able to unambiguously confirm the two-phase formation scenario proposed for the mass assembly of massive/giant ETGs (Oser et al. 2010).

Relics, UCMGs as old as the universe, are the only systems that, with current observing facilities, allow us to study the physical processes that shaped the mass assembly of massive galaxies in the high- $z$  universe with an amount of detail currently attainable only for the nearby universe.

D.S. is a member of the International Max Planck Research School (IMPRS) for Astronomy and Astrophysics at the Universities of Bonn and Cologne. C.T. acknowledges funding from the INAF PRIN-SKA 2017 program 1.05.01.88.04. M.S. acknowledges financial support from the VST project (PI: P. Schipani). C.S. has received funding from the European Union’s Horizon 2020 research and innovation programme under the Marie Skłodowska-Curie actions grant agreement No 664931. G.D. acknowledges support from CONICYT project Basal AFB-170002. M.B. acknowledges the *INAF PRIN-SKA*

*2017 program 1.05.01.88.04*, funding from *MIUR Premiale 2016: MITIC*, and financial contribution from the agreement ASI/INAF nr. 2018-23-HH.0 *Euclid mission scientific activities - Phase D*. The INT is operated on the island of La Palma by the Isaac Newton Group of Telescopes in the Spanish Observatorio del Roque de los Muchachos of the Instituto de Astrofísica de Canarias. Based on observations made with the Italian Telescopio Nazionale Galileo (TNG) and Isaac Newton (INT) telescopes operated by the Fundación Galileo Galilei of the INAF (Istituto Nazionale di Astrofisica) and the Isaac Newton Group of Telescopes, both of which are installed in the Spanish Observatorio del Roque de los Muchachos of the Instituto de Astrofísica de Canarias. Based on data products from observations made with ESO Telescopes at the La Silla Paranal Observatory under programme IDs 177.A-3016, 177.A-3017, and 177.A-3018, as well as on data products produced by Target/OmegaCEN, INAF-OACN, INAF-OAPD, and the KiDS production team, on behalf of the KiDS consortium. OmegaCEN and the KiDS production team acknowledge support by NOVA and NWO-M grants. Members of INAF-OAPD and INAF-OACN also acknowledge support from the Department of Physics & Astronomy of the University of Padova, as well as from the Department of Physics of the Univ. Federico II (Naples).

## Appendix

In order to quantify the impact of the systematics on the UCMG selection, we have created (in Section 4.2) the UCMG\_SPEC sample: a sample of 55 UCMGs with spectroscopic redshifts from the literature, similar to the sample used in T18, but selected with the new mass setup. We have gathered these spectroscopic redshifts from SDSS (Ahn et al. 2012, 2014), GAMA (Driver et al. 2011), which overlap the KiDS fields in the Northern cap, and 2dFLenS (Blake et al. 2016), observed in the Southern hemisphere. Here in this appendix, we provide the basic photometric and structural parameters for such 55 UCMGs in the spectroscopically selected sample. In particular, in Table A1 we show  $r$ -band Kron magnitude, aperture magnitudes used in the SED fitting, spectroscopic redshifts, and stellar masses (in decimal logarithm). Sérsic structural parameters from the 2DPHOT fit of  $g$ -,  $r$ -, and  $i$ -band KiDS surface photometry, such as  $\chi^2$ s and S/N values, are instead presented in Table A2.

**Table A1**  
Integrated Photometry for the 55 Systems in the UCMG\_SPEC Sample

ID	Name	MAG_AUTO_r	$u_6''$	$g_6''$	$r_6''$	$i_6''$	$z_{\text{phot}}$	$\log_{10} M_*/M_{\odot}$
L1	KIDS J025942.84–315933.74	18.96	22.61 ± 0.13	20.39 ± 0.008	18.97 ± 0.003	18.52 ± 0.007	0.29	11.00
L2	KIDS J032700.87–300112.34	20.37	23.02 ± 0.21	21.93 ± 0.04	20.34 ± 0.009	19.43 ± 0.01	0.33	11.00
L3	KIDS J084320.59–000543.77	18.52	21.55 ± 0.06	19.71 ± 0.005	18.53 ± 0.002	18.12 ± 0.005	0.24	10.93
L4	KIDS J084738.70+011220.57	18.41	21.78 ± 0.12	19.70 ± 0.006	18.44 ± 0.002	18.02 ± 0.005	0.18	11.00
L5	KIDS J085335.58+001805.97	18.84	21.67 ± 0.09	20.13 ± 0.009	18.95 ± 0.003	18.63 ± 0.008	0.33	10.94
L6	KIDS J085344.88+024948.47	18.49	21.63 ± 0.07	19.70 ± 0.005	18.50 ± 0.002	18.08 ± 0.005	0.23	10.93
L7	KIDS J090324.20+022645.50	17.25	20.24 ± 0.02	18.34 ± 0.002	17.34 ± 0.001	16.98 ± 0.001	0.19	11.21
L8	KIDS J090935.74+014716.81	18.68	22.52 ± 0.17	20.15 ± 0.008	18.75 ± 0.002	18.23 ± 0.006	0.22	11.02
L9	KIDS J092055.70+021245.66	18.87	22.80 ± 0.21	20.37 ± 0.01	18.89 ± 0.003	18.46 ± 0.005	0.28	11.01
L10	KIDS J102653.56+003329.15	17.39	20.49 ± 0.02	18.52 ± 0.002	17.45 ± 0.001	17.04 ± 0.002	0.17	11.17
L11	KIDS J112825.16–015303.29	20.94	23.90 ± 0.57	22.56 ± 0.06	20.91 ± 0.01	20.19 ± 0.04	0.46	10.94
L12	KIDS J113612.68+010316.86	19.01	22.07 ± 0.08	20.26 ± 0.007	19.02 ± 0.003	18.59 ± 0.005	0.22	10.97
L13	KIDS J114248.56+001215.63	17.02	19.72 ± 0.01	17.95 ± 0.002	17.14 ± 0.0008	16.71 ± 0.001	0.11	10.58
L14	KIDS J115652.47–002340.77	18.83	21.98 ± 0.09	20.06 ± 0.007	18.83 ± 0.003	18.08 ± 0.006	0.26	11.14
L15	KIDS J120251.61+013825.15	17.89	20.69 ± 0.03	19.39 ± 0.003	18.04 ± 0.001	17.75 ± 0.003	0.20	11.04
L16	KIDS J120818.93+004600.16	17.74	20.65 ± 0.03	18.88 ± 0.004	17.93 ± 0.001	17.56 ± 0.002	0.18	10.92
L17	KIDS J120902.53–010503.08	18.83	22.68 ± 0.21	20.16 ± 0.008	18.82 ± 0.003	18.36 ± 0.008	0.27	11.04
L18	KIDS J121152.97–014439.23	18.60	21.64 ± 0.08	19.79 ± 0.006	18.65 ± 0.003	18.23 ± 0.005	0.23	10.96
L19	KIDS J121555.27+022828.13	20.56	23.36 ± 0.32	22.21 ± 0.04	20.53 ± 0.01	19.81 ± 0.02	0.47	10.97
L20	KIDS J140620.09+010643.00	19.16	22.55 ± 0.13	20.68 ± 0.01	19.19 ± 0.004	18.70 ± 0.009	0.37	11.28
L21	KIDS J141108.94–003647.51	19.22	22.27 ± 0.14	20.57 ± 0.01	19.20 ± 0.004	18.74 ± 0.01	0.29	10.98
L22	KIDS J141200.92–002038.65	19.19	22.94 ± 0.27	20.76 ± 0.02	19.21 ± 0.005	18.69 ± 0.02	0.28	11.08
L23	KIDS J141213.62+021202.06	18.37	19.30 ± 0.01	19.14 ± 0.004	18.38 ± 0.002	18.16 ± 0.005	0.30	11.06
L24	KIDS J141415.53+000451.51	18.99	22.86 ± 0.17	20.41 ± 0.009	19.00 ± 0.003	18.50 ± 0.006	0.30	11.07
L25	KIDS J141417.33+002910.20	18.77	21.73 ± 0.07	20.04 ± 0.007	18.77 ± 0.003	18.34 ± 0.006	0.30	11.03
L26	KIDS J141728.44+010626.61	17.90	20.94 ± 0.04	19.06 ± 0.004	17.98 ± 0.002	17.59 ± 0.003	0.18	10.96
L27	KIDS J141828.24–013436.27	18.82	21.13 ± 0.07	19.90 ± 0.006	18.80 ± 0.003	18.39 ± 0.005	0.43	11.26
L28	KIDS J142033.15+012650.38	19.38	23.58 ± 0.38	20.79 ± 0.02	19.37 ± 0.005	18.89 ± 0.01	0.32	10.92
L29	KIDS J142041.17–003511.27	18.95	22.40 ± 0.14	20.37 ± 0.009	19.01 ± 0.003	18.51 ± 0.005	0.25	11.00
L30	KIDS J142235.50–014207.95	19.24	23.10 ± 0.27	20.65 ± 0.01	19.27 ± 0.004	18.82 ± 0.009	0.28	10.92
L31	KIDS J142606.67+015719.28	19.33	22.97 ± 0.22	20.69 ± 0.01	19.30 ± 0.005	18.86 ± 0.01	0.35	11.14
L32	KIDS J142800.20–001026.87	18.75	19.42 ± 0.01	19.33 ± 0.004	18.83 ± 0.003	18.56 ± 0.009	0.33	11.05
L33	KIDS J142922.11+011450.00	18.69	21.95 ± 0.12	20.09 ± 0.008	18.69 ± 0.003	18.35 ± 0.007	0.37	11.10
L34	KIDS J143025.44–023311.23	18.80	19.25 ± 0.01	19.13 ± 0.005	18.79 ± 0.003	18.49 ± 0.007	0.40	11.15
L35	KIDS J143155.56–000358.65	19.34	22.74 ± 0.18	20.73 ± 0.02	19.32 ± 0.004	18.82 ± 0.007	0.34	11.04
L36	KIDS J143419.53–005231.62	19.14	22.64 ± 0.17	20.79 ± 0.01	19.13 ± 0.004	18.57 ± 0.005	0.46	11.20
L37	KIDS J143459.11–010154.63	19.37	22.95 ± 0.25	20.70 ± 0.01	19.36 ± 0.004	18.88 ± 0.01	0.28	10.96
L38	KIDS J143528.88+013055.39	19.31	22.82 ± 0.33	20.65 ± 0.02	19.31 ± 0.004	18.81 ± 0.01	0.28	10.91
L39	KIDS J143607.24+003902.15	19.18	22.87 ± 0.23	20.64 ± 0.01	19.17 ± 0.004	18.72 ± 0.008	0.30	10.92
L40	KIDS J143611.55+000718.29	18.27	21.53 ± 0.06	19.57 ± 0.004	18.29 ± 0.002	17.87 ± 0.004	0.22	11.06
L41	KIDS J143616.24+004801.40	19.24	22.78 ± 0.25	20.62 ± 0.01	19.24 ± 0.004	18.76 ± 0.009	0.29	11.08
L42	KIDS J143805.25–012729.78	19.29	22.74 ± 0.19	20.64 ± 0.01	19.29 ± 0.004	18.73 ± 0.007	0.29	10.94
L43	KIDS J144138.27–011840.93	19.35	23.62 ± 0.48	20.78 ± 0.01	19.35 ± 0.004	18.83 ± 0.008	0.29	11.00
L44	KIDS J144557.12–013510.24	19.16	22.12 ± 0.13	20.45 ± 0.009	19.15 ± 0.004	18.73 ± 0.009	0.29	10.92
L45	KIDS J144751.78–014927.41	18.61	21.88 ± 0.11	19.87 ± 0.007	18.63 ± 0.003	18.17 ± 0.005	0.21	10.93
L46	KIDS J144924.11–013845.59	19.40	22.79 ± 0.24	20.82 ± 0.02	19.39 ± 0.005	18.89 ± 0.009	0.27	11.01
L47	KIDS J145245.48+025321.32	17.69	20.60 ± 0.03	18.74 ± 0.002	17.77 ± 0.001	17.50 ± 0.003	0.26	11.18
L48	KIDS J145356.13+001849.32	20.32	23.24 ± 0.30	22.06 ± 0.04	20.32 ± 0.009	19.68 ± 0.03	0.42	11.16
L49	KIDS J145638.63+010933.24	19.66	23.21 ± 0.26	21.31 ± 0.02	19.63 ± 0.006	19.09 ± 0.01	0.42	11.18
L50	KIDS J153936.50–003904.58	20.15	21.46 ± 0.09	20.76 ± 0.02	20.11 ± 0.01	19.70 ± 0.02	0.47	10.99
L51	KIDS J154949.48–003655.52	19.02	19.38 ± 0.01	19.19 ± 0.004	19.02 ± 0.004	18.86 ± 0.01	0.47	11.30
L52	KIDS J155133.16+005709.77	19.37	24.82 ± 1.76	20.95 ± 0.02	19.34 ± 0.005	18.86 ± 0.01	0.42	11.29
L53	KIDS J220453.48–311200.94	19.32	22.90 ± 0.23	20.84 ± 0.01	19.34 ± 0.004	18.87 ± 0.005	0.26	10.96
L54	KIDS J231410.93–324101.31	19.26	22.59 ± 0.16	20.56 ± 0.009	19.26 ± 0.004	18.75 ± 0.006	0.29	11.01
L55	KIDS J233148.39–333402.05	20.46	24.47 ± 0.74	22.12 ± 0.04	20.44 ± 0.009	19.78 ± 0.02	0.48	11.09

**Notes.** From left to right, we show: (a) progressive ID number; (b) KIDS identification name; (c)  $r$ -band KiDS MAG\_AUTO; (d)–(g)  $u$ -,  $g$ -,  $r$ -, and  $i$ -band KiDS magnitudes measured in an aperture of  $6''$  of diameter with  $1\sigma$  errors; (h) spectroscopic redshift. All the magnitudes have been corrected for Galactic extinction using Schlafly & Finkbeiner (2011) maps.

**Table A2**  
Structural Parameters Derived Running 2DPHOT on  $g$ -,  $r$ -, and  $i$ -bands for the 55 in the UCMG\_SPEC Sample














ID	g-band							r-band							i-band						
	$\Theta_e$	$R_e$	$n$	$q$	$\chi^2$	$\chi'^2$	S/N	$\Theta_e$	$R_e$	$n$	$q$	$\chi^2$	$\chi'^2$	S/N	$\Theta_e$	$R_e$	$n$	$q$	$\chi^2$	$\chi'^2$	S/N
L1	0.25	1.07	4.11	0.34	1.02	1.05	123	0.27	1.19	4.54	0.37	1.07	1.35	367	0.29	1.27	5.62	0.39	1.00	0.93	147
L2	0.05	0.24	4.66	0.12	1.01	0.98	32	0.16	0.74	4.03	0.33	1.02	1.01	127	0.24	1.12	2.96	0.42	0.98	0.87	96
L3	0.29	1.12	4.40	0.58	1.03	1.06	190	0.26	1.01	5.59	0.61	1.20	1.72	506	0.33	1.25	8.48	0.68	1.01	0.95	203
L4	0.46	1.36	3.06	0.27	1.01	1.04	165	0.46	1.39	4.38	0.25	1.07	1.42	462	0.45	1.35	3.33	0.27	1.01	0.96	177
L5	0.56	2.65	10.56	0.75	1.02	0.99	94	0.23	1.09	9.84	0.80	1.12	1.87	279	0.22	1.03	9.27	0.73	1.02	1.04	99
L6	0.39	1.44	3.83	0.46	1.02	1.03	185	0.34	1.25	4.13	0.44	1.08	1.47	443	0.34	1.26	4.00	0.42	1.05	1.10	190
L7	0.46	1.45	4.34	0.24	1.05	1.40	492	0.23	0.73	7.04	0.29	1.34	2.89	1003	0.54	1.70	4.82	0.26	1.06	1.32	641
L8	0.56	1.96	9.95	0.81	0.83	0.86	110	0.14	0.48	10.07	0.76	1.13	1.84	357	0.30	1.05	9.97	0.77	1.01	1.00	152
L9	0.41	1.76	1.97	0.34	1.03	1.13	95	0.34	1.46	1.99	0.32	1.04	1.34	351	0.28	1.20	3.02	0.30	1.00	1.04	206
L10	0.43	1.26	2.70	0.29	1.07	11.51	360	0.32	0.95	3.64	0.29	1.12	25.78	1092	0.34	1.01	3.18	0.29	1.03	9.58	464
L11	0.31	1.78	8.80	0.21	0.99	1.10	16	0.25	1.46	8.54	0.44	1.03	0.99	74	0.21	1.22	3.66	0.59	1.01	1.28	32
L12	0.29	1.02	4.03	0.26	1.07	1.03	130	0.14	0.48	7.96	0.27	1.05	1.20	327	0.11	0.40	8.07	0.25	1.02	0.96	188
L13	0.37	1.39	4.79	0.38	1.03	0.99	602	0.20	1.26	6.53	0.40	1.03	1.18	1109	0.26	1.39	8.63	0.38	1.01	0.94	618
L14	0.71	1.47	3.60	0.22	1.12	1.46	140	0.64	0.79	5.26	0.23	1.40	2.32	381	0.70	1.03	3.48	0.24	1.04	1.19	163
L15	0.28	0.93	9.55	0.72	1.08	1.54	275	0.35	1.15	7.85	0.64	1.31	3.19	621	0.45	1.50	10.06	0.73	1.04	1.13	239
L16	0.50	1.49	7.65	0.38	1.02	7.99	210	0.45	1.34	7.52	0.41	1.10	23.21	673	0.72	2.14	7.51	0.45	1.04	11.05	357
L17	0.36	1.49	2.64	0.30	1.01	0.91	127	0.35	1.47	2.88	0.28	1.12	1.51	410	0.35	1.46	2.42	0.27	1.01	0.94	128
L18	0.52	1.94	8.65	0.52	1.04	1.14	154	0.38	1.42	7.59	0.61	1.03	1.35	363	0.25	0.93	8.95	0.59	1.04	1.04	193
L19	0.17	1.01	0.69	0.14	0.98	0.95	29	0.20	1.19	3.60	0.51	0.98	0.98	97	0.17	1.04	4.96	0.49	1.00	1.01	69
L20	0.32	1.64	6.76	0.29	1.02	1.21	85	0.26	1.36	7.52	0.33	1.07	1.56	276	0.25	1.27	9.23	0.35	1.02	1.25	115
L21	0.40	1.76	2.80	0.56	1.04	1.07	76	0.30	1.32	3.13	0.45	1.01	1.09	261	0.25	1.10	4.71	0.40	0.99	0.86	75
L22	0.34	1.44	5.00	0.33	0.99	0.93	52	0.32	1.35	6.30	0.39	1.01	1.02	217	0.33	1.41	6.13	0.42	1.02	0.99	66
L23	0.18	0.81	7.66	0.61	1.06	1.24	265	0.28	1.21	7.51	0.58	1.28	2.27	507	0.76	3.33	3.62	0.60	1.05	1.17	175
L24	0.38	1.69	3.99	0.46	1.02	1.01	108	0.31	1.40	4.26	0.42	1.04	1.21	316	0.30	1.33	5.03	0.42	0.99	0.89	169
L25	0.31	1.36	5.12	0.81	1.02	0.97	142	0.32	1.41	4.72	0.85	1.04	1.22	383	0.27	1.18	7.84	0.88	1.02	0.96	173
L26	0.54	1.63	3.35	0.35	1.03	1.08	244	0.48	1.47	3.92	0.31	1.07	1.53	555	0.45	1.36	4.74	0.33	1.03	1.08	294
L27	0.22	1.22	3.66	0.52	1.02	1.83	168	0.23	1.30	3.95	0.58	1.02	6.89	399	0.24	1.36	3.15	0.56	1.05	2.85	232
L28	0.19	0.90	3.87	0.15	1.02	0.89	72	0.22	1.02	4.04	0.17	1.01	1.12	237	0.23	1.07	3.67	0.21	1.02	1.04	100
L29	0.37	1.42	6.64	0.64	1.08	1.04	94	0.31	1.23	4.76	0.62	1.03	1.25	299	0.34	1.34	5.67	0.61	1.01	0.94	156
L30	0.29	1.22	1.67	0.82	1.04	1.54	63	0.35	1.48	5.28	0.46	1.05	1.08	206	0.41	1.74	5.10	0.55	1.01	0.90	106
L31	0.28	1.39	7.43	0.35	1.01	1.02	77	0.18	0.89	8.44	0.30	1.50	1.17	244	0.28	1.37	6.47	0.25	1.00	0.94	115
L32	0.16	0.77	9.50	0.70	1.03	1.11	201	0.24	1.16	10.64	0.70	1.26	2.43	327	1.24	5.95	6.79	0.58	1.01	0.99	95
L33	0.29	1.51	5.90	0.87	1.01	0.99	126	0.26	1.36	3.77	0.88	1.08	1.33	368	0.26	1.32	4.10	0.86	1.00	0.91	139
L34	0.06	0.31	7.63	0.92	1.07	1.04	229	0.21	1.11	6.13	0.87	1.03	1.20	345	0.13	0.71	8.56	0.89	1.01	0.91	151
L35	0.26	1.26	4.24	0.70	0.95	0.87	69	0.28	1.36	3.31	0.78	1.02	1.11	272	0.30	1.47	2.89	0.70	1.00	0.90	174
L36	0.27	1.56	2.84	0.29	1.03	1.01	83	0.23	1.37	3.21	0.26	1.25	1.23	297	0.20	1.20	3.29	0.30	1.03	0.96	199
L37	0.17	0.71	6.34	0.53	1.01	0.98	82	0.19	0.84	5.21	0.50	1.02	1.06	249	0.18	0.80	7.52	0.34	1.01	0.98	72
L38	0.39	1.67	4.09	0.39	1.02	0.96	64	0.35	1.49	4.18	0.38	1.00	1.05	232	0.24	1.03	6.96	0.37	1.01	1.06	79
L39	0.36	1.62	3.16	0.27	1.00	1.01	96	0.33	1.47	3.77	0.32	1.10	1.56	311	0.30	1.32	3.25	0.31	1.01	0.90	132
L40	0.40	1.42	2.55	0.20	1.04	1.11	232	0.39	1.39	2.65	0.19	1.15	1.58	597	0.34	1.22	2.77	0.17	1.02	0.97	260
L41	0.51	2.26	5.63	0.53	0.97	0.95	81	0.33	1.47	7.59	0.56	1.03	1.33	255	0.30	1.33	8.73	0.50	0.99	0.91	108
L42	0.37	1.60	4.80	0.37	0.99	1.08	95	0.28	1.19	4.07	0.38	1.02	1.42	259	0.26	1.11	4.11	0.38	1.03	1.46	149
L43	0.37	1.61	6.28	0.28	1.00	0.92	89	0.32	1.40	4.73	0.29	1.03	1.25	246	0.32	1.42	6.48	0.29	1.03	0.90	137
L44	0.32	1.39	6.67	0.73	1.05	1.00	110	0.18	0.79	7.31	0.84	1.02	1.08	263	0.29	1.25	8.04	0.82	1.02	0.92	121
L45	0.44	1.50	2.93	0.47	1.03	1.04	143	0.39	1.31	3.06	0.40	1.06	1.45	349	0.4	1.53	3.08	0.45	1.00	1.00	195
L46	0.35	1.43	5.48	0.23	1.05	1.08	74	0.27	1.12	6.38	0.39	1.06	1.73	216	0.37	1.51	5.81	0.33	1.04	1.16	128
L47	0.31	1.27	8.90	0.67	1.13	1.46	357	0.33	1.33	9.29	0.63	1.19	1.85	694	0.29	1.19	9.37	0.72	1.04	1.07	282

**Table A2**  
(Continued)

ID	g-band							r-band							i-band						
	$\Theta_e$	$R_e$	$n$	$q$	$\chi^2$	$\chi'^2$	S/N	$\Theta_e$	$R_e$	$n$	$q$	$\chi^2$	$\chi'^2$	S/N	$\Theta_e$	$R_e$	$n$	$q$	$\chi^2$	$\chi'^2$	S/N
L48	0.22	1.20	6.55	0.33	1.00	0.93	23	0.36	1.99	7.11	0.47	1.01	1.03	109	0.23	1.30	6.66	0.44	1.01	1.00	39
L49	0.29	1.60	5.37	0.54	0.99	1.00	56	0.14	0.78	6.90	0.41	1.04	1.29	198	0.22	1.23	3.24	0.51	1.03	0.93	107
L50	0.08	0.47	6.49	0.52	0.99	0.91	65	0.19	1.11	9.04	0.48	1.04	1.11	114	0.61	3.63	1.10	0.65	1.06	1.20	72
L51	0.06	0.35	5.39	0.64	1.09	1.17	265	0.13	0.74	9.21	0.89	1.04	1.09	272	0.26	1.51	7.55	0.86	1.02	1.00	89
L52	0.14	0.76	6.14	0.28	1.05	1.02	54	0.09	0.51	4.83	0.32	1.04	1.25	239	0.13	0.74	4.45	0.28	1.02	0.96	105
L53	0.34	1.35	6.48	0.34	1.00	0.99	74	0.34	1.38	6.36	0.31	1.05	1.34	282	0.44	1.76	3.91	0.29	1.00	0.98	207
L54	0.36	1.59	4.71	0.46	1.02	0.94	106	0.29	1.29	5.14	0.43	1.04	1.18	286	0.30	1.34	3.52	0.43	1.03	0.97	159
L55	0.81	4.84	9.20	0.76	0.99	1.01	24	0.18	1.06	9.19	0.61	1.01	1.17	114	0.11	0.69	8.62	0.59	1.00	1.01	50

**Notes.** For each band, we show: (a) circularized effective radius  $\Theta_e$ , measured in arcsec, (b) circularized effective radius  $R_e$ , measured in kpc (calculated using  $z_{\text{phot}}$  values listed in Table 1), (c) Sérsic index  $n$ , (d) axis ratio  $q$ , (e)  $\chi^2$  of the surface photometry fit, (f)  $\chi'^2$  of the surface photometry fit including only central pixels, and (g) the signal-to-noise ratio S/N of the photometric images, defined as the inverse of the error in MAG\_AUTO.

## ORCID iDs

Diana Scognamiglio  <https://orcid.org/0000-0001-8450-7885>  
 Crescenzo Tortora  <https://orcid.org/0000-0001-7958-6531>  
 Marilena Spavone  <https://orcid.org/0000-0002-6427-7039>  
 Chiara Spiniello  <https://orcid.org/0000-0002-3909-6359>  
 Nicola R. Napolitano  <https://orcid.org/0000-0003-0911-8884>  
 Giuseppe D'Ago  <https://orcid.org/0000-0001-9697-7331>  
 Francesco La Barbera  <https://orcid.org/0000-0003-1181-6841>  
 Fedor Getman  <https://orcid.org/0000-0003-1550-0182>  
 Mario Radovich  <https://orcid.org/0000-0002-3585-866X>  
 Massimo Brescia  <https://orcid.org/0000-0001-9506-5680>  
 Stefano Cavuoti  <https://orcid.org/0000-0002-3787-4196>  
 Léon V. E. Koopmans  <https://orcid.org/0000-0003-1840-0312>  
 Giuseppe Longo  <https://orcid.org/0000-0002-9182-8414>

## References

- Ahn, C. P., Alexandroff, R., Allende Prieto, C., et al. 2012, *ApJS*, 203, 21  
 Ahn, C. P., Alexandroff, R., Allende Prieto, C., et al. 2014, *ApJS*, 211, 17  
 Arnouts, S., Cristiani, S., Moscardini, L., et al. 1999, *MNRAS*, 310, 540  
 Beasley, M. A., Trujillo, I., Leaman, R., & Montes, M. 2018, *Natur*, 555, 483  
 Bertin, E., & Arnouts, S. 1996, *A&AS*, 117, 393  
 Blake, C., Amon, A., Childress, M., et al. 2016, *MNRAS*, 462, 4240  
 Brescia, M., Cavuoti, S., D'Abrusco, R., Longo, G., & Mercurio, A. 2013, *ApJ*, 772, 140  
 Brescia, M., Cavuoti, S., Longo, G., & De Stefano, V. 2014, *A&A*, 568, A126  
 Bruzual, G., & Charlot, S. 2003, *MNRAS*, 344, 1000  
 Buitrago, F., Ferreras, I., Kelvin, L. S., et al. 2018, *A&A*, 619, A137  
 Capaccioli, M., & Schipani, P. 2011, *Msngr*, 146, 2  
 Cappellari, M. 2017, *MNRAS*, 466, 798  
 Cappellari, M., Bacon, R., Bureau, M., et al. 2006, *MNRAS*, 366, 1126  
 Cappellari, M., McDermid, R. M., Alatalo, K., et al. 2012, *Natur*, 484, 485  
 Cavuoti, S., Brescia, M., De Stefano, V., & Longo, G. 2015a, *ExA*, 39, 45  
 Cavuoti, S., Brescia, M., Tortora, C., et al. 2015b, *MNRAS*, 452, 3100  
 Cavuoti, S., Tortora, C., Brescia, M., et al. 2017, *MNRAS*, 466, 2039  
 Chabrier, G. 2001, *ApJ*, 554, 1274  
 Chabrier, G., Hennebelle, P., & Charlot, S. 2014, *ApJ*, 2, 75  
 Charbonnier, A., Huertas-Company, M., Gonçalves, T. S., et al. 2017, *MNRAS*, 469, 4523  
 Conroy, C., & van Dokkum, P. 2012, *ApJ*, 747, 69  
 Daddi, E., Renzini, A., Pirzkal, N., et al. 2005, *ApJ*, 626, 680  
 Damjanov, I., Abraham, R., Glazebrook, K., et al. 2011, *ApJL*, 739, L44  
 Damjanov, I., Abraham, R. G., McCarthy, P. J., & Glazebrook, K. 2009, *BAAS*, 41, 512  
 Damjanov, I., Geller, M. J., Zahid, H. J., & Hwang, H. S. 2015a, *ApJ*, 806, 158  
 Damjanov, I., Hwang, H. S., Geller, M. J., & Chilingarian, I. 2014, *ApJ*, 793, 39  
 Damjanov, I., Zahid, H. J., Geller, M. J., & Hwang, H. S. 2015b, *ApJ*, 806, 158  
 D'Ago, G., Napolitano, R. N., Tortora, C., Spiniello, C., & La Barbera, F. 2018, Central velocity dispersions of the GAMA spectroscopic database and synergies with KiDS, Zenodo, doi:10.5281/zenodo.1303318  
 de Jong, J. T. A., Kleijn, G. A., Erben, T., et al. 2017, *A&A*, 604, A134  
 de Jong, J. T. A., Verdoes Kleijn, G. A., Boxhoorn, D. R., et al. 2015, *A&A*, 582, A62  
 Dekel, A., & Burkert, A. 2014, *MNRAS*, 438, 1870  
 Driver, S. P., Hill, D. T., Kelvin, L. S., et al. 2011, *MNRAS*, 413, 971  
 Edge, A., Sutherland, W. & The Viking Team 2014, *yCat*, 2329, 0  
 Faber, S. M., & Jackson, R. E. 1976, *ApJ*, 204, 668  
 Fasano, G., Marmo, C., Varela, J., et al. 2006, *A&A*, 445, 805  
 Ferré-Mateu, A., Mezcuca, M., Trujillo, I., Balcells, M., & van den Bosch, R. C. E. 2015, *ApJ*, 808, 79  
 Ferré-Mateu, A., Trujillo, I., Martín-Navarro, I., et al. 2017, *MNRAS*, 467, 1929  
 Ferré-Mateu, A., Vazdekis, A., Trujillo, I., Sánchez-Blázquez, P., Ricciardelli, E., & de la Rosa, I. G. 2012, *MNRAS*, 423, 632  
 Gargiulo, A., Bolzonella, M., Scodreggio, M., et al. 2016, *A&A*, 592, A132  
 Guo, Q., White, S., Angulo, R. E., et al. 2013, *MNRAS*, 428, 1351  
 Guo, Q., White, S., Boylan-Kolchin, M., et al. 2011, *MNRAS*, 413, 101  
 Hopkins, A. M., Driver, S. P., Brough, S., et al. 2013, *MNRAS*, 430, 2047  
 Hopkins, P. F., Hernquist, L., Cox, T. J., Keres, D., & Wuyts, S. 2009, *ApJ*, 691, 1424  
 Hsu, L.-Y., Stockton, A., & Shih, H.-Y. 2014, *ApJ*, 796, 92  
 Hyde, J. B., & Bernardi, M. 2009, *MNRAS*, 394, 1978  
 Ilbert, O., Arnouts, S., McCracken, H. J., et al. 2006, *A&A*, 457, 841  
 Komatsu, E., Smith, K. M., Dunkley, J., et al. 2011, *ApJS*, 192, 18  
 La Barbera, F., de Carvalho, R. R., de La Rosa, I. G., et al. 2010, *MNRAS*, 408, 1313  
 La Barbera, F., de Carvalho, R. R., Kohl-Moreira, J. L., et al. 2008, *PASP*, 120, 681  
 La Barbera, F., Ferreras, I., Vazdekis, A., et al. 2013, *MNRAS*, 433, 3017  
 Lasker, R., van den Bosch, R. C. E., van de Ven, G., et al. 2013, *MNRAS*, 434, L31  
 Maraston, C., Pforr, J., Henriques, B. M., et al. 2013, *MNRAS*, 435, 2764  
 Martín-Navarro, I., La Barbera, F., Vazdekis, A., et al. 2015, *MNRAS*, 451, 1081  
 Oser, L., Ostriker, J. P., Naab, T., Johansson, P. H., & Burkert, A. 2010, *ApJ*, 725, 2312  
 Poggianti, B. M., Calvi, R., Bindoni, D., et al. 2013a, *ApJ*, 762, 77  
 Poggianti, B. M., Moretti, A., Calvi, R., et al. 2013b, *ApJ*, 77, 125  
 Quilis, V., & Trujillo, I., 2013, *ApJL*, 773, L8  
 Roy, N., Napolitano, N. R., La Barbera, F., et al. 2018, *MNRAS*, 480, 1057  
 Saulder, C., van den Bosch, R. C. E., & Mieske, S. 2015, *A&A*, 578, A134  
 Schlafly, E. F., & Finkbeiner, D. P. 2011, *ApJ*, 737, 103  
 Shih, H.-Y., & Stockton, A. 2011, *ApJ*, 733, 45  
 Spiniello, C., Barnabè, M., Koopmans, L. V. E., & Trager, S. C. 2015, *MNRAS*, 452, L21  
 Spiniello, C., Trager, S., Koopmans, L. V. E., & Conroy, C. 2014, *MNRAS*, 438, 1483  
 Spiniello, C., Trager, S. C., Koopmans, L. V. E., & Chen, Y. P. 2012, *ApJL*, 753, L32  
 Stockton, A., Shih, H.-Y., Larson, K., & Mann, A. W. 2014, *ApJ*, 780, 134  
 Stringer, M., Trujillo, I., Dalla Vecchia, C., & Martínez-Valpuesta, I. 2015, *MNRAS*, 449, 2396  
 Taylor, E. N., Franx, M., Glazebrook, K., et al. 2010, *ApJ*, 720, 723  
 Toft, S., Gallazzi, A., Zirm, A., et al. 2012, *ApJ*, 754, 3  
 Tortora, C., Napolitano, N. R., La Barbera, F., et al. 2016, *MNRAS*, 457, 2845  
 Tortora, C., Napolitano, N. R., Roy, N., et al. 2018a, *MNRAS*, 473, 969  
 Tortora, C., Napolitano, N. R., Saglia, R. P., et al. 2014, *MNRAS*, 445, 162  
 Tortora, C., Napolitano, N. R., & Spavone, M. 2018b, *MNRAS*, 481, 4728  
 Tortora, C., Romanowsky, A. J., & Napolitano, N. R. 2013, *ApJ*, 765, 8  
 Trenti, M., & Stiavelli, M. 2008, *ApJ*, 676, 767  
 Trujillo, I., Cenarro, A. J., de Lorenzo-Cáceres, A., et al. 2009, *ApJL*, 692, L118  
 Trujillo, I., Ferré-Mateu, A., Balcells, M., Vazdekis, A., & Sánchez-Blázquez, P. 2014, *ApJL*, 780, L20  
 Trujillo, I., Förster Schreiber, N. M., Rudnick, G., et al. 2006, *ApJ*, 650, 18  
 Valentinuzzi, T., Fritz, J., Poggianti, B. M., et al. 2010, *ApJ*, 712, 226  
 van den Bosch, R. C. E., Gebhardt, K., & Gültekin, K. 2015, *ApJS*, 218, 10  
 van den Bosch, R. C. E., Gebhardt, K., Gültekin, K., et al. 2012, *Natur*, 491, 729  
 van Dokkum, P. G., Kriek, M., & Franx, M. 2009, *Natur*, 460, 717  
 van Dokkum, P. G., Whitaker, K. E., Brammer, G., et al. 2010, *ApJ*, 709, 1018  
 Vazdekis, A., Sánchez-Blázquez, P., Falcón-Barroso, J., et al. 2010, *MNRAS*, 404, 1639  
 Wellons, S., Torrey, P., Ma, C. P., et al. 2015, *MNRAS*, 449, 361  
 Wellons, S., Torrey, P., Ma, C. P., et al. 2016, *MNRAS*, 456, 1030  
 Werner, N., Lakhchaura, K., Canning, R. E. A., Gaspari, M., & Simionescu, A. 2018, *MNRAS*, 477, 3886  
 Wright, A. H., Hildebrandt, H., Kuijken, K., et al. 2019, *A&A*, 632, A34  
 Yıldırım, A., van den Bosch, R. C. E., van de Ven, G., et al. 2015, *MNRAS*, 452, 1792



---

## Bibliography

---

- Abadi M. G., Navarro J. F., Steinmetz M., 2006, *Monthly Notices of the Royal Astronomical Society*, 365, 747
- Ahn C. P., et al., 2014, *Astrophysical Journal Supplement Series*, 211, 17
- Albrecht A., et al., 2006, Report of the Dark Energy Task Force, doi:10.48550/ARXIV.ASTRO-PH/0609591, <https://arxiv.org/abs/astro-ph/0609591>
- Amara A., Réfrégier A., 2008, *Monthly Notices of the Royal Astronomical Society*, 391, 228
- Amendola L., et al., 2013, *Living Reviews in Relativity*, 16
- Baldry I. K., Sullivan T., Rani R., Turner S., 2020, *Monthly Notices of the Royal Astronomical Society*, 500, 1557
- Bartelmann M., 2010, *Classical and Quantum Gravity*, 27, 233001
- Baugh C. M., 1996, *Monthly Notices of the Royal Astronomical Society*, 280, 267
- Belli S., Newman A. B., Ellis R. S., Konidaris N. P., 2014, *The Astrophysical Journal*, 788, L29
- Bernstein G. M., 2010, *Monthly Notices of the Royal Astronomical Society*, 406, 2793
- Bernstein G. M., Armstrong R., 2014, *Monthly Notices of the Royal Astronomical Society*, 438, 1880
- Bernstein G. M., Jarvis M., 2002, *The Astronomical Journal*, 123, 583
- Bertin E., Arnouts S., 1996a, *Astronomy & Astrophysics Supplement*, 117, 393

- Bertin E., Arnouts S., 1996b, *Astronomy & Astrophysics Supplement*, 117, 393
- Bertone E., Chavez M., 2011, *Astrophysics & Space Science*, 335, 69
- Bharadwaj S., Sethi S. K., Saini T. D., 2009, *Physical Review D*, 79, 083538
- Blinnikov S. I., Baklanov P. V., Kozyreva A. V., Sorokina E. I., 2005, in Turatto M., Benetti S., Zampieri L., Shea W., eds, *Astronomical Society of the Pacific Conference Series Vol. 342, 1604-2004: Supernovae as Cosmological Lighthouses*. p. 382 ([arXiv:astro-ph/0409396](https://arxiv.org/abs/astro-ph/0409396))
- Bradley L., et al., 2020, *astropy/photutils: 1.0.0*, doi:10.5281/zenodo.4044744, <https://doi.org/10.5281/zenodo.4044744>
- Brescia M., Cavuoti S., D'Abrusco R., Longo G., Mercurio A., 2013, *The Astrophysical Journal*, 772, 140
- Brescia M., Cavuoti S., Longo G., De Stefano V., 2014, *Astronomy & Astrophysics*, 568, A126
- Bridle S., et al., 2009, *Annals of Applied Statistics*, 3
- Bridle S., et al., 2010, *Monthly Notices of the Royal Astronomical Society*, 405, 2044
- Bruzual G., Charlot S., 2003, *Monthly Notices of the Royal Astronomical Society*, 344, 1000
- Buitrago F., Ferreras I., 2019, in Montesinos B., Asensio Ramos A., Buitrago F., Schödel R., Villaver E., Pérez-Hoyos S., Ordóñez-Etxeberria I., eds, *Highlights on Spanish Astrophysics X*. pp 204–204
- Buitrago F., Trujillo I., Conselice C. J., 2008, ] 10.48550/ARXIV.0811.2931
- Buitrago F., et al., 2018, *Astronomy & Astrophysics*, 619, A137
- Cappellari M., 2017, *Monthly Notices of the Royal Astronomical Society*, 466, 798
- Cappellari M., et al., 2011, *Monthly Notices of the Royal Astronomical Society*, 413, 813
- Carollo C. M., et al., 2013, *The Astrophysical Journal*, 773, 112
- Cassata P., et al., 2013, *The Astrophysical Journal*, 775, 106
- Cattaneo A., et al., 2009, *Nature*, 460, 213
- Cava A., et al., 2017, *Astronomy & Astrophysics*, 606, A108



- Cavuoti S., Brescia M., De Stefano V., Longo G., 2015, *Experimental Astronomy*, 39, 45
- Charbonnier A., et al., 2017, *Monthly Notices of the Royal Astronomical Society*, 469, 4523
- Conti I. F., Herbonnet R., Hoekstra H., Merten J., Miller L., Viola M., 2017, *Monthly Notices of the Royal Astronomical Society*, p. stx200
- Cox C., Niemi S.-M., 2011, in *Technical report, Evaluation of a temperature-based HST Focus model.*
- Cropper M., et al., 2013, *Monthly Notices of the Royal Astronomical Society*, 431, 3103
- Cropper M., et al., 2016, *Space Telescopes and Instrumentation 2016: Optical, Infrared, and Millimeter Wave*
- Cypriano E. S., Amara A., Voigt L. M., Bridle S. L., Abdalla F. B., Réfrégier A., Seiffert M., Rhodes J., 2010, *Monthly Notices of the Royal Astronomical Society*, 405, 494
- D'Ago G., Napolitano R. N., Tortora C., Spiniello C., La Barbera F., 2018, in *VST in the Era of the Large Sky Surveys*. p. 15, doi:10.5281/zenodo.1303318
- Daddi E., et al., 2005, *The Astrophysical Journal*, 626, 680
- Damjanov I., et al., 2011, *The Astrophysical Journal*, 739, L44
- Damjanov I., Hwang H. S., Geller M. J., Chilingarian I., 2014, *The Astrophysical Journal*, 793, 39
- Damjanov I., Geller M. J., Zahid H. J., Hwang H. S., 2015, *The Astrophysical Journal*, 806, 158
- Dekel A., Burkert A., 2013, *Monthly Notices of the Royal Astronomical Society*, 438, 1870
- Dyson F. W., Eddington A. S., Davidson C., 1920, *Philosophical Transactions of the Royal Society of London Series A*, 220, 291
- Einstein A., 1915, *Sitzungsberichte der Königlich Preußischen Akademie der Wissenschaften (Berlin)*, pp 844–847
- Eisenstein D. J., et al., 2011, *The Astronomical Journal*, 142, 72
- Er X., et al., 2018, *Monthly Notices of the Royal Astronomical Society*, 476, 5645

- Eriksen M., Hoekstra H., 2018, *Monthly Notices of the Royal Astronomical Society*, 477, 3433
- Evans I. N., Dopita M. A., 1987, *The Astrophysical Journal*, 319, 662
- Fabian A., 2012, *Annual Review of Astronomy & Astrophysics*, 50, 455
- Fasano G., et al., 2006, *Astronomy & Astrophysics*, 445, 805
- Ferré-Mateu A., Trujillo I., Martín-Navarro I., Vazdekis A., Mezcua M., Balcells M., Domínguez L., 2017, *Monthly Notices of the Royal Astronomical Society*, 467, 1929
- Ferré -Mateu A., Forbes D. A., McDermid R. M., Romanowsky A. J., Brodie J. P., 2019, *The Astrophysical Journal*, 878, 129
- Flores-Freitas R., Chies-Santos A. L., Furlanetto C., Rossi M. E. D., Ferreira L., Zenocratti L. J., Alamo-Martínez K. A., 2022, *Monthly Notices of the Royal Astronomical Society*, 512, 245
- Furlong M., et al., 2017, *Monthly Notices of the Royal Astronomical Society*, 465, 722
- Gabrielpillai A., Somerville R. S., Genel S., Rodriguez-Gomez V., Pandya V., Yung L. Y. A., Hernquist L., 2021, *Galaxy Formation in the Santa Cruz semi-analytic model compared with IllustrisTNG – I. Galaxy scaling relations, dispersions, and residuals at z=0*, doi:10.48550/ARXIV.2111.03077, <https://arxiv.org/abs/2111.03077>
- Gillis B. R., Schrabback T., Marggraf O., Mandelbaum R., Massey R., Rhodes J., Taylor A., 2020, *Monthly Notices of the Royal Astronomical Society*, 496, 5017
- Goldstein J. H., et al., 2003, *The Astrophysical Journal*, 599, 773
- Guo Q., et al., 2011, *Monthly Notices of the Royal Astronomical Society*, 413, 101
- Guo Q., White S., Angulo R. E., Henriques B., Lemson G., Boylan-Kolchin M., Thomas P., Short C., 2013, *Monthly Notices of the Royal Astronomical Society*, 428, 1351
- Gurvich A., Mandelbaum R., 2016, *Monthly Notices of the Royal Astronomical Society*, 457, 3522
- Gutkin J., Charlot S., Bruzual G., 2016, *Monthly Notices of the Royal Astronomical Society*, 462, 1757

- Guyonnet A., Astier P., Antilogus P., Regnault N., Doherty P., 2015, *Astronomy & Astrophysics*, 575, A41
- Hartlap J., Schrabback T., Simon P., Schneider P., 2009, *Astronomy & Astrophysics*, 504, 689
- Heckman T. M., Best P. N., 2014, *Annual Review of Astronomy and Astrophysics*, 52, 589
- Henriques B. M. B., White S. D. M., Thomas P. A., Angulo R. E., Guo Q., Lemson G., Wang W., 2017, *Monthly Notices of the Royal Astronomical Society*, 469, 2626
- Hernández-Martín B., et al., 2020, *Astronomy & Astrophysics*, 640, A117
- Heymans C., Heavens A., 2003, *Monthly Notices of the Royal Astronomical Society*, 339, 711
- Heymans C., et al., 2006, *Monthly Notices of the Royal Astronomical Society*, 368, 1323
- Heymans C., et al., 2012, *MNRAS*, 427, 146
- Hildebrandt H., et al., 2017, *Monthly Notices of the Royal Astronomical Society*, 465, 1454
- Hirata C., Seljak U., 2003, *Monthly Notices of the Royal Astronomical Society*, 343, 459
- Hirata C. M., et al., 2004, *Monthly Notices of the Royal Astronomical Society*, 353, 529
- Hoekstra H., Franx M., Kuijken K., Squires G., 1998, *The Astrophysical Journal*, 504, 636
- Hoekstra H., Franx M., Kuijken K., 2000, *The Astrophysical Journal*, 532, 88
- Hoekstra H., Viola M., Herbonnet R., 2017, *Monthly Notices of the Royal Astronomical Society*, 468, 3295
- Hoekstra H., Kannawadi A., Kitching T. D., 2021, *Astronomy & Astrophysics*, 646, A124
- Hopkins P. F., Cox T. J., Dutta S. N., Hernquist L., Kormendy J., Lauer T. R., 2009, *The Astrophysical Journal*, 181, 135
- Hopkins P. F., Quataert E., Murray N., 2012, *Monthly Notices of the Royal Astronomical Society*, 421, 3522

- Howell S. B., 1989, *PASP*, 101, 616
- Hubble E. P., 1926, *The Astrophysical Journal*, 64, 321
- Huff E., Mandelbaum R., 2017, *Metacalibration: Direct Self-Calibration of Biases in Shear Measurement*, doi:10.48550/ARXIV.1702.02600, <https://arxiv.org/abs/1702.02600>
- Hurtado-Gil L., Stoica R. S., Martínez V. J., Arnalte-Mur P., 2021, *Monthly Notices of the Royal Astronomical Society*, 507, 1710
- Huterer D., Takada M., Bernstein G., Jain B., 2006, *Monthly Notices of the Royal Astronomical Society*, 366, 101
- Ivezić Ž., et al., 2019, *The Astrophysical Journal*, 873, 111
- Jarvis M., et al., 2016, *Monthly Notices of the Royal Astronomical Society*, 460, 2245
- Joachimi B., Schneider P., 2010, *Astronomy & Astrophysics*, 517, A4
- Johansson P. H., Naab T., Ostriker J. P., 2009, *The Astrophysical Journal*, 697, L38
- Kacprzak T., Bridle S., Rowe B., Voigt L., Zuntz J., Hirsch M., MacCrann N., 2014, *Monthly Notices of the Royal Astronomical Society*, 441, 2528
- Kaiser N., 2000, *The Astrophysical Journal*, 537, 555
- Kaiser N., Squires G., 1993, *The Astrophysical Journal*, 404, 441
- Kaiser N., Squires G., Broadhurst T., 1995, *The Astrophysical Journal*, 449, 460
- Kamath S., Meyers J. E., and P. R. B., 2019, *The Astrophysical Journal*, 888, 23
- Kannawadi A., et al., 2019, *Astronomy & Astrophysics*, 624, A92
- Katz N., Gunn J. E., 1991, *The Astrophysical Journal*, 377, 365
- Kewley L. J., Dopita M. A., 2002, *The Astrophysical Journal*, 142, 35
- Kewley L. J., Nicholls D. C., Sutherland R. S., 2019, *Annual Review of Astronomy and Astrophysics*, 57, 511
- Kilbinger M., 2015, *Reports on Progress in Physics*, 78, 086901
- King L., Schneider P., 2002, *Astronomy & Astrophysics*, 396, 411
- Kitching T., et al., 2011, *The Annals of Applied Statistics*, 5

- Kitching T. D., et al., 2012, *Monthly Notices of the Royal Astronomical Society*, 423, 3163
- Kitching T. D., et al., 2013, *Astrophysical Journal Supplement Series*, 205, 12
- Komatsu E., et al., 2011, *Astrophysical Journal Supplement Series*, 192, 18
- Kormendy J., Ho L. C., 2013, *Annual Review of Astronomy & Astrophysics*, 51, 511
- Krist J., 1993, in Hanisch R. J., Brissenden R. J. V., Barnes J., eds, *Astronomical Society of the Pacific Conference Series Vol. 52, Astronomical Data Analysis Software and Systems II*. p. 536
- Krist J. E., Hook R. N., Stoehr F., 2011, in Kahan M. A., ed., *Society of Photo-Optical Instrumentation Engineers (SPIE) Conference Series Vol. 8127, Optical Modeling and Performance Predictions V*. p. 81270J, doi:10.1117/12.892762
- LSST Science Collaboration et al., 2009, arXiv e-prints, p. arXiv:0912.0201
- La Barbera F., de Carvalho R. R., Kohl-Moreira J. L., Gal R. R., Soares-Santos M., Capaccioli M., Santos R., Sant'anna N., 2008, *Publications of the Astronomical Society of the Pacific*, 120, 681
- La Barbera F., de Carvalho R. R., de La Rosa I. G., Lopes P. A. A., Kohl-Moreira J. L., Capelato H. V., 2010, *Monthly Notices of the Royal Astronomical Society*, 408, 1313
- Lallo M. D., Makidon R. B., Casertano S., Krist J. E., 2006, in Silva D. R., Doxsey R. E., eds, *Society of Photo-Optical Instrumentation Engineers (SPIE) Conference Series Vol. 6270, Society of Photo-Optical Instrumentation Engineers (SPIE) Conference Series*. p. 62701N, doi:10.1117/12.672040
- Lanusse F., Mandelbaum R., Ravanbakhsh S., Li C.-L., Freeman P., Póczos B., 2021, *Monthly Notices of the Royal Astronomical Society*, 504, 5543–5555
- Laureijs R., et al., 2011a, *Euclid Definition Study Report* ([arXiv:1110.3193](https://arxiv.org/abs/1110.3193))
- Laureijs R., et al., 2011b, arXiv e-prints, p. arXiv:1110.3193
- Leauthaud A., et al., 2007, *Astrophysical Journal Supplement Series*, 172, 219
- Lee J., et al., 2021, *The Astrophysical Journal*, 908, 11
- Luppino G. A., Kaiser N., 1997a, *The Astrophysical Journal*, 475, 20
- Luppino G. A., Kaiser N., 1997b, *The Astrophysical Journal*, 475, 20–28
- Mandelbaum R., 2018, *Annual Review of Astronomy & Astrophysics*, 56, 393

- Mandelbaum R., Hirata C. M., Leauthaud A., Massey R. J., Rhodes J., 2012, *Monthly Notices of the Royal Astronomical Society*, 420, 1518
- Mandelbaum R., et al., 2014a, *The Astrophysical Journal*, 212, 5
- Mandelbaum R., et al., 2014b, *Astrophysical Journal Supplement Series*, 212, 5
- Mandelbaum R., et al., 2015, *Monthly Notices of the Royal Astronomical Society*, 450, 2963–3007
- Maraston C., 1998, *Monthly Notices of the Royal Astronomical Society*, 300, 872
- Martinet N., et al., 2019, *Astronomy & Astrophysics*, 627, A59
- Massey R., 2010, *Monthly Notices of the Royal Astronomical Society*, 409, L109–L113
- Massey R., et al., 2007a, *Monthly Notices of the Royal Astronomical Society*, 376, 13
- Massey R., et al., 2007b, *Monthly Notices of the Royal Astronomical Society*, 376, 13
- Massey R., et al., 2012, *Monthly Notices of the Royal Astronomical Society*, 429, 661–678
- Massey R., et al., 2014, *Monthly Notices of the Royal Astronomical Society*, 439, 887
- Melchior P., Viola M., 2012, *Monthly Notices of the Royal Astronomical Society*, 424, 2757–2769
- Meyers J. E., Burchat P. R., 2015, *The Astrophysical Journal*, 807, 182
- Miller L., et al., 2013, *Monthly Notices of the Royal Astronomical Society*, 429, 2858–2880
- Miralles J. M., Erben T., Hämmerle H., Schneider P., Freudling W., Pirzkal N., Fosbury R. A. E., 2005, *Astronomy & Astrophysics*, 432, 797
- Naab T., Johansson P. H., Ostriker J. P., 2009a, *The Astrophysical Journal*, 699, L178
- Naab T., Johansson P. H., Ostriker J. P., 2009b, *The Astrophysical Journal*, 699, L178
- Naab T., et al., 2014, *Monthly Notices of the Royal Astronomical Society*, 444, 3357

- Nakajima R., Bernstein G., 2007, *The Astronomical Journal*, 133, 1763–1779
- Narayanan D., et al., 2021, *Astrophysical Journal Supplement Series*, 252, 12
- Niemi S.-M., Cropper M., Szafraniec M., Kitching T., 2015, *Experimental Astronomy*, 39, 207
- Nipoti C., Treu T., Bolton A. S., 2009a, *The Astrophysical Journal*, 703, 1531
- Nipoti C., Treu T., Auger M. W., Bolton A. S., 2009b, *The Astrophysical Journal*, 706, L86
- Oser L., Ostriker J. P., Naab T., Johansson P. H., Burkert A., 2010a, *The Astrophysical Journal*, 725, 2312
- Oser L., Ostriker J. P., Naab T., Johansson P. H., Burkert A., 2010b, *The Astrophysical Journal*, 725, 2312
- Paulin-Henriksson S., Amara A., Voigt L., Refregier A., Bridle S. L., 2008, *Astronomy & Astrophysics*, 484, 67–77
- Peebles P. J. E., 1978, *Astronomy & Astrophysics*, 68, 345
- Peebles P. J. E., 1982, *The Astrophysical Journal*, 258, 415
- Perlmutter S., et al., 1999, *The Astrophysical Journal*, 517, 565
- Pires S., et al., 2020, *Astronomy & Astrophysics*, 638, A141
- Planck Collaboration et al., 2020, *Astronomy & Astrophysics*, 641, A6
- Plazas A. A., Bernstein G., 2012, *Publications of the Astronomical Society of the Pacific*, 124, 1113
- Plazas A. A., Shapiro C., Smith R., Huff E., Rhodes J., 2018, *Publications of the Astronomical Society of the Pacific*, 130, 065004
- Poggianti B. M., Moretti A., Calvi R., D’Onofrio M., Valentinuzzi T., Fritz J., Renzini A., 2013, *The Astrophysical Journal*, 777, 125
- Pujol A., Kilbinger M., Sureau F., Bobin J., 2018, *Astronomy & Astrophysics*, 621, A2
- Pujol A., Bobin J., Sureau F., Guinot A., Kilbinger M., 2020, *Astronomy & Astrophysics*, 643, A158
- Pulsoni C., Gerhard O., Arnaboldi M., Pillepich A., Rodriguez-Gomez V., Nelson D., Hernquist L., Springel V., 2021, *Astronomy & Astrophysics*, 647, A95

- Quilis V., Trujillo I., 2013, *The Astrophysical Journal*, 773, L8
- Rebolo R., et al., 2004, *Monthly Notices of the Royal Astronomical Society*, 353, 747
- Refregier A., Amara A., Kitching T. D., Rassat A., Scaramella R., Weller J., 2010, *Euclid Imaging Consortium Science Book* ([arXiv:1001.0061](https://arxiv.org/abs/1001.0061))
- Refregier A., Kacprzak T., Amara A., Bridle S., Rowe B., 2012, *Monthly Notices of the Royal Astronomical Society*, 425, 1951–1957
- Rhodes J., Refregier A., Collins N. R., Gardner J. P., Groth E. J., Hill R. S., 2004, *The Astrophysical Journal*, 605, 29
- Rhodes J. D., et al., 2007, *Astrophysical Journal Supplement Series*, 172, 203–218
- Richard J., Kneib J.-P., Ebeling H., Stark D. P., Egami E., Fiedler A. K., 2011, *Monthly Notices of the Royal Astronomical Society: Letters*, 414, L31
- Riess A. G., et al., 1998, *The Astronomical Journal*, 116, 1009
- Robertson H. P., 1935, *The Astrophysical Journal*, 82, 284
- Rowe B. T. P., et al., 2015, *Astronomy and Computing*, 10, 121
- Ryon J. E., 2022, *Version 21.0* (Baltimore: STScI)
- Saulder C., van den Bosch R. C. E., Mieske S., 2015, *Astronomy & Astrophysics*, 578, A134
- Scaramella R., et al., 2022, *Astronomy & Astrophysics*, 662, A112
- Schmidt K. B., et al., 2017, *The Astrophysical Journal*, 839, 17
- Schrabback T., et al., 2010, *Astronomy & Astrophysics*, 516, A63
- Schrabback T., et al., 2018, *Monthly Notices of the Royal Astronomical Society*, 474, 2635
- Schreiber C., et al., 2017, *Astronomy & Astrophysics*, 602, A96
- Scognamiglio D., et al., 2020, *The Astrophysical Journal*, 893, 4
- Secco L., et al., 2022, *Physical Review D*, 105
- Semboloni E., et al., 2013, *Monthly Notices of the Royal Astronomical Society*, 432, 2385



- Sérsic J. L., 1963a, Boletín de la Asociación Argentina de Astronomía La Plata Argentina, 6, 41
- Sérsic J. L., 1963b, Boletín de la Asociación Argentina de Astronomía La Plata Argentina, 6, 41
- Sheldon E. S., Huff E. M., 2017, *The Astrophysical Journal*, 841, 24
- Sheldon E. S., Becker M. R., MacCrann N., Jarvis M., 2020, *The Astrophysical Journal*, 902, 138
- Shen S., Mo H. J., White S. D. M., Blanton M. R., Kauffmann G., Voges W., Brinkmann J., Csabai I., 2003, *Monthly Notices of the Royal Astronomical Society*, 343, 978
- Silk J., Rees M. J., 1998, *Astronomy & Astrophysics*, 331, L1
- Simon, P. King, L. J. Schneider, P. 2004, *Astronomy & Astrophysics*, 417, 873
- Somerville R. S., Davé R., 2015, *Annual Review of Astronomy & Astrophysics*, 53, 51
- Somerville R. S., Primack J. R., 1999, *Monthly Notices of the Royal Astronomical Society*, 310, 1087
- Spergel D., et al., 2015a, Wide-Field Infrared Survey Telescope-Astrophysics Focused Telescope Assets WFIRST-AFTA 2015 Report ([arXiv:1503.03757](https://arxiv.org/abs/1503.03757))
- Spergel D., et al., 2015b, arXiv e-prints, p. [arXiv:1503.03757](https://arxiv.org/abs/1503.03757)
- Spiniello C., et al., 2020, *Astronomy & Astrophysics*, 646, A28
- Spiniello C., et al., 2021, *Astronomy & Astrophysics*, 654, A136
- Springel V., Hernquist L., 2003, *Monthly Notices of the Royal Astronomical Society*, 339, 289
- Springel V., et al., 2005, *Nature*, 435, 629
- Stringer M., Trujillo I., Dalla Vecchia C., Martínez-Valpuesta I., 2015, *Monthly Notices of the Royal Astronomical Society*, 449, 2396
- Szomoru D., Franx M., van Dokkum P. G., 2012, *The Astrophysical Journal*, 749, 121
- Taylor E. N., Franx M., Glazebrook K., Brinchmann J., van der Wel A., van Dokkum P. G., 2010, *The Astrophysical Journal*, 720, 723

- Tewes M., Kuntzer T., Nakajima R., Courbin F., Hildebrandt H., Schrabback T., 2019, *Astronomy & Astrophysics*, 621, A36
- Tortora C., et al., 2016, *Monthly Notices of the Royal Astronomical Society*, 457, 2845
- Tortora C., et al., 2018, *Monthly Notices of the Royal Astronomical Society*, 481, 4728
- Tortora C., et al., 2020, *Astronomy & Astrophysics*, 638, L11
- Trager S. C., Faber S. M., Worthey G., González J. J., 2000, *The Astronomical Journal*, 120, 165
- Troxel M., Ishak M., 2015, *Physics Reports*, 558, 1
- Trujillo I., Cenarro A. J., de Lorenzo-Cáceres A., Vazdekis A., de la Rosa I. G., Cava A., 2009, *The Astrophysical Journal*, 692, L118
- Valentinuzzi T., et al., 2010, *The Astrophysical Journal*, 712, 226
- Vazdekis A., 1999, *The Astrophysical Journal*, 513, 224
- Viola M., Kitching T. D., Joachimi B., 2014, *Monthly Notices of the Royal Astronomical Society*, 439, 1909
- Vogelsberger M., Marinacci F., Torrey P., Puchwein E., 2020, *Nature Reviews Physics*, 2, 42
- Voigt L. M., Bridle S. L., 2010, *Monthly Notices of the Royal Astronomical Society*, 404, 458
- Voigt L. M., Bridle S. L., Amara A., Cropper M., Kitching T. D., Massey R., Rhodes J., Schrabback T., 2012, *Monthly Notices of the Royal Astronomical Society*, 421, 1385–1398
- Wagner J., 2022, Casting the  $H_0$  tension as a fitting problem of cosmologies, doi:10.48550/ARXIV.2203.11219, <https://arxiv.org/abs/2203.11219>
- Walker A. G., 1937, *Proceedings of the London Mathematical Society*, 42, 90
- Wang L.-L., et al., 2018, *Monthly Notices of the Royal Astronomical Society*, 474, 1873
- Wellons S., et al., 2015, *Monthly Notices of the Royal Astronomical Society*, 449, 361

- Wellons S., et al., 2016, *Monthly Notices of the Royal Astronomical Society*, 456, 1030
- Werner N., Lakhchaura K., Canning R. E. A., Gaspari M., Simionescu A., 2018, *Monthly Notices of the Royal Astronomical Society*, 477, 3886
- White S. D. M., Frenk C. S., 1991, *The Astrophysical Journal*, 379, 52
- White S. D. M., Rees M. J., 1978, *Monthly Notices of the Royal Astronomical Society*, 183, 341
- Worthey G., 1994, *The Astrophysical Journal*, 95, 107
- Wu P.-F., et al., 2021, *The Astronomical Journal*, 162, 201
- Zhang J., Komatsu E., 2011, *Monthly Notices of the Royal Astronomical Society*, 414, 1047
- Zolotov A., et al., 2015, *Monthly Notices of the Royal Astronomical Society*, 450, 2327
- de Jong J. T. A., et al., 2015, *Astronomy & Astrophysics*, 582, A62
- de Jong J. T. A., et al., 2017, *Astronomy & Astrophysics*, 604, A134
- de Vaucouleurs G., 1961, *The Astrophysical Journal*, 5, 233
- van Dokkum P. G., et al., 2008a, *The Astrophysical Journal*, 677, L5
- van Dokkum P. G., et al., 2008b, *The Astrophysical Journal*, 677, L5
- van den Bosch R. C. E., Gebhardt K., Gültekin K., van de Ven G., van der Wel A., Walsh J. L., 2012, *Nature*, 491, 729
- van den Bosch R. C. E., Gebhardt K., Gültekin K., Yildirim A., Walsh J. L., 2015, *Astrophysical Journal Supplement Series*, 218, 10



---

## List of Figures

---

2.1.	A representation of the evolution of the Universe. . . . .	6
2.2.	Different cosmological distance measures as a function of redshift $z$ . . .	10
2.3.	Slices through the SDSS 3-dimensional map of the distribution of galaxies obtained by the Sloan Digital Sky Survey (SDSS). . . . .	15
2.4.	The Hubble galaxy classification scheme. . . . .	16
2.5.	The two-phase formation scenario for the mass assembly and cosmic evolution of massive galaxies. . . . .	22
2.6.	UCMGs and relic number densities from $z \sim 0.54$ to the local universe computed from different observations and simulations. . . . .	25
2.7.	Sketch of a gravitational lensing system. . . . .	28
2.8.	Illustration of the first order effect of convergence $\kappa$ and shear $\gamma$ on an intrinsically round source with radius $R_0$ , which is mapped by the inverse Jacobian $A^{-1}$ onto an ellipse. . . . .	31
3.1.	The <i>Euclid</i> spacecraft with its payload and service modules. . . . .	42
3.2.	The HST's control and support systems and the instruments. . . . .	46
3.3.	The HST field-of-view. . . . .	47
3.4.	The Telescopio Nazionale Galileo dome. . . . .	49
3.5.	The Isaac Newton Telescope dome. . . . .	49
4.1.	Illustration of the testing environment to create Direct <i>Euclid</i> -like images to be compared with <i>Euclidized</i> images. . . . .	57
4.2.	Multiplicative (left) and additive (right) shear bias differences obtained employing a <i>Euclid</i> /VIS pixel scale of $0''.1$ . We also report the results employing a Gaussian PSF instead of the <i>Euclid</i> PSF. . . . .	65
4.3.	Results from the galaxy model fits for Test I using the native HST/ACS and <i>Euclid</i> /VIS pixel scales. . . . .	66

4.4.	Multiplicative (left) and additive (right) shear bias differences obtained employing a <i>Euclid</i> /VIS pixel scale of 0''1 and increasing the $S/N$ of the HST-like images by a factor 10. . . . .	67
4.5.	Multiplicative (left) and additive (right) shear bias differences obtained when deliberately using a pixel scale of 0''04. . . . .	67
4.6.	Multiplicative (left) and additive (right) shear bias differences obtained when using a pixel scale of 0''1 for D and a pixel scale of 0''05 that we re-bin to 0''1 for E. We also report the case employing a TinyTim PSF model in the filter F606W. . . . .	69
4.7.	Multiplicative (left) and additive (right) shear bias differences obtained when using a pixel scale of 0''1 for D and a pixel scale of 0''05 that we re-bin to 0''1 for E. We report the case without applying any noise symmetrization and the approach by Sheldon & Huff (2017). . .	70
4.8.	Multiplicative (left) and additive (right) shear bias differences obtained when using two different HST TinyTim PSF models for <i>HST conv</i> and <i>HST deconv</i> and a pixel scale of 0''04 (upper panels). The lower panels show the results applying an extra rotation after the deconvolution. . . . .	71
4.9.	Multiplicative (left) and additive (right) shear bias differences obtained when using a pixel scale of 0''1 for D and a pixel scale of 0''05 that we re-bin to 0''1 for E. We have employed in the euclidization procedure as PSF models a model stack and a star stack. . . . .	72
4.10.	Multiplicative (left) and additive (right) shear bias differences obtained when using a truncation radius for the input galaxies and a pixel scale of 0''04. . . . .	73
4.11.	The statistical parameter $\chi^2$ (on the left) and the quality-of-fit parameter $X^2$ (on the right) for each filter and chip plotted against the best-fit focus value of each of 205 star fields in F606W filter and 645 star fields in F814W filter. . . . .	76
4.12.	TinyTim PSF model stacks without background noise a) and with background noise b) and the residual images without noise c) and with noise d) for a star field observed in the F606W and in the F814W filter. . . . .	77
4.13.	Standard deviation ( $\sigma_{\Delta_f}$ ) of the difference between the recovered focus using bootstrapped star subsamples containing $N_{\text{star}}$ stars and the focus estimated using the full sample, for different sizes of the bootstrap sample for F606W and F814W and for both chips 1 and 2. . . . .	78
4.14.	Comparison between the measured $S/N_{\text{measured}}$ estimated within a customized aperture and with Photutils for D, HST-like, and E as a function of the half-light radius $R_e$ . . . . .	83

---

4.15. The best-fit focus values plotted against each component of the quality-of-fit parameter $Q$ for the filters F814W and F606W and both chips 1 and 2. . . . .	86
4.16. The best-fit focus offset values plotted against the first Principal Component coefficients for 205 star fields in the F606W filter and 640 star fields in the F814W filter and for both chips 1 and 2. . . . .	87
5.1. Two examples of PPXF fits obtained with OMEGA-K on the spectra of two different UCMGs, one of the best $HQ$ system and one of the worse $LQ$ system, thus representative of the whole sample, observed with two different telescopes. . . . .	94
5.2. Number density before and after the correction for systematics, for the analyzed sample in comparison with other studies. . . . .	98
5.3. Distribution on the $M_\star - \sigma$ plane for the 37 confirmed UCMGs compared with a sample of elliptical galaxies from the BOSS survey. . . . .	99





---

## List of Tables

---

4.1. Summary of the tests presented in Chapter 4. . . . .	64
4.2. Mean focus offset for the filter F606W and F814W in both chips 1 and 2. . . . .	79
5.1. Results of the spectroscopic analysis of the objects belonging to the three observational runs presented here: UCMG_INT_2017, UCMG_TNG_2017, UCMG_TNG_2018. . . . .	96
5.2. Same as Table 5.1, but for the samples UCMG_TNG_T18 and UCMG_NTT_T18. . . . .	97



---

## Acknowledgements

---

*“No one who achieves success does so without acknowledging the help of others.”*

- Alfred North Whitehead, *Source Unknown*

Even though I still cannot believe, the time has come to say thanks! Let me start with, first of all, heartfelt thanking my supervisor, Prof. Tim Schrabback. Thanks Tim for your support, advice, help, answering all my questions, clarifying my doubts, reading carefully my thesis (and not only and even during your moving to Austria) and providing comments to improve it. Thanks also for giving me the freedom to pursue my previous project. I would also like to thank my official supervisor Prof. Peter Schneider, for giving me the opportunity to do a PhD in his group and for his guidance in the research. I never thought that reading the ‘Gravitational lenses’ book during my Bachelor studies would lead me to join exactly your group some years later. I want to thank Dr. Malte Tewes, for your time and your work, always helping me to find a solution by making the ‘Euclidization’ procedure a less titanic task. I have learnt a lot from all three of you about cosmology, doing research and being a researcher in general.

I would like to thank the other ‘Euclideans’ of the Argelander-Institut für Astronomie (AIfA): Andres Navarro-Alsina for our complicated chats about the future, Dr. Laila Linke for helping me with the German language, Dr. Patrick Simon for his effort in organizing the lens seminar, Pierre Burger and Dr. Lucas Porth to be so quite but, ready to have a lot of fun, Dr. Reiko Nakajima for your bad and good news about *Euclid*, Sven Heydenreich for the amazing parties at your and Davit (Dato) Alkhanishvili’s place. A special thanks to Dr. Ole Margraff for always solving my computer problems and for retrieving my accidentally deleted

---

work several times.

A warm and heartfelt thanks goes to my *italian family*, which has grown more and more over the past three years. I have to start with the first Italian person I met at the institute, Dr. Luca Grassitelli (aka Nostro Signore). Thanks for our chats, laughs, coffee breaks, pizzas and for always listening me, my complaints and more and more. Thanks to Benedetta Spina (aka Cosetta) for your friendship and our funny adventures together. I will always remember our superlative and delicious ‘2-Michelin-star’ dinners we have prepared together. I cannot imagine having better PhD friends than you, guys!

I also want thank Dr. Emilio Romano Diaz (even if you will be always our ‘Mexican Chaparro’, I want to mention you here, among the Italians ☺), Dr. Giovanna Cenini, Julia Ziganshina, Anna Pugno, Claudia Spinelli, Geremia Torneri, Gabriele Turchetti for the great time we have spent together, for our conversations about random things, gossips, gossips, gossips, which often even included science and, for many other things which is better do not report here.

I would also to thank Florian Kleinebreil and Jonah Wagenfeld for tutoring with me the lab course and sharing exhausting but also funny moments. And a special mention goes to Dr. Hannah Zohren, who was not only a tutoring mate, but we also supported each other, talking about our research project problems and the future. Furthermore, I thank the other AIfA members, present and past: Dr. David Aguilera Dena, Dato Alkhanishvili, Toma Badescu, Dr. Ivana Bešlić, Dr. Matteo Cataneo, Maude Charmetant, Dr. Jakob den Brok, Ankur Dev, Cosima Eibenstein, Dr. Alex Eggemeier, Dr. Kevin Harrington, Dr. Beatriz Hernandez Martin, Christos Karoumpis, Prachi Khatri, Markus Klein, Dr. Joseph Kuruvilla, Fatimah Raihan, Dr. Martin Sommer, Luis Suelves, Dr. Sandra Unruh, Dr. Jan Luca van den Busch, Dr. Eleni Vardoulaki, Tsan-Ming Wang, Dr. Victoria Yankelevich. Each of you has enriched me as a person and I will keep with me the funny moments, the long walks and chats, the trips, the parties, the Daiquiri cocktails, the gossips, the laughs, the driving school classes, the German taxes, the lunches in the AIfA kitchen, the Astronomy on Tap at Fiddler’s and the incursions in my office for the organization, and the advice and the patience in listening my project updates during the weekly meetings. I wish you all the best and thank you for the time spent together.

During the course of the past three years and a half, I had the pleasure to work with many scientists, who contribute to a kind and helpful scientific environment. Being in the *Euclid* Consortium and part of the ‘Enabling Weak lensing Cosmology’ project gave me the opportunity to observe the organisation and management of being part of a team. It has been inspiring and has taught me so much in terms

of team interactions, project organisations, communication and, of course, science. In particular, I thank Prof. Henk Hoekstra for the scientific discussions, precious advice and support.

I also thank Prof. Cristiano Porciani, Prof. Peter Schilke and Prof. Walter Witke for accepting to be members of my thesis committee. Furthermore, thanks to Sabine Derdau and Ellen Fuhrmann, who helped me with the bureaucracy, not always easy to deal with for a foreign student, and the IT infrastructure team for providing solutions even during difficult times. Being a member of the International Max Planck Research School (IMPRS) during my PhD studies, gave me the chance to meet nice fellow PhD students from all over the world and join workshops and conferences. Thus, a special thanks goes to Dr. Rainer Mauersberger and Dr. Simone Pott.

Part of the work presented in this thesis could not have been carried out without my former group from the Observatory of Capodimonte, spread in places all over the world. Starting with Prof. Nicola R. Napolitano: thank you to give me the possibility to be part of your group, for all the scientific discussions and the silly chats, for your constant support and for having always the right word to say in my difficult moments. I am also deeply grateful to Dr. Crescenzo Tortora, Dr. Chiara Spiniello, Dr. Marilena Spavone for the discussions during the regular meetings and not only, to teaching me more about galaxies and spectroscopy. Thank you very much!

Grazie anche a Dr. Luigi Barretta, per il tempo dedicato e per essere sempre pronto ad aiutarmi.

A huge thanks to my parents and to my family, for their constant love, support and curiosity during my PhD experience. Finally, I would like to deeply thank Michele for the support and for making my life better. No matter the distance between us, if separated by 455.6 km or if confined in either 13 or 26 m<sup>2</sup>, you are always by my side ♡.

And now, it is time to dare mighty things...